MEDNARODNA
PODIPLOMSKA ŠOLA
JOŽEFA STEFANA

7. ŠTUDENTSKA KONFERENCA MEDNARODNE PODIPLOMSKE ŠOLE JOŽEFA STEFANA

Zbornik - 1. del

7th JOŽEF STEFAN INTERNATIONAL POSTGRADUATE SCHOOL STUDENTS' CONFERENCE

Proceedings - Part 1

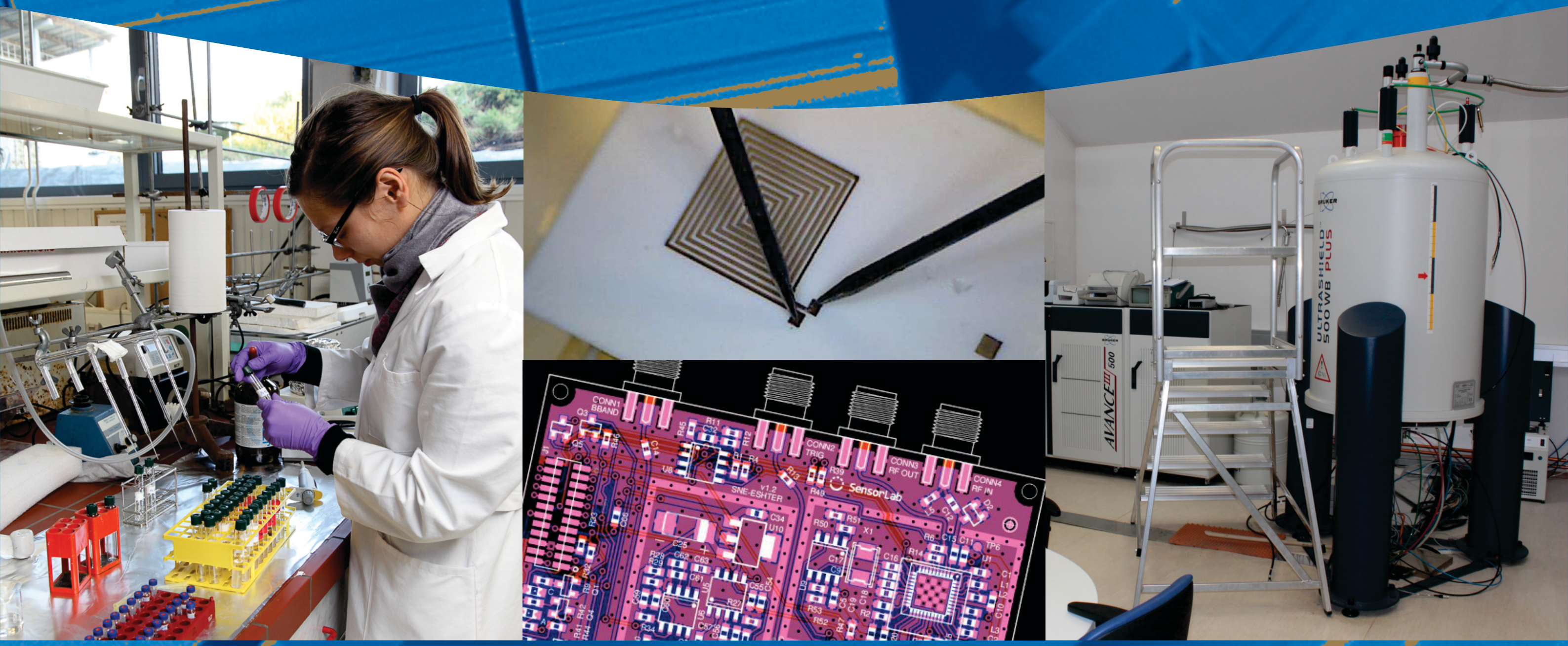

20. - 21. 05. 2015, Ljubljana

Zbornik 7. Študentske konference Mednarodne podiplomske šole Jožefa Stefana
(Proceedings of the 7th Jožef Stefan International Postgraduate School Students Conference)

Uredniki / Editors:
Andraž Rešetič
Ana Kroflič
Aleksander Matavž
Melisa Junuzović
Janja Vidmar
Maja Somrak

Založnik / Publisher:
Mednarodna podiplomska šola Jožefa Stefana, Ljubljana

Dosegljivo na / Attainable at:
http://ipssc.mps.si/2015/proceedingsIPSSC2015Papers.pdf

Ljubljana, maj 2015

Konferenco organizira Študentski Svet Mednarodne podiplomske šole Jožefa Štefana
(The Conference is organized by Jožef Stefan International Postgraduate School - IPS Student Council)

CIP - Kataložni zapis o publikaciji
Narodna in univerzitetna knjižnica, Ljubljana

5/6(082)
378.046-021.68:001.891(497.4)(082)

MEDNARODNA podiplomska šola Jožefa Stefana. Študentska konferenca (7 ; 2015 ; Ljubljana)
Zbornik = Proceedings / 7. študentska konferenca Mednarodne podiplomske šole Jožefa Stefana = 7th Jožef Stefan International Postgraduate School Students' Conference, 20.-22. 5. 2015, Ljubljana ; [organizira študentski svet Mednarodne podiplomske šole Jožefa Štefana = organized by Jožef Stefan International Postgraduate School - IPS Student Council] ; uredili, edited by Andraž Rešetič ... et al.]. - Ljubljana : Mednarodna podiplomska šola Jožefa Stefana, 2015

ISBN 978-961-92871-9-4
1. Rešetič, Andraž 2. Mednarodna podiplomska šola Jožefa Stefana (Ljubljana)
279459840

7. ŠTUDENTSKA KONFERENCA MEDNARODNE PODIPLOMSKE ŠOLE JOŽEFA STEFANA

ZBORNIK - 1. DEL

7th JOŽEF STEFAN INTERNATIONAL POSTGRADUATE SCHOOL STUDENTS' CONFERENCE

PROCEEDINGS - PART 1

Uredili / Edited by

Andraž Rešetič, Ana Kroflič, Aleksander Matavž, Melisa Junuzović, Janja Vidmar
in Maja Somrak

20. - 21. 05. 2015, Ljubljana

Organizacijski odbor / Organising Committee

Redakcijski odbor / Technical Review Committee

Beseda predsednika MPŠ

Smo v enajstem letu delovanja Mednarodne podiplomske šole Jožefa Stefana – MPŠ. V tem času je več kot uspešno podiplomska šola opravljala svoje poslanstvo, kar se kaže v večini primerov v izjemno kvalitetnih doktorskih in magistrskih delih. To je seveda rezultat uspešnega sodelovanja podiplomskih študentov in njihovih mentorjev. Seveda pa je potrebno na prvem mestu omeniti Institut »Jožef Stefan«, ki največ doprinaša k uspešnemu delu te šole z odlično opremo, vključno s Centri odličnosti in širokim ter kvalitetnim mentorskim potencialom. Prav tako pa je potrebno omeniti uspešno vključitev in sodelovanje Inštituta za kovinske materiale in tehnologije - IMT ter Nacionalnega inštituta za biologijo – NIB, kar je zlasti razširilo potenciale šole in prispevalo k še večji interdisciplinarnosti, ki je danes nujna za uspešno vključevanje tako v domačem kot v mednarodnem prostoru.

Dejstvo je, da se vpisujejo na področja delovanja te šole praviloma odlični mladi podiplomski študentje, ki s svojim znanjem, zagnanostjo in dosežki segajo v sam vrh kvalitetnih mladih raziskovalcev. Njihova kvaliteta raziskav se kaže z objavami v mednarodno uglednih in v nekaterih primerih vrhunskih revijah. Seveda teh uspehov ne bi bilo brez odličnih mentorjev in somentorjev, ki so prejeli za svoje delo vrsto domačih ter mednarodnih priznanj. Naj omenim še izjemno vzdušje in kolegialne odnose, ki vladajo med podiplomci in njihovimi mentorji. Vse to omogoča tudi izjemno uspešno vpetost v mednarodne povezave tako v Evropskem kot tudi globalnem prostoru. To znanje, pridobljeno na temeljnih in aplikativnih raziskavah, se naprej uporablja za nadgradnjo na področju znanosti kot tudi v njegovem prenosu v gospodarstvo. To je misija Mednarodne podiplomske šole Jožefa Stefana ter prispevek k pospešenemu zagonu slovenskega gospodarstva ter hitrejšemu prehodu iz vsesplošne krize v družbo znanja. Slovenija je zapadla v globoko ekonomsko krizo, ki pa so se ji v dobri meri izognile države, ki so se pravočasno zavedale pomena vlaganj v odlično znanost in raziskave. Med slednjimi so tudi mnoge nove članice EU. Še posebej pa se moramo zavedati, da ekonomsko uspešne države vlagajo pospešeno velika finančna sredstva v znanost in raziskave in ob tem privabljajo mnoge odlične maturante in diplomante s svojimi štipendijami in mnogimi ugodnostmi (odlična oprema in odlični kader) za potrebe njihovega nadaljnjega ekonomskega razvoja v tekmi na globalni ravni.

Žal krizi pri nas še ni videti konca in vsako zamujanje na področju znanosti in inovacij to kritično stanje samo še bolj poglablja. Vendar moramo vsi skupaj združiti svoje sile v borbi za pozitivne spremembe na tem področju družbene dejavnosti. Ne smemo prezreti tudi Odprtega pisma članov Evropske akademije mladih (YAE) s sedežem v Londonu, ki so 30. januarja 2015 jasno opozorili na podfinanciranje osnovnih raziskav, kar ima hude posledice za mnoge južnoevropske države, kamor sodi nedvomno tudi Slovenija. Slovenska država namenja v zadnjem letu rekordno nizka finančna sredstva doslej (0,31 do 0,35 % BDP), kar nas uvršča na dno EU ter enači z mnogimi nerazvitimi v svetu. V tej situaciji bi se morali mladi krepko angažirati v borbi za spremembo takega stanja, ki bo imelo pogubne posledice tako za gospodarstvo kot tudi celotno družbo.

Pot do ustanovitve MPŠ je bila dolgotrajna in zahtevna, vendar uspešna. Pričelo se je z razmišljanjem o ustanovitvi lastne podiplomske šole koncem 90-ih let. Po dokajšnih naporih je Svet za visoko šolstvo Republike Slovenije izdal soglasje za njeno ustanovitev 3. decembra 2003, kar je omogočilo, da so se prvi podiplomski študentje vpisali jeseni leta 2004 na področja nanoznanosti in nanotehnologije, informacijske in komunikacijske tehnologije, ekotehnologije ter s tem povezan menedžment. Teh področij v pretežni meri ni pokrivala univerza, predstavljala pa so moderne usmeritve v svetu. Ustanovitelji te šole so bili poleg Instituta »Jožef Stefan« še naši industrijski partnerji Gorenje, Kolektor, Salonit in Slovensko zavarovalno združenje, ki so najbolj razumeli potrebe po ustanovitvi te sodobne podiplomske šole. Kasneje so se pridružile šoli tudi druge gospodarske organizacije, in sicer Inštitut za kovinske materiale in tehnologije - IMT in Nacionalni inštitut za biologijo - NIB.

Dragi podiplomci, današnja predstavitev vaših raziskovalnih dosežkov, že sedma po vrsti, je ponoven dokaz vaše uspešnosti na področju raziskav. Seveda ne smemo pozabiti tudi na odlične publikacije, ki ste jih že mnogi med vami objavili v času študija. Moram omeniti tudi finančna sredstva, saj brez teh si danes ne moremo zamišljati moderne znanosti in iz nje izhajajočih tehnologij ter uspešne konkurenčnosti gospodarstva. Vsa zahvala gre Institutu »Jožef Stefan«, ki s svojim finančnim vložkom v veliki meri omogoča delovanje te šole, da ne omenjamo še enkrat kadrovskega potenciala in odlične raziskovalne opreme, ki vam je ves čas na voljo.

Zaradi situacije, v kateri se je znašla Slovenija in ki nam je vsem poznana, je nujno, da odgovorni v Republiki Sloveniji končno spoznajo, da brez odličnega znanja in odličnih tehnologij ne bo gospodarskega napredka. Mladi ste upravičeni do boljše prihodnosti, kot vam jo ponuja sedanjost! Do novih delovnih mest! Pravico imate, da se vam omogoči uspešno spopadanje z izzivi v domačem okolju, ne pa da iščete izpolnitve svojih ambicij in eksistenčnih možnosti z odhodom v tujino. To desetletje ali še krajša doba bo ključnega pomena za slovensko gospodarstvo ter ekonomsko in politično neodvisnost Slovenije, saj sedanje stanje vodi v izgubo gospodarske in politične moči države.

Še enkrat bom ponovil, kar sem že pred kratkim rekel: znanje je vrednota, ki omogoča narodu ekonomski razvoj in obstoj. V pismu, ki ga je objavila YAE, so zapisali: "da so osnovne raziskave v ospredju moderne kulture in nam pomagajo razumeti, kdo smo". Pri nas tega odgovorni očitno ne razumejo, kajti če bi razumeli, bi delali drugače!

Mladi vrhunski raziskovalci so pogoj za uspešen gospodarski in vsesplošen razvoj in so srce družbe znanja. Očitno so potrebne za to spoznanje globoke družbene spremembe.

Akad. prof. dr. Vito Turk
Predsednik MPŠ

Na poti v drugo desetletje:
7. Študentska konferenca MPŠ

Lani smo maja praznovali desetletni jubilej MPŠ in se – ne brez ponosa – ozirali na prehojeno pot: na več kot dvesto doktorjev in magistrov znanosti, ki so takoj dobili zaposlitev v več kot dvajsetih državah, na stotine vrhunskih raziskovalnih dosežkov, objavljenih v uglednih mednarodnih znanstvenih revijah, na delež pri inovacijah industrijskih partnerjev, na priznanja in nagrade, ki so jih pobirali tako študenti kot profesorji MPŠ doma in po svetu.

S 7. Študentsko konferenco MPŠ vstopamo letos v drugo desetletje naše šole, še vedno ponosni na njene dosežke, a tudi zaskrbljeni za preživetje in razvoj v kar naprej trdih pogojih okolja, ki se le zelo počasi spreminja na bolje. Visoka nezaposlenost, še posebej med mladimi izobraženci, hromi iniciative. Njihovo odhajanje v tujino po eni strani širi naša obzorja v upanju, da se bodo vrnili ali vsaj ohranili pretok z domovino, po drugi strani pa nas ta izguba najboljših tukaj in danes boli. In močno nas skrbi drsenje velikega dela prebivalstva v revščino – ne nazadnje zato, ker so prav v revščini ugodni pogoji za propagiranje totalitarnih rešitev.

Odgovor na vse te nevarnosti je lahko samo ustvarjalnost. Predvsem tista za mlade značilna ustvarjalnost, ki jo bogatita odločnost, celo zanesenost mladih uresničiti novo.

Takšno ustvarjalnost danes silno potrebuje naša družba. Mednarodno se po bogastvu največkrat primerjamo z bruto domačim proizvodom – BDP. Ta je vrednost vseh dokončanih proizvodov in storitev na določenem območju in v določenem obdobju. Svetovni BDP je bil za 2014 ocenjen na 76 trilijonov dolarjev. Če to delimo s številom svetovnega prebivalstva, ki je 7,3 milijarde, potem pride v povprečju dobrih deset tisoč dolarjev na svetovnega prebivalca.

Slovenski BDP na prebivalca se bliža tridesetim tisočakom, med dvesto državami smo v zgornji petini. Torej prav lahko pademo še globlje. In tudi bomo, če se ne bomo nehali izživljati predvsem v polivanju z gnojnico, namesto da bi gradili pot navzgor.

Kam usmeriti to pot navzgor? Surovin, razen žlice premoga, v Sloveniji nimamo. Sama lepota deželе je velik dar, a ne dovolj. Pregovorna slovenska pridnost? To je že bolj pravljica iz starih dni. Na Kitajskem komaj vedo, kaj je dopust, in sobote so zanje čisto normalen delovni dan.

Naša edina prednost je lahko, da bomo bolj pametni. In to hitreje kot drugi, kajti zlasti Kitajci s pettisočletno kulturo se izredno hitro učijo. Evropska unija upa, da bo razvoj šel hitreje, če se bo znanost veliko tesneje prepletla z gospodarstvom. V to smer razpisuje programe in projekte.

Žal je za to pri nas zaenkrat še kup hudih ovir. Tudi to, da tako znanost kot gospodarstvo še kar naprej ostajata vsak na svojem bregu. Pa vendar sta hitro razvijanje in hiter prenos znanja v delo in odločanje – hitrejše kot pri konkurentih – edino upanje. Navsezadnje je že stara modrost: *Vedeti ni dovolj – moramo uporabiti. Hoteti ni dovolj – moramo narediti.*

Temeljne raziskave moramo ohraniti in braniti, saj so abeceda za vsako razvojno zgodbo. Toda učiti se moramo to abecedo tudi uporabljati in razvojne zgodbe pisati.

In prav v tem je visoka kakovost in z njo bistvena vrednost študentskih konferenc MPŠ: temeljne raziskave vodijo do dosežkov, ki izzivajo razum za opredeljevanje novih neznank in iskanje novih odgovorov, a obenem tudi za razmišljanje, kako dosežke uporabiti za boljše življenje in večjo skladnost okolja. Za vse to pa mora čim več ljudi znanost tudi razumeti – tudi k temu se usmerja duh študentskih konferenc MPŠ.

Letošnja sedma študentska konferenca ostaja zvesta poslanstvu MPŠ: z raziskovalno-izobraževalnim pristopom visoke kakovosti prispevati k ustvarjanju znanja, z usposabljanjem za učinkovito razvojno raziskovanje k ustvarjanju materialnih in socialnih dobrin ter z napori za čim širše poglobljeno razumevanje znanosti in razvojnih možnosti, ki jih nudi, tudi k bogatenju nacionalne in ustvarjanju svetovne kulture.

Vse to prav gotovo zasluži naše spoštovanje in čestitke.

Aleksandra Kornhauser-Frazer
Dekan MPŠ

Beseda predstavnice gospodarstva

Na svetovnem trgu lahko nastopamo med vodilnimi proizvajalci samo, če imamo podporo raziskovalnih inštitucij. Za najboljše rešitve, ki se uvrščajo v svetovni vrh v specifičnem tržnem programu podjetja, so potrebni znanje, ustvarjalnost, pogum in izkušnje. Prav to pa dosežemo z združevanjem raziskovalnega dela, s posluhom za sodelovanje tako na strani industrije kot raziskovalcev in s hitrim prenosom znanj v rešitve in izdelke za globalni trg.

To omogoča tudi razvoj MPŠ skupaj z IJS, ki si vsako leto nabirata izkušnje z novimi projekti. Prav tako pa predstavniki iz industrije, ki imamo vizijo trajnostnih inovativnih rešitev in nenehnega iskanja boljših tržnih priložnosti, iz lastnih razvojnih področij in s podporo raziskovalnih inštitucij, med katerimi IJS in MPŠ igrata pomembno vlogo, ustvarjamo rešitve, ki so v samem vrhu v svetovnem merilu ali pa celo narekujemo svetovne trende v globalnih tržnih nišah.

Letna študentska konferenca MPŠ je priložnost za spoznavanje novih znanstvenih dosežkov podiplomskih študentov in iskanje presečnih polj med idejnimi in laboratorijskimi rešitvami s področja znanosti ter novih priložnosti na globalnem trgu, ki jih prepozna industrija.

Kjer se srečujejo različni ljudje in z različnih področij, ki si znajo prisluhniti in sodelovati, se rojevajo najboljše rešitve. Iz globokega znanja, mladostne svežine, poguma in vztrajnosti v sodelovanju z izkušeno in prekaljeno industrijo se bodo rodile nove rešitve za zahtevni globalni trg, ki pričakuje - celo terja - vedno boljše, izvirnejše, zanesljive in cenejše rešitve.

Dr. Jožica Rejec
Predsednica uprave Domel d. d.

Predstavi svoje delo ali inovacijo in bodi del prihodnosti!

Vsako leto se trudimo, da bi študentsko konferenco povzdignili še stopnico višje in tudi letos mislimo, da nam je to uspelo. Zato z največjim veseljem predstavljamo že 7. Študentsko konferenco Mednarodne podiplomske šole Jožefa Stefana, ki po kakovosti ne zaostaja, po programu pa presega predhodne konference. Tudi letošnja konferenca ima cilj vzpostaviti stik med študenti in industrijo ter pokazati predstavnikom podjetij delo naših podiplomskih študentov v upanju na morebitno skupno sodelovanje. Konferenca je odprta za vse obiskovalce, saj želimo znanost približati širši javnosti tudi z industrijskega in tržnega vidika.

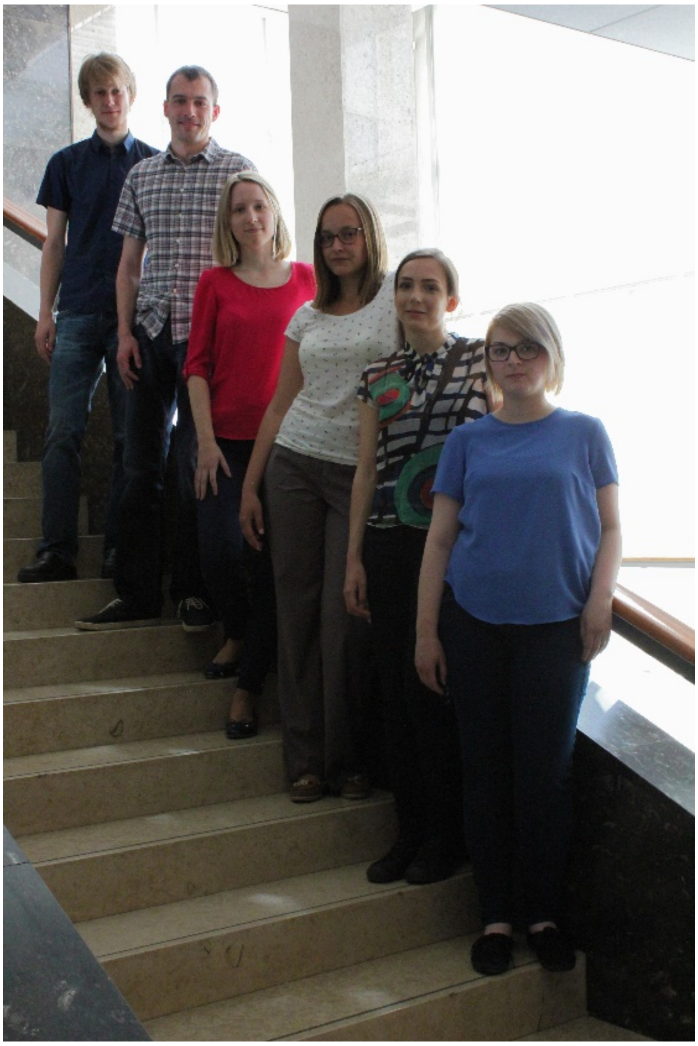

Z novim študentskim letom smo se zaradi študijskih obveznosti poslovili od večine stare ekipe, vendar pa smo pridobili odlične nove člane z novimi idejami in svežim zagonom. Letos smo se odločili, da bomo ohranili novosti iz lanskega leta, kot so predavanja mladih podjetij ter kratke govorne predstavitve študentov v stilu 'elevator pitch'-a. O podrobnostih priprav na konferenco smo razpravljali na sejah koordinacije in senata, kjer so bile marsikatere ideje pozitivno sprejete in pohvaljene. Na začetku leta smo obvestili tako študente kot mentorje o letošnji študentski konferenci in dogodek pričeli promovirati tudi preko spleta in socialnih omrežij. Čeprav smo letos prejeli nekaj prispevkov manj kot lani, je bilo teh še vedno veliko (26). Menimo, da je interes študentov za sodelovanje na konferenci še vedno velik, in pričakujemo, da se bo v naslednjih letih število prispevkov povečalo.

Za pregled in zagotavljanje kakovosti prispevkov je letos s kar dvema pregledoma skrbelo 11 članov redakcijskega odbora. Odbor je temeljito in profesionalno podal svoje ocene in predloge ter poskrbel za znanstveno korektnost in odličnost prispevkov. Pri tem so bili pozorni na pravilnost in strokovnost znanstvenega besedila, na razumljivost in obliko posterja, posebne pozornosti pa je bil deležen opis dela, namenjen širši javnosti. Le-ta je bistven za razumevanje raziskav izven

znanstvenega kroga in lahko služi kot most med raziskovalnim delom in industrijskim interesom.
Ker je bistvo konference povezovanje znanosti z industrijo, smo za udeležence tudi letos pripravili sklop predavanj z naslovom 'Od ideje do uspeha', kjer vabljena podjetja preko lastnih zgodb in pridobljenih izkušenj seznanijo študente z izzivi in ovirami, ki doletijo startup podjetja pri njihovi ustanovitvi in nadaljnjem vodenju. Za sklop predavanj smo letos pridobili tri podjetja: Adora, Greener Project in Izvor ter Ljubljanski univerzitetni inkubator (LUI), ki nas je letos še posebej razveselil s ponujeno pomočjo pri promoviranju konference. Dogovorili smo se tudi za postavitev LUI info točke, na kateri se spodbuja podjetništvo pri študentih in pridobi informacije ter pomoč pri prenosu znanja na trg. S takimi sodelovanji konferenca pridobiva na kakovosti in upamo, da se bodo v prihodnosti trenutna sodelovanja še poglabljala in ustvarjala nova. Na letošnji konferenci nadaljujemo tudi z dobro sprejetimi 'elevator-pitch' predstavitvami iz lanskega leta. Pri tem se študentje s kratkimi predstavitvami pomerijo v sposobnostih promoviranja in prodajanja svojega raziskovalnega znanja. Poslušalci pri tem aktivno sodelujejo in izberejo najboljšo predstavitev, ki je na koncu tudi nagrajena. Upamo, da bomo z našo konferenco vsaj malo prebudili podjetniško žilico pri sodelujočih in jim pomagali premagati strah, ki se pojavi, ko se študenti želijo podati v zahteven svet industrije. Če smo koga spodbudili, da se v ta svet poda, si to štejemo v ponos, saj je bil naš cilj več kot dosežen.

Za uspešno in zanimivo konferenco bi se v prvi vrsti radi zahvalili študentom in mentorjem, ki so s svojimi kakovostnimi deli, sodelovanjem in trudom prispevali k odličnosti in bistvu te konference. Za zanimiva predavanja in predstavitev izzivov, ki jih prinaša prenos znanosti na trg, se zahvaljujemo vsem sodelujočim podjetjem in organizacijam, ki so pokazala veliko zanimanje za sodelovanje in so poskrbela, da je bila konferenca nadvse uspešna in zanimiva. Zahvaljujemo se redakcijskemu odboru za njihov čas in znanje, ki so ga porabili za pregled in poskrbeli za visoko kvaliteto prispevkov. Posebne zahvale gredo tudi celotnemu osebju Mednarodne podiplomske šole Jožefa Stefana za vso pomoč pri organiziranju konference. Še posebej bi se radi zahvalili dekanu prof. dr. Aleksandri Kornhauser-Frazer za pomoč pri pridobivanju finančnih sredstev ter predvsem za njeno podporo in zavzemanje za naše ideje. Nazadnje bi se radi zahvalili tudi Tadeji Samec in Sergeji Vogrinčič, saj sta nam bili vedno na voljo za pomoč pri organizaciji in vodenju konference ter Maši Matijašević, za skrbno lektoriranje in popravo zbornika.

Uredniški odbor

Kazalo (Table of Contents)

Ekotehnologija (Ecotechnology) 1

Ekotehnologija (Ecotechnology)

Stability of dissolved gaseous Hg (DGM) and reactive Hg (RHg) in the absence and presence of preservatives in natural waters

Ermira Begu[1,2], Yaroslav Shlyapnikov[1,2], Kristina Obu-Vazner[2], Milena Horvat[1,2]

[1] Jožef Stefan Institute, Department of Environmental Sciences, Jamova 39, Ljubljana 1000, Slovenia
[2] Jožef Stefan International Postgraduate School, Jamova 39, Ljubljana 1000, Slovenia

ermira.begu@ijs.si

Abstract. The stability of mercury species at low levels during sampling, sample handling and storage is still problematic despite all the efforts invested into this problem over the years. The problem lies in the facts that mercury species are normally present at very low concentrations in the environment, especially in natural waters, and are also unstable. The likelihood of contamination and loss of Hg during sampling, sample handling (including filtering), storage and measurement is very high. The aim of the present work is to summarize recent studies related to the stability of dissolved gaseous mercury (DGM) and reactive-Hg (RHg) in water samples. Further, we have tested the stability of DGM and RHg in fresh river waters (without addition of preservation reagent) and in distilled, fresh and marine water after acidification with HNO_3 and the addition of $AuCl_3$ as a preservative. Due to low concentrations, the samples were spiked with Hg^0 solution and Hg^{2+} standard solution. Variation of the concentrations was followed with time. DGM concentrations were determined by double amalgamation and cold vapour atomic fluorescence (CV AFS) after pre-concentration of Hg in a gold trap. RHg was determined in the same way but with the addition of tin chloride ($SnCl_2$) prior to purging. The addition of $AuCl_3$ and HNO_3 as a preservative for these Hg species, was not useful in any of the four sample matrices tested.

Keywords: Dissolved gaseous mercury, reactive mercury, stability, HNO_3, $AuCl_3$

1 Introduction

The most common forms of Hg in natural waters are oxidized Hg (defined as the reducible inorganic form or reactive Hg (RHg)), methylmercury (MeHg), elemental mercury (Hg^0) and dimethylmercury (DMeHg). Hg^0 and DMeHg compromise the dissolved gaseous fractions of total Hg (DGM) in water systems, which consists of dissolved elemental Hg (DEM and other gaseous forms, such as DMeHg [1].Total mercury (THg) concentrations in natural, non-contaminated waters are at a level of a few $ng.L^{-1}$ and lower.

In marine waters, DGM constitutes between 10 and 50 % of total Hg. Its concentration varies significantly in space and time [3]. DMeHg is reported to be the dominant organic form of Hg in deeper ocean waters [1], while Hg^0 is found in the whole water column, with higher concentrations obtained at surface waters. Photochemical reactions where Hg^{2+} is reduced into Hg^0 [4, 5] and bacterial activity [6] are probably the main sources of volatile Hg^0 in surface waters [7]. Intensive tectonic activity and geological anomalies may also be important sources of Hg^0, especially in the Mediterranean Sea, which is tectonically very active [1]. In open surface freshwater, Hg^{2+} reduction is especially important to Hg cycling due to evasion of the produced Hg^0 to the atmosphere, particularly on windy summer days [8]. About 2000-2950 tons of Hg^0 are emitted from oceans every year. On the other hand, the presence of Hg^{2+} (RHg) leads to high potential of Hg to be transformed in MeHg, the most toxic form of Hg in the environment that tends to bio-concentrates and biomagnifies in food webs. Accurately determine Hg^0 flux to the atmosphere, requires accurate and reliable analytical methods for determination of dissolved elemental Hg (DEM) in surface waters. As DEM is a gas, it is preferable to perform measurements on site, immediately after sampling. Since this is not always possible the storage and transportation of the sample to the laboratory may lead to serious analytical errors. Therefore, volatilization of Hg from the sample, adsorption to the walls of the container, interchange between Hg species, and diffusion of Hg^0 through the walls of the container from the surrounding atmosphere into the sample, have to be carefully considered.

As a result, accurate determination may also depend on the use the appropriate containers and storage conditions. Hence, the goal of this paper, was to test the storage conditions under which the losses of the Hg species of interest (DGM and RHg) in natural water systems, are minimal.

It is generally agreed that Hg^{2+} is stabilized by lowering the pH of the sample. Low pH values and high ionic strength limit adsorption to the container walls. However, under such circumstances dissolved Hg^0 can easily be oxidized. The aim of this work was to study the stability of DEM and RHg in preserved and non-preserved natural water samples.

2. Materials and methods

2.1 Sampling and storage

Two experiments have been performed to study the stability of DGM and RHg in natural surface water samples (Fig. 1 and Fig. 2). The presence of DMeHg in the natural samples is not expected but, since it was not determined experimentally, we cannot report that it was not present. We therefore refer to the species studied as DGM, instead of just dissolved elemental mercury, Hg^0. All the samples were taken in the surface, at about 20 cm deep. The first experiment concerns the stability of DGM and RHg in freshwater samples without the addition of preservatives. Surface freshwater samples taken from Sava river, Ljubljana) and Stream water from Potočnikov Graben, North-West part of Slovenia affected by former mercury mine at Podljubelj , were collected in glass bottle. Samples were stored at room temperature (about 20 °C), exposed to ambient light, and, subsequently, in a refrigerator at 4 °C and in the dark (no preservatives were added to none of the samples).

During the second experiment, $AuCl_3$ and HNO_3 were added to the samples after collection. 4 different water media were tested: distilled water, tap water, freshwater (river) and seawater. The surface freshwater samples were collected in a small river in Ljubljana (part of Ljubljanica river, Ljubljana) while seawater samples were collected in Kaštela Bay, Croatia. The samples we stored at room temperature. No additional parameters were measured since the goal of the experiment was not to correlate Hg concentration with other physical/chemical parameters of the water but only to follow the variation after the preservative compounds were added to it. Simplified general scheme from sampling to detection for DGM and RHg species, is presented in Fig. 1.

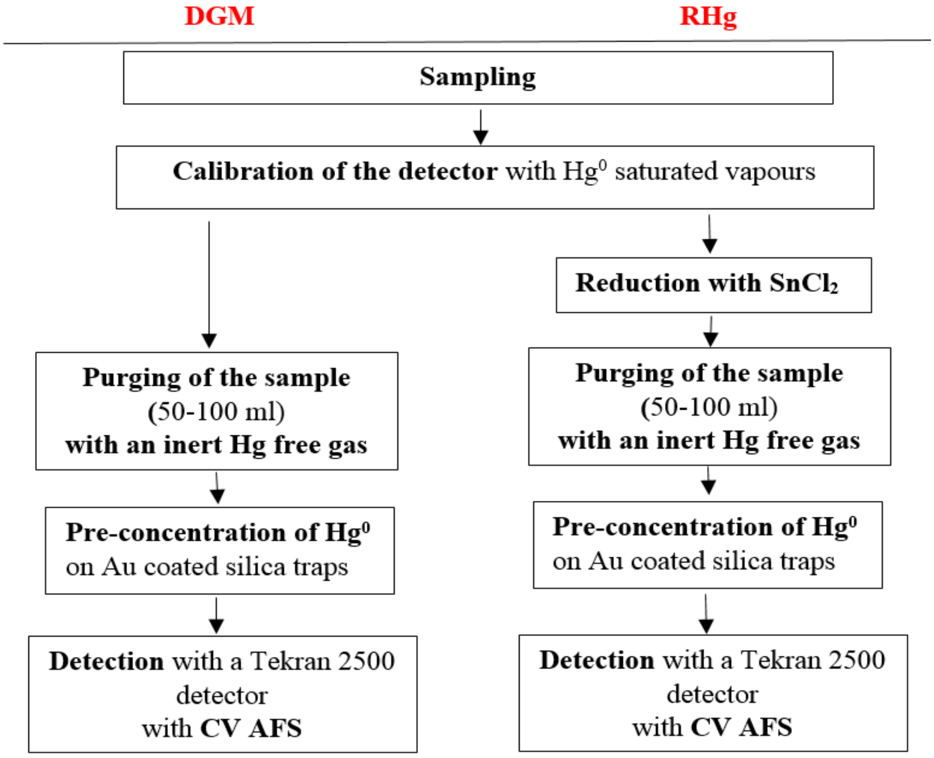

Figure 1. A simplified scheme of the measurement procedure for DGM and RHg. During the second experiment, after sampling, $AuCl_3$ and HNO_3 were added to the samples.

2.2 Calibration of the detector

Before every type of analysis is performed, calibration of the detector has to be performed. The main sources of error in most common analytical methods for determining DGM and RHg, are related to sampling and to calibration of the instruments (no reference materials are available). Calibration provides the evidence of traceability and comparability in time and space. Thus, prior analysis of the samples, a careful calibration of the detector (cold vapour atomic fluorescence spectrophotometry (CV AFS), Tekran 2500) was done. The detector was calibrated by gas phase Hg (Hg^0) kept at about 4 °C (Tekran, Model 2505, mercury vapour calibration unit) [9, 10]. An aliquot of Hg^0 (10 μL Hg^0 which is equal to about 56 pg Hg^0) was transferred with a gas-tight syringe (Hamilton, 25 μl) through a septum into the double amalgamation system. Repeated injections were made before and during the analysis of samples.

2.3 Determination of DGM

The manual method used for DGM determination comprises sampling, purging and measurement steps. 50 to 100 ml of sample was purged, in a borosilicate glass purging vessel (bubbler) with a frit, by Hg free N_2 with a flow of 300 - 400 ml min^{-1}. Samples were purged for 10 min and Hg^0 was amalgamated onto a sampling gold trap. A soda lime trap was used between the bubbler system and the collection trap (installed upstream the bubbler) functioning as a drying material for water vapours.

The Au trap with collected Hg, is then transferred to a double amalgamation system. Hg on the sampling trap is desorbed at 300 to 500 °C with a flow of Ar (60 ml min^{-1}) and detected by cold vapour atomic fluorescence spectrometer detector (Tekran, model 2500). The Limit of detection of the method is 0.005 ngL^{-1} and the uncertainty determined following GUM [11] was estimated to be about 20% (Fig. 2):

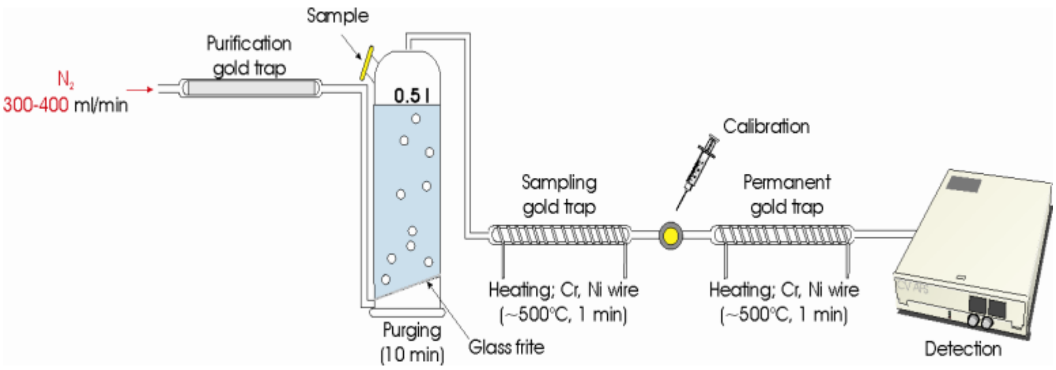

Figure 2. The system used for DGM determination

2.4 Description of the method for determining RHg

The method used for determining RHg is the same as that used for DGM except for the use of a reducing agent (tin chloride, $SnCl_2$). When RHg is to be measured, $SnCl_2$ is added to the sample prior to purging, in order to reduce the available oxidized Hg forms to Hg^0. Note that the previously determined results for DGM have to be subtracted from the results obtained for total RHg.

3. Results and discussion

3.1 Stability of DGM and RHg without the addition of preservatives

The results presented in Fig. 3 were obtained from the measurements of the samples collected from Sava River stored at room temperature (20-23°C) and in the fridge at 4°C.

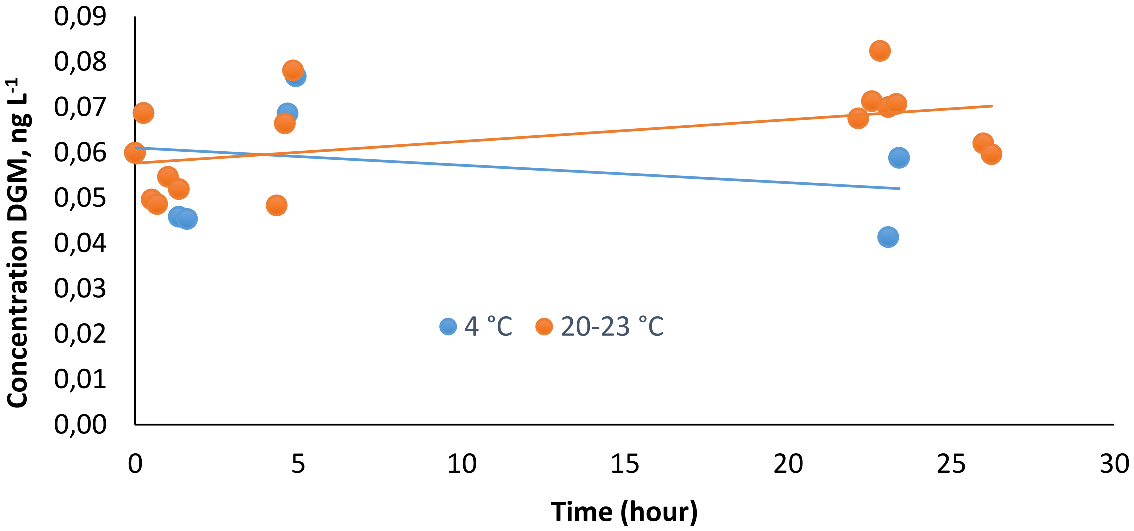

Figure 3. Stability of DGM (Hg^0) in Sava River stored at room temperature (20-23°C) and at 4°C

Evidently, storage of the river water at 4 ^{0}C protects concentrations of DGM over 24 hours storage period. Interestingly, when samples were stored at room temperature, the concentrations of DGM decreased after about 4 hours of storage from 0.06 ng L^{-1} to about 0.05 ng L^{-1} and increased in the next hours (after 23 hours) to about 0.07 ng L^{-1}. After 26 hours went back to the initial concentration. This indicates that some elemental mercury is oxidized to inorganic mercury and the latest was later reduced back to Hg^0 which can be explained by enhanced reduction potential occurring at room temperature.

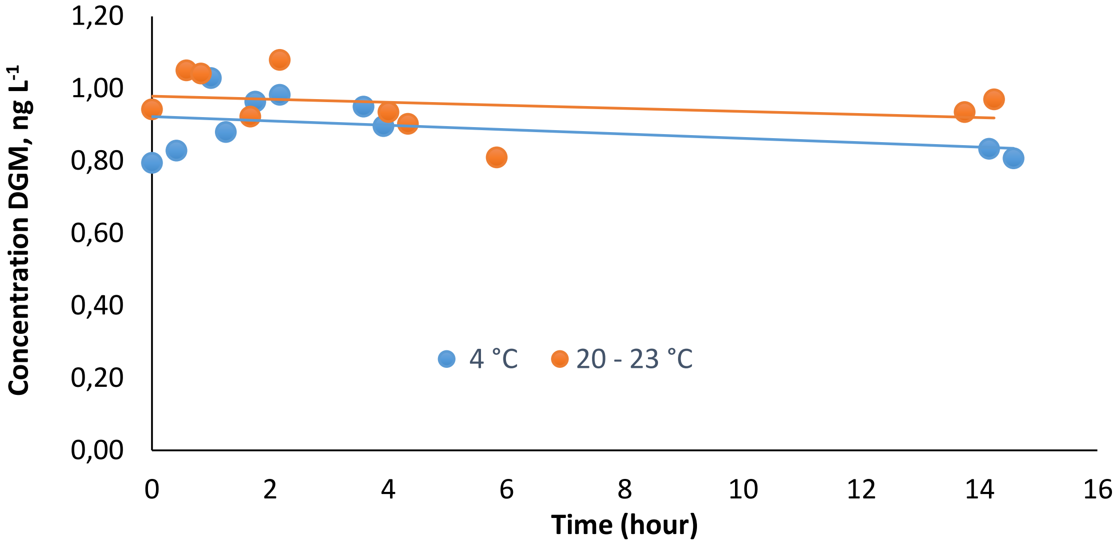

Figure 4. Stability of DGM (Hg^0) in stream water of Potočnikov Graben stored at room temperature (20-23°C) and at 4°C

In case of the stream water sample obtained from former mercury mining region (Fig. 4), where the concentrations were much higher than in the Sava river, a slight change in the concentration of DGM was observed after 5 hours for samples stored at room temperature (0.94 to 0.81 ng L^{-1}) and after 15 hours the measured concentrations rise up to 0.97 ng L^{-1}, comparable with the initial one. While for the samples in the fridge, a slight increase was observed after 1 hours of storage (0.80 to 1.03 ng L^{-1}) and after 15 hours, the concentrations were more or less stable.

The stability of DGM in water systems has been studied previously. The slight change in DGM concentration observed in in fresh water samples correspond to those reported by Amyot et, al. [12] and also by Bolte et, al. [13] where no DGM production was noticed in non-filtered samples. Further, no statistically significant concentration differences were observed by Rolfhus et at., [3] in coastal marine waters after 2 days of storage in a refrigerator in the dark. Parker et al., [14] allowed 10-20 hours to elapse before for measuring DGM, time in which DGM is supposed to be stable. In contrast, Lindberg et al. [8] showed that fresh water samples collected over short periods are not necessarily stable because of volatilisation and/or oxidation. Overall, it appears that meaningful measurements can be made within 4–6 h. However, we strongly recommend performing sample measurements as soon as possible after sampling, since rapid transformations may occur.

RHg was also measured in the samples from Sava River (Fig. 5).

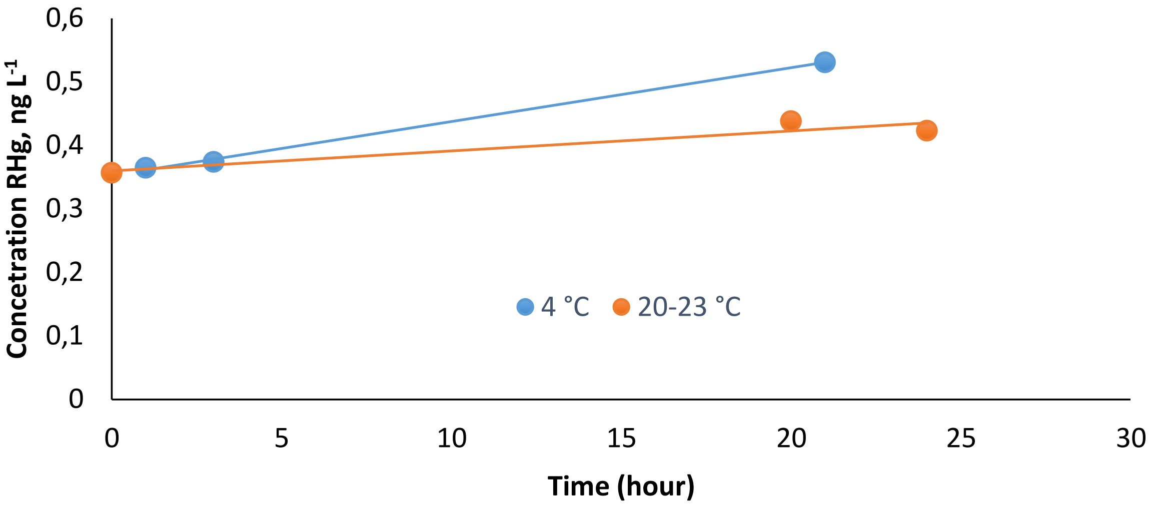

Figure 5. Stability of RHg in freshwater samples collected in River 1 and stored at room temperature (20-23 °C) and in the refrigerator (4°C)

An increase of RHg was observed when the sample was stored in dark conditions in the refrigerator. A possible explanation for this is either the diffusion of additional Hg^0 from the bottle walls into the sample or the oxidation of Hg^0, which is known to occur also in the dark at low temperatures [6]. No significant changes of RHg stored at room T were observed.

3.2 Stability of DGM and RHg after acidification and addition of $AuCl_3$

Due to low natural concentrations, the samples were spiked with additional known amounts of Hg^{2+} standard solution and Hg^0 and stability checked over a period of several hours and days as explained below. As reported by Environment Protection Agency (EPA) report [15] the gold stabilization method was thought to directly prevent deposition by keeping all Hg in solution in environmental water samples.The suggested procedure from EPA [14] was firstly applied. 1ppm (mg L^{-1}) $AuCl_3$ in 2% HNO_3 were added to the samples. In this case, we clearly observed Au precipitation in the glass filter of the bubbler for RHg measurements.

$$AuCl_3 + SnCl_2 \rightarrow SnCl_4 + Au^0 \downarrow$$

The presence of Au particles might lead to adsorption of Hg^0 already in the sample and this should be avoided. For this reason, we 're-optimized' the ratio $AuCl_3 : HNO_3$. The best ratio where almost no Au precipitation was observed, was when 0.5 mg L^{-1} $AuCl_3$ and 0.5% HNO_3 was used for sample conservation. The samples were stored under room conditions (the temperature in the laboratory during the experimental time ranged from 13 to 18 °C and the Hg concentration in air ranged from 80 to 200 ng m^{-3}). The results for the distilled water and seawater when spiked with the Hg solutions and the preservation agent was added, are shown in Figs. 6 and 7, respectively.

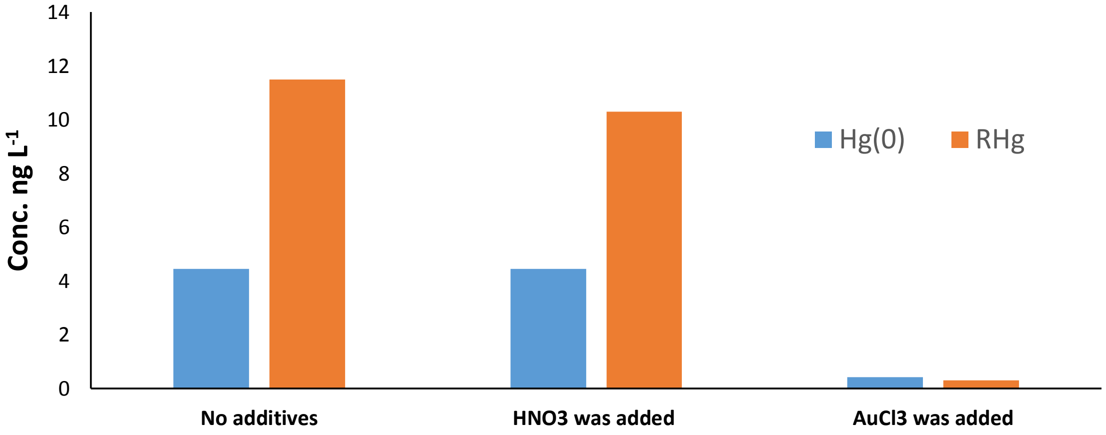

Figure 6. DGM (Hg^0) and RHg behaviour in distilled water before and after the addition of $AuCl_3$ and HNO_3

About 70% of decrease was observed immediately after the addition of $AuCl_3$ and HNO_3 in a distilled water sample spiked with Hg, but no difference in the DGM and RHg concentrations was observed after HNO_3 addition only. For the tap water and freshwater samples the same results were observed. About 50% of decrease in the RHg concentration was observed after the addition of the $AuCl_3$ and HNO_3, while about 80% decrease was recorded for DGM.

The experiment was repeated under the same conditions by using seawater (Fig. 7).

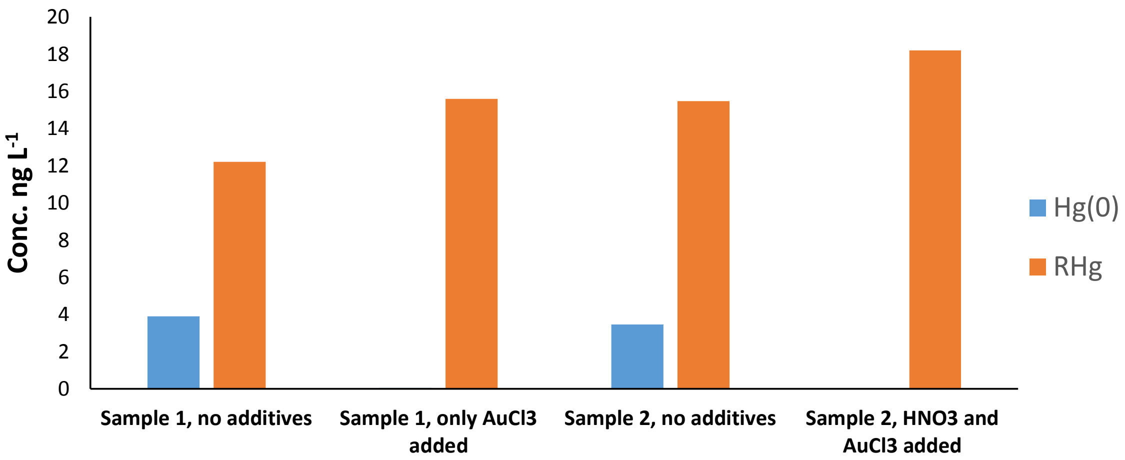

Figure 7. DGM (Hg^0) and RHg behaviour in seawater before and after the addition of $AuCl_3$ and HNO_3

In the case of seawater samples, different results were observed in all tests performed during the experiment. A representative example of the situation is shown in Fig. 8. The addition of $AuCl_3$ or a mixture, HNO_3 and $AuCl_3$, caused the 'oxidation/transformation' of Hg^0 into available Hg^{2+}. When the mass balance was performed, the concentrations before and after the addition were in a good agreement. When only HNO_3 was added, variable results were obtained. Earlier, it was shown that acidification of the sample can lead to unpredictable alterations of Hg^{2+}concentrations in water including either desorption of Hg^{2+} from particulates, oxidation of Hg^0 to Hg^{2+} or coagulation of DOC with the concomitant adsorption and precipitation of Hg^{2+}. When the seawater sample was spiked with 5 ng/L Hg^{2+} standard solution and measured at defined times for about 44 hours after the addition of HNO_3 and $AuCl_3$ (Fig. 8), differences between 3 and 7 % in RHg concentrations were observed, while no DGM was observed (LOD=0.26 ng L^{-1}). The difference in RHg concentration in the sample before and about 15 minutes after the addition of HNO_3 and $AuCl_3$, was about 2.5 %.

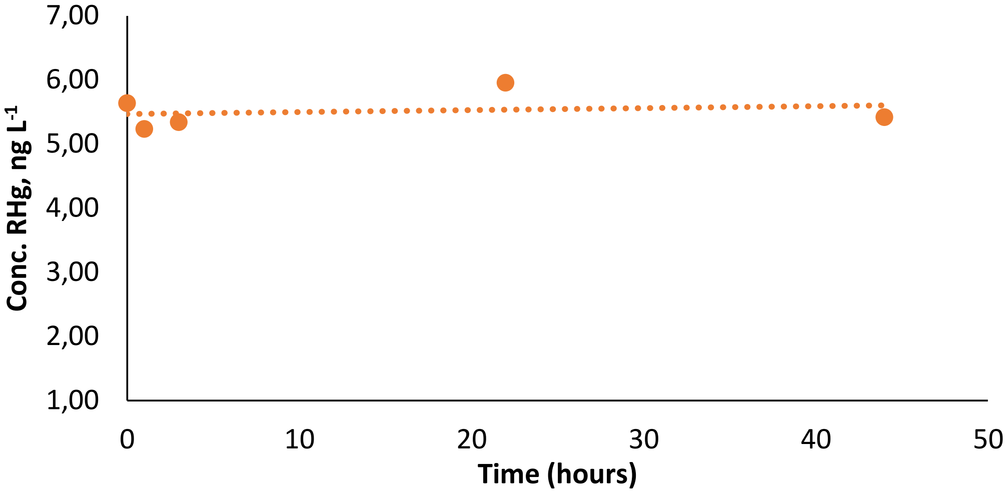

Figure 8. The stability of RHg in seawater over 44 hours when HNO_3 and $AuCl_3$ was added.

Conclusions

The overall conclusion stresses the need of on-spot measurements but when this is not possible, analysis of the sample about 24 hours after sampling, without the addition of any preservative agent or filtration, can ensure reliable results. Acidifying the sample or adding a preservative agent such as $AgCl_3$ and HNO_3, may lead to unpredictable results, depending on sample matrix.

References:

[1] Horvat M., Kotnik J., Logara M., Fajon V., Zvonaric T., Pirrone N.: Speciation of mercuryin surface and deep-sea waters in the Mediterranean Sea, *Atmospheric Environment, 2003*

[2] Wangberg I., Schmolke S., Schager P., Munthe J., Ebinghaus R., Iverfeldt A.: Estimates of air-sea exchange of mercury in the Baltic Sea, *Atmospheric Environment, 2001*

[3] Rolfhus K. R. and Fitzgerald W. F.: The evasion and spatial/temporal distribution of mercury species in Long Island Sound, CT-NY. *Geochimica et Cosmochimica Acta, 2001*

[4] Amyot M., Mierle G., Lean D. R. S., McQueen D. J.: Sunlight induced formation of dissolved gaseous mercury in lake waters, *Environ. Sci. Technol. 1994*

[5] Qureshi A., O'Driscoll N., Macleod M., Neuhold M., Hungerbuhler K.: Photoreactions of Mercury in Surface Ocean Water: Gross Reaction Kinetics and Possible Pathways, *Environ. Sci. Technol., 2009*

[6] Fantozzi L., Ferrara R., Frontini F.P., Dini F.: Dissolved gaseous mercury production in the dark: Evidence for the fundamental role of bacteria in different types of Mediterranean water bodies, *Science of the total environment, 2009*

[7] Costa M., Liss P.S.: Photoreduction of mercury in sea water and its possible implications for Hg0 air–sea fluxes, *Marine Chemistry, 1999*

[8] Lindberg S.E., Vette A.F., Miles C., Schaedlich F.: Mercury speciation in natural waters: Measurement of dissolved gaseous mercury with a field analyzer, Biogeochemistry, 2000

[9] Brown R. and Brown A.: Accurate calibration of mercury vapour measurements, *The Analyst, 2008*

[10] Gardfeldt K., Horvat M., Sommar J., Kotnik J., Fajon V., Wangberg I., Lindqvist O.: Comparison of procedures for measurements of dissolved gaseous mercury in seawater performed on a Mediterranean cruise, *Analytical and Bioanalytical Chemistry*., *2002*

[11] EURACHEM/CITAC Guide Quantifying Uncertainty in Analytical Measurement, Third Edition, 2012.

[12] Amyot M., Mierle G., Lean D. R. S., McQueen D. J. Effect of solar radiation on the formation of dissolved gaseous mercury in temperate lakes. *Geochimica Cosmochimica Acta, 1997.*

[13] Bolte M., Beucher C., Wong-Wah-Chung P., Richard C., Mailhot G., Cossa D. Dissolved gaseous mercury formation under UV irradiation of unamended tropical waters from French Guyana. *The Science of the Total Environment 2002*

[14] Parker J. L., Bloom N. S: Preservation and storage techniques for low – level aqeous mercury speciation, *Science of the Total Environment 2005*

[15] US Environmental Protection Agency, Mercury Preservation Techniques.

For wider interest

Evasion to the atmosphere of elemental mercury from surface ocean water constitutes an important source of Hg in the environment. Its availability in aqueous samples is affected by a number of factors such as light, temperature, the presence of other ions (Cl^- or Br^-), metals (Fe(III)), organic matter, biological activity, tectonic activity and wind speed. In addition, the presence of oxidized forms of Hg increases the chances of methylation processes where MeHg is formed. For these reasons the importance of DGM and RHg measurements is highly important in understanding and building on existing knowledge of Hg chemistry and in improving the analytical methods used. The timing of analysis after sampling is crucial for obtaining reliable results. Since it is not always possible to perform the analysis at the sampling location, storage developing conditions that least affect the described transformations need to be used. Finding a way to store these particular Hg species or developing continuous methods for on the spot measurements, would be of great help improving the quality of the results, which could be further used in the prediction of transformation processes in water and evasion of elemental Hg from water to the atmosphere.

Assymetry of molecular processes during abscission in tomato (*Solanum lycopersicum* L.)

Marko Chersicola[1, 2], **Aleš Kladnik**[3], **Amon Lers**[4], **Marina Dermastia**[1]
[1] Department of Biotechnology and System biology, National Institute of Biology, Ljubljana, Slovenia
[2] Jožef Stefan International Postgraduate School, Ljubljana, Slovenia
[3]Department of Biology, Biotechnical Faculty, University of Ljubljana, Vecna pot 111, SI-1000 Ljubljana, Slovenia
[4]Department of Postharvest Science of Fresh Produce, ARO, The Volcani Center, Bet Dagan 50250, Israel
marko.chersicola@nib.si

Abstract. Abscission is a highly regulated process in which various organs are separated from the mother plant during development. Abscission occurs specifically in the abscission zone (AZ) tissue. It has been shown that various abscission related processes occur asymmetrically between the AZ proximal and distal sides. In this study, we showed the asymmetric immunolocalization of LX ribonuclease (LX RNase) in the wild type and in LX RNase inhibited tomato lines. In addition, the expression of LX RNase gene was evaluated by real-time RT PCR both in the wild type and LX RNase inhibited lines. The findings of this study further elucidate the asymmetry of molecular processes in abscission with a potential use in biotechnology for the controlled abscission of fruits and manipulation of abscission time.

Keywords: abscission, LX RNase, tomato, ethylene, asymmetry

1 Introduction

Abscission is a natural part of plant development in which leaves, flowers or fruits, separate from the plant in a highly temporally and spatially regulated way [1], [2]. The basis for organ abscission is a cell separation process that occurs specifically in the preformed abscission zone (AZ) tissue located at the base of the organ to be shed. The abscission zone is morphologically and physiologically distinct from neighbouring cells and includes smaller sized, cytoplasmically dense cells [2], [3]. Although not much is known about the molecular regulation of abscission, based on knowledge accumulated from anatomical, physiological, genetic and molecular studies, the abscission process is suggested to require four successive phases for its successful execution [4], [2]. In many cases, the abscission process is induced by ethylene, while the rate and degree of abscission depends upon the endogenous balance between auxin and ethylene levels in the tissue [1], [5], [6]. Auxin concentrations must be reduced in the AZ for rendering its sensitivity to ethylene, which promotes the advancement of abscission [7], [8].

Previously, it has been observed that a delay of tomato leaf abscission occurs with inhibited LX ribonuclease (LX RNase)[10]. The tomato LX RNase is a member of the T2/S-like RNases. Expression of the LX RNase gene is highly induced during leaf and petal senescence but can be induced also in young leaves by ethylene. Specific induction of the LX RNase protein has been detected in the distal side of the mature tomato's AZ tissue and was inactivated by either pre-treatment with the ethylene action inhibitor, 1methylcyclopropene (1MCP), or by application of auxin to the pedicel [11].

We have recently shown [11, 14] that AZs of tomato leaf or flower are structured in an asymmetric manner after the abscission is triggered. In this study, we aim to explore the implications of these asymmetries on the process of abscission by analysing the localisation of LX RNase in leaf AZ of transgenic tomato lines with differentially delayed leaf abscission. In addition, we studied the expression profile of LX RNase encoding gene in specific cells of the AZ in the wild type plants.

2 Material and Methods

2.1 Plant Growth Conditions and Treatments

Wild type tomato plants (*Solanum lycopersicum* cv VF36) and two LX RNase inhibited transgenic lines of the same cultivar (named 20-2 and 7-5) were grown in growth chambers at 25°C, 75% relative humidity and a 16/8-h day/night cycle. For induction of abscission, the leaf blades of up to four bottom leaves were removed with a sharp razor, leaving most of the petioles intact. For abscission acceleration, ethylene was applied 36 h later to the debladed tomato plants by placing them for 24 hours in sealed containers with 50ppm ethylene atmosphere.

2.2 Quantitative Reverse Transcription Real-Time PCR

To analyse gene expression during abscission, the leaf abscission zone samples of the wild type plants were excised from paraffin embedded tissue sections using a PALM MicroBeam microscope (Zeiss). Four different regions of tissue were sampled: distal AZ, proximal AZ, epidermis and axillary bud (Figure 1a). Samples from the same region were taken from five sequential tissue sections and collected in a single tube (Zeiss). RNA was extracted using RNeasy FFPE kit (Qiagen).The quantitative reverse transcription real-time PCR was performed in an ABI PRISM 7900 HT Fast Real-Time PCR (Applied Biosystems) with Custom TaqMan Gene Expression Assays (Applied Biosystems) and AgPath ID mastermix reagents. All genes were normalized relative to the expression of a reference gene, COX (for cytochrome oxidase) and the expression data were analysed by the relative standard curve method. All experiments were carried with non-template control.

2.3 Immunolocalization of the LX RNase protein

Paraplast Plus–embedded tissue sections were placed on Superfrost Ultra Plus slides (Menzel-Gläser). Sections were dewaxed in xylene and rehydrated in an ethanol series to distilled water. Antigen retrieval was performed by incubating slides in sodium citrate buffer (10 mM sodium citrate, pH 6.0) for 15 min in a boiling water bath and washed gently in running tap water. Sections were incubated in blocking solution (1× TRIS buffered saline, pH 7.6, 1% [w/v] BSA, 0.025% [v/v] Triton X-100, and 5% [v/v] normal goat serum) for 1 h at room temperature. For LX RNase immunolocalisation, blocking solution was then replaced with anti-LX RNase serum [10] diluted 1:10^5 in blocking solution and incubated overnight at 4°C. Preimmune serum was used for negative controls. Sections were washed the next day in 1× TRIS buffered saline for 5 min, followed by three washes in distilled water with 0.2% Tween 20. Sections were then incubated with alkaline phosphatase–labeled anti-rabbit antibodies (Jackson ImmunoResearch), diluted 1:1000 in blocking solution, for 1 h at room temperature, followed by washing as above. Staining was developed in nitro blue tetrazolium chloride/5-bromo-4-chloro-3-indolyl-phosphate substrate solution (Roche Diagnostics) following the manufacturer's instructions, washed with water, dehydrated quickly through an ethanol series and xylene, and mounted in Permount (Electron Microscopy Sciences). The purple precipitate at the sites of primary antibody binding to LX RNase protein was photographed using a Zeiss AxioImager Z1 microscope and AxioCam HRc color digital camera.

3 Results

3.1 Expression analysis of the LX RNase gene

The analysis of LX RNase transcripts by a real-time PCR in specific parts of the AZ showed a strong signal in the distal AZ and a very weak signal in the proximal side of the AZ. In addition there was some expression detected in the axillary bud and in the leaf petiole epidermis (Figure 1).

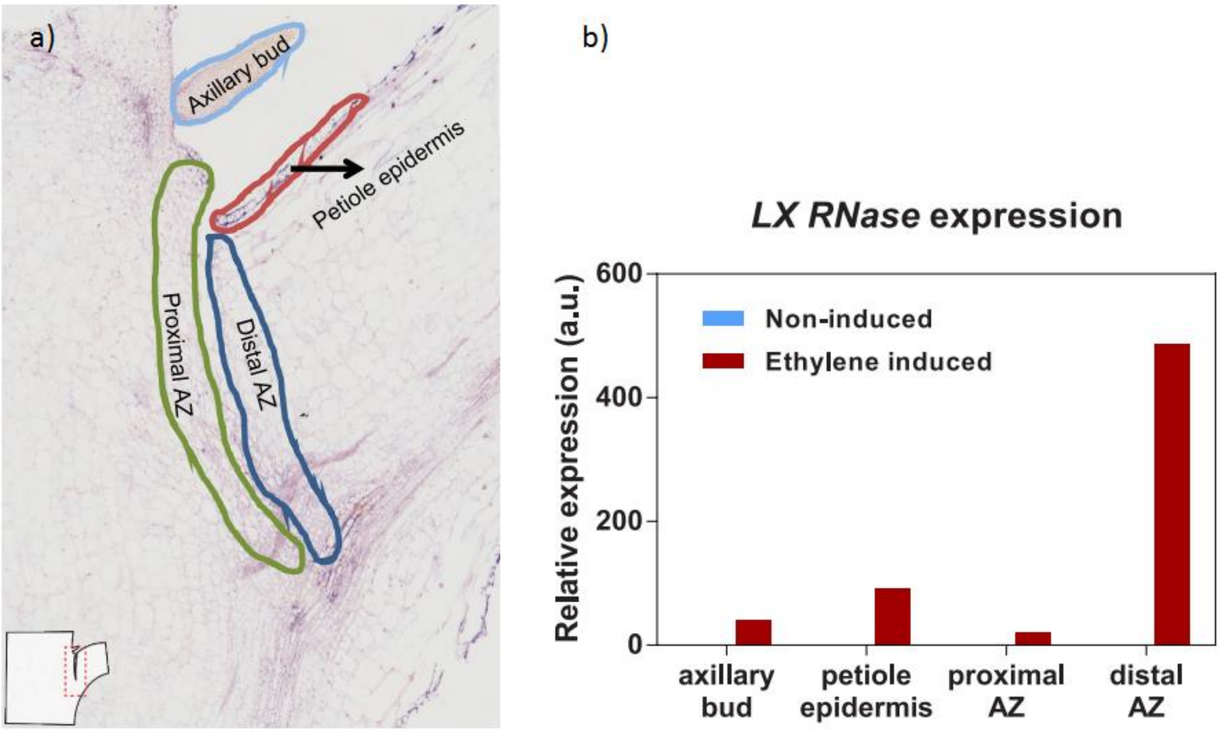

Figure 1: Expression analysis of LX RNase gene in leaf samples. a) tissue zones sampled with laser microdissection technique, b) relative expression of LX RNase in different tissues of the leaf AZ.

3.2 Immunolocalization of the LX RNase protein in the leaf AZ samples

Immunolocalization of LX RNase in the wild type showed its presence in the known site of the protein in the distal part of the AZ and additionally in the leaf petiole epidermis (Figure 2). The signal was limited to only a few cell rows. On the contrary, there was no protein detected in the AZ of any of the transgenic lines with differentially delayed leaf abscission. However, there were still strong immunolocalization signals in their petiole epidermises (Figure 2).

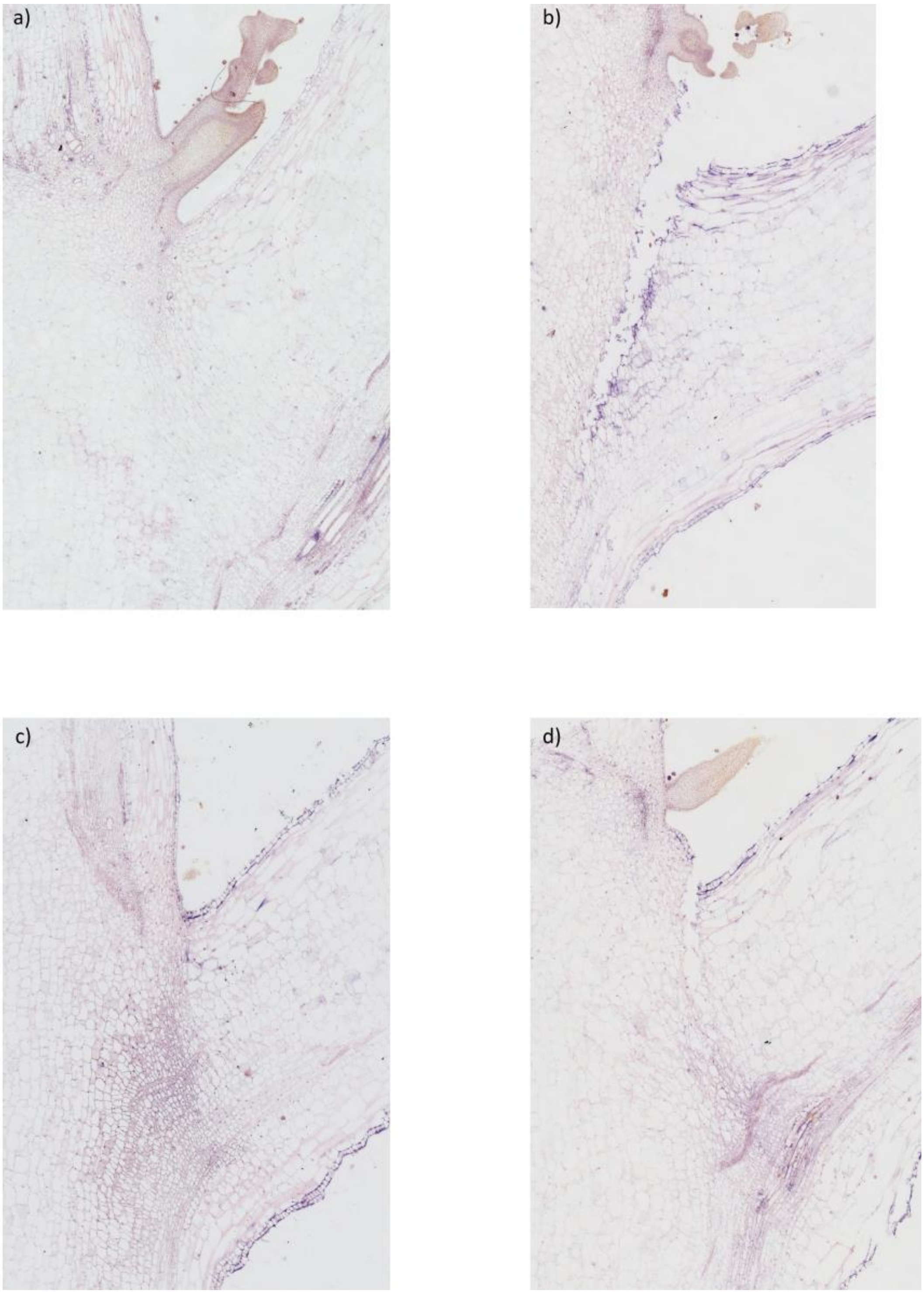

Figure 2: Immunolocalization of the LX RNase protein in different tomato lines: a) non-induced control, b) wild type, c) and d) transgenic lines. The LX RNase signal is dark blue colour.

4 Discussion

In our previous studies we have shown that the LX RNase protein localizes to the distal part of the leaf AZ [11, 14]. Here we wanted to explore if the LX RNase gene expression correlates with the localization of its protein product. For this experiment, we adopted a special microscopic technique. Applied laser microdissection allowed us to isolate only specifically chosen cells of the AZ and afterwards to isolate RNA from collected samples. With precise detection, laser microdissection and laser transport we obtained homogenous analysis material necessary for meaningful scientific results. It was not contaminated with unwanted cells which may alter our results. Using this technique we confirmed a strong LX RNase expression in only a few cell rows in the distal AZ (Figure 1). In addition, its expression also correlates with the protein detection in the leaf petiole epidermis, when it was shown for the first time (Figure 1, 2). However, a very faint signal was also detected in the proximal AZ and some in the axillary bud (Figure 1).

In various transgenic plants with inhibited LX RNase synthesis, the process of leaf abscission fracture formation and eventually the abscission itself are delayed [10]. It could be expected that the strength of the LX RNase signal in a particular transgenic line is related to the time of the actual abscission. However, we showed no signal for LX RNase protein in the distal side of the AZ fracture in any of transgenic lines (Figure 2). Currently it is not known if the LX RNase gene expression is in accordance with those findings. It is noteworthy that the LX RNase signal remained present in the leaf petiole epidermis of transgenic lines (Figure 2).

Acknowledgements

This research was supported by the research ARRS grants J1-5444 and grant for the young researcher M.C. The authors thank dr. Tanja Mrak for her help with dissection with the PALM MicroBeam microscope.

References:

[1] J.A. Roberts, K.A. Elliott, Z.H. González-Carranza. Abscission, dehiscence, and other cell separation processes. *Annu. Rev. Plant Biol.*, 53: 131–158, 2002

[2] M.E. Leslie, M.W. Lewis, S.J. Liljegren. *Organ abscission. Plant Cell Separation and Adhesion*, Roberts J.A., González-Carranza Z.H., editors., (Oxford, UK: Blackwell Publishing), 2007

[3] S. van Nocker. Development of the abscission zone. *Stewart Postharvest Rev.* 5: 1–6, 2009

[4] M.C. Jarvis, S.P.H. Briggs, J.P. Knox. Intercellular adhesion and cell separation in plants. *Plant Cell Environ.* 26: 977–989, 2003

[5] S.Meir, D.A. Hunter, J.C. Chen, V. Halaly, M.S. Reid. Molecular changes occurring during acquisition of abscission competence following auxin depletion in Mirabilis jalapa. *Plant Physiol.*, 141: 1604–1616, 2006

[6] S. Meir, S. Philosoph-Hadas, S. Sundaresan, K.S. Selvaraj, S. Burd, R. Ophir, B. Kochanek, M.S. Reid, C.-Z. Jiang, A. Lers. Microarray analysis of the abscission-related transcriptome in the tomato flower abscission zone in response to auxin depletion. *Plant Physiol.*, 154: 1929–1956, 2010

[7] F.B. Abeles, B. Rubinstein. Regulation of ethylene evolution and leaf abscission by auxin. *Plant Physiol.*, 39: 963–969, 1964

[8] R. Sexton, J.A. Roberts. Cell biology of abscission. *Annu. Rev. Plant Physiol. Plant Mol. Biol.*, 33: 133–162, 1982

[9] S.J. Dorling, M.T. McManus. *The Fate of ACC in Higher Plants. In Annual Plant Reviews Volume 44* (WileyBlackwell), 2012

[10] A. Lers, L. Sonego, P.J. Green, S. Burd. Suppression of LX ribonuclease in tomato results in a delay of leaf senescence and abscission. *Plant Physiol.*, 142: 710–721, 2006

[11] T. Bar-Dror, M. Dermastia, A. Kladnik, M. T. Žnidarič, M. P. Novak, S. Meir, … A. Lers. Programmed Cell Death Occurs Asymmetrically during Abscission in Tomato. *The Plant Cell*, 23(11), 4146–4163, 2011

[12] K. N.Chang, S. Zhong, … J. R. Ecker. Temporal transcriptional response to ethylene gas drives growth hormone cross-regulation in Arabidopsis. *eLife*, 2, 2013

[13] Z. Lin, S. Zhong, D. Grierson. Recent advances in ethylene research. *Journal of Experimental Botany,* 60, 3311–3336, 2009

[14] Marina Dermastia, Aleš Kladnik, Tal Bar-Dror and Amnon Lers. Endoreduplication preferentially occurs at the proximal side of the abscission zone during abscission of tomato leaf *Plant Signal Behav.* 2012 Sep 1; 7(9): 1106–1109.

For wider interest

Abscission is a highly regulated process in which various organs, including leaves, flowers and fruits, are separated from the mother plant as a natural stage of plant development. Abscission occurs specifically in the abscission zone (AZ) tissue. AZ is located at the base of the organ to be shed, between fruit, flower or leaf and the plant body and is comprised of few layers of differentiated cells. AZ has a crucial role in the process. Not much is known about the molecular regulation of abscission. However, we have recently shown that the programmed cell death (PCD) is involved in the abscission of tomato leaves and flowers and suggested that various abscission-related processes occur asymmetrically between the AZ proximal and distal sides. The current research is aimed to further characterize the identified asymmetry in the AZ and investigate its functional significance for the abscission process of leaves in tomato. We examine changes of expression of LX RNase gene previously shown to be related to the abscission, using quantitative real-time PCR and immunolocalisation of its protein product to determine in what AZ cells the gene transcripts and synthesized proteins are localized in the wild type and transgenic lines with inhibited LX RNase. The results of this and further research will supply information required for determining the functional significance of the observed asymmetry in the AZ. The results could reveal novel and significant insights in the functional organization of the AZ in respect to the late execution stage of the process and the role of ethylene as a signal for inducing LX RNase and abscission. The findings of this study will contribute to the overall basic knowledge on the process of abscission that is still extremely rudimentary. Results will be directly applicable in agriculture and biotechnology for controlled abscission of fruits and manipulation of abscission time.

Iodine and selenium content in different parts of pea sprouts

Ana Jerše[1,2,] **Ana Kroflič**[1,2], **Nina Kacjan Maršič**[3], **Mateja Germ**[3], **Helena Šircelj**[3], **Radojko Jaćimović**[1], **Vekoslava Stibilj**[1,2]

[1] Department of Environmental Sciences, Jožef Stefan Institute, Ljubljana, Slovenia
[2] Jožef Stefan International Postgraduate School, Ljubljana, Slovenia
[3] Biotechincal Faculty, University of Ljubljana, Ljubljana, Slovenia

ana.jerse@ijs.si

Abstract. Iodine and selenium are essential elements for humans and animals, important for normal thyroid function and thyroid hormones synthesis. Both elements come into the body by food consumption. The uptake of I and Se in pea sprouts from seeds, soaked in I and/or Se was investigated. I and Se were determined in sprouts, roots and seed residues. For iodine determination comparison between ICP-MS and k_0-INAA and for selenium determination comparison between HG-AFS and ICP-MS were done. Good agreement was observed for both comparisons. High concentrations of iodine were found in all parts of the plants, but significant difference in concentrations between different parts of the plants was observed. For selenium, high concentrations were observed, too. However, the uptake of Se(VI) was higher than the uptake of Se(IV). Iodine influenced on the selenium uptake and *vice versa*.

Keywords: iodine, selenium, ICP-MS, HG-AFS, k_0-INAA, I and Se enriched cultivated plants

1 Introduction

Iodine and selenium are essential elements for humans and animals, important for normal thyroid function and thyroid hormones synthesis. Both elements come into the body by food consumption. The main source of iodine for humans is iodized salt, but recommended decrease of salt in nutrition [1] would reduce also the intake of iodine. Slovenia is known as a country with low selenium content in soil and consequently also food contains low amounts of selenium. Naturally plants are low in concentrations of both elements. To avoid health problems caused by iodine or selenium deficiency, other sources of these two elements should be found. Iodine and/or selenium enriched cultivated plants could be an effective way to improve food quality and to provide sufficient intake of these elements for humans [2–5].

The effects of selected elements on plants are only partially known and there is a great lack of data about the interactions between these two elements in plants [3]. Therefore, it is necessary to investigate how vegetables uptake added iodine and selenium and the effects of present iodine on the uptake of selenium and *vice versa*.

The aim of our study was to investigate the iodine and selenium uptake in sprouts from seeds, soaked in I and/or Se solution. Peas belong to the group of pulse and are commonly consumed vegetable that contain a high amount of albumins. The sprouts are also used in nutrition in some cultures [6].

2 Materials and methods

Plant growing and preparation for analyses. 160 g of pea seeds were soaked for 8 h in 200 mL solution of iodide, iodate, selenite, selenate and combination of different forms of both elements. Concentration of iodine in the soaking solution was 1000 mg/L (7.88 mmol/L) and concentration of selenium was 10 mg/L (0.127 mmol/L). Control seeds were soaked in tap water. Then the seeds were arranged on plates with moisture filter paper. For the first two days, plates were covered with wet paper to keep high humidity. The day room temperature was 22–25 °C and night temperature was 18–20 °C. After 15 days of germination, plants were divided to sprouts (stems with leaves), roots and seed residues (testa and partially exhausted cotyledons) part of seed that remained after germination) and lyophilised (Gamma 1-16 LSC, Martin Christ, Germany). Dry samples were milled in the MM 200 mill (Retsch, Germany). The germination was 85.7–98.2 % successful.

Iodine and selenium determination by ICP-MS. Around 0.15 g of lyophilised milled sample of pea sprouts, roots or seed residues were weighed into quartz vessels. 10 mL of MilliQ water and 2 mL of 25 % tetramethylammonium hydroxide (TMAH) were added into each vessel. The solution was carefully mixed and then the extraction in microwave oven (Ethos One, Millstone, USA) was performed with the following programme: 20 min ramp to temperature 200 °C, 5 min hold on 200 °C. After cooling to room temperature, vessels were opened and the solution was quantitatively transferred to 30 mL polypropylene tubes and filled with MilliQ water. Due to the insoluble residue, samples were filtered through the 0.45 μm PVDF syringe filters. Before the measurement, samples were diluted to 0.1 % TMAH and tellurium was added as an internal standard. Iodine (^{127}I) and selenium (^{78}Se) determination was performed by inductively coupled plasma mass spectrometry (ICP-MS, 7500ce Agilent Technologies, Tokyo, Japan) with the following conditions: power 1500 W, sample flow 0.1 rps, carrier gas (Ar) 0.9 L/min, make up gas (Ar) 0.1 L/min, integration time in each mode (He for iodine and H_2 for selenium measurement) 0.2 s, for sample introduction MicroMist nebulizer was used. For calibration curves, KIO_3 and Selenium ICP standard (SeO_2 in 2–3% HNO_3) were used. Accuracy and precision of the results were checked by reference materials BCR 129 (Hay powder) and NIST SRM 1573a (Tomato leaves). The obtained values with standard deviation (0.143 ± 0.018) μg/g and (0.74 ± 0.04) μg/g, respectively, were in a good agreement with certified value for iodine in hay powder (0.167 ± 0.024) μg/g (k = 2) and informative value for iodine in tomato leaves 0.85 μg/g. The repeatability of the measurements was 6 % (calculated as relative standard deviation of the *k* of calibration curves, obtained during three months).

Iodine determination by k_0-INAA. k_0-INAA was used as a reference method for iodine determination due to the lack of reference materials. 0.2 g of samples were compressed by Specac press (Model 25.011; UK) in pellet with diameter 10 mm. Each pellet was irradiated with the Al-0,1 % Au standard (IRMM-530R alloy) for 5 minutes in the TRIGA Mark II reactor with a thermal neutron flux of 1.1×10^{12} cm^{-2}s^{-1}. Gamma activity of induced radionuclide ^{128}I ($t_{½}$ = 24.99 min) was measured after 10 and 30 min of cooling on absolutely calibrated HPGe detector with 45 % relative efficiency [7].

Selenium determination by HG-AFS. Around 0.20 g of lyophilized pea sprouts were digested in a 50 mL PTFE tubes by addition of 0.5 mL 96 % H_2SO_4 (s.p.) and 1.5 mL 65 % HNO_3 (s.p.). Closed tubes were heated for 4 h at 80 °C and then 60 min at 130 °C in an aluminium block. After cooling, 2 mL of 30 % H_2O_2 (p.a.) were added to the solution and heated again for 10 min at 115 °C. Then 0.1 mL of 40 % HF (s.p.) was added and heated for 10 min at 115 °C. Further, 2 mL of 30 %

H_2O_2 were added and heated for 10 min at 115 °C. Finally, the addition of 36 % HCl (s.p.) and heating at 90 °C for 10 min was needed for reduction to Se(IV). Samples were afterwards diluted with MilliQ water. Concentrations of Se were determined by hydride generation atomic fluorescence spectrometry (HG-AFS; Excalibur, PS Analytical, Orpington, UK) [8]. Accuracy and precision was checked with standard reference material NIST 1570a (Trace elements in spinach leaves) in every series of determination. Good agreement between determined value with standard deviation (0.121 ± 0.002) µg/g and certified values (0.117 ± 0.009) µg/g was obtained. The repeatability of the measurements was 9 %.

3 Results and discussion

3.1 Comparison between methods used for iodine determination

Iodine was primary determined by ICP-MS after alkaline extraction. However, k_0-INAA was used as a reference method and some samples of sprouts were analysed by both methods. As shown in the Figure 1, very good agreement between obtained results was observed. The linear agreement was observed also for higher concentrations (around 300 µg/g; not shown in Figure 1).

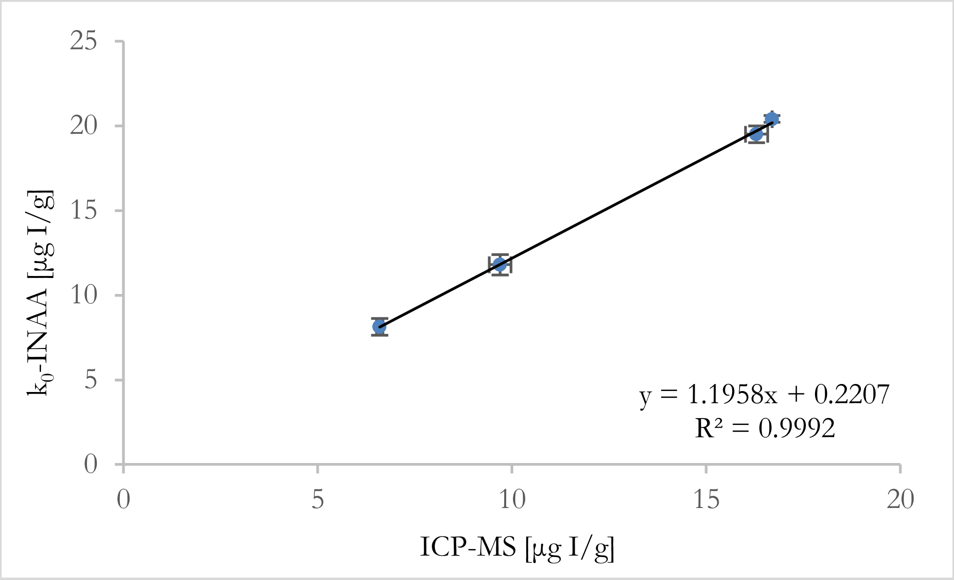

Figure 1: Comparison between iodine concentrations obtained with two different methods.

3.2 Comparison between methods used for selenium determination

The comparison between Se content in pea sprouts, roots and seed residues determined with two different methods is shown in Figure 2. In the first method Se was determined by HG-AFS after acid digestion and in the second method with ICP-MS after alkaline microwave-assisted extraction. Since the preparation and detections steps were completely different, a good agreement between values can be observed. Large standard deviation was observed for samples with concentrations around 9 µg/g probably due to the inhomogeneity of the sample.

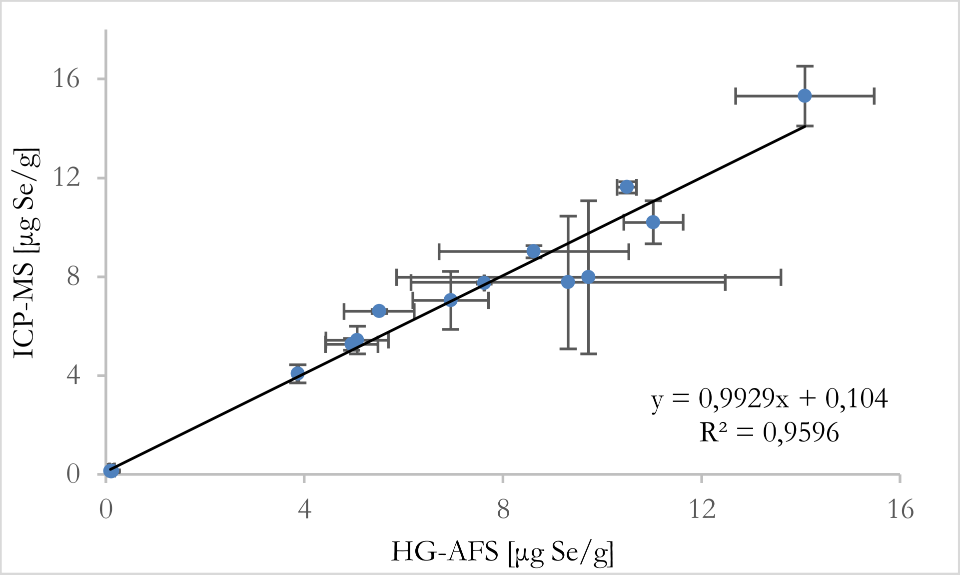

Figure 2: Comparison between selenium concentrations obtained with two different methods.

3.3 Iodine content in pea plants

Iodine concentrations in different parts of plants, obtained by ICP-MS, and the uptakes are summarized in the Table 1. The uptake is an approximation and was calculated as iodine mass in the part of plant divided by the mass of iodine in the seed after soaking. The supposition of the same passing of water and iodine into seeds was made. It was estimated that there was 8 % of dry mass in sprout and roots and 25 % of dry mass in seed residue.

Results in Table 1 show very high concentrations of iodine in all parts of the treated plants in comparison with the control plants, but there is a big difference in iodine content between different parts. Treated sprouts contained the lowest

Table 1: Iodine concentrations [µg/g dry mass], determined by ICP-MS, and uptakes [%] in different parts of pea plants.

	Sprouts		Roots		Seed residues	
Treating	c [µg/g DM]	Uptake [%]	c [µg/g DM]	Uptake [%]	c [µg/g DM]	Remained I [%]
Control	3.18 ± 1.10	-	26.3 ± 1.3	-	12.3 ± 5.0	-
I(–I)	188 ± 23	4	334 ± 47	5	419 ± 17	26
I(–I) + Se(IV)	186 ± 10	4	341 ± 76	5	468 ± 20	30
I(–I) + Se(VI)	247 ± 20	5	306 ± 52	4	566 ± 19	34
I(V)	211 ± 35	4	355 ± 67	6	460 ± 34	28
I(V) + Se(IV)	152 ± 15	3	275 ± 5	4	498 ± 22	31
I(V) + Se(VI)	216 ± 6	4	326 ± 77	5	520 ± 49	30

Table 2: Se concentrations [µg/g dry mass], determined by HG-AFS, and uptakes [%] in different parts of pea plants.

	Sprouts		Roots		Seed residues	
Treating	c [µg/g DM]	Uptake [%]	c [µg/g DM]	Uptake [%]	c [µg/g DM]	Remained Se [%]
Control	0.11 ± 0.03	-	0.13 ± 0.05	-	0.10 ± 0.05	-
Se(IV)	5.60 ± 0.21	15	10.13 ± 3.17	19	12.50 ± 2.64	63
Se(IV) + I(–I)	5.07 ± 0.63	11	11.03 ± 0.60	16	9.31 ± 3.17	59
Se(IV) + I(V)	3.87 ± 0.02	8	4.95 ± 0.53	7	9.73 ± 3.87	61
Se(VI)	14.73 ± 1.96	38	7.07 ± 1.85	12	7.35 ± 1.83	33
Se(VI) + I(–I)	14.08 ± 1.39	27	6.95 ± 0.76	10	8.62 ± 1.91	52
Se(VI) + I(V)	10.5 ± 0.2	20	5.51 ± 0.71	9	7.62 ± 0.01	44

Results in Table 1 and 2 are given as average value with standard deviation.

concentration of iodine in comparison with other parts of plants, while seed residues contained the highest amount of iodine, probably due to the high amount of starch that binds iodine regardless to its form. All parts of the plants contained a slightly higher amount of iodine when treated with I(V) in comparison with I(–I). However, the uptakes were quite low. The sum of percents of uptakes in sprouts and roots and percent of iodine in seed residues was around 40 %. One of the possible reasons is that passing of iodine into seeds is much slower than water. The other possible reason could be volatilisation of iodine during plant growing. It is also possible that iodine was rinsed from seeds with water for moistening the filter paper during the germination.

Selenium has different effects on iodine uptake. In sprouts, Se(IV) has no effect on the uptake of iodide, but decreases the uptake of iodate, while Se(VI) has no effect on the uptake of iodate but increases the uptake of iodide. In roots, selenium has no significant effect on the uptake of iodide. Although the trend of uptake of iodate in roots is similar, as in sprouts, due to the large standard deviation we cannot claim that the presence of selenium influence the iodine uptake.

According to our knowledge, there is no literature data about the iodine determination or iodine and selenium interactions in sprouts or adult pea plants. However, some data about iodine uptake in the presence of selenium in plants can be found. Zhu et. al. [2] have determined iodine and selenium content in hydroponically grown spinach shoots and roots. The plants were treated with I(V) and/or Se(VI) in concentrations of 0, 10 and 50 μM for both. They reported a slight inhibition of iodine uptake in shoots in the presence of higher concentrations of selenium, while the concentration in the roots remained at a comparable level. Similar results have been reported by Smoleń et. al. [3] for iodine concentrations in lettuce treated with I(V) and/or Se(VI) in nutrient medium (concentrations of I was 1 mg/L and of Se 0.5 or 1.5 mg/L) and foliarly (0.05 % solution of I and 0.005 % solution of Se). Although the literature data show decreased I(V) uptake in the green part of the plant in the presence of Se(VI), our results did not show the same trend since the concentrations of iodine were independent on selenium presence.

3.4 Selenium content in pea plants

Results show that pea seeds accumulated a great amount of selenium, regardless to the form in soaking solution (Table 2). However, a higher amount of selenium in roots was present when treated with Se(IV), while in the sprouts, higher amount can be observed in plants, treated with Se(VI). Due to the lower toxicity, the transport of Se(VI) is much easier in comparison with Se(IV) or organic selenium, such as SeMet [9]. This can also be seen from percent of Se uptake in sprouts, which is higher in case of treatment with Se(VI) solution. In literature selenium content and uptake in buckwheat sprout can be found. After soaking of buckwheat seeds in 10 mg/L solution of Se(IV) and Se(VI), concentrations of selenium in sprouts were (1.87 ± 0.02) μg/g and (7.08 ± 0.18) μg/g (uptakes (73 ± 2) % and (19 ± 1) %), respectively [4]. In selenium enriched bean seeds, grown from seeds, soaked in Se(VI) solution (10 mg Se(VI)/L), Se concentrations between 0.47 and 0.65 μg/g were obtained [10]. Results from present study are therefore comparable with literature data.

Iodine had different effects on selenium uptake and depends on their forms (Table 2). I(–I) had no impact on the uptake of selenium in the form of selenite for all parts of the plants. The presence of I(V) in soaking solution decreases the uptake of Se(IV) for about 50 % in sprouts and 60 % in roots. The same trend can be observed also for Se(VI) in combination with both forms of iodine.

4 Conclusions

Iodine and selenium were determined in different parts of pea plants, treated with iodine and/or selenium in different forms. Both elements were determined with two methods and in both cases, good agreement between values obtained by ICP-MS and k_0-INAA for iodine and HG-AFS and ICP-MS for selenium were ascertained. For both I and Se higher concentrations were observed in pea plants where elements were added in comparison with control plants. For iodine, the lowest concentrations were determined in sprouts and the highest in seed residues, while for selenium the concentration especially depended on the form of soaking solution. Although selenium increased or decreased the concentrations of iodine in plants in some cases (max. ± 30 %), iodide had greater influence on selenium concentrations in plants (up to –50 %). On the other hand, iodate had no significant effect on selenium concentration in plants (± 10 %). However, the lowest concentrations of iodine and selenium were found in plants, treated with I(V) and Se(IV) due to their higher toxicity in comparison to I(–I) and Se(VI).

By further investigations these plants could be introduced into the nutrition, but first iodine and selenium species need to be obtained due to the different bioavailability of various forms of these elements. The concentrations of soaking solutions should also be optimised to provide the recommended nutrition intakes.

References:

[1] F. Delahaye. Should we eat less salt?. *Archives of Cardiovascular Disease,* **106:**324–332, 2013

[2] Y.G. Zhu, et al. Interactions between selenium and iodine uptake by spinach (Spinacia oleracea L.) in solution culture. *Plant and soil*, 261:99–105, 2004

[3] S. Smolen, et al. Assessment of biofortification with iodine and selenium of lettuce cultivated in the NFT hydroponic system. *Scientia Horticulturae*, 166:9–16, 2014

[4] P. Cuderman, et al. Extraction of Se species in buckwheat sprouts grown from seeds soaked in various Se solutions. *Food Chemistry*, 123:941–948, 2010

[5] P. Smrkolj, et al. Respiratory potential and Se compounds in pea (Pisum sativum L.) plants grown from Se-enriched seeds. *Journal of Experimental Botany*, 57:3595–3600, 2006

[6] R. Hoover, et al. Composition, molecular structure, properties, and modification of pulse starches: a review. *Food Research International*, 45:399–413, 2010

[7] R. Jaćimović, et al. k_0-INAA quality assessment by analysis of different certified reference materials using the KAYZERO/SOLCOI software. *Journal of Radioanalytical and Nuclear Chemistry*, 257:259–663, 2003

[8] P. Smrkolj, et al. Determination of selenium in vegetables by hydride generation atomic fluorescence spectrometry. *Analytica Chimica Acta*, 512:11–17, 2004

[9] N. Terry, et al. Selenium in higher plants. *Annual Review of Plant Physiology and Plant Molecular Biology*, 51:401–432, 2000

[10] P. Smrkolj, et al. Selenium uptake and species distribution in selenium-enriched bean (*Phaseolus vulgairs* L.) seeds obtained by two different cultivations. *European Food Research Technology*, 225:233–237, 2007

For wider interest

Iodine and selenium are essential elements, important for normal thyroid function and thyroid hormones synthesis. They both come into the body by food consumption.

Slovenia is a country with low concentrations of these elements in nutrition. For iodine, the main source is salt, but recommended decrease of salt in nutrition would reduce also the intake of iodine. To avoid health problems caused by iodine or selenium deficiency, other food sources of the elements should be found.

Because naturally plants are low in concentrations of both elements, our aim was to cultivate iodine and selenium enriched pea plants. By some further optimisations, these plants could be introduced into the nutrition. This would be an effective way to improve food quality and to provide sufficient intake of these elements for humans.

Iridium-catalysed synthesis of α-haloketones

Štefan Možina[1,2], **Antonio Bermejo Gómez**[3]**,** **Belén Martín-Matute**[3], **Stojan Stavber**[1,4], **Jernej Iskra**[4]
[1]Centre of Excellence for Integrated Approaches in Chemistry and Biology of Proteins (CIPKeBiP), Ljubljana, Slovenia
[2]Jožef Stefan International Postgraduate School, Ljubljana, Slovenia
[3]Department of Organic Chemistry and Berzelii Center EXSELENT, Arrhenius Laboratory, Stockholm University, Stockholm, Sweden
[4]Department of Physical and Organic Chemistry, Jožef Stefan Institute, Ljubljana, Slovenia
stefan.mozina@ijs.si

Abstract. α-Haloketones and α-haloaldehydes are essential intermediates in organic synthesis, nevertheless their formation from unsymmetrical ketones was proven to be difficult. Selective synthesis of α-haloketones was studied by iridium catalysed 1,3-hydrogen shift of allylic alcohol with concomitant halogenation with dihaloiodonium(I) reagents. Selectivity of reaction was very sensitive on solvent mixture and by using $HIBr_2$, α-bromoketones were obtained with good conversion and high selectivity in THF/H_2O solvent mixture. On the other hand, in $EtOH/H_2O$ solvent mixture only moderate selectivity was obtained for the synthesis of α-iodoketones.

Keywords: halogenation, iridium catalyst, α-haloketones, hypervalent iodine compounds

1 Introduction

α-Haloketones are important and versatile building blocks for the synthesis of biologically active compounds. They are used for various transformations such as formation of heterocycles, C-C coupling reaction and nucleophilic substitution [1]. In the past, for direct conversion of carbonyl compounds into α-haloketones or α-haloaldehydes various halogenating reagents were mostly used causing problems with incompatibility of certain functional groups with the reaction conditions [2].

In case of halogenation of carbonyl compounds various protocols have been developed in the presence of protic or Lewis acid. Nevertheless there are several drawbacks present as toxicity, difficult handling and low selectivity [3]. On the other hand there is significant lack of methods for synthesis of α-iodocarbonyl compounds. Reported methods use iodine as an iodinating agent [4] which usually demands additional compounds in stoichiometric or sub- stoichiometric amounts such as selenium dioxide [5], ceric(IV) ammonium nitrate [6], mercury(II) chloride [7]. In some cases α-iodoketones were not formed directly from ketones but through enol acetates [8], alkenes [9] and nucleophilic substitution [10]. Low electrophilic character of molecular iodine makes its use difficult. One solution of this problem represents an oxidative iodination method. By using H_2O_2 or O_2 this method obtained "green" potential. Reactivity was further improved by using hypervalent iodine as reagent e. g. iodine(I) compounds [11].

Despite a number of methods have been reported for synthesis of α-haloketones and α-haloaldehydes, most have been containing only one enolisable position [12]. The same reaction on unsymmetrical ketones, which have two enolisable positions (α and α'), has been challenging and a mixture of products is usually obtained causing the challenging separation of constitutional isomers (Figure 1). Most methods control selectivity by steric or electronic differentiation of two enolisable positions consequently resulting in selective halogenation [13]. Nevertheless, for many ketones the latter approach does not lead to complete regioselectivity. Serious problems for selective halogenation are also present when steric and electronic influences favour undesirable enolisable positions (Figure 1) [12].

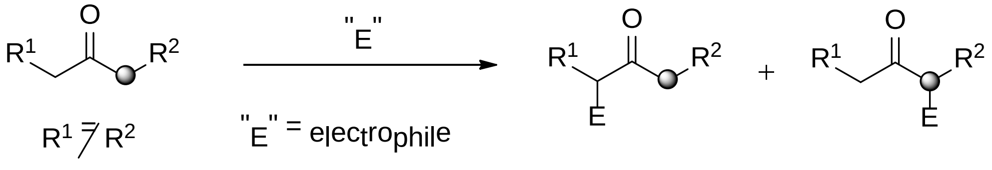

Figure 1: Classical synthesis of α-haloketones

In last few years, Martín-Matute et al. reported alternative selective methods for synthesis α-fluoro [14], α-chloro [12] and α-bromo [13] ketones and aldehydes. By using iridium catalyst for 1,3-hydrogen shift on allylic alcohols in presence of electrophilic halogenating reagent selective formation of α-fluoro, α-chloro and α-bromocarbonyl compounds were prepared. We envisaged that by combining iridium catalyst for 1,3-hydrogen shift on allylic alcohols with dihaloiodine(I) species we could selectively introduce halogen atom (Figure 2).

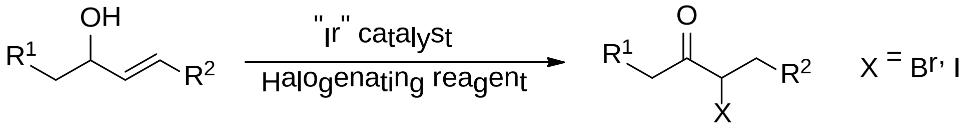

Figure 2: Synthesis of α-haloketones by using iridium-catalysed isomerisation/halogenation of allylic alcohols

2 Results and discussion

We first investigated domino reaction 1,3-hydrogen shift/halogenation of oct-1-en-3-ol as starting allylic alcohol in different solvents with $[IrCp^*Cl_2]_2$ (2 mol %) as the catalyst and M^+ IX_2^- (M=H, $N(CH_3)_4$) as iodinating reagent. Dichloroiodo(I) species were chosen from other dihaloiodo(I) reagents as they had best selectivity for iodination [11, 15]. After scanning different solvents no desired product has been detected, indicating that halogenating agent and catalyst were incompatible, proving difficulty of synthesis of α-iodoketones (Figure 3).

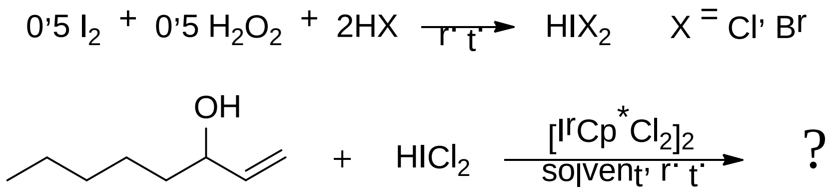

Figure 3: Synthesis of HIX_2 reagent and its use in case of $HICl_2$ on oct-1 en-3-ol formed only unknown compounds

We therefore switched our focus of research on dibromoiodo(I) reagents for which it is known that can act as brominating as well as iodinating agents [11, 15]. We screened reaction conditions starting with different solvent compositions. With THF/H_2O mixture best result was obtained, however reaction was very sensitive on ratio of solvents (Table 1).

Table 1: Screening different solvent compositions for synthesis of α-haloketones[a]

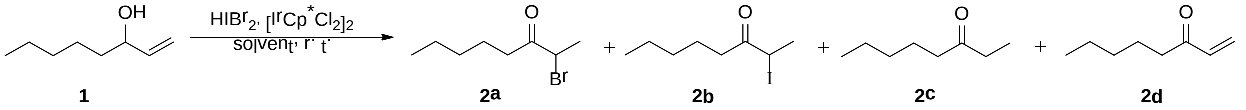

Entry	Solvent	Time [h]	Conversion [%][b]	2a	2b	2c	2d
1[c]	THF	23	92	33	–	7	–
2	THF/H_2O (20 : 1)	16	37	89	–	11	–
3	THF/H_2O (2 : 1)	23	34	41	12	44	3
4	**THF/H_2O (1 : 1)**	**16**	**73**	**81**	**–**	**16**	**3**
5	THF/H_2O (1 : 2)	20	77	51	15	21	13
6[c]	THF/H_2O (1 : 20)	6	98	–	–	–	–

[a] Reaction conditions: 1 (1.0 mmol, 0.2 M), 1.0 mmol HIB_2, $[IrCp^*Cl_2]_2$ (2.0 mol%) at room temperature. [b] Determined by ^{1}H NMR spectroscopic analysis.
[c] Additional products were present but could not be identified.

Further optimization studies were done with THF/H_2O (1:1) mixture, where we obtained the highest selectivity for formation of 2-bromooctan-3-one and good conversion. With this conditions undesired side products were still formed (**2c** and **2d**), for which challenging purification is needed, and therefore different iridium catalyst were tested. The highest conversion was obtained for $[IrCp^*I_2]_2$ catalyst (Table 2).

Table 2: Screening of different iridium catalyst[a]

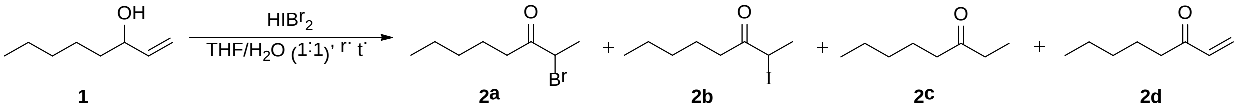

Entry	Catalyst	Time [h]	Conversion [%][b]	2a	2b	2c	2d
1	$[IrCp^*Cl_2]_2$	16	73	81	–	16	3
2	$[IrCp^*Br_2]_2$	23	77	42	–	56	2
3	**$[IrCp^*I_2]_2$**	**21**	**89**	**75**	**–**	**25**	**–**
4[c]	$[IrCp^*(H_2O)_3]SO_4$	24	77	73	18	9	trace
5	$(IrCp^*)_2(OH)_3]OH$	21	83	81	–	19	–

[a] Unless otherwise noted: **1** (1.0 mmol, 0.2 M), 5.0 mL THF/H_2O (1:1), 2.0 mol% Ir-catalyst at room temperature. [b] Determined by ^{1}H NMR spectroscopic analysis.
[c] 4.0 mol % Ir-catalyst.

Since eliminating formation of **2c** was unsuccessful, we examined whether acidity of reagent is a cause for formation of side product **2c**. $N(CH_3)_4IBr_2$ was prepared according to literature [15] and the reaction was carried out in optimised solvent THF/H_2O (1:1) in the presence of iridium catalysts with different ligands (Table 3). The best result (95 % conversion) was obtained when $[(IrCp^*)_2(OH)_3]OH$ was used as catalyst (Table 3, entry 5). Although conversion was high in these conditions, octane-3-one was still formed as side product.

Table 3: Iridium catalysed 1,3-hydrogen shift/halogenation with $N(CH_3)_4IBr_2$ of 1-octene-3-ol[a]

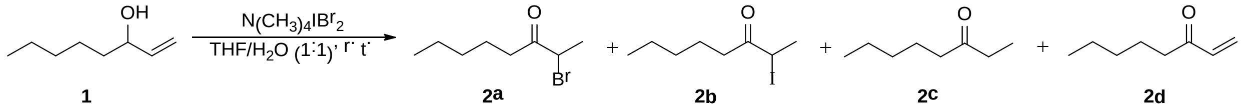

Entry	Catalyst	Time [h]	Conversion [%][b]	2a	2b	2c
1	$[IrCp^*Cl_2]_2$	20	81	80	–	20
2	$[IrCp^*Br_2]_2$	20	80	75	14	9
3	$[IrCp^*I_2]_2$	22	85	73	16	9
4[c]	$[IrCp^*(H_2O)_3]SO_4$	22	89	84	–	16
5	**$[(IrCp^*)_2(OH)_3]OH$**	**22**	**95**	**86**	**–**	**14**

[a] Unless otherwise noted: 1 (1.0 mmol, 0.2 M), 5.0 mL THF/H_2O (1:1), 2.0 mol % Ir-catalyst at room temperature. [b] Determined by ^1H NMR spectroscopic analysis. [c] 4.0 mol % Ir-catalyst.

In some of previous cases we observed formation of **2b** in small amounts. Since **2b** is very interesting for further modifications and there are only few known methods for its synthesis, we wanted to improve selectivity for its formation. Among different solvent mixtures the highest formation of **2b** was obtained in solvent mixture EtOH/H_2O (1:1). By additional research and changing ratio of EtOH/H_2O it was possible to further increase selectivity for **2b.** The best result with moderate selectivity was obtained with EtOH/H_2O (2:3) (Table 4).

Table 4: Effect of solvent mixture on selectivity of formation **2b**[a]

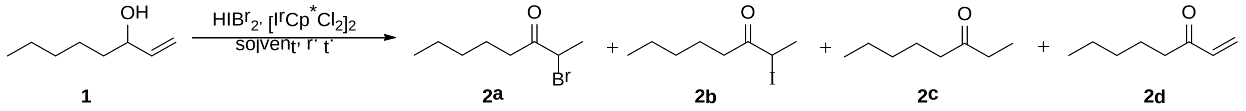

Entry	Solvent	Time [h]	Conversion [%][b]	2a	2b	2c	2d
1	EtOH/H_2O (2:1)	22	60	77	–	23	–
2	EtOH/H_2O (3:2)	25	58	57	12	21	2
3	EtOH/H_2O (1:1)	22	70	29	31	13	7
4	**EtOH/H_2O (2:3)**	**25**	**77**	**21**	**56**	**8**	**1**
5	EtOH/H_2O (1:2)	22	96	10	5	9	trace

[a] Unless otherwise noted: 1 (1.0 mmol, 0.2 M), 2.0 mol % Ir-catalyst at room temperature. [b] Determined by ^1H NMR spectroscopic analysis.

The reaction scope was then expanded by exploring the 1,3-hydrogen shift/halogenation on two additional allylic alcohols (Figure 4). Phenyl derivate **3** showed similar pattern of transformation and **4a** was main product. Even though **1** and **5** are very similar in structure, the same reaction conditions resulted in introduction of different halogen atom. In the case of **5** mostly iodination proceeded and **6b** was main product (Figure 4).

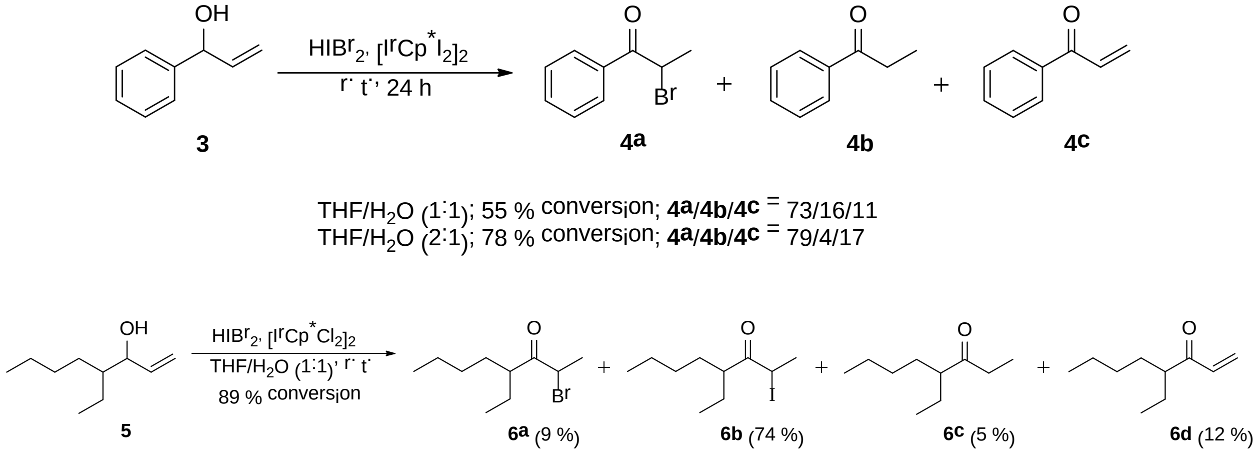

Figure 4: Expanded scope of 1,3-hydrogen shift/halogenation on other allylic alcohols

3 Conclusion

We have developed new method for synthesis α-bromoketones and α-iodoketones by the use of $HIBr_2$ as halogenating agent in the presence of iridium catalyst. On the other hand iodination with $HICl_2$ in the presence of iridium catalyst was not successful and no desired product was observed. In case of bromination very high selectivity and conversion were obtained while in iodination only moderate selectivity was observed. In the future our research will focus on improving selectivity of iodination as well as increasing of the variety of tested allylic alcohols.

4 Acknowledgment

The financial support of the Slovenian Research Agency is greatly appreciated. The authors are grateful to COST action (CM1205 CARISMA) for STSM.

5 Reference

[1] A. Erian, S. Sherif and H. Gaber. The Chemistry of α-Haloketones and Their Utility in Heterocyclic Synthesis. *Molecules*, 8(11): 793-865, 2003.

[2] Z.-W. Chen, D.-N. Ye, M. Ye, Z.-G. Zhou, S.-H. Li and L.-X. Liu. AgF/TFA-promoted highly efficient synthesis of α-haloketones from haloalkynes. *Tetrahedron Letters*, 55(7): 1373-1375, 2014.

[3] A. Podgoršek, S. Stavber, M. Zupan and J. Iskra. Bromination of ketones with H_2O_2-HBr "on water". *Green Chemistry*, 9(11): 1212-1218, 2007.

[4] M. L. N. Rao and D. N. Jadhav. Metal catalyst-free direct α-iodination of ketones with molecular iodine. *Tetrahedron Letters*, 47(38): 6883-6886, 2006.

[5] A. Bekaert, O. Barberan, M. Gervais and J.-D. Brion. Direct α-iodination of ketones using iodine/SeO_2. *Tetrahedron Letters*, 41(16): 2903-2905, 2000.

[6] C. A. Horiuchi and S. Kiji. A New α-Iodination of Ketones Using Iodine/Cerium(IV) Ammonium Nitrate. *Chemistry Letters*, 17(1): 31-34, 1988.

[7] J. Barluenga, J. M. Martinez-Gallo, C. Najera and M. Yus. Mercury(II) Chloride-Iodine: A Useful Reagent for the Direct and Regiospecific Synthesis of α-Iodocarbonyl Compounds. *Synthesis*, 1986(08): 678-680, 1986.

[8] D. Dolenc. Iodination of Enol Acetates and 1,3-Diones Using N-Iodosaccharin. *Synthetic Communications*, 33(16): 2917-2924, 2003.

[9] J. S. Yadav, B. V. Subba Reddy, A. P. Singh and A. K. Basak. IBX/I_2-mediated oxidation of alkenes and alkynes in water: a facile synthesis of α-iodoketones. *Tetrahedron Letters*, 49(41): 5880-5882, 2008.

[10] J. C. Lee and Y. S. Jin. Efficient Method for α-Iodination of Ketones. *Synthetic Communications*, 29(16): 2769-2774, 1999.

[11] L. Bedrač and J. Iskra. Iodine(I) Reagents in Hydrochloric Acid-Catalyzed Oxidative Iodination of Aromatic Compounds by Hydrogen Peroxide and Iodine. *Advanced Synthesis & Catalysis*, 355(7): 1243-1248, 2013.

[12] N. Ahlsten, A. Bermejo Gómez and B. Martín-Matute. Iridium-Catalyzed 1,3-Hydrogen Shift/Chlorination of Allylic Alcohols. *Angewandte Chemie International Edition*, 52(24): 6273-6276, 2013.

[13] A. B. Gómez, E. Erbing, M. Batuecas, A. Vázquez-Romero and B. Martín-Matute. Iridium-Catalyzed Isomerization/Bromination of Allylic Alcohols: Synthesis of α-Bromocarbonyl Compounds. *Chemistry – A European Journal*, 20(34): 10703-10709, 2014.

[14] N. Ahlsten and B. Martin-Matute. Ir-catalysed formation of C-F bonds. From allylic alcohols to α-fluoroketones. *Chemical Communications*, 47(29): 8331-8333, 2011.

[15] L. Bedrač and J. Iskra. Dihaloiodates(I): synthesis with hydrogen peroxide and their halogenating activity. *Tetrahedron Letters*, 53(41): 5555-5558, 2012.

Iridium-catalysed synthesis of α-haloketones

Štefan Možina[1,2], **Antonio Bermejo Gómez**[3], **Belén Martín-Matute**[3], **Stojan Stavber**[1,4], **Jernej Iskra**[4]

[1]Centre of Excellence for Integrated Approaches in Chemistry and Biology of Proteins (CIPKeBiP), Ljubljana, Slovenia
[2]Jožef Stefan International Postgraduate School, Ljubljana, Slovenia
[3]Department of Organic Chemistry and Berzelii Center EXSELENT, Arrhenius Laboratory, Stockholm University, Stockholm, Sweden
[4]Department of Physical and Organic Chemistry, Jožef Stefan Institute, Ljubljana, Slovenia

stefan.mozina@ijs.si

α-Haloketones are important and versatile building blocks for the synthesis of biologically active compounds. They are also used for various molecular transformations such as formation of heterocycles, C-C coupling reaction and nucleophilic substitution. A difficulty commonly encountered during synthesis of halogenated compounds is a lack of regioselectivity. In the halogenation of unsymmetrical ketones, reaction can proceed on α and α' site and two products are usually obtained. By using iridium catalyst for 1,3-hydrogen shift on allylic alcohols combined with oxidative halogenation/dihaloiodine(I) agents complete regiocontrol of formation of α-haloketones was achieved.

Determination of geographical origin of milk in Slovenian by elemental and stable isotope analysis

Igor Perišić[1,2] , Doris Potočnik[1,2], Marijan Nečemer[3], Darja Mazej[1], Nives Ogrinc[1,2]

[1] Department of Environmental Sciences, Jožef Stefan Institute, Ljubljana, Slovenia

[2] Jožef Stefan International Postgraduate School, Ljubljana, Slovenia

[3]Department Low and Intermediate Energy Physics

igor.perisic@ijs.si

Abstract. The presented work uses stable isotope ratios and elemental composition to determine the regional provenance of milk. The first database of authentic Slovenian cow milk has been established. The database includes isotope values of oxygen and hydrogen ($\delta^{18}O$ and $\delta^{2}H$) in milk, the isotopic composition of carbon and nitrogen in casein ($\delta^{13}C$ and $\delta^{15}N$) and the elemental composition from four different geographical regions in Slovenia: the Alps, the Dinaric Alps, the Pannonian Plain and the Mediterranean.
Stable isotope data were obtained by measurements on Isotope Ratio Mass Spectrometry (IRMS). Concentrations of P, S, Cl, K, Ca, Zn, Br, Rb, Sr were analysed using reflection X-ray fluorescence spectrometry (XRF), while trace elements (Mn, Fe, Cu, As, Se, Cd, Pb) were determined using inductively coupled plasma mass spectrometry (ICP-MS). The results show that the use of stable isotopes in a combination with elemental composition is the most appropriate method for verifying the declared geographical origin. The most significant variables were Cl, Ca, Zn, K in $\delta^{13}C$ during summer, while in winter Cl, K, P, S, Mn and $\delta^{15}N$ were more significant. The overall prediction ability was 91.4%. This research represents a part of the ERA Chair ISO-FOOD for isotope techniques in food quality, safety and traceability.

Keywords: Stable isotopes, milk, origin, IRMS, ICP-MS, XRF

1. Introduction

Milk contains numerous nutrients and it makes a significant contribution to meeting the body's needs for calcium, magnesium, selenium, riboflavin, vitamin B12 and pantothenic acid (vitamin B5). In human diet, milk and dairy products contribute between 18% - 24%. Composition of milk is affected by various factors, including stage of lactation, breed differences, number of calving's (parity), seasonal variations, age and health of animal, feed and management effects including number of milkings per day and herd size. Milk and dairy product are used extensively and therefore vulnerable to economic adulterations. Therefore there is a high risk of intentionally mislabelled products especially when price is a factor. The determination of the geographic origin of milk and milk products has recently become possible, by measuring the stable isotope ratios of oxygen ($\delta^{18}O$) in milk water together with the hydrogen ($\delta^{2}H$), nitrogen ($\delta^{15}N$) and carbon ($\delta^{13}C$) isotope contents of specific milk fractions. [1] The quality of the product is closely linked to its geographical origin.

The $\delta^{18}O$ content in milk water reflects the isotope composition of the ground water drunk by an animal which, in turn is influenced by geographical factors such as altitude, latitude, and distance from the sea. [2] In summer, milk water has higher $\delta^{2}H$ and $\delta^{18}O$ values because animals eat fresh plants containing $\delta^{18}O$-enriched water due to evapotranspiration phenomena in leaves.

The $\delta^{13}C$ values were found to be highly dependent on the composition of the diet, particularly with regard to maize, a C_4 plant. C_3 plants have lower $\delta^{13}C$ values ranging from -30 and -23‰, while C4 plants such as maize have higher $\delta^{13}C$ values ranging from -11 to -14 ‰. [3]

The $\delta^{15}N$ depends on the inorganic nitrogen present in the soil (the primary source of nitrogen for the plants), agricultural practices, water stress and the pedoclimatic conditions of the locations. The $\delta^{15}N$ values in dairy products reflect through the plants consumed by animals and the isotope composition of the original soil. The presence of nitrogen-fixing plants in the diet can lead to lower values, because these plants use both atmospheric and soil nitrogen as a nitrogen source, which results in lower $\delta^{15}N$ content than in plants relying only on soil nitrogen. [1]

Evaluation of trace element content has been also proposed to assure the geographical origin of an agricultural product. Sacco et al. (2009) analysed milk samples from different geographical areas including Italy and some EU countries (Austria, Croatia, Hungary, Germany and Slovenia) to determine whether their chemical composition could be used to identify their geographical origin [8]. Metal concentrations (Ba, Mn, Zn, Fe and Cu) were determined together with C and N isotopic ratios.

A common theme of food authentication and traceability studies is the requirement for a database of genuine samples to which the sample can be compared to establish its authenticity. Parameters can be then statistically evaluated in order to identify key tracers that differentiate the regions or countries of interest. [5]

The aim of this work is to use the isotopic and elemental composition in order to determine geographical origin of Slovenian milk. Important part of this research is to examine the effect of season and geographical location changes in milk content in relation to the diet composition.

2. Materials and methods

2.1 Samples

The sampling of cow's milk was performed two times per year in June and December from different geographical regions in Slovenia (Alpine, Mediterranean, Dinaric and Pannonian). Samples were provided by five Slovenian diary producers: Ljubljanske mlekarne d.d., Pomurske mlekarne d.d., Mlekarna Planika d.o.o. and Mlekarna Celeia d.o.o.). The samples were stored at −20°C before analysis. All together 80 samples were provided for analysis.

2.2 Isolation of casein

Milk fat was removed by centrifugation (10 min at 4500 rpm) and casein precipitated from the skimmed milk by acidification at pH 4.3 with 2M HCl and then centrifuged. The precipitate was rinsed with water and freeze-dried.

2.3 Stable isotope analysis

The δ^2H and $\delta^{18}O$ were measured directly in milk after equilibration with reference CO_2. The equilibration for δ^2H measurements is carried in the presence of Pt as a catalyst. The equilibration for $\delta^{18}O$ is carried out at 25°C for 24 h, while for δ^2H determination the equilibration is carried out at constant temperature of 40°C for 6

h. Measurements were performed on an IRMS (GV Instruments) with IsoPrime MultiFlow Bio equilibration unit. Dry casein samples were put directly into a tin capsule, closed with tweezers and put into automatic sampler of the elemental analyser. All analyses were performed separately on a Europa Scientific 20-20 continuous flow mass spectrometer with an ANCA-SL solid-liquid preparation module. Analyses were calibrated against international standards. The reproducibility of measurements was ±1.0‰ for $\delta^{2}H$, ±0.1‰ for $\delta^{18}O$, ±0.2‰ for $\delta^{13}C$ and ±0.3‰ for $\delta^{15}N$.

2.4 Multi-elemental analysis

Concentration of macro- and micro-elements (P, S, Cl, K, Ca, Cu, Br, Rb, Sr) were performed on freeze-dried samples by Energy Dispersive X-ray Fluorescence Spectrometry (XRF). For trace elements microwave digestion (Microwave system ETHOS 1, Milestone SN 130 471) with nitric acid and hydrogen peroxide and dilution with a solution containing ammonia, EDTA and Triton X-100. Concentrations of elements in the prepared solutions were determined by an Octapole Reaction System (ORS) Inductively Coupled Plasma Mass Spectrometer (7500ce, Agilent) equipped with an ASX-510 Autosampler (Cetac) [6]. Limits of detection for Cd, Pb, As, Se, Cu, Zn and Mn, calculated as three times the standard deviations of the blank sample, are 0.04, 0.4, 0.04, 0.9, 6, 20, 0.4 ng/g milk sample, respectively.

3. Results and discussion

Throughout the period of sampling, the isotopic composition of water varies between -9.12 and -6.73‰. $\delta^{2}H$ values in milk vary between -55.0 and -32.1‰. The $\delta^{2}H$ and $\delta^{18}O$ values in milk samples were isotopically enriched relative to cow drinking water. The mean difference between milk and cow drinking water was 11% for $\delta^{2}H$ values ($1\sigma = 3\%$) and 2.2% for $\delta^{18}O$ values ($1\sigma = 0.7\%$). Seasonal differences are quite obvious. Isotopic enrichment in milk in relation to the cow drinking water is explained by the influence of seasonal factors especially when the animal-feeding regimen changes during the year from dry to fresh plants. In fact, due to evapotranspiration phenomena the water of fresh plants is enriched in ^{18}O. Transpiration from the animals staying on pasture over the summer also leads to ^{18}O-enrichment of their body waters and thus to further increase in $\delta^{18}O$ values in milk. The differences obtained in δ^2H and $\delta^{18}O$ in milk from different geographical areas can be explained by environmental and ecophysiological factors that affect the isotopic composition of water and the resulting milk.

These results can be seen in the following Table 1. The table contains results only from December 2013 and results for $\delta^{18}O$ values in milk and ground water are from period December 2013 to June 2014.

Table 1. The summary of stable isotope and elemental data in Slovenian milk in December 2013

Parameters	*Mediterranean*	*Pannonia*	*Alpine*	*Dinaric*
Stable isotopes				
$\delta^{18}O_{water}$ (‰)	-5.0 ± 0.5	-5.3 ± 0.4	-5.2 ± 0.8	-5.3 ± 0.6
$\delta^{13}C_{casein}$ (‰)	-24.9 ± 2.3	-21.0 ± 1.1	-23.0 ± 1.6	-22.3 ± 2.1
$\delta^{15}N_{casein}$ (‰)	4.2 ± 0.7	6.5 ± 0.5	5.7 ± 1.1	5.8 ± 0.6
Macro and micro elements				
Ca (mg/ 100 g)	110 ± 14	113 ± 11	113 ± 15	111 ± 14
K (mg/100 g)	128 ± 20	145 ± 14	146 ± 20	144 ± 18
Cl (mg/ 100 g)	74 ± 17	84 ± 9	89 ± 10	91 ± 13
S (mg/100 g)	24 ± 3	27 ± 4	26 ± 5	28 ± 5
P (mg/ 100 g)	62 ± 12	77 ± 10	78 ± 13	76 ± 12
Na (mg/ 100 g)	33 ± 4	35 ± 2	35 ± 3	33 ± 7
Zn (µg/100 g)	329 ± 57	392 ± 28	374 ± 34	368 ± 34
Br (µg/ 100 g)	147 ± 32	106 ± 14	139 ± 40	197 ± 71
Rb (µg/100 g)	190 ± 100	196 ± 67	210 ± 63	215 ± 40
Sr (µg/ 100 g	27 ± 6	29 ± 5	30 ± 15	20 ± 7
Fe (µg/ 100 g)	33 ± 3	25 ± 6	28 ± 5	29 ± 5
Trace elements				
Ni (µg/ 100 g)	4.5 ± 0.7	4.6 ± 1.2	4.5 ± 1.0	5.6 ± 1.1
Mo (µg/ 100 g)	7.4 ± 1.2	7.5 ± 2.5	8.7 ± 1.8	8.8 ± 2.2
Mn (µg/ 100 g)	3.9 ± 0.9	2.8 ± 1.1	2.4 ± 0.8	2.9 ± 0.8
Cu (µg/ 100 g)	7.0 ± 3.4	4.6 ± 1.2	4.4 ± 1.4	5.3 ± 1.5
Se (µg/ 100 g)	2.0 ± 0.2	1.6 ± 0.4	1.6 ± 0.5	2.0 ± 0.8
As (µg/ 100 g)	0,043 ± 0.004	0.042 ± 0.017	0.043 ± 0.015	0.057 ± 23
Cd (µg/ 100 g)	0.006 ± 0.004	0.005 ± 0.003	0.004 ± 0.002	0.007 ± 0.004
Pb (µg/ 100 g)	0.076 ± 0.051	0.055 ± 0.035	0.0076 ± 0.057	0.064 ± 0.027

We observed a large range in δ^{13}C and δ^{15}N values in casein of cow's milk between different geographic areas and realised that there are variations of these elements. δ^{13}C values vary between -28.5 and -18.7 ‰, while δ^{15}N values vary between 4.2 and 8.6 ‰. δ^{13}C values of casein vary quite similarly according to the feeding regime of the animal. Where the animal-feeding rules allow large amounts of maize silage. There was a strong linear relationship between the δ^{13}C of the casein and maize in diet. Values δ^{15}N are also processed by means of feeding type. As factors that influence the δ^{15}N values of the feed, the natural conditions of climate and soil, the agricultural practice (crop or greenland farming, plant composition of the pasture) and the fertilizers applied have to be taken into account. "Pannonia" and "Alpine" area showed the highest δ^{15}N values, which reflect the conditions of more extensive use of organic fertilisers in these parts of Slovenia. The significantly lower values obtained in "Mediterranean" and "Dinaric" may be explained due to extensive agricultural practices. The combination of δ^{13}C and δ^{15}N values provide useful information about the geographical and agricultural origin of milk (extensive production based on greenland feed, or more intensive farming with a higher degree of corn) and thus on its quality.

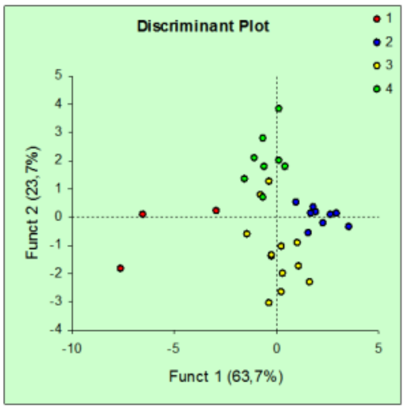

Figure 1: Discrimination between geographical regions using significant isotopic and elemental parameters. Function 1 represents 63.7% of variability, while function 2 represents 23.7% of variability. Macro-regions: 1 - Mediterranean, 2 – Pannonia, 3 – Alpine, 4 – Dinaric.

Elemental composition according to the concentrations is as follows K > Ca > P, Cl > S > Zn > Rb > Br > Fe > Sr > Cu, Pb > Mn > Se > As > Cd. The content of the elements, such as Cd, Cu, Fe, Mg, Mn, Ni, Pb, Sr and Zn is influenced by feed and environmental conditions.

The obtained results were statistically evaluated using Linear Discriminant Analysis (LDA). The results from December 2013 are presented in Figure 1. We get a good separation between areas with the most important factors of Ca, Zn, K, P, S, Cl and $\delta^{13}C$ values. The milk samples form Mediterranean and Pannonia region were well separated from each other and from Alpine and Dinaric regions. Although the milk from Alpine and Dinaric region was not completely separated, the prediction ability from these two regions was 83%, which can be considered satisfactory.

4. Conclusion

In order to determine the origin of food or to prove its quality we can measure stable isotope ratios in food product. Stable isotope ratios and major/trace elements are complementary and very useful for the determination of origin. Most of these parameters are however influenced by the season due to variation in the forage composition. It was found that stable isotope data and elemental composition can differentiate between the milk from different geographical regions in Slovenia. The most important factors affecting the geographical origin in December 2013 were Ca, Zn, K, P, S, Cl and $\delta^{13}C$ values.

Acknowledgements

The work was performed within the project V4-1108 entitled "The use of specific methods for determination and prevention of adulteration of milk and dairy products" financially supported by Slovenian Research Agency and Ministry of Agriculture and the Environment. We thank Ljubljanske mlekarne, d.d., Pomurske mlekarne, d.d., Mlekarna Vipava d.d., Mlekarna Planika predelava mleka d.o.o. and Mlekarna Celeia for supplying cow samples. This research represents a part of the ERA Chair ISO-FOOD for isotope techniques in food quality, safety and traceability.

References:

[1] Kornexl B.E., Werner T., Rossmann A., Schmidt H.L. Food Research and Technology, 1997, 205, 19-24.I. H. Witten and E. Frank. *Data Mining: Practical machine learning tools and techniques, 2nd Edition*. Morgan Kaufmann, 2005.

[2] Clark I., Fritz P. Environmental isotopes in Hydrogeology. New York: Lewis Publishers, 1997.

[3] Camin F., Wietzerbin, K., Blanch Cortes A., Haberhauer G., Lees M. Versini G. Journal of Agricultural and Food Chemistry, 2004, 52, 6592-6601.

[4] Camin F., Perini M., Colombari G., Bontempo L., Versini G. Rapid Communication in Mass Spectrometry, 2008, 22, 1690-1696.

[5] Camin F., Wietzerbin, K., Blanch Cortes A., Haberhauer G., Lees M. Versini G. Journal of Agricultural and Food Chemistry, 2004, 52, 6592-6601.

[6] Kelly S., Hearton K., Hoogewerff J., Trends in Food Science and Technology, 2005, 16, 555-567.

[7] Nečemer M., Kump P., Ščančar J., Jaćimović R., Simčič J., Pelicon P., Budnar M., Jeran Z., Pongrac P., Regvar M., Vogel-Mikuš K., Spectrochim. Acta B, 63, 2008, 1240-1244.

[8] Sacco D., Brescia M.A., Sgaramella A., Casiello G., Buccolieri A., Ogrinc N., Sacco A. Food Chemistry, 2009, 114, 1559-1563.

[9] Bontempo L., Larcher R., Camin F., Hölzl S. Rossmann A., Horn P., Nicolini G. International Dairy Journal, 2011, 21, 441-446.

[10] Pillonel L., Badertscher R., Froidevaux P., Haberhauer G., Horn P., Jacob A., Pfammatter E., Piantini U., Rossmann A., Tabacchi R., Bosset J.O. Lebensmittel Wissenschaft und Technologie, 2003, 36, 615-623.

For wider interest

Determination of the geographical origin in foodstuffs is becoming of increasing to consumers and producers, since it may be used as criterion for certifying quality and authenticity. The price of some product is strongly dependent on the origin and denomination. Another important aim could be to study and quantify the alteration of stable isotope ratios in milk by substituting a C_3 plant diet with maize. This could be important in order to protect milk and dairy products using traditional or „organic“ practices of pasture compared with products produced diets based on maize derivatives. Information obtained during this research could be used to protect consumers and high-quality of Slovenian dairy products.

Characterization of Slovenian milk using the composition and stable isotopes of fatty acids

Doris Potočnik[1,2], **Nives Ogrinc**[1,2]

[1] Department of Environmental Science, Jožef Stefan Institute, Ljubljana, Slovenia

[2] Jožef Stefan International Postgraduate School, Ljubljana, Slovenia

Doris.potocnik@ijs.si

Abstract.

Milk and dairy products are important everyday nutrition and are a major source of fat and fatty acids in the human diet. Because of their importance, they are in considerable demand and are relatively expensive. Since it is possible, in dairy industry, to influent the quality of milk products, the determination of geographical origin represents an important strategic issue for providers and consumers. In this study fatty acid (FA) composition is used to obtain information about authenticity of milk. Milk samples from different geographical regions in Slovenia (Alpine, Pannonia, Dinaric, Mediterranean) were collected two times per year and used to determine the content, as well as isotopic composition, of individual FA. FA composition was determined using the *in-situ trans*-esterification method and characterized by gas chromatography with FID detector (GC-FID), while compound specific isotope ratio mass spectrometry (CS-IRMS) was used to determine the isotopic composition of individual FA.

Keywords: fatty acids, isotopes, geographical origin, GC-FID, GC-C-IRMS

1 Introduction

In Slovenia people are becoming increasingly aware that food contains micro components that may have potential beneficial effects on health and disease prevention, therefore the agricultural research is increasingly more focused on improving the nutrient profile of food products. Dairy industry is one of such examples, where it is possible to influent the quality of products, thus the verification of geographical origin of milk products represents an important strategic issues in food science [1].

Milk and dairy products are essential and irreplaceable part of a healthy diet, due to high abundance of nutrient such as proteins, many vitamins and minerals. In milk there is about 4 % fat, which is composed of lipids (95 %), especially triacylglycerols that are consisting of fatty acids of different length and saturation [2]. The proportion of saturated (SFA), monounsaturated (MUFA) and polyunsaturated (PUFA) fatty acids in milk is mostly determined by the diet of the dairy cows, as well as theirs metabolism [3]. Since increasing proportion of fresh forages, compared with conserved forages or cereal concentrates, reduces the content of SFA and enhances the concentration of certain unsaturated FA, it is possible to distinguish between milk from the highland and lowlands, and between milk from different seasons. Diet modification from pasture, to a meal dominated on corn silage, results in increase of the SFA content and decrease in C18:3ω–3 (α-linolenic acid, ω-3 fatty acids) content, due to a small amount of unsaturated fatty acids present in corn silage [4, 5]. Differences in the botanic composition of grass in the mountains could explain the low content of SFA and high content of MUFA and PUFA from cows grazing in the highland pasture. Large amount of grazing generally increases the C18:3ω-3 and CLA (conjugated linoleic acid) concentrations, but at the same time increases the *trans* fatty acids content, due to incomplete biohydrogenation of dietary unsaturated fatty acids in the rumen. Highest concentration of *trans* FA in the summer period could also be explained by increased intake of substrates [6].

As the content, as well as isotopic composition of FA, is influenced by diet in dairy cows, the stable isotope composition becomes a useful tool for providing information about geographical origin of dairy product. Different effects of feeding, pasture or maize silage, can be tracked using stable isotope composition, since the $^{13}C/^{12}C$ ratio gives the information on the type of forage fed to the cows. The climatic condition such as temperature and humidity are known to promote shift in $\delta^{13}C$ isotopic values in plants from different regions due to effects of evapotranspiration and photosynthesis. The natural differences between feed from C3 plants (pasture, cereals) and C4 plants (maize, sugar cane) are especially observable. The metabolism of C4 plants using the Hatch-Slack cycle discriminates less against ^{13}C during the photosynthetic fixation of atmospheric CO_2, thus have a higher relative ^{13}C content ($\delta^{13}C$ −16 to −9‰), while the C3 plants follow the Calvin-Benson cycle and have lower $\delta^{13}C$ values ranging from −34 and −22‰ [7, 8, 9]. These differences could also be observed in the isotopic composition of individual FA compounds. The largest variation was observed on the C4:0 and C6:0, where C4:0 have the lowest $\delta^{13}C$ among the short-chain FAs. Ehtesham et al. (2013) conclude that these FAs can be utilized as biomarkers in milk sample to convey reliable isotopic information, which can be used for tracking milk back to their origin [10, 11].

The aim of this presentation is to characterized Slovenian milk using composition of individual FA and its isotopic composition. The obtained data were further evaluated in order to separate milk according to geographical origin using linear discriminant analysis (LDA).

2 Materials and methods

Milk collection and storage

The sampling of cow's milk was performed four times per year covering different geographical regions (Mediterranean, Pannonia, Dinaric and Alpine) in Slovenia. Forty samples were obtained from five Slovenian diary producers at each sampling period. The samples were stored in plastic containers and frozen at □ 20°C before analysis.

Sample preparation

For identification and quantification of FA the *in-situ trans*-esterification method was used. Total lipids content from milk samples were extracted with dichloromethane and sodium hydroxide in methanol, than purged with nitrogen and heated for 10 minutes at 90°C. Afterwards samples were cooled. To complete the reaction fatty acids methyl esters (FAMEs) were formed by addition of 14% BF3-methanol solution and heated again for 10 minutes at 90°C. After fast cooling, the fatty acids methyl esters (FAMEs) were extracted into hexane phase.

Gas chromatography of fatty acids

The characterization of FAMEs was performed by gas chromatography with FID detector (GC-FID), equipped with a capillary column (Omegawax 320, 30 m × 0.32 mm, × 0.25 μm) with split ratio of 100:1. The temperature program started at 50°C for 2 minutes, than increased by 4°C/min to 220°C which was kept for 20 minutes. The carrier gas was helium at a flow rate of 1mL/min, makeup gases were nitrogen at 45 mL/min, hydrogen at 40 mL/min and air flow rate at 450 mL/min. Total running time was 74.5 min. The individual fatty acids were identified and quantified by comparing their retention times with those of the standard (Supleco 37 component FAME Mix) and expressed as weight percent of total fatty acids. To support the quality of the data, procedural blank was performed with each set of samples. Standard (Supleco 37 component FAME mix) was analysed after every 10 samples to verify the stability of the analytical system. Precision of the method, based on replicate of real samples, was up to 5%.

Isotope ratio mass spectrometry of fatty acids

Isotopic compositions of FA were determined using Isoprime GV GC-C-IRMS system. Carbon isotope measurements were reported in delta notation (δ) relative to the Vienna-Pee Dee Belemnite (V-PDB) standard and expressed in per mile (‰). The precision of measurements ranged between 0.3 and 0.5‰.

QA/QC for stable isotope analysis

As there are no standards available with known isotopic composition at the moment, the following approach was used. FA C19:0 standard (methyl nanodecanoate, RESTEK Corporation) was first analysed using elemental analyser coupled to IRMS (EA-IRMS.). The isotope value of EA-IRMS was taken as "true values" of the standard and was compared with GC-C-IRMS measurements. In order to validate integrity of analytical system and to monitor the conditions of the chromatographic and detection systems for GC-C-IRMS analysis, a solution containing C20:0 standard enriched in ^{13}C (icosanioc acid methyl ester, Indiana University, USA), with the known isotopic composition, was analysed prior to any sequence of samples. Since the nonlinearity causes shifts in the isotopic values, evaluation of the potential occurrence of nonlinearity of the system was performed with C19:0 standard. The isotopic shift due to the carbon introduced in the fatty acid methylation was then corrected by mass balance.

3 Results and discussion

Our first preliminary results indicated that it was possible to differentiate milk from different geographical origin base on fatty acids composition depending on the area and season of the sampling, which is a further help in determining the geographical origin of milk. We observed that milk produced in summer is healthier for the consumer, due to the highest content of essential fatty acids such as MUFA and PUFA and lowest content of SFA. The concentration of CLA in dairy cows, which main diet is composed of pasture, is highest in Alpine region in the summer. In milk fat, where dairy cows are associated with grazing, high concentration of ω-3 (especially

C18:3ω–3) and lower concentration of SFA can be observed. The feeding of grass conservation product (hay or silage) also increases the SFA content in milk fat. Thus, the lowest concentration of SFAs was observed in Alpine milk in summer, while the highest concentration of ω-3 FAs was observed in Mediterranean milk. The results were further evaluated using chemometric method, such as linear discriminant analysis (LDA). Milk samples from different geographical areas (Mediterranean, Alpine, Dinaric and Pannonian) are statistically separated (Figure 1). The main parameters that contributed to the separation were CLA, C14:0, C16:0.

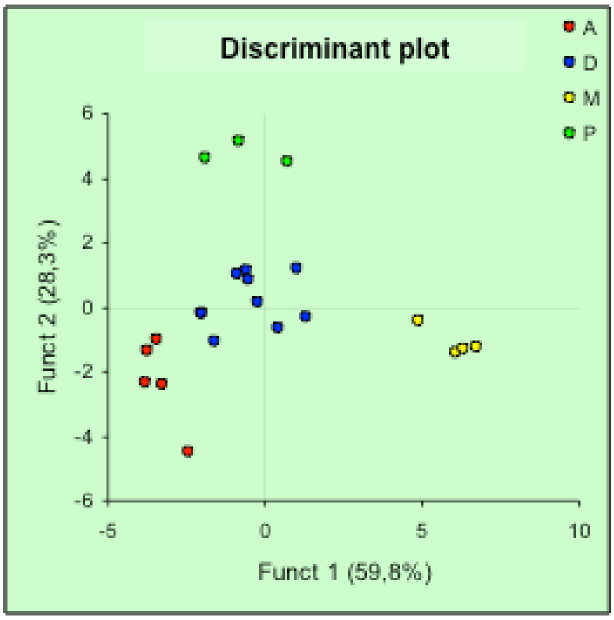

A- Alpine, D – Dinaric, M – Mediterranean, P - Pannonian

Figure 1: Classification of milk samples in June 2012 according to the geographical origin in relation to the content of fatty acids

For the separation of milk depending on the geographical origin, we can use the measurements of isotope composition of individual fatty acids, since the stable isotope composition in milk, reflects the isotopic composition of ingested food and drinking water. The stable isotope composition of individual fatty acid in milk varies with the highest obtained value in C16:0 FA and the lowest values in C15:0, C16:1, C18:0 FAs. Stable carbon isotope compositions of individual fatty acids from different geographical region are statistically different. $\delta^{13}C$ values in FAs from Mediterranean were −28.8‰ or lower and were statistically different from δ^{13}C values in FAs from Pannonia (> −22.4‰), indicating an increased use of corn in the diet (Table 1).

Table 1: Stable isotope composition of individual fatty acids from different geographical areas in Slovenia

Fatty acids	Alpine	Pannonian	Mediterranean	Dinaric
C10:0	-28.9 ± 2.4	-25.4 ± 2.7	-31.3 ± 2.0	-27.5 ± 3.1
C12:0	-29.8 ± 2.3	-26.4 ± 2.7	-33.4 ± 2.0	-28.2 ± 3.3
C14:0	-27.2 ± 2.8	-23.9 ± 2.8	-30.4 ± 2.4	-25.6 ± 3.4
C15:0	-39.2 ± 2.0	-36.3 ± 2.2	-41.9 ± 2.7	-38.1 ± 3.1
C16:0	-27.7 ± 4.1	-22.4 ± 2.8	-28.8 ± 3.3	-25.0 ± 1.9
C16:1	-34.7 ± 2.5	-32.6 ± 2.0	-38.5 ± 4.1	-33.9 ± 3.5
C18:0	-32.1 ± 3.9	-29.0 ± 2.8	-35.5 ± 3.1	-30.2 ± 4.5
C18:1	-29.6 ± 3.5	-26.3 ± 2.7	-32.7 ± 3.3	-28.1 ± 4.3
C18:2	-31.8 ± 2.6	-29.9 ± 1.7	-35.4 ± 3.0	-29.2 ± 2.9

4 Conclusion

Our study indicated that FA composition is suitable for determining geographical origin by using gas chromatography coupled with isotope ratio spectrometry (CG-C-IRMS) and gas chromatography with FID detector (GC-FID). Since the content, as well as isotopic composition of individual FA, is observed in diet of dairy cows, we were able to differentiate the geographical origin based on FA composition. The differences between C4 (maize) and C3 (pasture) diets were partly preserved in the cow's milk. Increased amount of ω-3 FA and CLA content and consequently lower δ^{13}C values in FAs are observed in area where food is based on grass silage. Grass silage in the diet of dairy cows is reflected in decreased level of SFA. Milk originating from Mediterranean region has increased amount of ω-3 FA and CLA content and lower δ^{13}C values in FAs, since the food in this area is based on grass silage. Grass silage in the diet of dairy cows is reflected in decreased level of SFA.

Although the method showed that it is suitable for detection the geographical origin of Slovenian milk, further research is still needed, since we must provide a reliable database of samples on an annual level. We need at least 6 samples from each region (Alpine, Mediterranean, Dinaric, Pannonian) in summer and in winter period.

Acknowledgements

The work was performed within the project V4-1108 entitled "The use of specific methods for determination and prevention of adulteration of milk and dairy products" financially supported by Slovenian Research Agency and Ministry of Agriculture and the Environment. We thank Ljubljanske mlekarne, d.d., Pomurske mlekarne, d.d., Mlekarna Vipava d.d., Mlekarna Planika predelava mleka d.o.o. and Mlekarna Celeia for supplying cow samples. This research represents a part of the ERA Chair ISO-FOOD for isotope techniques in food quality, safety and traceability.

References:

[1] A. L. Lock, D. E. Bauman. Modifying Milk Fat Composition of Dairy Cows to Enhance Fatty Acids Beneficial to Human Health. *Lipids*, 39(12): 1197 – 1206, 2004

[2] J. Renou, C. Deponge, P. Gachon, J. Bonnefoy, J. Coulon, J. Gerel, R. Verite, P. Ritz. Characterization of animal products according to geographic origin and feeding diet using nuclear magnetic resonance and isotopic ratio mass spectrometry: cow milk. *Food Chemistry*, 85: 63 – 66, 2004

[3] K. E. Kliem, K. J. Shingfield, K. M. Livingstone, D. I. Givens. Seasonal variation in the fatty acid composition of milk available at retail in the United Kingdom and implications for dietary intake. *Food Chemistry*, 141: 274 – 281, 2013

[4] M. Collomb, U. Butikofera, R. Sieber, B. Jeangrous, J. Bosset. Correlation between fatty acids in cow's milk fat produced in the Lowlands, Mointains and Highlands of Switzerland and botanical composition of the footer. *International Dairy Journal* 12: 661 – 666, 2002

[5] M. Collomb, U. Butikofera, R. Sieber, B. Jeangrous, J. Bosset. Correlation between fatty acids in cow's milk fat produced in the lowlands, mointains and highlands of Switzerland usinghigh-resolution gas chromatography. *International Dairy Journal* 12: 649 – 659, 2002

[6] M. Collomb, W. Bisig, U. Butikofer, R. Sieber, M. Bregy, L. Etter. Seasonal variation in the fatty acid composition of milk supplied to dairies in the mountain regions of Switzerland. *Dairy Science Technology*, 88; 631 – 647, 2008

[7] J. Molikentin and A. Giesemann. Differentiation of organically and conventionally produced milk by stable isotope and fatty acid analysis. *Analytical and Bioanalytical Chemistry*, 388: 297 – 305, 2007

[8] E. Richer, J. Spangenberg, F. Elevenhusen, C. Soliva, M. Kreuzer, F. Leiber. Stabile Carbon Isotope Composition of the c9,t11-Conjugated Linoleic Acid in Cow's Milk as Related to Dietary Fatty Acids, *Lipids*, 47; 161 – 169

[9] R. Crittenden, A. Andrew, M. LeFournour, M.D. Young, H. Middleton, R. Stockmann. Determination the geographical origin of Australasia using multi-element stable isotope ratio analysis. International Dairy Journal 17; 421 – 428, 2007

[10]E. Ehteshman, A. Hayman, K.McComb, R.Hale, R.Frew. Correlation of Geographical Location with Stable Isotope Values of Hydrogen and Carbon of Fatty Acids from New Zealand Milk and Bulk Milk Powder. Journal of Agricultural and Food Chemistry, 61; 8914 – 8923, 2013

Milk and dairy products are important everyday nutrition and are a major source of fat and fatty acids in the human diet. Because of their beneficial effects on human health, the quality of these products becomes important for the consumer. Due to the high price on the market, they are vulnerable to adulteration and incorrect labelling. Information available through our study should be used to increase the transparency of milk and dairy products supply chain and provide information related to authenticity.

Sizing of nanoscale titanium dioxide and its quantification in the presence of dissolved titanium by single particle inductively coupled plasma mass spectrometry

Janja Vidmar[1,2], **Radmila Milačič**[1,2], **Janez Ščančar**[1,2]

[1] Department of Environmental Sciences, Jožef Stefan Institute, Ljubljana, Slovenia
[2] Jožef Stefan International Postgraduate School, Ljubljana, Slovenia
janja.vidmar@ijs.si

Abstract. As a consequence of their applications in various industrial products, titanium dioxide nanoparticles (TiO_2NPs) have been released into the environment where they can act as stressors towards biota. In the present work, a new analytical approach was applied for the determination of total concentration and size distribution of TiO_2NPs in anatase and rutile in aqueous samples by the use of single particle inductively coupled plasma mass spectrometry (SP-ICP-MS). It requires minimal sample preparation, offers superior sensitivity, and enables simultaneous characterization of analyte in nanosize and dissolved form. For SP-ICP-MS measurements, suspensions of NPs must be sufficiently diluted (ng L^{-1} level) and short integration time (10 ms or less) used in order to measure the intensity of single particle as a single pulse. Under such conditions, the frequency of pulses is proportional to the number concentration of NPs and the number of counts of each pulse is related to the NP size. The accuracy of the quantification of TiO_2NPs by SP-ICP-MS was verified by calculating the recoveries between the determined and expected Ti concentrations, while calculated size distributions were checked by comparison with manufacturer reported sizes. To the best of our knowledge, this study is the first report on simultaneous quantitative determination of nanosize Ti and its dissolved forms by SP-ICP-MS. The procedure developed can be applied to the analysis of different TiO_2NPs in environmental water samples.

Keywords: TiO_2NPs, dissolved Ti, anatase, rutile, sizing, simultaneous quantification, single particle ICP-MS

1 Introduction

Titanium dioxide nanoparticles (TiO_2NPs) are the third most common nanomaterial, which are used in a wide range of applications. As a white pigment, they are added to foodstuffs, paints and coatings and are, due to their UV light resistance properties, used in photocatalytic sensors, pharmaceuticals and cosmetics, such as toothpaste and sunscreens [1]. As a result of their increasing production and use, TiO_2NPs have been released into the environment. They can be found in treated wastewaters, sewage sludge, sludge treated soils and sediments, where their presence represents potential health threat for living organisms. Many studies that have been performed *in vivo* and *in vitro* have shown several impacts of TiO_2NPs on algae, higher plants, aquatic and terrestrial invertebrates and freshwater fish. This is related to the formation of reactive oxygen species causing oxidative stress in organisms and damaging lipids, carbohydrates, proteins and DNA [2-4]. Moreover, TiO_2NPs can enhance uptake and toxicity of other pollutants (metal ions) [5]. Their toxic effects in biological systems largely depend on their concentration, surface properties and size, with smaller particles being more toxic [6]. Moreover, the crystallinity of TiO_2NPs is also relevant for their toxicity in living organisms. It has been demonstrated that only TiO_2NPs in anatase crystalline phase induce the generation of reactive oxygen species [7], while the mixture of anatase and rutile causes mild DNA damage in human intestinal Caco-2 cells [8].

In order to evaluate the impact of TiO_2NPs on the environment, it is necessary to develop reliable and sensitive analytical methods for the determination of their total concentration and size distribution under environmental conditions. Existing analytical methods for NPs characterization, for instance liquid chromatography, field flow fractionation or different microscopic techniques, have some limitations in environmental applications, especially due to the low NPs concentrations (<ng mL^{-1}), which are lower than limits of detection for most of the methods listed. During these analytical procedures alteration of original NPs properties may also occur.

As an alternative to the analytical methods described above, novel single particle inductively coupled plasma mass spectrometry (SP-ICP-MS) approach for quantification and characterization of metal-containing NPs has been developed by Degueldre et al. [9]. It provides information about NPs number concentration and size distribution at mass concentration levels down to the ng L^{-1}. It also enables simultaneous measurement of both, soluble and particulate species, as well as size distribution analysis for polydispersed NPs [10]. Advantages of SP-ICP-MS technique are low invasive sample treatment druring measurement procedure, superior sensitivity and element specificity that may overcome interferences of complex matrices with background natural particles. So far, there are only few reports in the literature available for quantitative determination and sizing of TiO_2NPs [11, 12].

2 Materials and methods

2.1 Instrumentation

SP-ICP-MS measurements were performed on two different ICP-MS instruments from Agilent Technologies (Tokyo, Japan); 7700x and 7900. Both ICP-MS models were equipped with quadrupole mass analyzer. In SP-ICP-MS measurements the data acquisition for the instrument was set to time-resolved analysis (TRA) mode in order to collect the intensity for a single particle as it is vaporized and ionized in the plasma. The measurement duration of each run for TiO_2NPs and AgNPs was 100 s or 30 s with short integration dwell time of 10 ms or 3 ms per reading, respectively. The peristaltic pump was set to 0.3 rps for all experiments, which corresponded to a sample flow rate of 1.01 ± 0.02 mL min^{-1}. Ti in standard solutions was analysed at its most abundant isotope ^{48}Ti (73.72 %). To avoid possible polyatomic interferences from sulphur compounds ($^{32}S^{16}O^+$ and $^{34}S^{14}N^+$), ^{48}Ti isotope was monitored in helium collision mode (4.3 mL min^{-1} He gas flow), which effectively removes the interferences.

For stabilization of TiO_2NPs during the analytical procedure sonication was performed using an ultrasonic homogeniser, 4710 series, Cole-Parmer Instrument Co. (Chicago, IL, USA), equipped with 6 mm diameter microprobe. It operated at 10 % power output and 50 % pulsed operation mode for 3 minutes.

A Mettler AE 163 (Zürich, Switzerland) analytical balance was used for all weighting.

2.2 Reagents and materials

Milli-Q water (18.2 MΩ cm) (Milipore, Bedford, MA, USA) was used for sample preparations and sample dilutions. Standard TiO_2NPs dispersions were prepared using anatase TiO_2 nanopowder (<25 nm particle size, spherical shape) (#637254) and rutile TiO_2 nanopowder (<100 nm particle size, rod shape with diameter of about 10 nm and length of 40 nm) (#637262) from Sigma-Aldrich (St. Louis, USA). The declared specific surface area of anatase and rutile was 45-55 $m^2\ g^{-1}$ and 130-190 $m^2\ g^{-1}$, respectively. The declared densities at 25°C for anatase and rutile were 3.9 g mL^{-1} and 4.17 g mL^{-1}, respectively. According to manufacturer, rutile nanopowder may contain up to 5 wt. % silicon dioxide (SiO_2) as a surface coating. Approximately 10 mg of anatase or rutile was dispersed in 50 mL of water sonicated for 3 min by ultrasonic homogeniser with a probe. The suspensions were then immediately diluted in several subsequent dilution steps to obtain final suspensions with Ti concentration ranging from 0.01 to 1 ng mL^{-1}.

Standard dispersions of silver NPs (AgNPs) with 20 and 40 nm diameters, purchased from Sigma-Aldrich (St. Louis, USA) were used for the determination of the transport efficiency. Suspensions were supplied at a nominal concentration of 0.020 ± 0.001 mg Ag L^{-1} and were stabilized in aqueous sodium citrate buffer. The declared nominal sizes of AgNPs, determined by TEM, were 20 ± 4 nm and 40 ± 4 nm.

Dissolved Ti and Ag stock standard solutions (Merck) of 1000 ± 4 mg L^{-1} were used for preparation of the calibration curves.

2.3 Determination of transport efficiency of NPs

Due to its low transport (nebulization) efficiency (η_{neb}), only a small fraction of NPs suspension reaches the ICP, where particles are vaporized and ionized. Establishing the accurate η_{neb}, defined as the ratio of the amount of analyte entering the plasma to the amount of analyte aspirated, is crucial for quantification and sizing of NPs. In our study, the particle size method for the determination of η_{neb} described by Pace et al. was applied [8]. Intensity-mass calibration curves were established using Ag standards in dissolved form and reference monodisperse AgNPs with known particle sizes. The most common pulse intensities (i.e. the peak positions of the raw data histogram) were plotted against the total mass entering the sample introduction system. By assuming that nanoparticulate Ag behaves the same as dissolved Ag in the plasma, the ratio of the slope of the calibration curve of dissolved Ag (m_{diss}) over the slope of the calibration curve of particulate Ag (m_{NP}) will give the accurate η_{neb}. η_{neb} was measured daily and was found to be 0.81 ± 0.08 %.

3 Results and discussion

3.1 Determination of TiO_2NPs size distribution

The intensity of the pulses that are generated by single NPs and detected by ICP-MS is a function of the number of atoms in the NP and hence of its size. For TiO_2NPs, standards with known size are not available. Therefore, for sizing dissolved Ti standards were used to prepare a calibration curve by plotting mass concentration versus signal intensity of the dissolved Ti solutions (Figure 1: D-3). Mass concentration was then converted into total mass transported into the plasma (mass flux) in a given dwell time through the η_{neb} (Figure 1: D-4). Before sizing, the background intensity of dissolved Ti was subtracted from TiO_2NPs pulse intensity. Finally, individual pulses from TiO_2NPs dataset (Figure 1: A2, R2) was transformed to particle mass using the mass flux calibration curve. Each particle mass was then converted to particle diameter, creating a size distribution histogram with 5 nm diameter bins (Figure 1: A3, R3) [13].

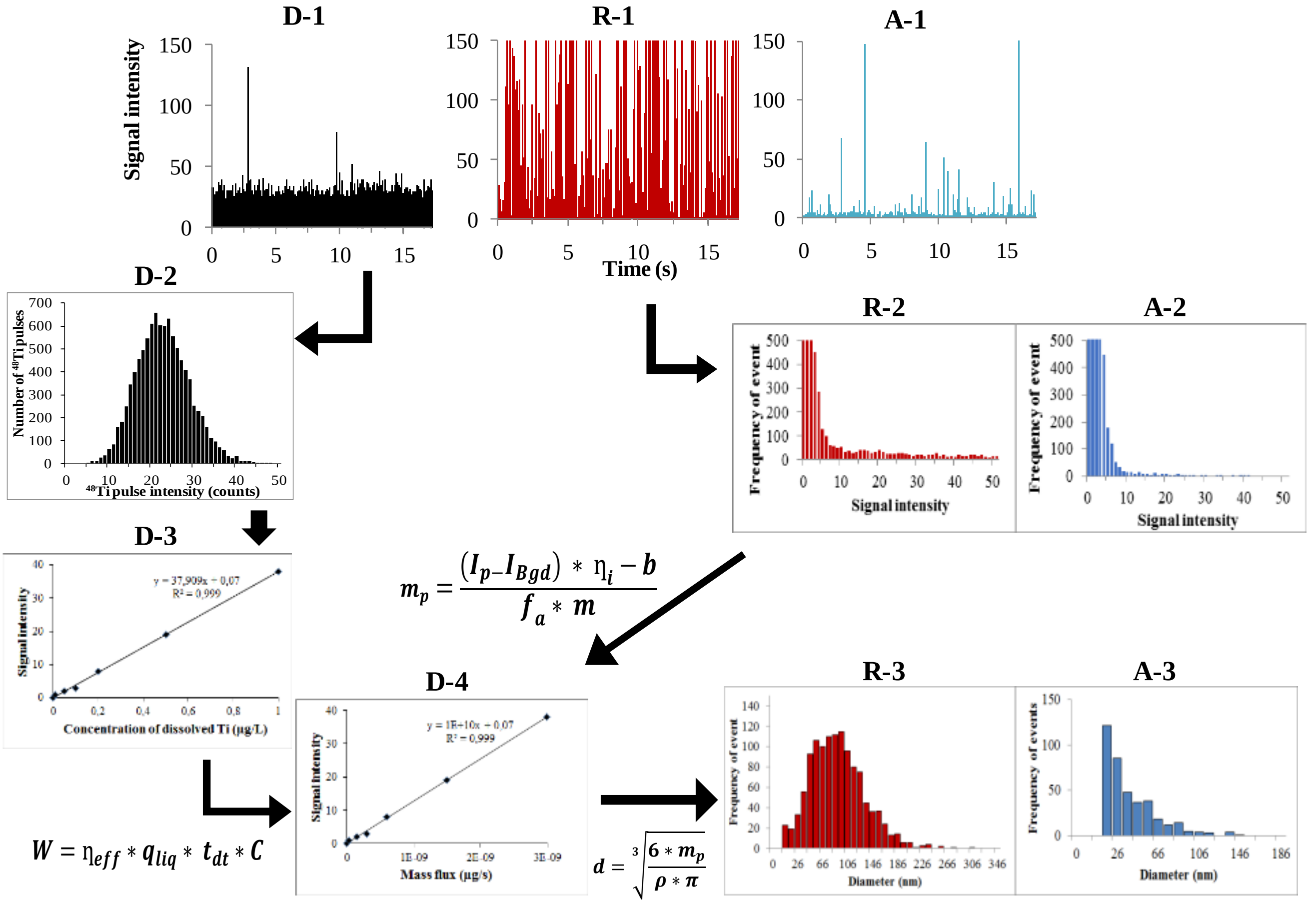

Figure 1: Data processing for sizing TiO_2NPs using SP-ICP-MS. Time scans for 0.5 ng mL^{-1} of dissolved Ti (D-1), TiO_2NPs in 0.2 ng Ti mL^{-1} of anatase (A-1) and 0.6 ng Ti mL^{-1} of rutile (R-1); Corresponding signal distribution histograms for dissolved Ti (D-2), TiO_2NPs in anatase (A-2) and rutile (R-2); Size distribution histograms for TiO_2NPs in anatase (A-3) and rutile (R-3); Calibration curve of dissolved Ti standards created for particle size calculation (D-3); Transformed calibration curve from concentration to mass per event (D-4).

As evident from the Figure 1, a large number of pulses above the background are obtained for anatase (A-1) and rutile (R-1) NPs, whereas continuous background signal with only few single pulses can be seen for dissolved Ti (D-1). Smaller frequency and intensity of pulses for TiO_2NPs in anatase in comparison to rutile are related to lower Ti concentration and smaller NPs size in anatase. From data of Figure 1 (R-3 and A-3) it can be seen that the mean diameter for TiO_2NPs in anatase is 32 nm and for TiO_2NPs in rutile is 107 nm. Thus determined diameters are in a good agreement with the manufacturer reported sizes, measured by TEM. The peak tailing in size distribution histograms is associated with formation of larger particles due to NPs agglomeration. The wide size distribution peaks of TiO_2NPs indicate on polydisperse nature of anatase and rutile.

Limit of detection for NP diameter (LOD_d) was related to the capability of a NP to produce a pulse with a number of counts equal to three times the standard deviation of the background (Milli Q water) [14]. From background signals (2 counts per dwell time of 10 ms) with standard deviations of 1 count, the LOD_d was calculated and found to be 37 nm. The LOD_d for TiO_2NPs determined in this study is much lower than the reported ones (approximately 100 nm) [10].

3.1 Simultaneous quantification of TiO_2NPs and dissolved Ti

In order to evaluate the capability of SP-ICP-MS method for the determination of Ti mass concentration in TiO_2NPs, dispersions of anatase and rutile were prepared and the recoveries between the determined and added Ti in TiO_2NPs calculated (Figure 2). Particle concentration was determined by dividing the frequency of pulse events by the sample flow rate multiplied by the transport efficiency.

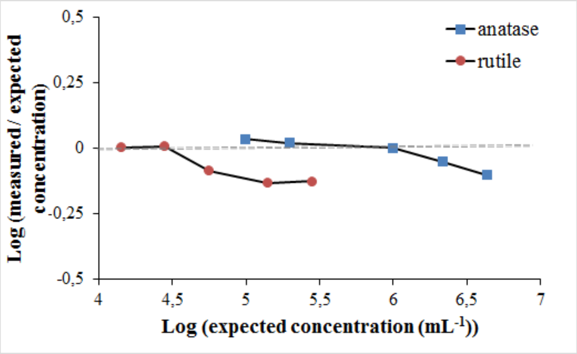

Figure 2: Log(measured/expected number concentration) as a function of log (expected number concentration) for anatase and rutile TiO_2NPs, measured by SP-ICP-MS at 10 ms dwell time.

Dashed line in the Figure 2 represents a linear range where the slope of log between measured and expected concentration is zero and recoveries between measured and expected concentration are 100 %. With increasing NPs concentrations the recoveries are decreasing due to the occurrence of multiple particle events in one dwell time that are each counted as one particle event, causing an underestimation of the particle concentration. This behavior is observed for both rutile and anatase, therefore regardless of NPs size.

Simultaneous determination of mass concentration of nanoparticulate and dissolved Ti in rutile and anatase samples to which dissolved Ti was added, was also performed by SP-ICP-MS. To validate the procedure for resolving dissolved and nanoparticulate forms, monodispersed standard AgNPs with 40 nm size in the presence of silver ions was quantified (Figure 3). In the signal distribution histogram, first distribution, which was fitted to Poisson distribution, represents the signal of dissolved Ag. The second distribution, which is well resolved from the first one and was fitted to Gaussian distribution, represents the signal of AgNPs. Once the dissolved and NP fractions have been resolved, each fraction was quantified. For the dissolved fraction, calibration curve was obtained by plotting the integration data of histograms (sum of the number of counts multiplied by the number of events) versus different concentrations of dissolved Ag. For the NP fraction, after subtracting mean dissolved background intensity from the pulse intensity, the intensity was converted to mass by using the η_{neb}, which enabled calculations of NPs mass concentrations [14].

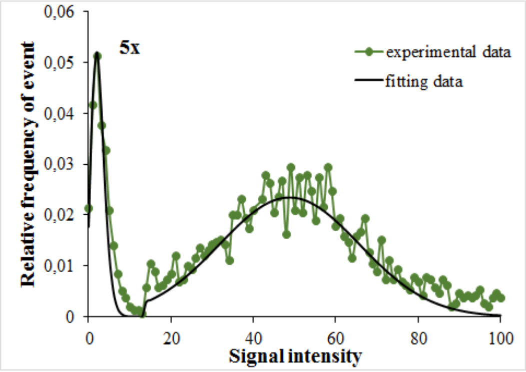

Figure 3: Signal distribution histogram for the mixture of 40 nm AgNPs (10 ng L^{-1}) and dissolved Ag (10 ng L^{-1}). Signals from dissolved Ag are fitted to Poisson distribution, signals from AgNPs are fitted to Gaussian distribution.

Recoveries for the mixture of 40 nm AgNPs (10 ng L^{-1}) and dissolved Ag (10 ng L^{-1}) determined by using the procedure described above were 95 % and 98 % for AgNPs and dissolved Ag, respectively.

The same approach for resolution between nanoparticulate and dissolved form and for their quantification was applied to the sample containing TiO_2NPs in the presence of dissolved Ti (Figure 4). An example of a time scan and signal distribution histogram for TiO_2NPs in rutile in the presence of dissolved Ti is presented in Figure 4.

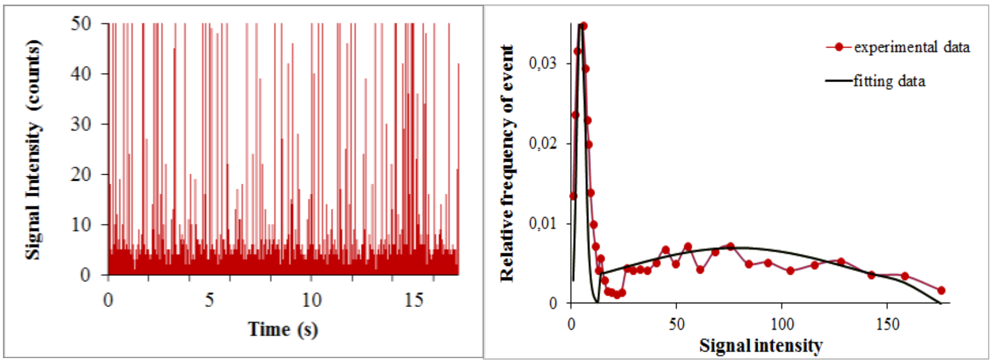

Figure 4: Time scan (left) and signal distribution histogram (right) for the mixture of TiO_2NPs (0.3 ng Ti mL^{-1}, rutile) and dissolved Ti (0.5 ng Ti mL^{-1}). Signals from dissolved Ti are fitted to Poisson distribution, signals from TiO_2NPs are fitted to Gaussian distribution.

From the time scan, pulses of TiO_2NPs as well as continuous background of dissolved Ti can be seen. In corresponding signal distribution histogram the presence of both, dissolved Ti and TiO_2NPs, can be resolved and quantified. The quantification procedure was the same as procedure applied for the mixture of AgNPs and dissolved Ag. The results of recovery tests for the simultaneous determination of Ti mass concentration in TiO_2NPs and dissolved Ti are summarised in Table 1.

Table 1: Recoveries between determined and expected mass concentrations for the simultaneous determination of Ti mass concentration in TiO_2NPs and dissolved Ti by SP-ICP-MS. Results represent the mean value of three replicates with the standard deviation of the measurements.

	Ti(IV) added ng mL^{-1}	TiNP added ng mL^{-1}	Ti(IV) measured ng mL^{-1}	TiNP measured ng mL^{-1}	Recovery TiNP (%)
rutile	0.500	0.298	0.456 ± 0.031	0.298 ± 0.034	100
	0.05	0.0323	0.047 ± 0.003	0.0312 ± 0.0024	97
anatase	0.500	0.580	0.525 ± 0.024	0.480 ± 0.020	83
	0.05	0.0348	0.0628 ± 0.001	0.0301 ± 0.0033	87
	0.05	0.0580	0.0558 ± 0.0007	0.0562 ± 0.0010	97

Data from Table 1 demonstrate that the recoveries for Ti in a mixture of rutile NPs and dissolved Ti are between 97 and 100 % for nanosized rutile, and between 91 and 94 % for dissolved form. From the Table 1 it can be further seen that the recoveries for anatase in the presence of dissolved Ti are between 83 and 97 % for nanosized anatase and between 105 and 126 % for dissolved form. Lower recoveries for TiNPs in anatase are due to smaller size of NPs, which are partially overlapped with the dissolved Ti background, making the discrimination of dissolved and NPs form more difficult. Namely, overlapping between dissolved and particulate signal distribution increases with decreasing NPs size. For the same reason, the recoveries higher than 100 % were observed for dissolved Ti.

The SP-ICP-MS cannot distinguish between naturally present and engineered TiO_2NPs as well as between NPs in different crystalline phases. However, with this technique it is possible to follow the aggregation of NPs and detect and quantify both dissolved and nano form of TiO_2, which can be present in environmental water samples.

Conclusions

SP-ICP-MS enables quantitative determination of the mass concentration and size distribution of TiO_2NPs in aqueous suspensions of anatase and rutile. The accuracy of the determination of Ti mass concentration in TiO_2NPs was verified by the calculation of the recoveries between the determined and added Ti. The determined size distribution agreed with manufacturer reported sizes. In addition, SP-ICP-MS technique enabled also simultaneous quantification and sizing of TiO_2NPs and its dissolved forms. To the best of our knowledge, this is the first report on quantitative determination of Ti in both, NPs and dissolved forms, by SP-ICP-MS. The procedure developed extends the applicability of SP-ICP-MS for sizing and quantification of TiO_2NPs in environmental water samples, which is the aim of the following research.

References:

[1] A. Weir, P. Westerhoff, L. Fabricius, K. Hristovski and N. von Goetz. Titanium Dioxide Nanoparticles in Food and Personal Care Products. *Environmental Science and Technology*, 46: 2242-2250, 2012

[2] C. Som, P. Wick, H. Krug and B. Nowack. Environmental and health effects of nanomaterials in nanotextiles and façade coatings. *Environment International,* 37: 1131-1142, 2011

[3] A. Menard, D. Drobne and A. Jemec. Ecotoxicity of nanosized TiO2. Review of in vivo data. *Environment Pollution*, 159: 677-684, 2011

[4] G. Federici, B. J. Shaw and R. D. Handy. Toxicity of titanium dioxide nanoparticles to rainbow trout (*Oncorhynchus mykiss*): Gill injury, oxidative stress, and other physiological effects. *Aquatic Toxicology,* 84: 415-430, 2007

[5] W. Fan, M. Cui, H. Liu, C. Wang, Z. Shi, C. Tan and X. Yang. Nano-TiO_2 enhances the toxicity of copper in natural water to Daphnia magna. *Environment Pollution*, 159: 729-734, 2011

[6] D. B. Warheit, T. R. Webb, K. L. Reed, S. Frerichs, C. M. Sayes. Pulmonary toxicity study in rats with three forms of ultrafine-TiO2 particles: Differential responses related to surface properties. *Toxicology*, 230: 90-104, 2007

[7] C. Jin, Y. Tang, F. G. Yang, X. Lin Li, S. Xu, X. Yan Fan, Y. Ying Huang, Y. Ji Yang. Cellular Toxicity of TiO_2 Nanoparticles in Anatase and Rutile Crystal Phase. *Biological Trace Element Research*, 141: 3-15, 2011

[8] K. Gerloff, I. Fenoglio, E. Carella, J. Kolling, C. Albrecht, A. W. Boots, I. Foerster, R. P. F. Schins. Distinctive Toxicity of TiO2 Rutile/Anatase Mixed Phase Nanoparticles on Caco-2 Cells. *Chemical research in toxicology,* 25: 646−655, 2012

[9] C. Degueldre, P.-Y. Favarger and S. Wold. Gold colloid analysis by inductively coupled plasma-mass spectrometry in a single particle mode. *Analitica Chimica Acta*, 555: 263-268, 2006

[10] F. Laborda, E. Bolea and J. Jiménez-Lamana. Single Particle Inductively Coupled Plasma Mass Spectrometry: A Powerful Tool for Nanoanalysis. *Analytical Chemistry*, 86 : 2270-2278, 2014

[11] A. P. Gondikas, F. Von Der Kammer, R. B. Reed, S. Wagner, J. F. Ranville, T. Hofmann. Release of TiO_2 Nanoparticles from Sunscreens into Surface Waters: A One-Year Survey at the Old Danube Recreational Lake. *Environmental Science of Technology*, 48: 5415–5422, 2014

[12] R. B. Reed, C. P. Higgins, P. Westerhoff, S. Tadjiki, J. F. Ranville. Overcoming challenges in analysis of polydisperse metal-containing nanoparticles by single particle inductively coupled plasma mass spectrometry. *Journal of Analytical Atomic Spectrometry*, 27: 1093-1100, 2012

[13] H. E. Pace, N. J. Rogers, C. Jarolimek, V. A. Coleman, C. P. Higgins and J. F. Ranville. Determining Transport Efficiency for the Purpose of Counting and Sizing Nanoparticles via Single Particle Inductively Coupled Plasma Mass Spectrometry. *Analytical Chemistry*, 83: 9361-9368, 2011

[14] F. Laborda, J. Jiménez-Lamana, E. Bolea and J. R. Castillo. Selective identification, characterization and determination of dissolved silver (I) and silver nanoparticles based on single particle detection by inductively coupled plasma mass spectrometry. *Journal of Analytical Atomic Spectrometry*, 26: 1362-1371, 2011

For wider interest

Titanium dioxide nanoparticles (TiO_2NPs) are widely used in medicine, cosmetics, food additives, paints and industrial and urban applications. Due to their wide use, TiO_2NPs have emerged in the environment where they can act as stressors towards biota. TiO_2NPs as strong oxidants are able to form reactive oxygen species causing oxidative stress in organisms and damaging lipids, carbohydrates, proteins and DNA. For evaluating the environmental impact of TiO_2NPs it is important to know how to quantify and characterize them.

For quantitative determination of concentration and size distribution of TiO_2NPs in anatase and rutile, new approach by the use of single particle (SP)-ICP-MS was applied. Advantages of SP-ICP-MS technique are minimal sample preparation, superior sensitivity and element specificity that may overcome complex matrices with background natural particles, as well as simultaneous characterization of analyte in nanosize and dissolved form. In our study, the accuracy of the determination of Ti mass concentration in TiO_2NPs was verified by the recoveries between the determined and added Ti. The size distribution determined by SP-ICP-MS is in good accordance with the manufacturer reported sizes.

To the best of our knowledge, this is the first report on simultaneous quantitative determination of Ti in both, NPs and dissolved forms by SP-ICP-MS. The procedure developed exhibit great potential to be applied to the analysis of TiO_2NPs in environmental water samples.

Conceptual model of Ljubljansko polje aquifer

Janja Vrzel[1,2], Goran Vižintin[3], Nives Ogrinc[2,4]
[1]Ecological engineering institute d.o.o., Maribor, Slovenia
[2] Jožef Stefan International Postgraduate School, Ljubljana, Slovenia
[3]Department of Mining and Geotechnology, Faculty of Natural Sciences and Engineering, Ljubljana, Slovenia
[4] Department of Environmental Sciences, Jožef Stefan Institute, Ljubljana, Slovenia
janja.vrzel@ijs.si

Abstract. The regional steady state model of groundwater flow in Ljubljansko polje aquifer is under preparation. It will provide a framework for the development of regional transient state groundwater flow model, which will be extended into transport model, where $\delta^{18}O$, $\delta^{2}H$ and ^{3}H isotopes will be used as transport materials. The model is constructed with software FEFLOW® 6.1. At the present the conceptual model with precise geometry of the study area is available. The model will extend our knowledge about interactions between surface and groundwater.

Keywords: Groundwater modelling, conceptual model, Ljubljansko polje, FEFLOW

1 Introduction

A model may be defined as an approximation of a real system or process in general, while a mathematical model simulates a real system indirectly using a set of governing equations. These equations describe physical processes that occur in the system and numerical methods yield approximate solutions to the governing equation by discretization of space and time [1]. Thus groundwater flow model of an aquifer with a porous medium is based on Darcy's law and the conservation of mass [2, 3]. Groundwater modelling applications may be of three different types: (1) predictive, used as a framework for prediction of future conditions, (2) interpretative, used for studying system dynamics or organizing data, and (3) generic, used to analyse the hypothetical hydrogeologic systems [1].

There are several steps of developing a transient state groundwater model including: (1) conceptual model development, (2) numerical model implementation, (3) development of a steady state model, (4) extension of the steady state model to the transient model, (5) extension of the hydrodynamic model into transport model, (6) the calibration and sensitivity analysis follow after development of each model. However, an approach of modelling depends on the purposes of models [4].

Many software were written to solve the governing equations for the different spatial, geological and hydrological conditions (e.g. FEFLOW and MOFLOW). The finite element flow simulation system FEFLOW® v6.1 from MIKE Powered by Danish Hydraulic Institute (DHI) is a software package for three dimensional (3D) visualization of groundwater flow, mass transfer and heat transport in porous media. This software has the following advantages: (1) an ability to treat irregular shapes of a complex model boundary; (2) to refine the density of the mesh around features (e.g. wells, rivers, border, etc); (3) to simulate a groundwater age and transport of stable isotopes [5].

The aim of our work is to develop a regional steady state model that will provide a framework for the development of regional transient groundwater model for the whole Ljubljansko polje aquifer system. The groundwater will be extended into a transport model describing the transport of stable isotopes of O and H and ^{3}H activity. Further high resolution of the surface description is also needed in the groundwater model, therefore the geometry of Sava's bed was precisely included in the model.

2 The study area

The study area for the modelling comprises the full extent of the Ljubljansko polje aquifer system in the central part of Slovenia (Fig. 1), which is one of the most important drinking water sources for Ljubljana, the capital of Slovenia, and its surroundings. The aquifer covers an area of greater than 70.85 km^{2} and is bounded approximately by the latitudes 46.12°N and 46.08°N and the longitudes 14.43°E and 14.64°E. The unconfined aquifer has an intergranular porosity and it is composed of fluvial sediments, which are Pleistocene and Holocene silty sand gravel and sandy gravel with lens of conglomerates. Layers of clay or clay with gravel-stone are located only in the local spots. The fluvial sediments represent the main aquifer in the area. Their thicknesses increase towards the center of the field and exceeding 100 m in the deepest parts [6]. On the other hand, outcrops of the hardpan appear in Šentjakob, Črnuče and in the north-western part around Tacen. The hardpan is considered as impermeable rock, therefore at these locations river water-groundwater interactions are not present.

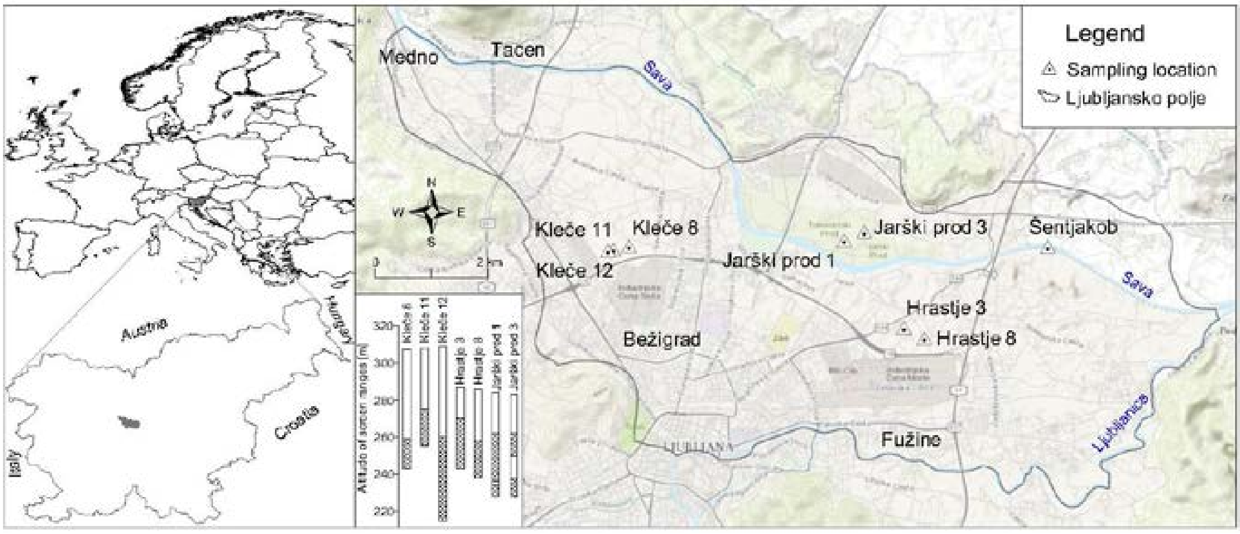

Figure 1: The map of Study area - Ljubljansko polje

3 Conceptual hydrological model

The conceptual model helps to improve our knowledge on the natural groundwater system by including all available data [7]. However, the data are usually limited, incomplete or non-existing, therefore several assumptions have to be taken into account. The model is prepared in D48/GK coordinate system.

3.1 Available data

Many data are required for groundwater modelling, which were obtained from the following institutions/companies: (1) drilling reports from the Javno podjetje Vodovod-Kanalizacija d.o.o. (VO-KA) and Pivovarna Union d.d; (2) the counter map of the hardpan depth from VO-KA; (3) depths of piezometric groundwater table and groundwater abstractions from wells from the VO-KA and Pivovarna Union d.d; (4) DEM from The Surveying and Mapping Authority of the Republic of

Slovenia; (5) LiDAR data for Sava floodplain from Holding Slovenske Elektrarne d.o.o. (HSE d.o.o.); (6) Sava cross-sections from the City Municipality of Ljubljana (MOL); (7) infiltration of precipitation in studied area from the Environmental Agency of Slovenia (ARSO); (8) isotopic analyses from the Jožef Stefan Institute. The ArcMap and AutoCAD Map were used for data processing before using FEFLOW. All three software FEFLOW, ArcMap and AutoCAD Map are fully integrated allowing quite easy transfer of the data between them.

3.2 Hydrodynamics in Ljubljansko polje aquifer

The direction of groundwater flow within the Ljubljansko polje aquifer is toward southeast in general. There are three groundwater sources: (1) an infiltration of precipitation, (2) an infiltration of river water, and (3) an underground inflow. An amount of infiltration of precipitation into the aquifer was calculated with GROWA (**Gr**oßräumiges **Wa**sserhaushaltsmodel) model by the ARSO. The inflow was calculated through real evapotranspiration, where further parameters were taken into account: climate conditions, surface water, land use, soil feature, topography, geological composition and depth to the water table [8]. The Sava is a very important source of groundwater in Ljubljansko polje aquifer. Vrzel et al. [9] reported that the proportion of Sava in one of the pumping stations Jarški prod supposed to be rich 97%. There are two sections where the Sava inflows into the aquifer in Ljubljansko polje: between Tacen and Gameljščica triburtary, and between Tomačevo and Šentjaob [10]. It was estimated that underground water inflows occur as well, especially when water table is high, at the following locations: Trnovska vrata, Dravlje, between Črnuče and Soteški hrib, as well as between Soteški hrib and Kamniška Bistrica [11]. Only some rough estimation exists of the quantities of the underground water inflow and thus some more investigation should be performed.

An important loss of groundwater is water supply. There are four pumping stations: Kleče, Jarški prod, Hrastje and Šentvid. Kleče is the largest pumping station where 55% of drinking water was pumped in 2003, which represented 650 l s^{-1} [12]. The groundwater discharges into the Sava in section between Šentjakob and confluence of the Sava, Ljubljanica and Kamniška Bistrica, which represents another important loss of groundwater in the aquifer.

3.3 Model Geometry

A lot of effort was put into the construction of the model geometry. The outcrops of the hardpan, the Ljubljanica and Kamniška Bistrica rivers were the main criteria when the border of the study area was defined. The counter map of the hardpan, which was defined by hydrogeologists, was reconstructed according to later drilling reports and digitalized geological map. Five layers, which extend from the surface to the impermeable hardpan of Ljubljansko polje, were identified according to the geological composition of the aquifer. The surface was generated with digital elevation model 25 x 25 m (DEM) and Sava's alluvial plain with LiDAR data 10 x 10 m, where the Akima interpolation method was used (Fig. 2). Since, the LiDAR techniques are unable to measure the area covered by water, the wet area of the Sava's bed was generated with cross-sections of the river bed. In this case the Inverse Distance Weighting interpolation method was used. Approximately 126 river cross-sections data sets are available, which were measured in 2007 and 2010. The distances between cross-sections range from approximately 20 m to 690 m along the flow path.

LiDAR (**L**ight **D**etection **A**nd **R**anging) data were provided as ASCII files, so called LAS (**L**og **A**SCII **S**tandard) files, which is an industry standard binary format for storing airborne LiDAR data [13]. The LAS files were indirectly transformed into SHP files (shapefile) through a Terrain file and Raster file (10 x 10 m) before using them in FEFLOW. The ArcMap 10.2.2 was used in this purpose. The terrain dataset is a collection of participating feature classes that are contained in a feature dataset [13]. The borders between dry and wet areas in Sava's bed were precisely defined in TIN (**T**riangular **I**rregular **N**etwork) file.

The mesh was generated with 95,788 finite elements by triangle algorithm. Its density is higher in floodplain, around the Sava, wells and piezometers. The model includes two types of boundary conditions (BC): (1) Neumann BC where underground recharge is present, and (2) Cauchy BC where river water-groundwater interactions are present.

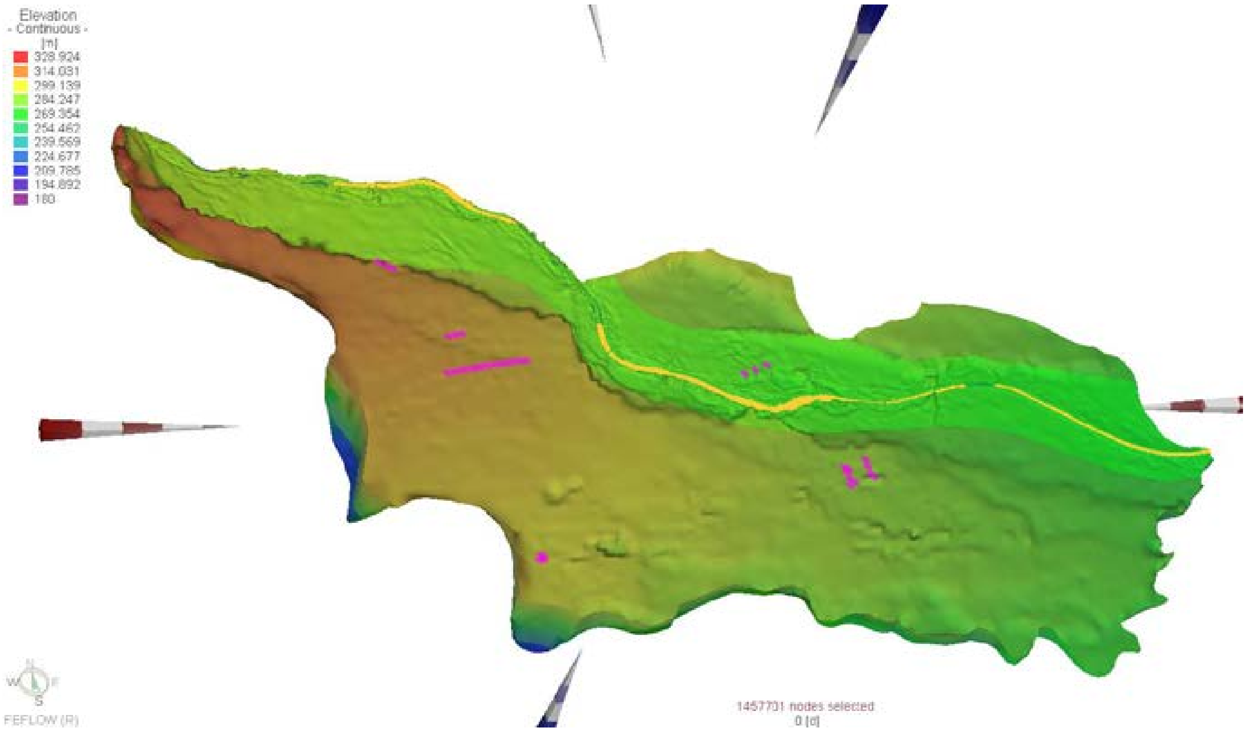

Figure 2: The surface of the conceptual model with wells (pink points)

4 Conclusion

The conceptual model of Ljubljansko polje aquifer was constructed, which will be further developed into the regional groundwater flow model. The main advantage of conceptual model is the construction of very precise geometry of the study area, especially the topography of the Sava bed, which was constructed with LiDAR data and river cross sections. The hardpan is determined as the bottom border of the five model layers. The existing counter hardpan map was updated according to later drilling reports and digitalized geological map. In the next step calibration of the model will be performed.

Acknowledgements

The model is under preparation as a part of the on going EU 7th Research Project – GLOBAQUA (Managing the effects of multiple stressors on aquatic ecosystem under water scarcity). The research is partially supported by the Environmental Social Found (KROP 2012). The authors would like to thank all those who allow to use their data: Javno Podjetje Vodovod-Kanalizacija Ljubljana, The City Municipality of Ljubljana, Holding Slovenske Elektrarne d.o.o., Pivovarna Union d.d., Slovenian Environmental Agency and The Surveying and Mapping Authority of the Republic of Slovenia.

References:

[1] M. P. Anderson, W. W. Woessner. *Applied Groundwater Modelling*. Academic Press, San Diego, USA, 1992.

[2] G. Vižintin, Z. Mikulič. Risk of groundwater pollution hazard in groundwater protection zones. In *Groundwater Modelling*, Ljubljana, Slovenia, 2008.

[3] H. Darcy. *Les Fontaines Publiques de la Ville de Dijon*, Victor Dalmont, 1856.

[4] A. Knapton. *Regional Groundwater Modelling of the Cambrian Limestone Aquifer System of the Wiso Basin. Georgia Basin and Daly Basin*. Department of Natural Resources, Environmental & The Arts, 2006.

[5] MIKE Provided by DHI. FEFLOW, Advanced groundwater modelling. http://www.mikepoweredbydhi.com/products/feflow, 2015

[6] B. Bračič Železnik, M. Pintar, J. Urbanc. Naravne razmere vodonosnika. In *Podtalnica Ljubljanskega polja*, Založba ZRC, 2005.

[7] B. Barnett, L. R. Townley, V. Post, R. E. Evans, R. J. Hunt, L. Peeters, S. Richardson, A. D. Wermer, A. Knapton, A. Boronkay. *Australian groundwater modelling guidelines*. National Water Commission, Canberra, Australia, 2012.

[8] M. Andjelov, Z. Mikulič, J. Uhan, M. Dolinar. Vodna bilanca z modelom GROWA-SI za količinsko ocenjevanje vodnih virov Slovenije. In *Mišičevi vodarski dnevi 2013*, Slovenia, 2013.

[9] J. Vrzel, D. K. Solomon, Ž. Blažeka, N. Ogrinc. *The study of the interactions between groundwater and Sava River in Ljubljansko polje aquifer (Slovenia)*. In press.

[10]M. Andjelov, M. Bat, P. Frantar, Z. Mikulič, V. Savić, J. Uhan. Pregled elementov vodne bilance. In *Podtalnica Ljubljanskega polja*, Ljubljana, Slovenija, 2005.

[11]S. Cerar, J. Urbanc. Carbonate Chenistry and isotope characteristics of groundwater of Ljubljansko polje and Ljubljansko barje aquifers in Slovenia. *The Scientific World Journal,* 2013:1–11, 2013

[12]B. Bračič-Železnik, B. Jamnik. Javna oskrba s pitno vodo. In *Podtalnica Ljubljanskega polja*, Ljubljana, Slovenija, 2005.

[13]ArcGIS Help 10.1. http://resources.arcgis.com/en/help/, 2015

Additional remarks: (FOR SUBMISSION DELETE THIS)

- to print the paper, please, use BLACK and WHITE laser printer
- pictures and diagrams should be of high resolution and quality
- send papers to IPSSC page: http://ipssc.mps.si/submission.asp
- if you need any help please contact IPSSC organization committee at ipssc@mps.si

For wider interest

The aim of our work is to develop a regional steady state model that will provide a framework for the development of regional transient groundwater model for the whole Ljubljansko polje aquifer system. The groundwater will be extended into a transport model describing the transport of conservative tracers: O and H stable isotopes and ^{3}H activity. The model is constructed with software FEFLOW® 6.1.

The groundwater model will be useful for better interpretation of the Ljubljansko polje aquifer system. It is expected that it will help us to extend our knowledge about interactions between surface water and groundwater. Further it will contribute to the future protection of water resources and management.

Informacijske in komunikacijske tehnologije (Information and Communication Technologies)

Developing API for efficient and secure access to IoT resources and data

Matej Celarc[1], Adnan Bekan[1, 2], Matevž Vučnik[1, 2], Mihael Mohorčič[1, 2]
[1] Department of Communication Systems, Jožef Stefan Institute, Ljubljana, Slovenia
[2] Jožef Stefan International Postgraduate School, Ljubljana, Slovenia
matejcelarc@gmail.com

Abstract. In this paper we present a solution for an IoT platform API, based on an example IoT platform Videk. The platform runs several services with different requirements, such as database manipulation using CRUD operations, future-proof architecture with machine and human readable resource representation, real-time data delivery and security. We developed an API using REST architecture style and WebSocket protocol for real-time data delivery. Performance evaluation of the proposed API confirmed its suitability also for collecting measurements in fast changing environment and dynamically configurable connected devices.

Keywords: API, REST, WebSocket, publish/subscribe, Internet of Things (IoT), wireless sensor network (WSN)

1 Introduction

Wireless sensor networks (WSNs) are comprised of nodes with embedded sensors and are typically capable of communicating both with each other and through a gateway node to the Internet. Each node within such WSN that has an access to the Internet can be considered an Internet of Things (IoT) device. IoT as a concept thus refers to a network of physical objects that are equipped with sensors and are able to connect to the Internet to provide services by exchanging data.

The data generated by sensor nodes is typically stored in a database that is part of the IoT platform. It is then processed and presented in a seamless, efficient and easily interpretable form. To get the data from the node to the IoT platform over the

Internet, we need to expose an Application Programming Interface (API). API is a set of instructions, an interface for software-to-software communication, which allows a platform to access data from its database, sensor nodes and/or other services. In this paper we propose a solution for time efficient and secure managing of sensor resources and accessing measurement data, combining two widely used API architectures and thus benefiting from advantages of both.

The rest of the paper is structured as follows. Section 2 presents requirements for building an IoT platform API. In Section 3 we propose a solution that conforms to these requirements and describe the implementation on an existing IoT platform called Videk. In Section 4 we present some performance evaluation results obtained with the proposed implementation, while Section 5 concludes the paper.

2 IoT platform requirements

Each connected device, i.e. a "thing", inside the Internet of Things, such as a sensor node, generates sensing or measurement data from its embedded sensors. This measurement data typically has to be stored in the platform database, thus requiring an appropriate API providing functionality to interact with the database.

The stored data is not meaningful by itself and needs to be put in context by analytical and visualization platforms. These platforms have different requirements. An analytical platform such as the ParCom Analytics Platform[1] processes historical data based on certain criteria. In order to process the stored measurement data it requires an API to access data from specific sensor time series. This API thus needs to provide different query parameters so the platform can search the database for specific measurements. When visualizing real-time measurements data, a platform needs to be updated with new entries to the database. This has to be done with low latency and low overhead. Another example of a platform that also supports connected device management is SeeControl[2]. This platform includes device connection status, health, data usage, firmware configuration and remote

---

[1] http://www.parstream.com

[2] http://www.seecontrol.com

setting/instruction, thus requiring an API that provides methods to update device's status and change its settings.

In order to efficiently cope with fast changing environment and dynamic configurations of connected devices a single IoT platform should combine data storing and device/network management functionalities. Thus, an API for such a platform has to conform to all above requirements and provide scalable architecture, with an Uniform Resource Identifier (URI) scheme that represents database resources. The resources have to be represented in a device and human readable format and the access to them can only be made available to authorized users.

3 Proposed IoT platform API combining RESTful architecture and WebSocket protocol

In order to show an example of API that conforms to the specified requirement we built an API for the Videk[3] IoT platform. The Videk platform with conceptual architecture shown in Figure 1, is a NodeJS[4] application written in JavaScript. It includes an asset management system that keeps track of deployed sensor nodes, how those nodes are organized into clusters and which components and sensors are attached to individual nodes. The same platform also collects and stores the measurement data and metadata from the connected nodes. This data is stored in JSON-like documents (field and value pairs) in a MongoDB[5] database, classified as NoSQL/document-oriented database. For the proposed API we will store documents within the following collections: nodes, clusters, sensors and measurements. All functional blocks of the platform can be accessed and configured using the front-end web user interface, while all data visualization tools and Qminer[6] analytic platform are using the dedicated API block to interact with the platform.

In order to meet the outlined requirements and support both real-time and non-real-time access to the database we propose a solution based on two APIs. One follows

---

[3] http://sms.ijs.si

[4] http://nodejs.org

[5] http://www.mongodb.org

[6] http://qminer.ijs.si

the REST architectural style, which conforms to all requirements except providing real-time database updates, and the other uses the WebSocket protocol to provide also real-time updates:

- RESTful API provides URIs to create, read, edit and delete documents in database collections, and can only be accessed by an authorized user with a valid authentication token. The REST API architecture and URI scheme are presented in detail in Sections 3.1 and 3.2.
- WebSocket API [6] is in charge of providing clients with new entries to the database. It makes use of the WebSocket protocol and publish/subscribe mechanism. The protocol and the solution are described in Section 3.3.

Generally, RESTful API with HTTP long-polling could also be used for real-time access by continuously checking for updates in the database, but our assumption was it was slower and demanded more overhead compared the WebSocket protocol. This assumption was evaluated in Section 4 .

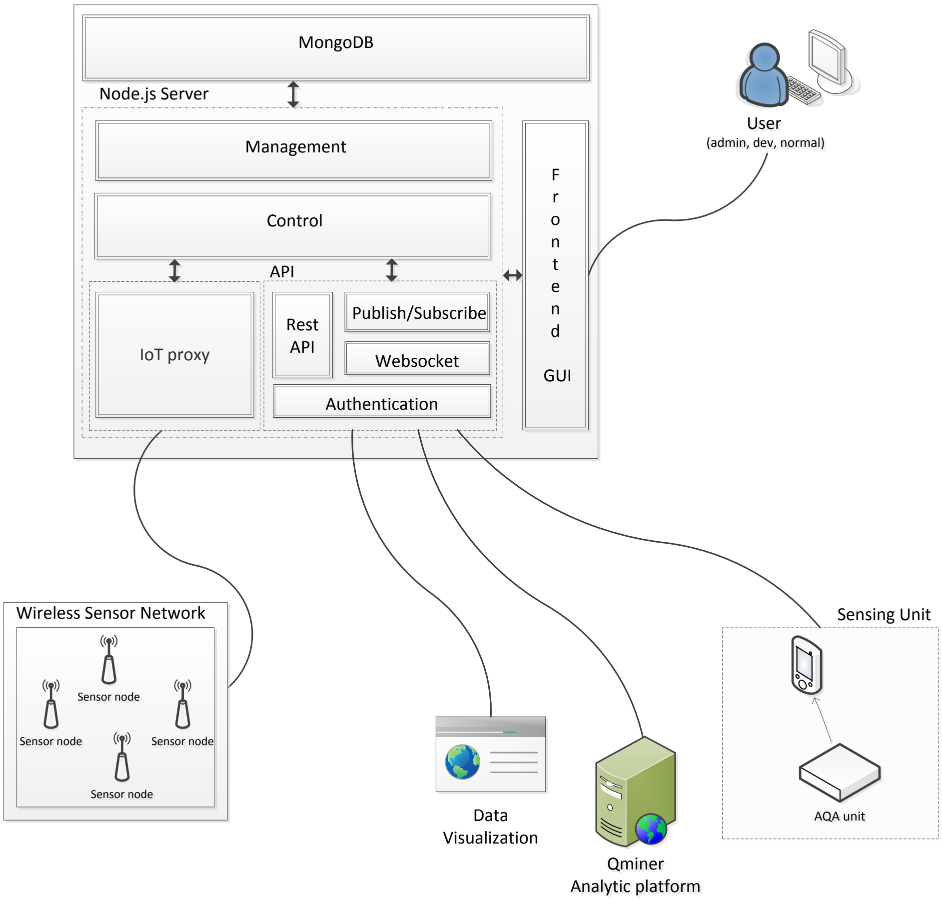

Figure 1: Videk platform architecture with the proposed API

3.1 RESTful API

The REpresentational State Transfer (REST) [1] is a software architecture style that uses the HTTP communication protocol [2]. It provides a set of constraints that, when implemented, make the API more performant and scalable. These constraints for a RESTful web service include the client-server model, which provides the separation of concerns between the two. That means that the server is not concerned with the user interface or user state (is stateless), which makes it simpler and more scalable. The resources are offered over a web server, are uniquely identified and accessed over URIs. The CRUD (Create, Read, Update, Delete) operations of a user interface are accessed over HTTP methods POST, GET, PUT and DELETE. Resources can be represented in different standardized formats, including HTML, XML and JSON. This constraint is called the representation of a resource. Independently of the format used, these representation messages have to be self-descriptive, which means they provide enough information to describe how to process the message. Every representation of a resource has to provide enough information for the client to be able to modify and/or delete it. Responses use HTTP status codes.

As mentioned above, one of REST architectural constraints is a stateless server. This means there is no client data stored on the server between requests. When accessing a protected API such as our RESTful API, each request has to include user credentials. To achieve this, we generate a token for every user, which contains 24 randomly chosen characters encoded in MIME's Base64 scheme. It has to be included as the "Authorization" field in the header of every request sent to the REST API. Since we are using JSON as the representational format to describe resources, we must include a header to define the format as well.

The RESTful API is accessible over HTTP protocol and its methods POST, GET, PUT and DELETE. The URI scheme (structure), which represents paths to database collections, is described in chapter 3.2 and is also provided at API entry point "/api".

3.2 URI scheme

REST API uses URIs to address resources. Each of the four collections mentioned in Section 3 (i.e. nodes, clusters, sensors, measurements) have assigned URI as seen in Table 1.

Table 1: RESTful API resource URIs and available methods.

URI	Available methods
/api	GET
/api/nodes	GET, POST
/api/nodes/:node_id	GET, PUT, DELETE
/api/clusters	GET, POST
/api/clusters/:cluster_id	GET, PUT, DELETE
/api/sensors	GET, POST
/api/sensors/:sensors_id	GET, PUT, DELETE
/api/measurements	GET, POST
/api/measurements/:measurements_id	GET, PUT, DELETE

The first URI is the API entry point. It has only a GET request available and the response is a list of available resources and their URIs. These are the same URIs as listed in Table 1. If we use any of these resources' URIs, we can either send a GET request to receive all the documents in the corresponding collection or add query parameters to the URI to receive the documents that match the provided parameters. A sample URI including query parameters to receive measurements that were added by a sensor with id "54da2cf5f683562dc21e25ef" and taken between 2015-01-01 and 2015-03-01 is as follows:

```
/api/measurements?from=2015-01-01&to=2015-03-01&sensor_id=
54da2cf5f683562dc21e25ef
```

If we send a POST request to a resource's URI, the data that is included in the request body forms a new document inside a collection. It has to be formatted in JSON and, in the case of the "measurements" collection, it has to include fields for sensor_id and the value (n.b. even if the timestamp field is not present, it is created and filled with current time as its value).

To access a specific document inside a collection, the document's id has to be added to the resource URI, following a forward slash separator. An example of URI for the measurement with id "54da35226dd77866261d044a" is as follows:

```
/api/measurements/54da35226dd77866261d044a
```

This URI can be used to either send a GET request to receive the document, a PUT request to update the document (with the data inside request body) or a DELETE request to delete the document.

3.3 WebSockets with publish/subscribe mechanism

WebSocket is a protocol that enables bi-directional communication over a single TCP connection [3]. It provides an enormous reduction in unnecessary network traffic and latency compared to the unscalable polling[7] and long-polling solutions that were used to simulate a full-duplex connection by maintaining two connections.

This part of the proposed API for an IoT platform is developed using Socket.IO library that implements WebSocket protocol and publish/subscribe mechanism. This is a messaging pattern where messages are not sent directly from one client to another. Rather, senders (publishers) can publish the messages to specific channels, and receivers (subscribers) can subscribe to these channels. An intermediary broker filters all the messages and forwards them to subscribed clients.

Each channel in the proposed API corresponds to a specific sensor and its measurements. Upon insertion of new measurement data to the database via RESTful API, it is also published to the sensor's channel, which the broker then forwards to the clients that subscribed to it.

4 Performance evaluation of the proposed API

In Section 3 we assumed RESTful API was not best fit for real-time data acquisition by the IoT platform, so we implemented also a WebSocket protocol with

---

[7] en.wikipedia.org/wiki/Polling_(computer_science)

publish/subscribe mechanism. In order to confirm or reject the above assumption as well as to evaluate the overall suitability of the proposed API we carried out performance evaluation from the perspective of a visualization platform. In fact, this is the most typical web application requiring real-time access to measurements from a certain sensor. To emulate its need for a fast delivery of new measurements, we implemented two web applications. One used HTTP long-polling and the other used the WebSocket protocol to retrieve newly inserted data. When a new measurement was posted to the API, it got a timestamp, it was inserted in the database and published to the sensor's channel.

For the evaluation purposes we opened two browser windows, each running one of the above mentioned web applications. When a measurement was received in the browser either over WebSocket protocol or HTTP long-polling, its timestamp was compared to the current system time. In this way we got the time elapsed from when the measurement was posted to the RESTful API and when the measurement was received in the browser. We refer to this as the elapsed time.

We repeated the evaluation with different number of measurements inserted in the database and summed elapsed times. For each number of inserted measurements *n*, the test was repeated 10 times and mean average sum of elapsed times was calculated. The measurement data was in JSON format and was always the same. The results are presented in Table 2.

Table 2: Mean average sum of elapsed times for different number of measurements

n	HTTP long-polling [ms]	WebSocket [ms]	Ratio
1	75,4	6,7	11,253731
10	221,8	23,6	9,3983051
100	1288,4	179,7	7,1697273
500	4769,3	915,8	5,2077965
1000	8738,6	1442,3	6,058795
5000	55134,8	7427,9	7,4226632
10000	139603,2	14467,8	9,6492349

Based on these results, also graphically depicted in Figure 2, it is evident that the WebSocket protocol is faster than HTTP long-polling by a factor of 5 to 11. Also we can see that long-polling for a certain number of messages try to decrease the ratio, most likely this is happening due to longer querying times as the MongoDB database grows.

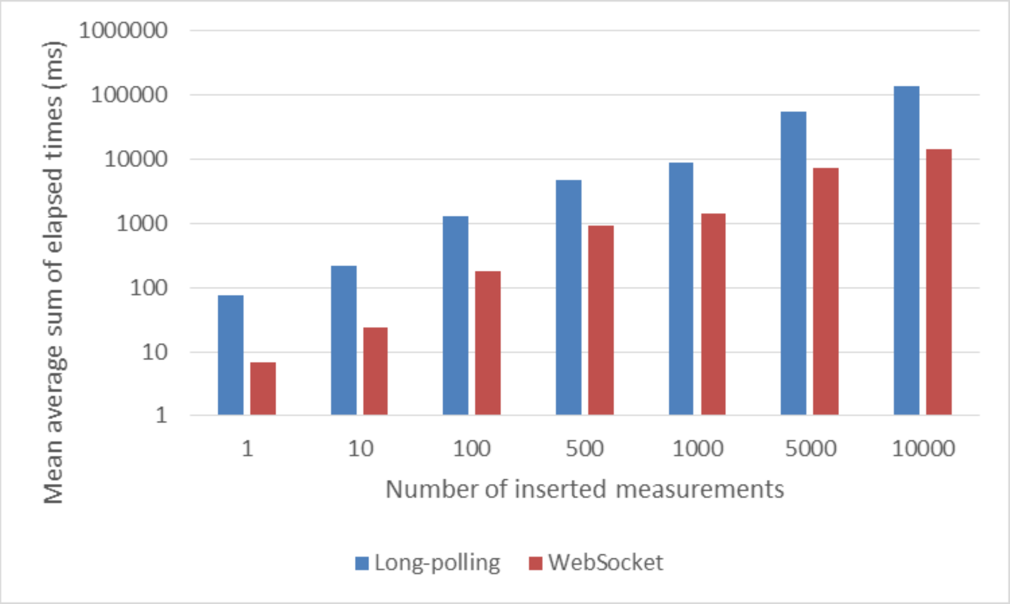

Figure 2: Mean average sum of elapsed times for different number of measurements

5 Conclusion

The Internet of things concept is based on the presumption that different devices with embedded sensors or actuators are connected to and accessible from the Internet. In order to facilitate this access for different platforms, in which data can be stored, or for the direct access by plethora of services and applications, an appropriate API needs to be exposed. In this paper we proposed and evaluated a solution based on two APIs, one using a RESTful architecture and the other using WebSocket protocol, suitable also for fast changing environment and dynamic configurations of connected devices.

The performance evaluation confirmed our expectation that the WebSocket protocol based API is faster for providing real-time data compared to HTTP long-polling. Thus, in order to provide a fast API for real-time updates, it makes sense to take advantage of the benefits that the WebSocket protocol brings. However, RESTful architecture also brings many advantages not supported by the WebSocket protocol, so we believe the combination of REST API and WebSocket protocol make an excellent combination for IoT platforms, meeting all the basic API requirements, i.e. database manipulation using CRUD operations, support for query parameters, future-proof machine and human readable architecture, real-time data delivery and security.

6 Acknowledgment

This work has been in part funded by the European Union from the European Regional Development Fund under the Operational Programme for Strengthening Regional Development Potentials for period 2007-2013, Development Priority: Economic development infrastructure, Priority axes: Information Society, within the project OSU (op. no. 3330-15-549012).

References:

[1] R. T. Fielding. Architectural Styles and the Design of Network-based Software Architectures. *University of California, Irvine*, 2000

[2] IETF, RFC 6216 - Hypertext Transfer Protocol -- HTTP/1.1. *IETF Std.,* June 1999.

[3] IETF, RFC 6455 - The WebSocket Protocol. *IETF Std.,* December 2011.

[4] J. Gubbi, R. Buyya, S. Marusic, M. Palaniswami. Internet of Things (IoT): A vision, architectural elements, and future directions. *Future Generation Computer Systems,* September 2013

[5] L. Aztori, A. Iera, G. Morabito. The Internet of Things: A Survey. *Computer networks,* 2010

[6] A. Wessels, M. Purvis, J. Jackson, S. Rahman. Remote Data Visualization through WebSockets. *Eighth International Conference on Information Technology: New Generations*, 2011

For wider interest

Internet of Things (IoT) represents a concept in which physical objects, comprised of electronics, sensors and embedded software, can access and/or are accessible through the Internet and are providing services and networking capabilities to exchange data with other devices. The data generated by these "things" is not useful until put into context by analytical, visualization or other platform. To get the data from these devices to platforms where it is stored and processed, we need an intermediary software, called an API.

In this paper we presented requirements for, implementation and performance evaluation of an IoT platform API supporting (i) database manipulation using CRUD operations, (ii) database querying with parameters, (iii) machine and human readable architecture, (iv) real-time data delivery and (v) secure access to the database. The proposed API was developed as a part of Videk platform that conforms to identified IoT platform requirements by following REST architecture style and supporting the WebSocket protocol.

Condition monitoring of mechanical drives based on entropy indices

Boštjan Dolenc [1,2], **Pavle Boškoski** [1], **Đani Juričić** [1]
[1] Department of Systems and Control, Jožef Stefan Institute, Ljubljana, Slovenia
[2] Jožef Stefan International Postgraduate School, Ljubljana, Slovenia
bostjan.dolenc@ijs.si

Abstract. Reliable fault diagnosis of mechanical drives can become nontrivial task in case of restricted instrumentation and variable operating conditions. Under such circumstances changes in the calculated features cannot be unambiguously associated with change in system condition. In this paper we propose a feature appropriate for diagnosing faults in mechanical drives that is robust to fluctuations in operating conditions. Moreover, its time evolution seems to be correlated only with the machine condition. Instead of relying on spectral properties of the vibrational signal, we rather observe changes in the statistical patterns of the derived distribution functions. The effectiveness of the algorithm was evaluated on three datasets comprising both gear and bearing faults under constant and variable load. Additionally, the newly proposed feature was adapted for condition monitoring of the turbine of milling machine. The proposed methodology shows considerable correlation between feature and the actual state of milling machine.

Keywords: change detection, condition monitoring, vibration analysis, Jensen-Rényi divergence, non-stationary operation

1 Introduction

Condition monitoring (CM) and diagnosis of mechanical drives aims to detect, localise and identify the onset of a fault in a machine. Traditional diagnostic techniques rely on monitoring the characteristic spectral components in measured vibrations [1]. These methodologies proved effective under constant operating conditions. However, without exact knowledge of the operating conditions it is not easy to determine the cause of the increased feature value.

By definition, a feature should be related solely to the machine condition, while being insensitive to variations in the operating conditions. The currently available diagnostic approaches fall into three main groups. Those from the first group rely on features that require information about the operating conditions [2, 3]. The second group utilises statistical models for specifying gear health indices [4]. The approaches from the third group specify features that describe specific statistical properties of the generated vibrations [5]. A feature robust to the variations in operating conditions can be built by characterising the distribution of energy in the generated vibrations [6]. Firstly, the feature values show non-monotonic behaviour. Secondly, parameters required for feature calculation need to be estimated each time a new machine is applied.

In this paper we employ stochastic signal processing techniques for CM of the rotating machinery in non-stationary operation. We proposes a feature based on generalised Jensen-Rényi divergence of the envelope distribution obtained from vibrations. Such a feature is shown to be practically insensitive to variations in rotational speed and load. In particular, JR divergence is employed to measure the rate of change in the vibrational envelope due to the evolving degradation

The paper is organised as follows. Section 2 presents two conceptual models describing gear and bearing faults. The background of JR divergence and its properties, as well as its applicability for condition monitoring (CM) of gears and bearings, is presented in Section 3. Finally, the evaluation results are presented in Section 4.

2 Fault models

Gears and bearings have different mechanisms that generate vibrations. At the first glance it seems that each component should be considered separately. However, it will be shown that the distribution of the energy of the generated vibrations is sufficiently accurate indicator of their condition [6].

Gear fault signature. The main source of vibration in fault-free gears is variation in the contact stiffness [7]. Under constant rotational speed the generated vibrations $x(t)$ can be represented as:

$$x(t) = \sum_{m=1}^{M} A_m\big(1 + a_m(t)\big)\cos\big(2\pi mt + \beta_m + b_m(t)\big), \tag{1}$$

where f_{gmf} is gear mesh frequency, $a_m(t)$ is modulating signal due to incipient localized teeth damages, M is the highest harmonic of interest and A_m is the amplitude of the m^{th} harmonic of the gear mesh frequency. The components $b_m(t)$ represent phase modulations, and β_m is the initial phase.

Faults in gears evolve through several stages: scuffing, initial pitting, pitting and spalling [8]. Regardless of the severity, localised gear faults influence only a limited number of teeth. Therefore, when these teeth mesh, the contact stiffness changes so that the amplitude modulation $a_m(t)$ in (1) changes accordingly. Hence, the amplitude modulation $a_m(t)$ contains all the essential diagnostic information [9].

Unlike gears, fault-free bearings produce negligible vibrations. When surface fault occurs, each time a rolling element passes across the damaged area, the impulse responses $s(t)$ are excited. The generated vibrations $x(t)$ can be represented as [10]:

$$x(t) = \sum_{i=-\infty}^{\infty} A_i(t - \tau_i) + n(t), \tag{2}$$

where A_i is the amplitude of force that excites the entire structure and τ_i is the time of its occurrence. The term $n(t)$ defines an additive random component. The time moments τ_i can be considered as random and distributed with inverse Gaussian distribution [10]. Similarly, the amplitudes A_i of the impulses should be considered as random process [11].

The diagnostic information is contained in the time instants τ_i. Under constant rotational speed, the frequency of their occurrence can be directly related to a localised bearing fault. From the macroscopic point of view, impacts can be considered as amplitude modulation of a carrier signal whose frequency is the same as the excited eigenfrequency.

3 Application of the Jensen-Rényi divergence for diagnostic purposes

Change in the envelope of the vibrational signal can be associated with the change in condition. Here we will explore the potential of the generalised Jensen-Rényi (JR) divergence in quantifying the amount of change in envelope probability density function (pdf) due to change in machine's condition.

3.1 Entropy: from Shannon to Rényi

Entropy quantifies uncertainty involved in predicting the value of a random variable (r.v.). Shannon entropy reads:

$$H(P) = -\sum_{i=1}^{N} p_i \, ln(p_i), \tag{3}$$

where P is probability distribution of a discrete r.v., i.e. $P = \{p_1, \dots, p_n\}$.

The results presented in this paper are based on a generalised version of the Shannon entropy i.e. the Rényi entropy [12]:

$$H_\alpha(P) = \frac{1}{1-\alpha} ln \sum_{i=1}^{N} p_i^\alpha, \tag{4}$$

By proper selection of parameter α one can place focus on a particular part of the analysed pdf. For $\alpha \to 1$, (4) reduces to Shannon entropy.

3.2 Jensen-Rényi divergence

To quantify the distinction between two or more pdfs the relative entropy or *divergence* is often employed. Several divergence measures are applicable depending on the analysed data [13]. Here we employ the generalised Jensen-Rényi divergence JR_α^w to quantify the dissimilarity among n pdfs:

$$JR_\alpha^w(P_1, \dots, P_n) = H_\alpha\left(\sum_{i=1}^{n} w_i P_i\right) - \sum_{i=1}^{n} w_i H_\alpha(P_i), \text{where} \sum_{i=1}^{n} w_i = 1. \tag{5}$$

In (5), H_α is Rényi entropy. The selection of weights w_i in (5) is in principle arbitrary. With w_i selected uniformly i.e. $w_i = 1/n$, the divergence reaches maximal value. As shown later on, the selection of weights w_i significantly affects the behaviour of JR divergence.

JR divergence quantifies shared information among n random variables. If they are identical, i.e. $P_1 = P_2 = \cdots = P_n$, divergence is zero. However, if one of them deviates even slightly, the divergence becomes greater than zero. Therefore, JR divergence carries information about dissimilarity among n pdfs.

A simple example demonstrates the basic concept of JR divergence. Figure 1(a) shows three Rice pdfs with different scale and location parameters. Here we consider JR divergence in its simplest pairwise form where only two pdfs are considered and $w_i = 1/2$:

$$JR_\alpha^w(P,Q) = H_\alpha\left(\frac{1}{2}(P+Q)\right) - \frac{1}{2}(H_\alpha(P) + H_\alpha(Q)), \tag{6}$$

where P and Q are pdfs of interest and $\alpha \in [0,1]$. JR divergence between P_1 and P_2 from Figure 1 (left) is 0.017 ($\alpha = 0.5$). The dissimilarity between P_1 and P_3 is even greater, hence higher value of JR divergence (0.0714). Clearly the divergence is able to characterise relative dissimilarity among the analysed pdfs.

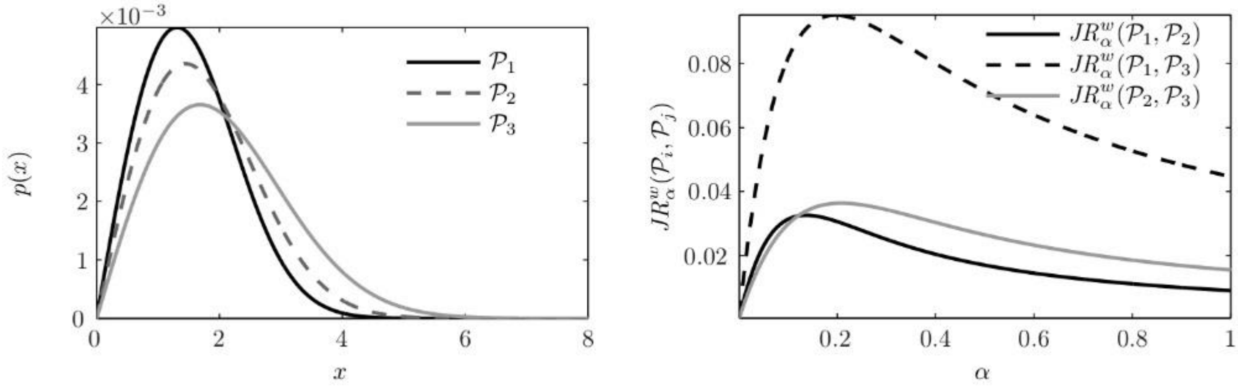

Figure 1: Pdfs of the simulated signals (left) and the resulting JR divergence as a function of α (right).

The effect of the parameter α is shown in Figure 1 (right). Low value of α ($\alpha \approx 0$) emphasizes the dissimilarity among pdfs in low probable region ($\alpha \in (6,8)$) where pdfs do not differ much, hence low divergence values. In the middle region ($x \approx$, $\alpha \approx 0.2$) the pdfs differ the most, hence the highest values of JR divergence. Finally, for $\alpha \in (0.6,1)$, which captures the region of the bulk probability masses, the divergence value drops in a relatively linear manner.

3.3 The influence of weights w_i

The selection of weights w_i has significant influence on behaviour of the JR divergence. In this paper the exponential weights w_i are suggested. The weights w_i are calculated using the exponential function of the following form:

$$w_i = C \cdot e^{-\frac{\lambda}{n}i} \tag{7}$$

where λ is sensitivity parameter, n is number of the components in (5), $i = 1, 2, \dots, n$ and C is normalising constant. One can easily see that (7) reduces to the uniform weighting for $\lambda \to 0$ and $n \to \infty$.

The influence of weights w_i on JR divergence can be illustrated by a simple example. We first generate N sequences of a normal r.v. simulating abrupt change in shape of a pdf. Than we calculate JR divergence using (5) which results in divergence value after each measurement session i: $JR_\alpha^w(P_1, P_2, \dots, P_i)$ for $i = 1, \dots, 21$.

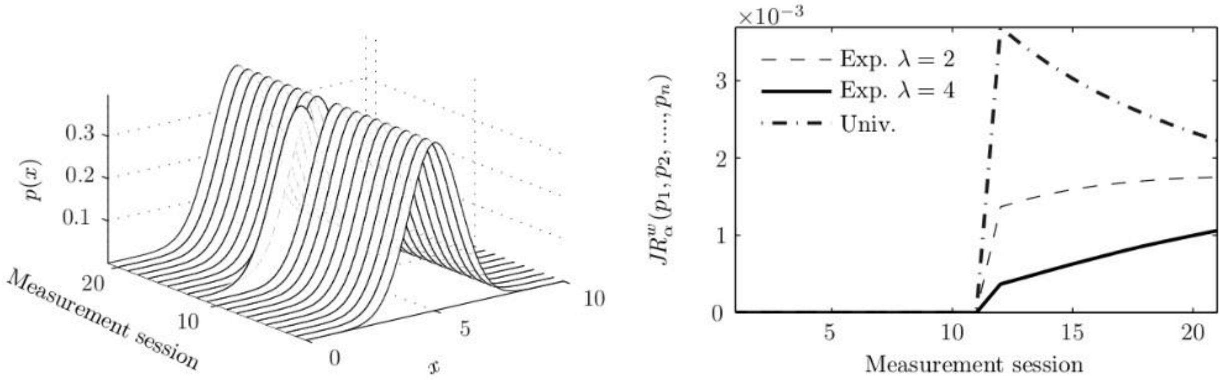

Figure 2: The evolution of JR divergence after measurement sessions. Note that all pdfs are equal except the pdf #11. Pdfs of the simulated signals associated to the measurement sessions $1, \dots, 21$ (left) and JR divergence (right).

The generated signals simulate an abrupt change in pdfs' shape. The corresponding pdfs are shown in Figure 2 (left). The JR divergence is calculated after each measurement session. First 10 pdfs are identical, hence the dissimilarity among them equals 0. Once the 11th pdf is included in the calculation of JR divergence (5) an increase in value is observed. The following 10 pdfs are identical to the first one, therefore the dissimilarity among them decreases. The rate of change in JR divergence is conditioned with the selection of weights as shown in Figure 2 (right). The most notable increase is observed if uniform weighting is applied. The exponential weighting results in small impact.

4 Experimental evaluation

The proposed feature based on the generalised JR divergence was evaluated on four different experiments:

- natural evolution of gear faults under constant operating conditions;
- natural evolution of gear faults under variable load;
- evolution of bearing faults under constant operating conditions [14], and
- progressing erosion on the blades of milling machine.

In order to show the performance of the generalised JR divergence, classical spectral features were also calculated. It should be noted that the calculation of the proposed feature was done without any information regarding the operating conditions, although the employed experimental data include such information.

Pdfs were estimated by means of histogram. The divergence $JR_{\alpha}^{w}(P_1, P_2, \dots, P_n)$ was calculated using (5). Parameter α in (4) was set to $\alpha = 0.9999$ for gear, and $\alpha = 0.8$ for bearing experiment. The JR divergence was calculated with exponential weights w_i according to (7) where $\lambda = 10$.

4.1 Gear experiment

Figure 3 (left) shows the time evolution of two classical spectral features from the first gear experiment (under constant load). The first feature is the amplitude of the spectral component at the gear mesh frequency (GMF). The second feature is the sum of the amplitudes of the side-bands around the GMF. As expected, the side-bands are more sensitive to the localised gear faults. The first increase in the side-band energy is visible around the 120th measurement. Although, an increasing trend is visible, both features show local non-monotonic behaviour, despite constant operating conditions.

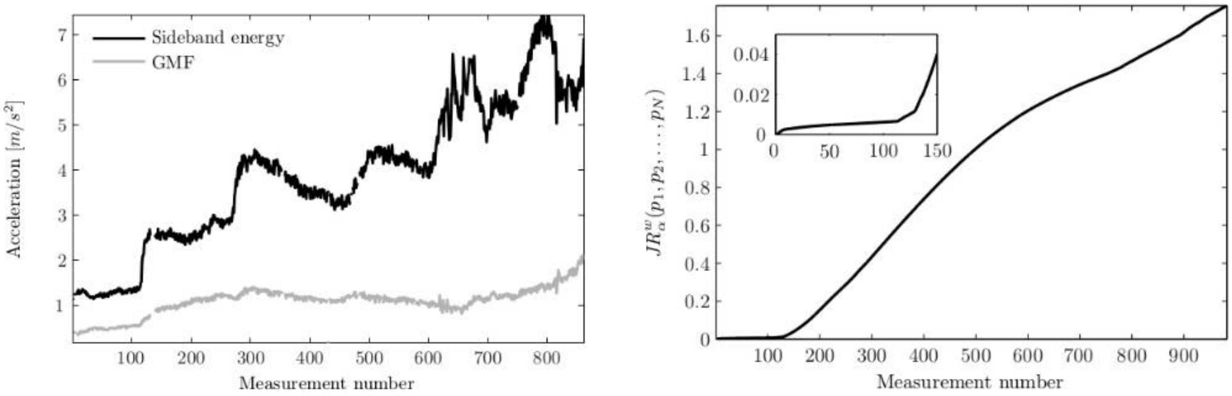

Figure 3: Time evolution of features related to gear experiment under constant load: classical spectral components (left) and generalised JR divergence (right).

Figure 3 (right) shows the time evolution of the generalised JR divergence. At the beginning of the experiment the pdfs of vibrations envelope are similar, hence JR divergence takes low value ($\approx 10^{-3}$). As soon as a fault occurs in the gear couple, its envelope changes and, unlike the classical spectral features, the value of the JR divergence monotonically increases.

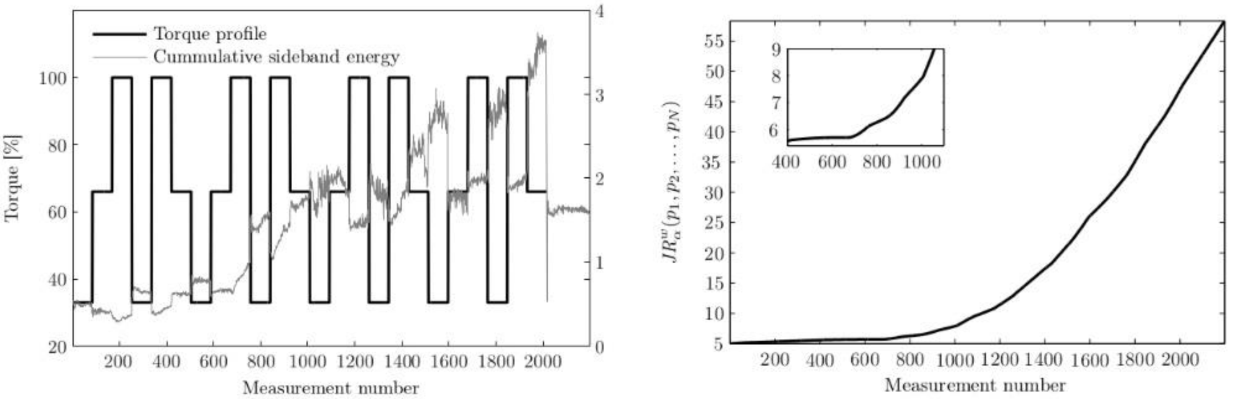

Figure 4: Time evolution of features for gear experiment under variable load: classical features and torque profile (left) and generalised JR divergence feature (right).

In case of variable load, classical spectral features were calculated from generated vibrations in the same manner as before. The time evolution of cumulative side-band energy is shown in Figure 4 (left). The influence of load variations is clearly visible. Although an increasing trend can be seen, without precise load measurements it is impossible to determine the proper cause for the abrupt changes in the features. Conversely, the time evolution of the generalised JR divergence shows smooth and monotonic increase, as shown in Figure 4 (right). Therefore, the generalised JR divergence can be considered as sufficiently robust to variations in the operating conditions while preserving the fault sensitivity.

4.2 Bearing experiment

Generally, bearing condition is estimated based on the amplitude of the characteristic spectral components such as: BPFO (*ball pass frequency outer*), BPFI (*ball pass frequency inner*) and BSF (*ball spin frequency*) as shown in Figure 5 (left). It is noticeable that the outer race fault occurs soon after the 130th measurement session. However, the monotone behaviour of this feature is not preserved. Towards the end of the experiment its value changes in a non-monotonic manner. This can be attributed to the fixed band pass in which the envelope of the generated vibrations is calculated.

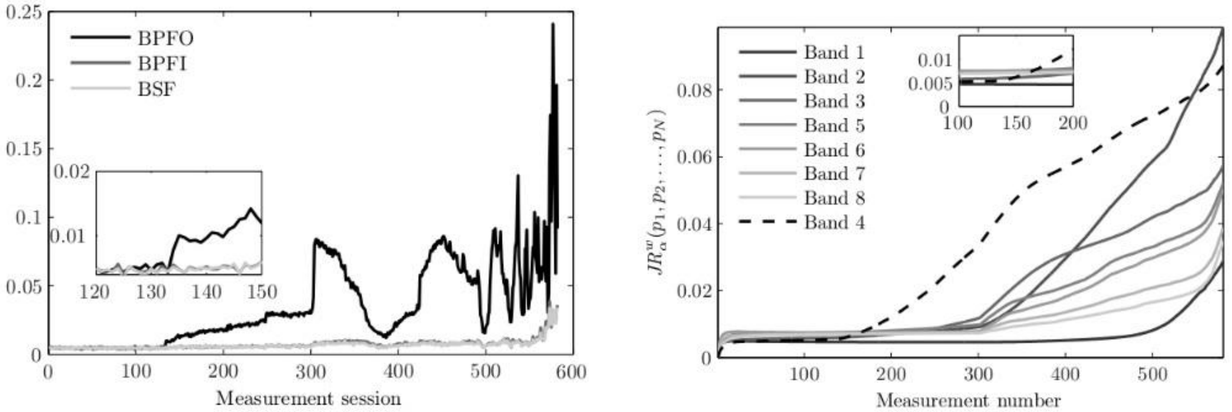

Figure 5: Extracted features from the bearing dataset: classic features (left) and generalised JR divergence (right).

As expected, at the beginning, the JR divergence is almost zero. As surface faults start to emerge, around the 150th measurement session, the JR divergence starts to increase. Unlike the standard features, the increase of the JR divergence is monotone. JR divergence covering the 4th frequency band includes the frequency band determined by the spectral kurtosis method.

4.3 Milling machine experiment

Accurate estimation of the remaining useful life (RUL) can have significant operational and financial benefits. In the light of estimating RUL, the proposed feature was further investigated as a promising health index candidate for a milling machine. As in previous experiments, vibrations were measured at the housing of the turbine. Additionally, photos of the erosion suffered by the blades of the milling machine were taken during the experiment.

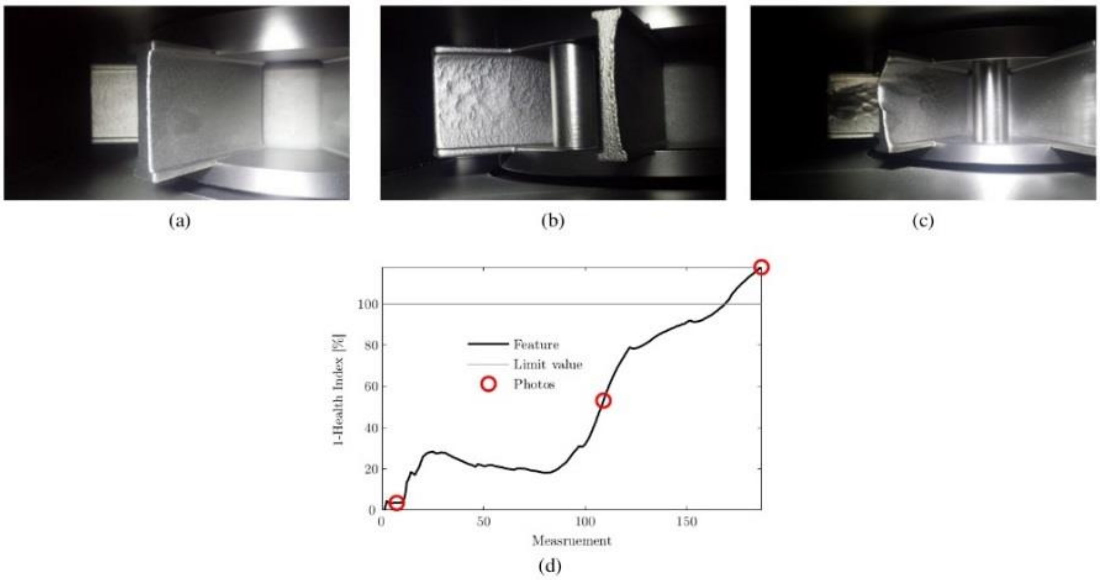

Figure 6: The correlation between fault progression and evolution of the entropy index. Figures (a-c) correspond to the time points indicated by red circles on the health index plot (d) from left to right, respectively.

The trend of the health index in Figure 6(d) has clear correlation with deterioration of the machine. Figures 6(a-c) correspond to the time points indicated by red circles on the health index plot from left to right, respectively.

5 Conclusion

The generalised JR divergence is a suitable feature for condition monitoring, however further testing is required. It characterises changes in the pdf calculated from the envelope of the generated vibrations. As a result, the calculated feature is robust to variations of the operating conditions, while in the same time it preserves its monotone time evolution which seems to be correlated with component degradation. Additionally, feature shows great potential for remaining useful life estimation applicable to rotating machinery. This issue will be studied in a more detail in the follow up of this research.

References:

[1] A. K. S. Jardine, D. Lin and D. Banjevic, "A review on machinery diagnostics and prognostics implementing condition-based maintenance," *Mechanical Systems and Signal Processing,* vol. 20, pp. 1483-1510, 2006.

[2] R. Zimroz, W. Bartelmus, T. Barszcz and J. Urbanek, "Diagnostics of bearings in presence of strong operating conditions non-stationarity—A procedure of load-dependent features processing with application to wind turbine bearings," *Mechanical Systems and Signal Processing ,* vol. 46, no. 1, pp. 16-27, 2014.

[3] W. Bartelmus and R. Zimroz, "A new feature for monitoring the condition of gearboxes in non--stationary operating conditions," *Mechanical Systems and Signal Processing,* vol. 23, no. 5, pp. 1528-1534, 2009.

[4] L. F. Villa, A. Renones, J. R. Peran and L. J. de Miguel, "Statistical fault diagnosis based on vibration analysis for gear test-bench under non-stationary conditions of speed and load," *Mechanical Systems and Signal Processing,* vol. 29, pp. 436-446, #may# 2012.

[5] P. Chen, M. Taniguchi, T. Toyota and Z. He, "Fault diagnosis method for machinery in unsteady operating condition by instantaneous power spectrum and genetic programming," *Mechanical Systems and Signal Processing,* vol. 19, no. 1, pp. 175-194, 2005.

[6] P. Boškoski and Đ. Juričić, "Fault detection of mechanical drives under variable operating conditions based on wavelet packet Rényi entropy signatures," *Mechanical Systems and Signal Processing,* vol. 31, pp. 369-381, 2012.

[7] W. Wang, "Early Detection of gear tooth cracking using the resonance demodulation technique," *Mechanical Systems and Signal Processing,* vol. 15, pp. 887-903, 2001.

[8] GfT, "Arbeitsblatt 7 Tribologie Definitionen, Begriffe, Prufung (in German)," 2002.

[9] R. Randall, "A new method of modeling gear faults," *Journal of Mechanical Design,* vol. 104, pp. 259-267, 1982.

[10] P. Boškoski and Đ. Juričić, "Inverse Gaussian mixtures models of bearing vibrations under local faults," *Mechanical Systems and Signal Processing,* p. Under review, 2014.

[11] J. Antoni and R. B. Randall, "A stochastic model for simulation and diagnostics of rolling element bearings with localized faults," *Journal of Vibration and Acoustics,* vol. 125, no. 3, pp. 282-289, 2003.

[12] A. Rényi, "On measures of information and entropy," *4th Berkeley Symposium on Mathematical Statistics and Probability,* vol. 1, pp. 547-561, 1960.

[13] M. Basseville, "Divergence measures for statistical data processing - An annotated bibliography," *Signal Processing,* vol. 93, pp. 621-633, 2013.

[14] J. Lee, H. Qiu, G. Yu, J. Lin and R. T. Services, *Bearing Data Set, IMS, University of Cincinnati,* 2007.

For wider interest

Condition-based maintenance is a maintenance strategy which recommends maintenance actions based on the information collected through on-line condition monitoring (CM). By doing maintenance only when needed, the machines can be maximally exploited, which in turn reduces maintenance cost and maximises the overall availability and reliability of the industrial equipment. In order to optimise maintenance strategy, a time-to-failure of the machine needs to be known prior to the machine breakage. With such information at hand, maintenance action can be done at optimal time and the machines life can be fully exploited.

In this paper we presented a condition monitoring methodology with application to mechanical drives. The CM indices build on statistical properties of the relevant variables. The approach was successfully applied to different types of mechanical components, i.e. bearings, bears and turbines. Furthermore, due to the generality of the approach, the methodology seems to be applicable in various fields.

Towards Unobtrusive Stress Detection

Martin Gjoreski[1,2], Hristijan Gjoreski[1,2], Mitja Luštrek[1,2], Matjaž Gams[1,2]

[1] Department of Intelligent Systems, Jožef Stefan Institute, Ljubljana, Slovenia
[2] Jožef Stefan International Postgraduate School, Ljubljana, Slovenia
martin.gjoreski@ijs.si

Abstract. This paper presents a machine-learning method for unobtrusive stress detection system. The idea is to automatically monitor three components of the stress response, i.e. emotional, behavioural and physiological. The emotional response is monitored using smartphone's microphone and emotional voice analysis. The physiological response is monitored using a sensor-equipped wristband and bio-signal analysis. And, the behavioural response is monitored using smartphone's sensors and smartphone-usage analysis. All three modules are combined using machine-learning methods to predict stress levels. We present approaches to monitor three components of the stress response with preliminary results and an indication of the feasibility of the proposed system.

Keywords: Stress Detection, Emotion Recognition, Stress Behaviour, Physiological Signs, Machine Learning.

1 Introduction

In the 21 century, stress has become one of the important health concerns impacting human life and human society. Among the negative consequences of chronic stress are raised blood pressure, bad sleep, increased vulnerability to infections, slower body recovery processes [1], and overall decreased mental performance. The National Alliance on Mental Illness's survey [2] revealed that 64% of the students who drop out of college do so for mental health reasons. In a recent EU-funded project [3], the cost to Europe of work-related mental health problems was estimated to €617 billion annually. In Slovenia, the economic cost of work-related stress in 2009 was estimated to €1.2 billion, or approximately €1.300 per worker annually [4]. Therefore, a system for early detection of stress leading to appropriate counter-measures could improve many aspects of human life, including general health, education and economy.

Our research is based on the definition of stress by Ice and James [5]: “Stress is considered a process by which a stimulus elicits an emotional, behavioural and/or physiological response, which is conditioned by an individual’s personal, biological and cultural context”. Figure 1 illustrates the stress process. Stressors are defined as stimuli which elicit a response; mediators and moderators affect one’s appraisal of stressors and influence the emotional, behavioural and physiological responses; appraisal determines which potential stressors result in stress response. All components of the stress response influence one’s physical and mental health.

We focus only on the stress response, including its three components (emotional, behavioural and physiological), in order to develop an unobtrusive stress detection system.

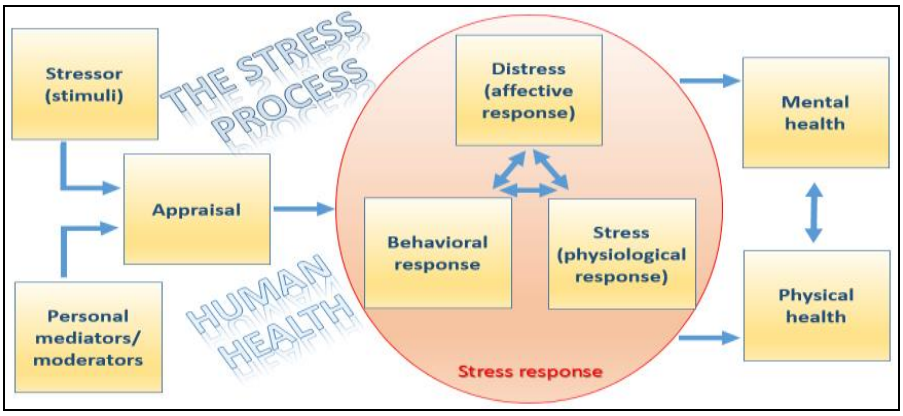

Figure 1. The stress process

2 Related work

The following section provides literature overview through the prism of computer science and engineering. In general, three different approaches exist for stress detection. The first uses physiological sensors (e.g. sensors for sweating rate, heart rate, etc.), the second uses voice analysis and the third is uses smartphone sensors.

The most exploited approach, presented in studies such as [6][7][8][9], is tested in controlled laboratory environment where the subjects’ physiological signs are monitored and stress is invoked intentionally by using some kind of stress test [10]. Healey and Picard [11] presented quite an accurate stress detection system in a real-life scenario (while the subject is driving a car), but the drawback is the number physiological sensors.

Another approach to stress detection includes the subject's voice analysis [12][13][14]. For example, recently Aguilar et al. [15] presented a stress detection system using voice analysis where the subjects' were taking an exam.

The enhanced technology of mobile devices has significantly contributed to the direction of using smartphones for stress detection. "MoodSense" [16] and similar approach [17] try to infer stress-related changes in people's behavioural through their smartphone usage patterns and location information. "StressSense" [18] detects stress using speech cues from dialogues. Few studies exist where combination of wearable sensors and smartphones are used [19][20].

3 Proposed approach for unobtrusive stress detection

Figure 2 shows the proposed approach for unobtrusive stress detection. The idea is to automatically monitor all three components of the stress response, namely emotional, physiological and behavioural response. For the emotional response, smartphone microphone is used along with emotional voice analysis. The subjects occasionally record an audio message, or some of their phone calls can be analysed while respecting their privacy (e.g. on-the-fly voice analysis which extracts features from the audio recording without saving the actual recording). For the physiological response, a wrist worn device is be used to provide readings of the subjects physiological signals (e.g. blood volume pulse, sweating rate, heart rate, skin temperature, etc.). To extract features from the subject's physiological signs, bio-signals analysis can be used. For the behavioural response, data from the smartphone sensors (accelerometers, light sensor, GPS, Wi-Fi, etc.) and smartphone usage data (e.g., when was the smartphone last used and for how long), can be analysed. All the features (cues) extracted using voice analysis, bio-signal analysis and smartphone sensor and usage analysis, can be combined to extract useful high level information which can be either real-time information (e.g. emotional state, physiological state, location, activity, …) or general information (e.g. sleep hygiene, energy expenditure,…). Finally, the high level information can be used to detect real-time stress and overall daily stress levels.

The following three subsections provide short overview of two conducted studies and one ongoing study, which are in line with the proposed unobtrusive stress detection system.

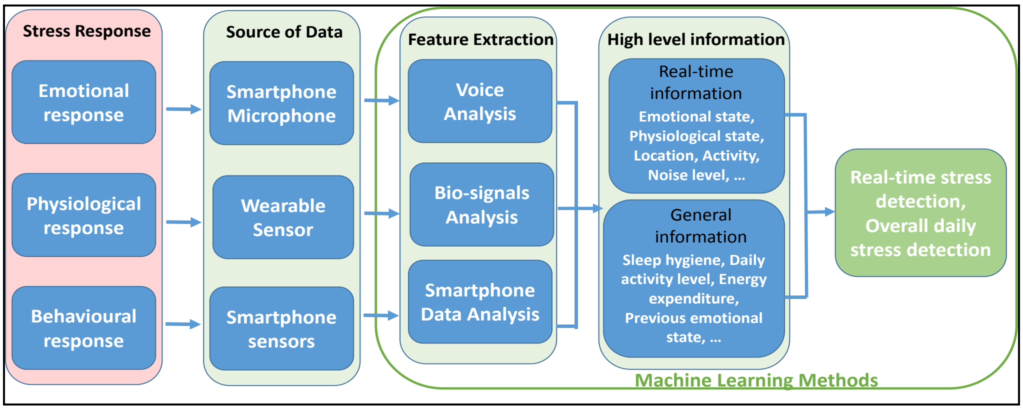

Figure 2. Proposed approach for unobtrusive stress detection

3.1 Emotion recognition from speech (Emotional response)

Disruptive, unpleasant thoughts and emotions play a major role both in contributing to stress and as key components in the manifestation of reactions to stress [21], so an emotion recognition module should be considered as a part of a stress detection system. The goal of a voice-based emotion recognition module is to recognize the emotional state experienced by the speaker. Compared to stress detection, emotion recognition is a much better explored subject in the research community and much better results are achieved so far. Figure 3 shows the machine-learning approach presented in our previous research [22]. Berlin emotional speech database [23] was used, which is one of the most exploited databases for speech emotion analysis. It consists of 535 audio files, where ten actors (five male and five female) are pronouncing ten sentences (five short and five long). The feature extraction tool used in this research is OpenSmile [24]. For feature selection, features were ranked with an algorithm for feature ranking and experiments were performed with varying numbers of top ranked features. Three commonly used algorithms for classification were tested, K-Nearest Neighbours, Naïve Bayes and Support Vector Machine. The models were evaluated with 10-fold and leave-one-speaker-out cross-validation.

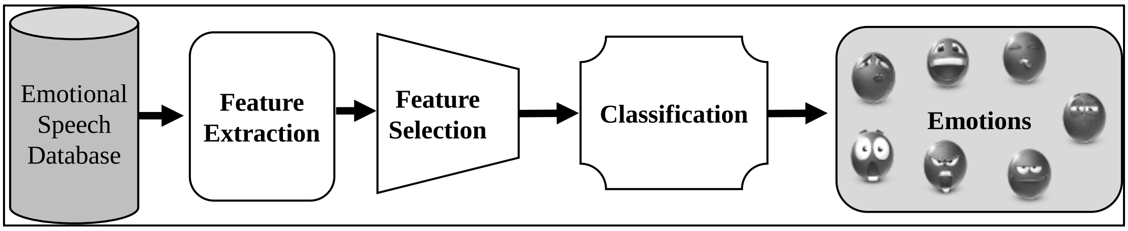

Figure 3. Emotions recognition from speech

Figure 4 shows per-emotion accuracy results obtained by the machine-learning methods compared with human recognition accuracy. The human recognition accuracy is obtained during the construction of the database where twenty volunteers had been asked to recognize the emotions by listening the audio files in random order. The recognition accuracy achieved by the SVM using 10 fold cross-validation is similar to the one achieved by human; in both cases the accuracy is 86%.

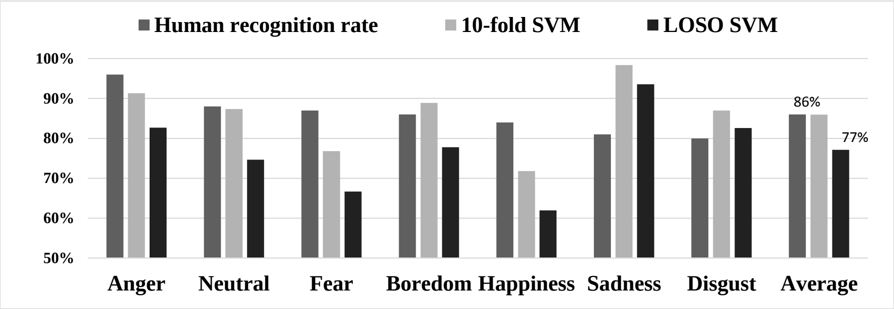

Figure 4. Per-emotion accuracy

3.2 Stress detection by monitoring behavioural changes (Behavioural response)

When an individual is confronted with a stressor they may adopt a number of behaviours which may have a positive, negative or neutral effect on the emotional and physiological response to stressors [5]. Part of one's behavioural response to a stressor can include sleep-hygiene changes (e.g. sleep duration, sleep quality), changes in social behaviour (e.g. avoiding social meetings, conversations), changes in activity levels (e.g. avoiding exercise), etc. Bauer at al. [16] concluded that smartphones can detect stress-related behavioural changes. The team of the StudentLife study [25] concluded that a significant correlation exists between students' mental health and smartphone automatic sensing data. In our study [26] we tried to take the findings of the StudentLife study one step further by implementing a machine-learning method to detect the students' stress levels. We used their data (data of the StudentLife study), which is freely available on web [27]. The goal was to develop a machine-learning model that can unobtrusively detect the stress level in students using data from several smartphone sources: accelerometers, audio recorder, GPS, Wi-Fi, call log and light sensor. From these, features were constructed describing the students' deviation from usual behaviour.

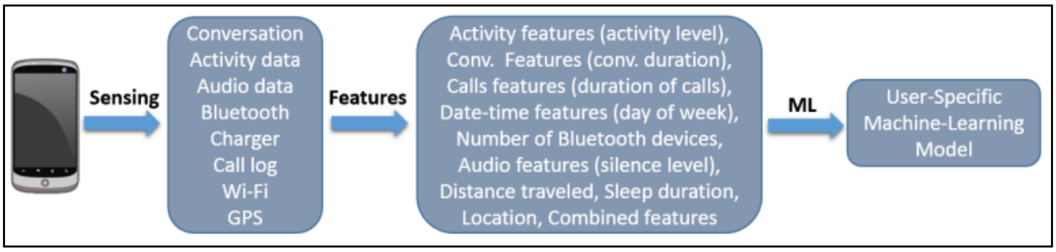

Figure 5. Stress detection using smartphones

As ground truth, we used the data obtained from stress level questionnaires with three possible stress levels: "Not stressed", "Slightly stressed" and "Stressed". Figure 5 shows our proposed approach.

Several machine-learning approaches were tested: building a general models for all the students, building a model for clusters of similar students, and building student-specific models. Our findings showed that significantly better results than majority class cannot be achieved even by clustering students' with similar behaviour using automatic sensing data, and building cluster-specific classification models. Figure 6 shows stress recognition accuracy for leave-one-user-out experimental setup where additionally the data of each test user is split in two parts, one part included in the training set, and one used as test set. The number of instances included in the training set is represented on the x-axis. The "General RF" classifier was trained on the whole training data, while the "Specific" classifiers were trained only on the user-specific training data. The approach that yielded the best accuracy was building a person-specific classification model using the Random Forest algorithm. Once the person-specific algorithm (red) had enough data to build a model, it performed better than the user-specific majority class classifier (Specific ZeroR, blue) and the general classifier (General RF, orange).

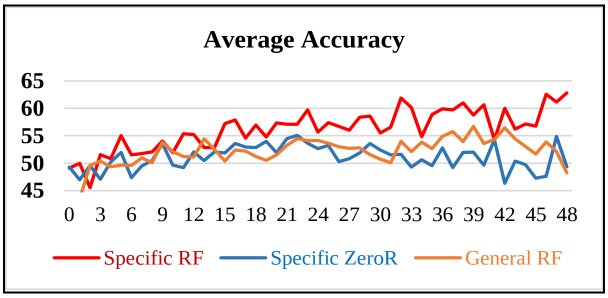

Figure 6. Accuracy with respect to the number of user-specific train instances

Perceived stress is very subjective and each individual is specific, so smartphone stress detection based on behavioural analysis can be performed by building person-specific models, where certain period of time (e.g. 20-25 days) user input is needed.

3.3 Physiological response

In our ongoing study subjects' stress levels are monitored in real-life scenarios. This study aims to integrate the previous two approaches (emotion recognition and stress detection by monitoring behavioural changes) and an approach for stress detection using physiological signs monitored by a wristband with sensors for electrodermal activity (EDA), blood volume pulse, skin temperature, heart rate (HR), and accelerometers [28]. Since the study is at its beginning, we cannot go into details yet. However, we are going to present some interesting preliminary findings. Figure 7 shows an example for physiological signals (EDA and HR) extracted from two real-life scenarios. The signals under stressful conditions (first two graphs) are extracted when the subject was taking a group exam (several students at once). The exam lasted three hours including two presentations and one question-answering session per student. The second two graphs present the subject's physiological signals during an ordinary work-day. During the stressful event, the subject's maximum EDA is near 8 μS, whereas during the ordinary work-day his maximum EDA is near 5 μS. Similarly, during the stressful event, the subject's average HR is near 80-90 bpm, whereas during the ordinary work-day his average HR is around 60 bpm. This means the subject's EDA and HR are significantly increased during the stressful event.

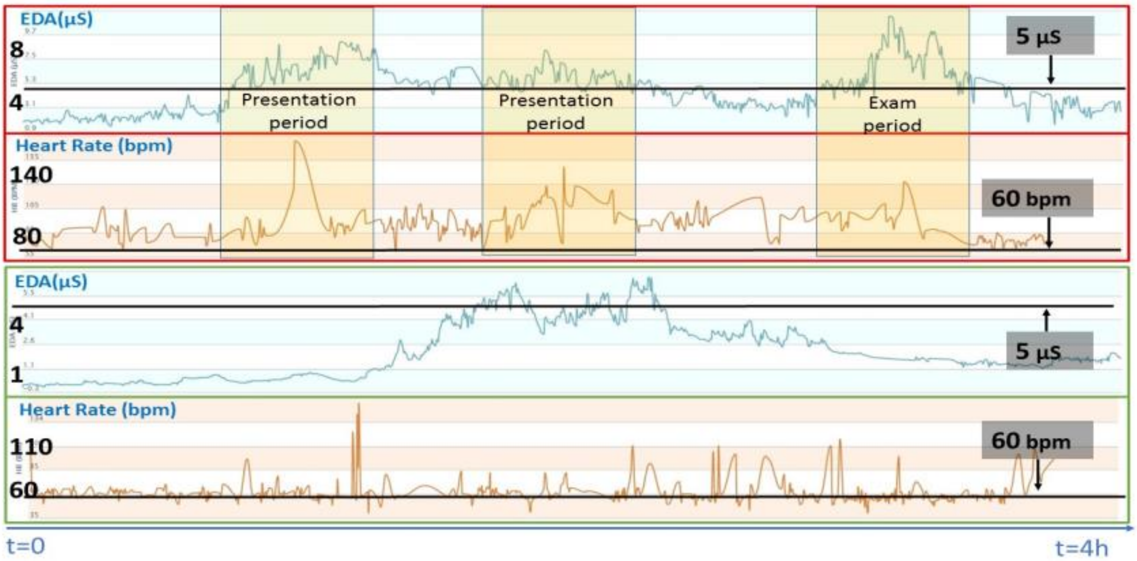

Figure 7. EDA and HR for stressful (upper two graphs) and non-stressful

4 Conclusion and Discussion

The proposed machine-learning method for unobtrusive stress detection by monitoring three components of the stress response (emotional, behavioural and physiological) is in line with the medical theory behind stress. The proposed approach for emotion recognition showed promising results, but it was tested for recognizing acted emotions. Recognizing real-life emotions brings additional problems (e.g. less clearly expressed emotions, recordings quality, privacy, obtaining ground truth, etc.). The proposed approach for stress detection using smartphones by monitoring subjects' behavioural changes is a real-life study, but it appears not to be adequate on its own. The approach for stress detection using physiological signs is a reasonably well researched but nevertheless quite challenging topic. Finally, integrating all three approaches into a single multimodal stress detection system has – to our knowledge – not been done before, but we hope it will be able to overcome the problems of individual approaches and offer better performance than any of them.

References:

[1] S.C. Segerstrom, G.E. Miller. Psychological stress and the human immune system: a meta-analytic study of 30 years of inquiry, Psychological Bulletin 130 (2004) 601.

[2] http://www2.nami.org/Content/NavigationMenu/Find_Support/NAMI_on_Campus1/collegereport.pdf]ess detection which should improve the conventional approaches.

[3] http://ec.europa.eu/health/mental_health/docs/matrix_economic_analysis_mh_promotion_en .pdf.

[4] http://www.produktivnost.si/stres-na-delovnem-mestu-raziskave-in-statistika/#.

[5] H. G._Ice, G. D. James. Measuring Stress in Humans: A practical Guide for the field. Cambridge university press, 2007.

[6] J. Wijsman, B. Grundlehner, H. Hermens, "Wearable physiological sensors reflect mental stress State in office-like situations," in the proceeding of the 2013 Humaine Association Conference on Affective Computing and Intelligent Interaction.

[7] D. McDuff, S. Gontarek, R. Picard, "Remote measurement of cognitive stress via heart rate variability," in the 36th Annual International Conference of the IEEE Engineering in Medicine and Biology Society (EMBC), Chicago, August, 2014.

[8] B. Ionut-Vlad, G. Ovidiu, "A study about feature extraction for stress detection". The 8th International Symposium on Advanced Topics in Electrical Engineering, 2013.

[9] A. de S. Sierra, C. S. Ávila, J. G. Casanova, G. B. del Pozo. Real-Time Stress Detection by Means of Physiological Signals. Recent Application in Biometrics, 2011.

[10] B. M. Kudielka, D. H. Hellhammer, C. Kirschbaum. Ten years of research with the Trier Social Stress Test (TSST) – revisited. Guilford Press, 2007, p: 56-83.

[11] J. A. Healey, R. W. Picard. Detecting Stress During Real-World Driving Tasks Using Physiological Sensors. IEEE Transactions on Intelligent Transportation Systems, 2005.

[12] S. Scherer et al., “Emotion recognition from speech: Stress experiment,” in Proceedings of the Sixth International Language Resources and Evaluation (LREC'08), pp. 1325-1330, Marrakech, Morocco, 2008.

[13] Phil Adams et al., “Towards personal stress informatics: Comparing minimally invasive techniques for measuring daily stress in the wild,” in the 8th International Conference on Pervasive Computing Technologies for Healthcare, 2014.

[14] J. Hernandez, R. R. Morris, R. W. Picard, “Call center stress recognition with person-specific models,” in Affective Computing and Intelligent Interaction, pp. 125– 134. Springer, 2011.

[15] A. Aguiar et al. VOCE Corpus: Ecologically Collected Speech Annotated with Physiological and Psychological Stress Assessments. In proceedings of the 9th International Conference on Language Resources and Evaluation, 2014.

[16] G. Bauer, P. Lukowicz, “Can Smartphones Detect Stress-Related Changes in the Behaviour of Individuals?” in Pervasive Comp and Comm Workshops (2012) IEEE International Conference. DOI: 10.1109/PerComW.2012.6197525.

[17] R. LiKamWa, Y. Liu, N. Lane, and L. Zhong. Can your smart- phone infer your mood? In Proc. ACM Embedded Networked Sen- sor Systems (SenSys), 2011.

[18] Lu H et al., StressSense: Detecting Stress in Unconstrained Acoustic Environments using Smartphones, ACM UbiComp 2012.

[19] A. Sano, R.W. Picard. Stress Recognition using Wearable Sensors and Mobile Phones. In proceedings of the 2013 Humaine Association Conference on Affective Computing and Intelligent Interaction.

[20] A. Muaremi, B. Arnrich, G. Troster, “Towards measuring stress with smartphones and wearable devices during workday and sleep”. BioNanoSci. (2013) 3:172–183 DOI 10.1007/s12668-013-0089-2.

[21] M. M. Parker, R. H. Ettinger. Understanding Psychology. Horizon Textbook Publishing, 2007

[22] M. Gjoreski, H. Gjoreski, A. Kulakov. Machine Learning Approach for Emotion Recognition in Speech. Informatica : an international journal of computing and informatics, 2014.

[23] F. Burkhardt, A. Paeschke, M. Rolfes, W. Sendlmeier, B. Weiss. A Database of German Emotional Speech. 2005. In: Proc. Interspeech. pp. 1517–1520.

[24] F. Eyben, M. Wöllmer, B. Schuller. OpenSMILE - The Munich Versatile and Fast Open-Source Audio Feature Extractor. 2010.

[25] R. Wang et al. StudentLife: Assessing mental health, academic performance and behavioral trends of college students using smartphones. In proceedings of the ACM Conference on Ubiquitous Computing, 2014.

[26] M. Gjoreski, H. Gjoreski, M. Luštrek, M. Gams. Automatic detection of perceived stress in campus students using smartphones. Accepted at The 11th International Conference on Intelligent Environments, 2015.

[27] http://studentlife.cs.dartmouth.edu/

[28] M, Garbarino, M. Lai, D. Bender, R. W. Picard, S. Tognetti. Empatica E3 - A wearable wireless multi-sensor device for real-time computerized biofeedback and data acquisition. In the proceedings of the 4th International Conference on Wireless Mobile Communication and Healthcare, 2014.

For wider interest

A system for early detection of stress leading to appropriate counter-measures could improve many aspects of human life, including general health, education and economy. Among the negative consequences of chronic stress are raised blood pressure, bad sleep, increased vulnerability to infections, and overall decreased mental performance. One survey revealed that 64% of the students who drop out of college do so for mental health reasons. The cost to **Europe** of work-related mental-health problems in 2013 was estimated **to €617 billion** annually. In **Slovenia**, the economic costs for work-related stress in 2009 was estimated to **€1.2 billion**, or approximately **€1.300** per worker annually.

This paper presents a method for developing a system that can unobtrusively monitor (detect) human stress levels. The idea is to automatically monitor three components of the stress, i.e. **emotional, behavioural and physiological.** The emotional response is monitored using smartphone's microphone and emotional voice analysis. The physiological response is monitored using a sensor-equipped wristband and bio-signal analysis. And, the behavioural response is monitored using smartphone's sensors and smartphone-usage analysis.

Regarding the **emotional response,** we conducted a study for voce-based emotion recognition which showed promising results. The recognition accuracy for 7 basic emotions (happiness, anger, boredom, fear, disgust, sadness and neutral) is 86%.

Regarding the **behavioural response**, we conducted another study for detecting stress level in students using data from several smartphone sources: accelerometers, audio recorder, GPS, Wi-Fi, call log and light sensor. From these sources, information is extracted for describing the students' deviation from usual behaviour. We concluded that smartphone stress detection based on behavioural analysis can be performed by building person-specific models.

In our ongoing study subjects' stress levels are monitored in real-life scenarios. This study aims to integrate the previous two approaches (**emotion** recognition and stress detection by monitoring **behavioural** changes) and an approach for stress detection using **physiological** signs monitored by a wristband equipped with sensors for electrodermal activity, blood volume pulse, skin temperature, heart rate, and accelerometers. The final idea is integrating all three approaches into a single multimodal stress detection system, which – to our knowledge – has not been done before.

Improving QSAR models by exploiting unlabeled data from public databases of bioactive drug-like molecules

Jurica Levatić[1,2], **Fran Supek**[3,4], **Sašo Džeroski**[1,2]
[1] Department of Knowledge Technologies, Jožef Stefan Institute, Ljubljana, Slovenia
[2] Jožef Stefan International Postgraduate School, Ljubljana, Slovenia
[3] Division of Electronics, Institut Ruđer Bošković, Zagreb, Croatia.
[4] Centre for Genomic Regulation and Universitat Pompeu Fabra, Barcelona, Spain

jurica.levatic@ijs.si

Abstract. Quantitative structure-activity relationship (QSAR) modelling is concerned with predicting biological effects of chemicals, with the aim of reducing the cost and duration of drug development. Due to the expensive annotation procedure, labeled datasets are often small in the domain of QSAR modelling, but unlabeled data are abundant. This represents a limitation for traditional supervised machine learning methods, which rely on labeled data only. On the contrary, semi-supervised methods use both labeled and unlabeled data, with the goal to improve performance of supervised methods. In this work, we explore the possibility of exploiting public databases of drug-like molecules as a source of unlabeled data for semi-supervised learning. To develop QSAR models, we use our recently proposed semi-supervised method based on predictive clustering trees for multi-target regression. The results show that unlabeled molecules extracted from the ChEMBL database helped to improve the predictive performance of the QSAR model for predicting cytostatic properties of potential antimalarial medications on human cells. This suggests that public databases can indeed be used as a valuable source of unlabeled data to improve performance of QSAR models – at no additional cost.

Keywords: semi-supervised learning, multi-target regression, QSAR, machine learning, structured output prediction, predictive clustering trees, primaquine

1 Introduction

Pharmaceutical industry spends huge amounts of money on research and development of new drugs. The estimated cost of new drug development is over 800 millions of US$ [1]. This cost is to a large extend related to failures: Only a small fraction of promising drugs will ever progress to clinical trials due to the undesired biological effects.

Establishing a connection between biological effects and structural and/or physicochemical properties of chemicals is the task of quantitative structure-activity relationship or QSAR modelling. Formal studies of such relationships are the basis for the development of predictive models that can provide insight into the biological activity of a molecule without the need to synthesize it. This leads to a number of benefits, including savings in the cost and duration of product development (e.g., in the pharmaceutical or pesticide industries), reduction of the need for animal testing, and prediction of unwelcome or toxic environmental impact [2].

Most commonly, to build predictive QSAR models, supervised machine learning methods are used. Supervised learning is the traditional machine learning paradigm, where only labeled data are used. However, in many real-world scenarios, labeled data are scarce due to a costly and/or time-consuming labeling procedure; while unlabeled data abound and are easy to obtain. The paradigm of semi-supervised learning (SSL) examines how to exploit both labeled and unlabeled data, aiming to improve the performance of traditional supervised methods by exploiting the information that unlabeled data bring.

The application of SSL to the domain of QSAR modeling is particularly attractive since the premise: “labeled data are scarce, while unlabeled data abound” is generally satisfied in this domain. Public databases with (hundreds of) thousands of chemical compounds are available (such as ChEMBL or ZINC databases), while labeled datasets sizes typically range from tens to hundreds and rarely surpass a thousand molecules.

The main goal of this study is to investigate whether we can improve predictive performance of the QSAR models by exploiting such public sources of unlabeled data. We predict the *in vitro* cytostatic activity against 12 human tumor cell lines of a small dataset of primaqune-like molecules. Primaquine is a medication used in the treatment and prophylaxis of malaria. To build QSAR models, we use our recently proposed semi-supervised method based on ensembles of predictive clustering trees (PCTs) for multi-target regression (MTR) [3].

MTR is a structured output prediction task where the goal is to simultaneously predict multiple continuous target variables (e.g., cytostatic activity against different cell lines, as considered in this study). Semi-supervised methods able to solve MTR problems are scarce. Most commonly, SSL methods for structured output prediction are dealing with discrete output. On the other hand, SSL for single-target regression has received more attention in the past [4]. While it is possible to decompose a MTR problem into several single-target ones and use such methods, there are several advantages of learning a global multi-target model over learning a separate local model for each target variable: global models are typically easier to interpret, may perform better and overfit less than a collection of single-target models [5], [6].

In our recent work, we proposed a global semi-supervised method for MTR. We showed that the proposed method can achieve greater predictive performance than supervised random forest of PCTs for MTR. It was suggested before that SSL can improve QSAR models [7], [8], however to the best of our knowledge, public databases of compounds were not considered as sources of unlabeled data for SSL. In this study, we extracted unlabeled data for SSL from ChEMBL database, which contains more than a million of small bioactive drug-like molecules. Our results show that the semi-supervised QSAR model outperformed the supervised one, suggesting that public databases of compounds can be used to improve (at no additional cost) the traditional supervised QSAR models.

2 Semi-supervised learning for MTR with ensembles of PCTs

The basis of the semi-supervised method proposed in this study is the use of PCTs in an ensemble learning setup. The PCT framework views a decision tree as a hierarchy of clusters: the top-node corresponds to one cluster containing all data, which is recursively partitioned into smaller clusters while moving down the tree. The PCT framework, including PCTs for MTR and ensembles thereof, is implemented in the CLUS system [5], available at http://clus.sourceforge.net

To perform semi-supervised learning with ensembles of PCTs for MTR, we adapt a self-training approach. In self-training, a predictive model (i.e., a random forest of PCTs) is constructed by using the available labeled instances. The unlabeled instances are first labeled by using the obtained predictive model. Next, the examples with the most reliable predictions are selected and added to the training set. A predictive model is then constructed again and the procedure is repeated until a stopping criterion is satisfied. The pseudo-code of the self-training algorithm for MTR with ensembles of PCTs (named CLUS-SSL) is outlined in Table 1.

Table 1 The learning algorithm for self-training with random forests of PCTs (Clus-SSL). Here, $\boldsymbol{E_l}$ is set of the labeled examples, $\boldsymbol{E_u}$ is a set of unlabeled examples, $\boldsymbol{k}$ is the number of trees in the forest, $\boldsymbol{f(D)}$ is the size of the feature subset considered at each node during tree construction for random forests and $\boldsymbol{\tau}$ is the threshold for the reliability of predictions.

```
procedure CLUS-SSL ($E_l, E_u, \tau, k, f(D)$)
returns Forest
repeat
    $F = RForest(E_l, k, f(D))$
    $E'_u = predict(F, E_u)$
    for each $e_u \in E'_u$ do
        if $Reliability^F(e_u) \geq \tau$ then
        move $e_u$ from $E'_u$ to $E_l$
        drop $e_u$ from $E_u$
until stopping_criterion()
return $F$
```

Self-training strongly relies on the assumption that its own (most reliable) predictions are correct. Hence, the most crucial part of the algorithm is to define a proper reliability scoring function. A good reliability scoring function should be able to discern correct predictions (thus assigning them high scores) from wrong predictions (thus assigning them low scores). For this purpose, we exploit a solution provided directly by ensemble learning – we use the variance of the votes of an ensemble as an indicator of reliability [9]. When a prediction is made for an unlabeled example by a random forest, we consider it reliable if the predictions of the individual trees (i.e., votes) in the ensemble are coherent. Otherwise, if the predictions by the individual trees in the ensemble are very heterogeneous, we consider the prediction unreliable.

More specifically, first, for each unlabeled example $e_u \in E_u$,the per-target standard deviation of votes of the ensemble is calculated. In order to weigh equally the contribution of each target attribute, we normalize the per-target standard deviations to the interval [0,1]. After normalization, the overall reliability score for an example e_u is computed as the average of its normalized per-target standard deviations. Calculation of the reliability score is presented in more detail in [3].

Selecting the unlabeled examples that should be added to the training set requires a user-defined threshold ($\tau \in [0,1]$) on the reliability score. If the reliability of the prediction for an unlabeled example is greater than τ, the example is moved from the unlabeled set (E_u) to the training set (E_l), together with the predicted values of its target variables. This procedure is iterated until the stopping criterion is met, i.e., no unlabeled example is moved from the set E_u to the set E_l.

3 Experimental design

3.1 Data description

The labeled dataset we consider in this study consists of 40 primaquine-like molecules [10]–[14] which are currently under consideration as novel antimalarial medications. For these chemicals, 12 different properties were measured: (i) cytostatic activity against 8 different human tumor cell lines, (ii) free radical scavenging ability (interaction with DPPH), (iii) inhibition of the soybean lipoxygenase enzyme and (iv) inhibition of lipid peroxidation. The goal of QSAR models we develop in this study is to predict, as accurately as possible, these 12 properties of primaquine-like molecules.

The molecules were represented by 127 2D molecular descriptors calculated with Chemistry Development Kit [15], which are used as descriptive attributes during the training of machine learning methods.

3.2 Extraction of unlabeled data from the ChEMBL database

As a source of unlabeled data for semi-supervised learning, we consider the ChEMBL database [16]. This database contains almost 1.5 million of bioactive drug-like small molecules, and is one of the biggest and most complete such databases.

To obtain unlabeled molecules, we search the ChEBML database for molecules similar to the ones in our dataset (i.e., we search for primaquine-like molecules within ChEMBL database). For each of the 40 molecules in the labeled dataset, we extract from ChEBML all of the molecules with at least 80% similarity according to the Tanimoto similarity measure [17] over molecular fingerprints[1], ensuring that the extracted molecules are within the applicability domain of the model. From the obtained list of molecules, we remove duplicates and the ones which have identical counterpart in the labeled dataset. This procedure yielded a dataset of 61 molecules, which were fed as unlabeled data to the semi-supervised algorithm.

3.3 Experimental setup and evaluation procedure

The SSL method for MTR proposed in this study (CLUS-SSL) iteratively trains random forest ensembles for MTR. Hence, we compare the predictive performance of the self-training approach to the performance of a supervised random forest (CLUS-RF) – a baseline in the experimental evaluation. In all of the experiments, we construct random forests consisting of 100 predictive clustering trees for MTR. The trees are not pruned and the number of random features at each internal node is set to $\lfloor \log_2(D)+1 \rfloor$, where D is the total number of features [18].

To evaluate the predictive performance of the models, we use a 10-fold cross validation procedure. The CLUS-RF is trained by using labeled data only, while CLUS-SSL in addition uses the unlabeled data extracted from the ChEMBL database. We assess the predictive performance of the algorithms by using the relative root-mean-square error (RRMSE).

For the CLUS-SSL algorithm, a threshold τ on the reliability score needs to be set. The threshold is then used throughout the iterations of the self-training. To determine the optimal threshold, we cross-validate the CLUS-SSL algorithm with 15 different thresholds: $\tau = \{0.1, 0.2, 0.3, 0.4, 0.5, 0.55, 0.6, 0.65, 0.7, 0.75, 0.8, 0.85, 0.9, 0.95, 0.99\}$. The threshold $\tau = 0.55$ was selected as an optimal one (i.e., it yielded the best predictive performance).

---

[1] Tanimoto (or Jaccard) similarity is the most popular similarity measure for comparing chemical structures, where the two structures are usually considered similar if similarity is greater than 0.8.

4 Results

The results of experimental evaluation are presented on Figure 1. We can observe that CLUS-SSL outperforms CLUS-RF on 10 out of 12 target variables. Furthermore, overall RRMSE error (i.e., across all 12 target variables) of CLUS-SSL is lower than the error of CLUS-RF.

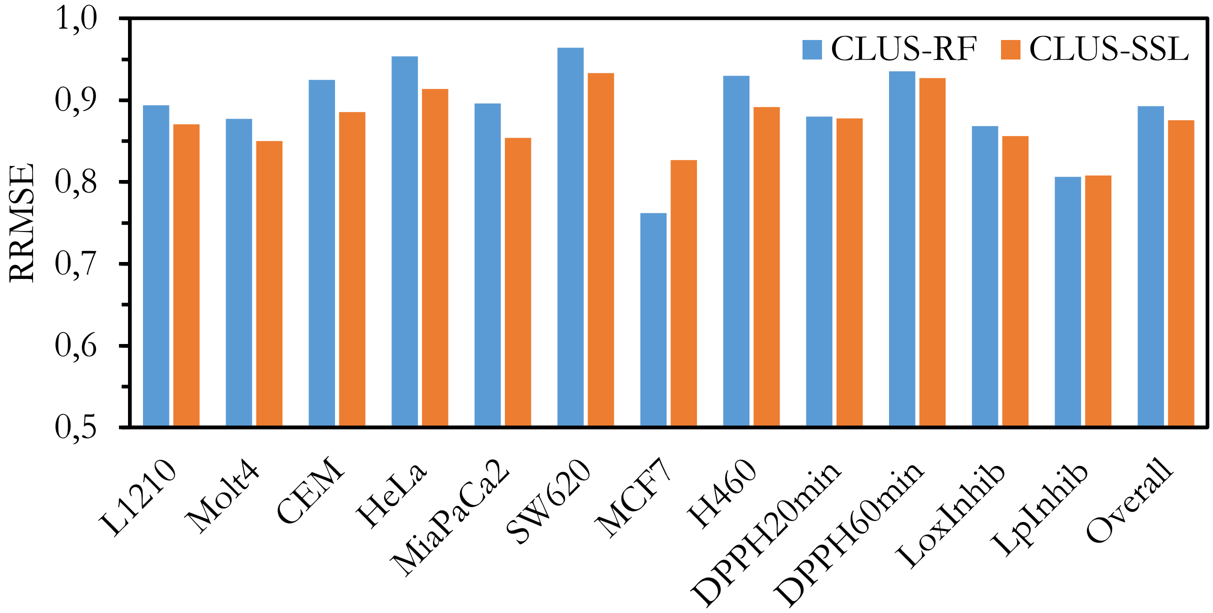

Figure 1. Comparison of predictive performance for random forests (CLUS-RF) and semi-supervised self-training (CLUS-SSL).

On the two target variables, *MCF7* and *LPInhib*, semi-supervised learning did not improve the performance of CLUS-RF. On the latter target variable (*LpInhib*), the predictive performance of CLUS-SSL and CLUS-RF is very similar, however on the former (*MCF7*), the usage of unlabeled data by CLUS-SSL led to a degradation in performance of CLUS-RF.

Self-training can also degrade the performance of the underlying method, especially if a sub-optimal threshold is chosen. To exemplify this, we present the results with varying values of the reliability threshold on Figure 2. In particular, if a too permissive threshold is selected, it can allow wrongly predicted examples to enter in the training set. A prediction error made in the earliest iterations can reinforce itself in the next iterations, leading to degradation of performance. On the other hand, if a too stringent threshold is set, it is possible that none, or very few, of the unlabeled examples enter the training set, meaning that we miss the opportunity to improve performance by using unlabeled data.

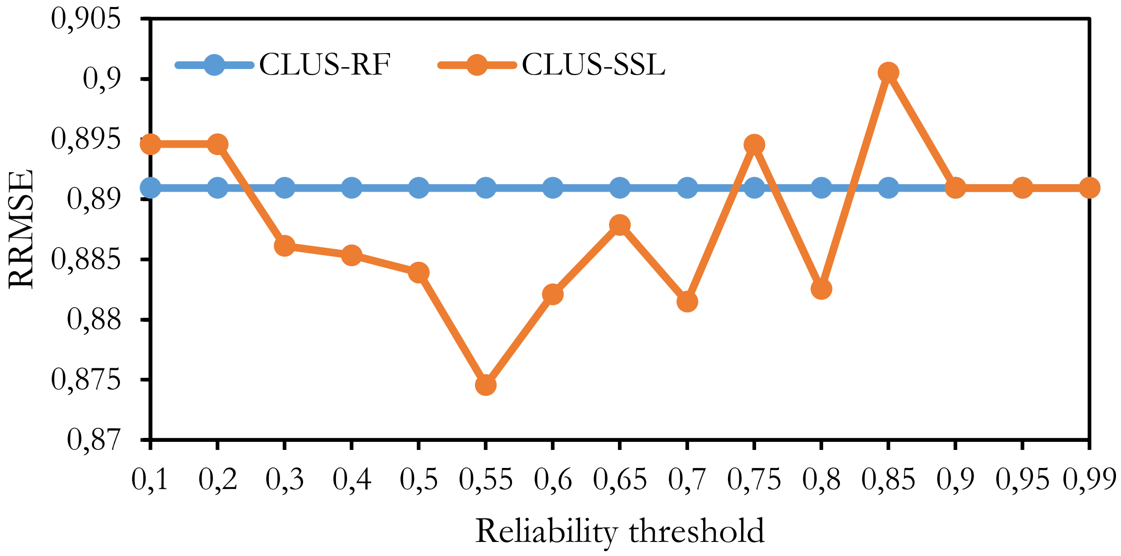

Figure 2. Comparison of predictive performance of random forest (CLUS-RF) and semi-supervised self-training (CLUS-SSL) with varying threshold for reliability of predictions exemplifies the possible effects of choosing a sub-optimal threshold:

5 Conclusion

In this work, we investigate wheatear predictive performance of QSAR models can be improved for 'free'. Namely, we propose the usage of public databases of drug-like molecules as a source of unlabeled data for QSAR modelling with semi-supervised learning algorithms. We develop a QSAR model for predicting 12 important properties of primaquine-like molecules – chemicals under consideration as potential antimalarial medications. For this purpose, we use semi-supervised method for multi-target regression based on ensembles of predictive clustering trees. We extract a set of unlabeled molecules from ChEMBL database, which are used in addition to labeled data by the semi-supervised method. Experimental evaluation showed that the semi-supervised QSAR model achieved better predictive performance than the model which relies only on labeled data. This result suggest that public databases of chemical compounds are useful source of unlabeled data for QSAR modelling with semi-supervised learning.

Acknowledgements We acknowledge the financial support of the Slovenian Research Agency, via the grant P2-0103 and a young researcher grant to the first author, as well as the European Commission, via the grants ICT-2013-612944 MAESTRA and ICT-2013-604102 HBP.

References:

[1] J. A. DiMasi, R. W. Hansen, and H. G. Grabowski, “The price of innovation: new estimates of drug development costs,” *J. Health Econ.*, vol. 22, no. 2, pp. 151–185, Mar. 2003.

[2] M. T. D. Cronin, “Quantitative Structure–Activity Relationships (QSARs) – Applications and Methodology,” in *Recent Advances in QSAR Studies*, T. Puzyn, J. Leszczynski, and M. T. Cronin, Eds. Springer Netherlands, 2010, pp. 3–11.

[3] J. Levatić, M. Ceci, D. Kocev, and S. Džeroski, “Semi-supervised learning for multi-target regression,” in *New Frontiers in Mining Complex Patterns, LNCS*, 2015.

[4] X. Zhu, “Semi-supervised learning literature survey,” *Comput. Sci. Univ. Wis.-Madison*, vol. 2, p. 3, 2006.

[5] D. Kocev, C. Vens, J. Struyf, and S. Džeroski, “Tree ensembles for predicting structured outputs,” *Pattern Recognit.*, vol. 46, no. 3, pp. 817–833, Mar. 2013.

[6] J. Levatić, D. Kocev, and S. Džeroski, “The importance of the label hierarchy in hierarchical multi-label classification,” *J. Intell. Inf. Syst.*, Dec. 2014.

[7] L. Guo-Zheng, Y. Y. Jack, L. Wen-Cong, L. Dan, and Q. Y. Mary, “Improving Prediction Accuracy of Drug Activities by Utilizing Unlabeled Instances with Feature Selection,” *Int. J. Comput. Biol. Drug Des.*, vol. 1, no. 1, pp. 1–13, 2008.

[8] J. Levatić, S. Džeroski, F. Supek, and T. Šmuc, “Semi-Supervised Learning for Quantitative Structure-Activity Modeling,” *Inform. Slov.*, pp. 173–179.

[9] Z. Bosnić and I. Kononenko, “Comparison of approaches for estimating reliability of individual regression predictions,” *Data Knowl. Eng.*, vol. 67, no. 3, pp. 504–516, Dec. 2008.

[10] G. Džimbeg, B. Zorc, M. Kralj, K. Ester, K. Pavelić, G. Andrei, R. Snoeck, J. Balzarini, E. De Clercq, and M. Mintas, “The novel primaquine derivatives of N-alkyl, cycloalkyl or aryl urea: Synthesis, cytostatic and antiviral activity evaluations,” *Eur. J. Med. Chem.*, vol. 43, no. 6, pp. 1180–1187, Jun. 2008.

[11] M. Šimunović, I. Perković, B. Zorc, K. Ester, M. Kralj, D. Hadjipavlou-Litina, and E. Pontiki, “Urea and carbamate derivatives of primaquine: Synthesis, cytostatic and antioxidant activities,” *Bioorg. Med. Chem.*, vol. 17, no. 15, pp. 5605–5613, Aug. 2009.

[12] Z. Rajić, M. Končić, K. Miloloža, I. Perković, I. Butula, F. Bucar, and B. Zorc, “Primaquine-NSAID twin drugs: Synthesis, radical scavenging, antioxidant and Fe2+ chelating activity,” *Acta Pharm.*, vol. 60, no. 3, pp. 325–337, Sep. 2010.

[13] K. Pavić, I. Perković, M. Cindrić, M. Pranjić, I. Martin-Kleiner, M. Kralj, D. Schols, D. Hadjipavlou-Litina, A.-M. Katsori, and B. Zorc, “Novel semicarbazides and ureas of primaquine with bulky aryl or hydroxyalkyl substituents: Synthesis, cytostatic and antioxidative activity,” *Eur. J. Med. Chem.*, vol. 86, pp. 502–514, Oct. 2014.

[14] I. Perković, S. Tršinar, J. Žanetić, M. Kralj, I. Martin-Kleiner, J. Balzarini, D. Hadjipavlou-Litina, A. M. Katsori, and B. Zorc, “Novel 1-acyl-4-substituted semicarbazide derivatives of primaquine − synthesis, cytostatic, antiviral and antioxidative studies,” *J. Enzyme Inhib. Med. Chem.*, vol. 28, no. 3, pp. 601–610, Mar. 2012.

[15] C. Steinbeck, Y. Han, S. Kuhn, O. Horlacher, E. Luttmann, and E. Willighagen, “The Chemistry Development Kit (CDK): An Open-Source Java Library for Chemo- and Bioinformatics,” *J. Chem. Inf. Comput. Sci.*, vol. 43, no. 2, pp. 493–500, 2003.

[16] A. P. Bento, A. Gaulton, A. Hersey, L. J. Bellis, J. Chambers, M. Davies, F. A. Krüger, Y. Light, L. Mak, S. McGlinchey, M. Nowotka, G. Papadatos, R. Santos, and J. P. Overington, “The ChEMBL bioactivity database: an update,” *Nucleic Acids Res.*, vol. 42, no. D1, pp. D1083–D1090, Jan. 2014.

[17] N. Nikolova and J. Jaworska, “Approaches to Measure Chemical Similarity – a Review,” *QSAR Comb. Sci.*, vol. 22, no. 9–10, pp. 1006–1026, Dec. 2003.

[18] L. Breiman, “Random forests,” *Mach. Learn.*, vol. 45, no. 1, pp. 5–32, 2001.

For wider interest

Pharmaceutical industry spends huge amounts of money on research and development of new drugs. The U.S. pharmaceutical industry's advocacy group, PhRMA, estimated the cost of $1.3 billion to bring a new drug to market. This cost is to a large extend related to failures: Only a small fraction of promising drugs will ever progress to clinical trials due to the undesired chemical properties. Thus, it will be useful to predict these failures in order to reduce the cost of drug development.

Data mining methods are commonly used to build models which can predict the properties of chemical compounds and filter out potential failures. Such models are called quantitative structure-activity relationship (QSAR) models, since they attempt to relate the structural features of a compound to its biological or physicochemical activity. Their main value is that they provide insight into the activity of a molecule without the need to synthesize it.

The development of QSAR model requires a collection of data for the property of interest, i.e., training dataset which is used by data mining methods to build a model. Predictive ability of QSAR models is largely dependent on the size and quality of the training dataset. However, since the property of interest needs to be measured for each of the chemical compounds in the training dataset, their number is often fairly small, presenting a limiting factor for the QSAR models.

To overcome this limit, so called *semi-supervised* data mining techniques can be used. These techniques use, in addition to the training dataset, also the data for which the property of interest is unknown (i.e., unlabeled data). The goal is to improve predictive accuracy over traditional methods which use labeled data alone.

In this work, we explore the possibility of improving accuracy of QSAR models by extracting unlabelled data from public databases of chemical compounds. We develop QSAR models for predicting 12 different properties of (potential) medications for treatment and prophylaxis of malaria (i.e., primaquines). Our results show that accuracy of the QSAR model is improved by the use of unlabeled data extracted from the ChEBML database, suggesting that public databases of compounds can be used to improve traditional QSAR models - at no additional cost.

Nanoznanosti in nanotehnologije (Nanosciences and Nanotechnologies)

Comprehensive transformation of alcohols catalysed by new type of metal-free and acid-free catalysts under solvent-free reaction conditions

Njomza Ajvazi[1] **and Stojan Stavber**[2,3]
[1] Jožef Stefan International Postgraduate School, Ljubljana, Slovenia
[2] Department of Organic and Bioorganic Chemistry, Jožef Stefan Institute, Ljubljana, Slovenia
[3] Centre of excellence for integrated approaches in chemistry and biology of proteins
`njomzaajvazi@hotmail.com`

Abstract. We introduce a new type of metal-free and acid-free catalysts for comprehensive transformation of various types of alcohols with different nucleophile sources under high substrate concentration reaction conditions (HCRC) or solvent-free reaction conditions (SFRC). In the absence of nucleophile, dimerization occurred, in the presence of methanol, etherification took place, while in the case of electro-rich alkenes, aryls or β-dicarbonyl compounds, new C-C bond were formed, and in the presence of acetonitrile or anilines, C-N bond were formed. When trimethyl substituted silanes were used, as sources of nucleophiles, halogenation, etherification or isothiocyanation took place, while in some cases silylation was observed.

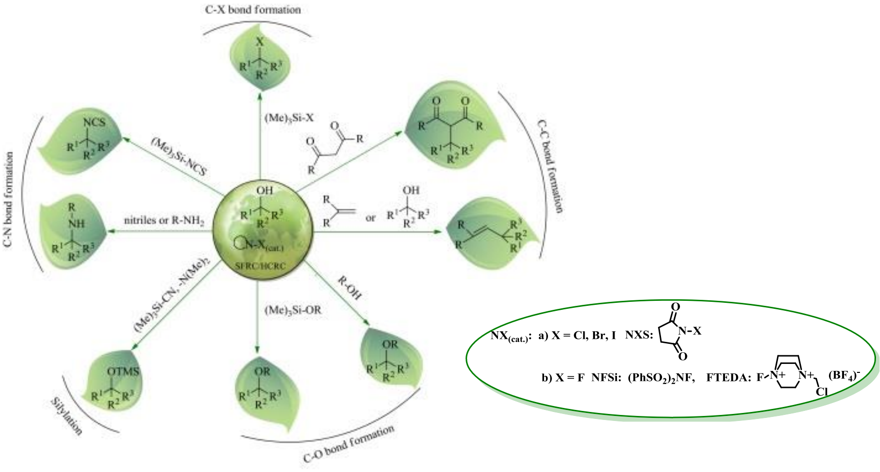

Keywords: green chemistry, *N*-halo compounds, alcohols, solvent-free.

1 Introduction

Development of protocols for the transformation of organic compounds under more environmentally acceptable conditions and achievement of high atom economy, selectivity and yields at the same time is one of the main trends in organic synthesis nowadays. From this point of view, planning organic reactions and processes following the principles of green chemistry is one of the major challenges in organic chemistry [1]. Organic reactions in water or under solvent-free reaction conditions (SFRC) mainly fulfill these principles.

Since alcohols are versatile compounds, their direct transformation under green reaction conditions would be important process to provide useful building blocks in organic synthesis. In order to manipulate particular transformation of the hydroxyl moiety, its activation is usually necessary.

Numerous related methodologies have been elaborated using catalytic amount of molecular iodine [2], metals such as indium [3], bismuth [4], or iridium [5] and Bronsted acids such as *p*-toluensulfonic acid [6] or trifluoromethanesulfonic acid [7]. However, all these methods have some disadvantages, such as multiple step protocols, use of toxic and expensive reagents or environmental undesirable solvents, long reaction time and high temperature.

The aim of this work is to develop a new methodology for comprehensive direct transformation of various alcohols catalysed by new type of metal-free and acid-free catalysts, which are environmentally acceptable, selective and efficient, in order to obtain new C-C and C-heteroatom bond formation under SFRC or high substrate concentration reaction conditions (HCRC). We report the introduction of *N*-halo organic compounds as a new type of non-metal and non-acidic, and environmentally friendly catalysts for comprehensive transformation of alcohols selectively and efficiently under SFRC or HCRC.

2 Results and discussion

Initially, we chose diphenylmethanol (1) as the basic model substrate to check the efficiency of a catalyst from *N*-halo compounds family and find the best reaction conditions for alcohol transformation. We showed that transformation of diphenylmethanol (1) catalysed by *N*-halo compound in the presence of methyl alcohol under high concentration reaction conditions gave ether (3), while in its absence under solvent-free reaction conditions, dimerization took place (2, Scheme

1). Under both reaction conditions, but in the absence of a catalytic amount of *N*-halo compound, no transformation of diphenylmethanol was observed.

Scheme 1. Transformation of diphenylmethanol (1) catalysed by *N*-halo compound under SFRC.

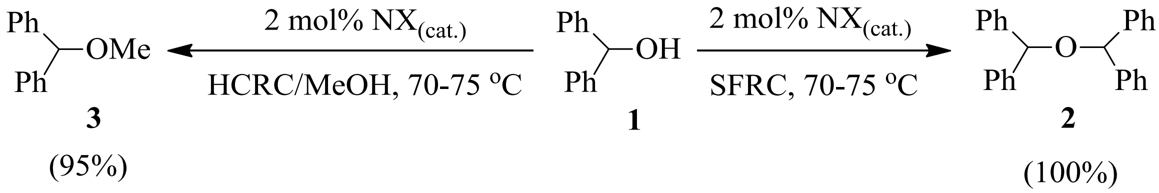

Inspired by this result, we further tested the role of *N*-halo compounds as catalysts by direct etherification of diphenylmethanol (1) with primary benzyl alcohols under solvent-free reaction conditions. Etherification of diphenylmethanol (1) with 4-chloro benzyl alcohol (4) was performed employing *N*-halo compound as a catalyst under solvent-free reaction conditions which leads to the ether (5) in up to 95% yield, accompanied with a small amount of oxidized alcohol and dimeric ether (Scheme 2).

Scheme 2. Etherification of diphenylmethanol (1) with primary benzyl alcohol catalysed by *N*-halocompound under SFRC.

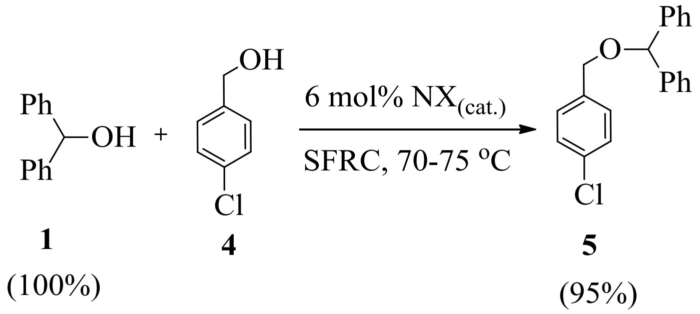

We further investigated reactions of primary benzyl alcohols with trimethylchlorosilane (TMSCl) and impact of *N*-halo catalyst in these transformations. Results are collected in Table 1. In the case of performing the reaction of benzyl alcohol (6a) without the presence of the catalyst, we observed moderate conversion of starting material (entries 1, Table 1). By adding *N*-halo catalyst, quantitative conversion of starting material into corresponding chloride (7a) was observed, while only a small amount of dimer was detected as the side product (8a). In the case of performing the reaction of 3-trifluoromethylbenzyl (6b) without the presence of the catalyst we did not observe any conversion of starting material (entries 3, Table 1). By adding *N*-halo catalyst, quantitative conversion of starting material into corresponding chloride (7b) accompanied by a small amount of dimer (8b) was achieved. The pathway of this reaction is thus connected with the stabilization of benzylic carbocation intermediates, which represents a basic characteristic of nucleophilic substitution transformation following the S_N1 reaction course. In order to verify this assumption, we chose 1-phenyl-1,2-ethanediol (9, Scheme 3) as the additional testing compound. We established the quantitative formation of 2-chloro-2-phenylmethanole (10) when (9) treated with TMSCl, with or without catalyst under SFRC, thus proving the S_N1 reaction pathway of the substitution.

Table 1. Chlorination of various primary benzyl alcohols (6) with TMSCl catalysed by *N*-halo compound under SFRC.

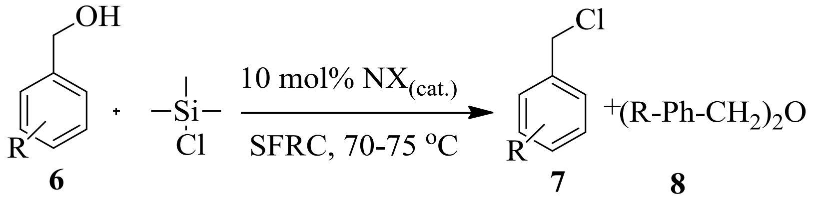

Entry	R	Conv.(%)^b of **6**	Relative	distribution(%)^b
			7	**8**
1^c	H **(7a)**	78	68	10
2	H **(7a)**	100	92	8
3^c	3-CF_3 **(7b)**	/	/	/
4	3-CF_3 **(7b)**	91	79	12

[a] Reaction conditions: Benzyl alcohol 6 (0.5 mmol), TMSCl (0.55 mmol).
[b] Determined from 1H NMR spectra of isolated crude reaction mixtures.
[c] In the absence of the catalyst

Scheme 3. Chlorination of 1-phenyl-1,2-ethanediol (9) with TMSCl under SFRC.

9 **10**

Based on transformations of alcohols with TMSCl we were curious to find out if it is possible to introduce other functional groups in the similar way, such as dimethylamine, ethoxy and isotiocyanate into organic molecules. We performed the reactions of diphenylmethanol (1) and phenyl(p-tolyl)methanol (12) as a model compound under the mentioned reaction conditions using *N,N*-Dimethyltrimethylsilylamine [TMSN(Me)$_2$], ethoxytrimethylsilane (TMSOEt), (Trimethylsilyl)isothiocyanate (TMSNCS) as the sources of nucleophiles. The courses of reactions were noticed to be quite different in the case of (TMSN(CH$_3$)$_2$), and the formation of trimethylsilyl ethers (11, Scheme 4) as the sole product was observed. In the case of (TMSOEt) and (TMSNCS), ethoxy or isotiocyanate were introduced into organic molecules (13a and 13b) (Scheme 5).

Scheme 4. Trimethylsilylation of diohenylmethanol (1) with TMSN(CH$_3$)$_2$ catalysed by *N*-halo organic compound under SFRC.

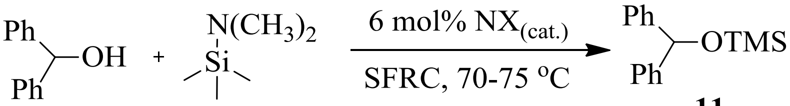

1 **11**

(100%)

Scheme 5. Isothiocyanation or ethoxylation of phenyl(p-tolyl)methanol (12) with (TMSOEt), (TMSNCS) catalysed by *N*-halo compound under SFRC.

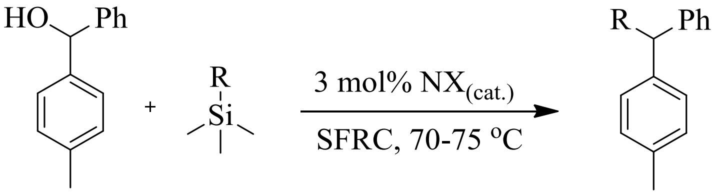

12 **a** R: NCS
b R: OEt

13a (100%)
13b (90%)

Furthermore, we investigated the role of *N*-halo organic compounds as catalysts for direct new C-C bond formation by coupling reactions of β-dicarbonyl compounds, electron-rich alkenes or tertiary benzyl alcohols bearing vicinal hydrogen atom, with secondary benzyl alcohol.

We have examined the reaction of diphenylmethanol (1) with benzoylacetone (14) under solvent-free reaction conditions. In the absence of catalyst, the reaction did not occur. However, in the presence of our original catalyst, the coupling of benzyl moiety with one of β-dicarbonyl took place, providing product (15) with the new C-C bond formed between benzyl carbon atom and C-2 carbon of di-carbonyl target (Scheme 6).

Scheme 6. Reactions of β-dicarbonyl compound (14) with diphenylmethanol (1) catalysed by *N*-halo compound under SFRC.

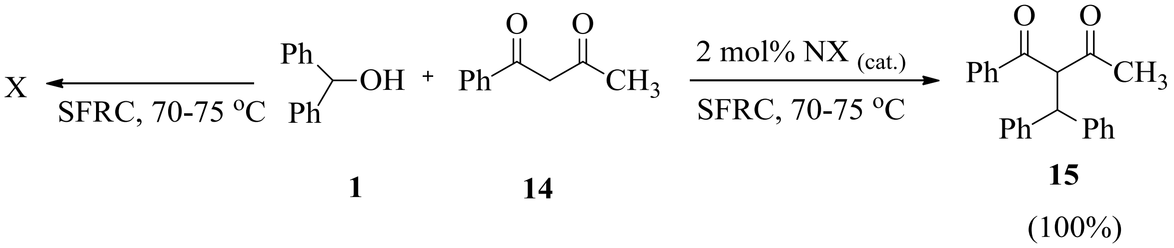

On the other hand, C-C bond formation could also be achieved by direct coupling of alcohols with electron-rich alkenes in the presence of *N*-halo organic compound as a catalyst under solvent-free reaction conditions. Initially, we chose 1,2 dihydronaphtene (16) and diphenylmethanol (1) as model compounds to find the best reaction conditions for this reaction. Coupling of 1,2 dihydronaphtene (16) with diphenylmethanol (1) catalysed by *N*-halo organic compound under solvent-free reaction conditions produced the corresponding substituted alkene (17) in up to 89% yield, accompanied with a small amount of dimeric ether (Scheme 7).

Scheme 7. Direct coupling of diphenylmethanol (1) with 1,2 dihydronaphtene (16) catalysed by *N*-halo compound under SFRC.

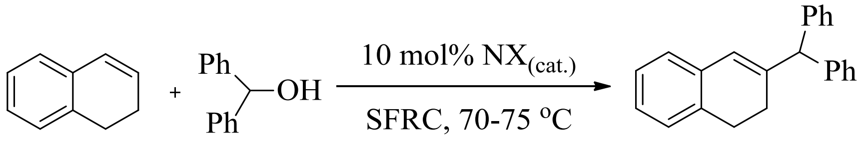

16 (100%)   **1**   **17** (89%)

The role of *N*-halo compound as a catalyst was observed also in reactions of alcohols with acetonitrile or anilines under high substrate concentration reaction conditions, where products with new C-N bond formation could be obtained. The example of this possibility was demonstrated by the reaction 1-(*p*-tolyl)ethan-1-ol (18), with acetonitrile, producing efficiently the corresponding N-alkylated compound (19) in good yield, accompanied with small amount of oxidized alcohol (Scheme 8).

Scheme 8. Direct coupling of 1-(*p*-tolyl)ethan-1-ol (18) with acetonitrile catalysed by *N*-halo compound under HCRC.

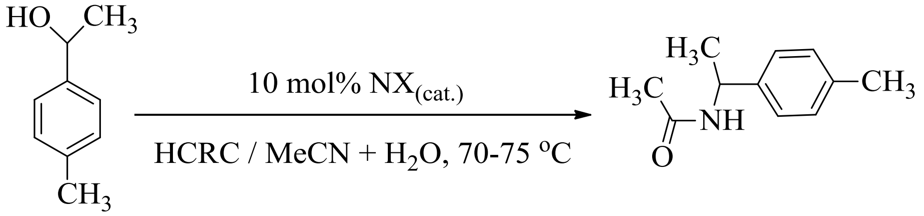

18 (84%)   **19** (80%)

3 Conclusions

We have introduced *N*-halo organic compounds as a new group of non-metal and non-acidic and environmentally friendly catalysts for comprehensive transformation of hydroxyl functional group which are capable to mediate selectively and efficiently comprehensive type of their transformation under high substrate concentration reaction conditions or solvent-free reaction conditions. Novel, efficient and selective, metal-free method for direct transformation of alcohols to dimeric ethers were demonstrated employing *N*-halo compounds as catalysts under solvent-free reaction conditions, while under alkyl alcohol high concentration reaction conditions, alkyl aryl ethers were produced. Moreover, we have showed that the etherification could also be achieved by cross coupling of two different benzyl alcohols catalysed by *N*-halo compounds under solvent-free reaction conditions. This new type of catalysts were also found as convenient catalysts for direct conversion of benzyl alcohols to corresponding chlorides, ethers and isothiocyanate by nucleophilic substitution of hydroxyl group using trimethyl substituted silanes as sources of nucleophiles. Reactions performed under solvent-free reaction conditions gave high to quantitative yield of products, while under similar reaction conditions using *N,N*-dimethyltrimethylsilylamine. trimethylsilylation of the hydroxyl group in target molecules was produced. Furthermore, we have successfully developed a general, simple and efficient methodology for the direct C-2 benzylation of β-dicarbonyl compounds with various benzyl alcohols using *N*-halo compound as a catalyst under solvent-free reaction conditions. We demonstrated an efficient *N*-halo compound-catalysed direct coupling of alkenes with benzyl alcohols and cross-coupling of benzyl alcohols with tertiary alcohols bearing vicinal hydrogen atom to give the corresponding substituted alkenes under solvent-free reaction conditions. Finally, we have developed convenient C-N bond formation reactions of alcohols with anilines or acetonitrile under solvent-free reaction conditions or high substrate concentration reaction conditions catalysed by *N*-halo compound with a good yield. From the green chemical point of view, the presented methodology is the new, highly efficient and easy to perform approach to the synthesis of comprehensive new type of derivatives starting from hydroxyl functional group targets and applying solvent-free reaction conditions or high substrate concentration reaction conditions.

References:

[1] P. T. Anastas and J. C. Warner, *Green Chemistry: Theory and Practice*, Oxford University Press, 1998.

[2] M. Jereb, D. Vražič, M. Zupan, *Tetrahedron,* 67, 1355-1387, 2011

[3] M. Yasuda, S. Yamasaki, Y. Onishi, A. Baba, *Journal of the American Chemical Society,* 126, 7186-7187, 2004

[4] E. Callens, A. J. Burton, A. G. M. Barrett, *Tetrahedron Letters,* 47, 8699-8701, 2006

[5] B. Blank, M. Madalska, R. Kempe, *Advanced Synthesis & Catalysis,* 350, 749-758, 2008

[6] R. Sanz, D. Miguel, A. Martínez, J. M. Álvarez-Gutiérrez, F. Rodríguez, *Organic Letters,* 9, 727-730, 2007

[7] H.-L. Yue, W. Wei, M.-M. Li, Y.-R. Yang, J.-X. Ji, *Advanced Synthesis & Catlaysis,* 353, 3139-3145, 2011

For wider interest

Aim of this work was to develop a new methodology for direct conversion of various types of alcohols catalysed by *N*-halo compounds (as a new group of metal-free and acid-free catalysts, environmentally acceptable, selective and efficient) with different nucleophile sources in order to obtain new C-C and C-heteroatom bond formation under reaction conditions which follow as much as possible the principles of green chemistry. In the absence of a nucleophile, dimerization occurred; in the presence of O-nucleophiles, we got new C-O bond formation; in the presence of electro-rich alkenes, aryls or β- dicarbonyl compounds, we got new C-C bond formation; while in the presence of amines, nitriles or (trimethylsilyl)isothiocyanate, we got new C-N bond formation; and in the presence of halosilanes, we got new C-halogen bond formation.

New methodology could have considerable effect to pharmaceutical industry in the area of new, easier and greener approach to synthesis of active pharmaceutical ingredients (API).

Invention and development of new related methods which possess considerably improved green chemical profile is ultimate challenge in modern organic chemistry.

Magnetic properties of nanoplatelet composite nanoparticles composed of hard-magnetic hexaferrite and soft-magnetic maghemite

Blaž Belec [1, 2], **Darko Makovec** [1, 2]
[1] Department of Material synthesis, Jožef Stefan Institute, Jamova cesta 39, Ljubljana, Slovenia
[2] Jožef Stefan International Postgraduate School, Jamova cesta 39, 1000 Ljubljana, Slovenia
blaz.belec@ijs.si

Abstract: Magnetic properties of bi-magnetic sandwich-like composite nanoparticles, composed of a hard-magnetic barium hexaferrite ($BaFe_{12}O_{19}$) platelet core positioned in between two soft-magnetic spinel iron-oxide (maghemite, γ-Fe_2O_3) layers, will be presented. The composite nanoparticles were prepared with simple method based on co-precipitation of Fe^{3+}/Fe^{2+} ions in colloidal suspension of the core nanoparticles. The spinel formed exclusively as the layers at the core nanoparticles. The magnetic properties of the composite nanoparticles were measured using vibrating sample magnetometer perpendicular and parallel to their preferential magnetic orientation. For this purpose, the nanoparticles were hydrophobized with dodecylbenzene sulphonic acid (DBSa), dispersed in a hot liquid wax and magnetically oriented in a homogeneous magnetic field of 1T. The composite nanoparticles exhibit single-phase magnetic hysteresis, suggesting that the two phases are exchange coupled. The difference between in-plane and out-of-plane magnetic hysteresis showed some degree of magnetic orientation of the nanoparticles. The comparison between in-plane magnetic hysteresis of the core and the composite nanoparticles showed a large increase in saturation magnetization (M_S) and remanence (M_R), and decrease in coercivity (H_C) for the composite nanoparticles.

Keywords: Composite nanoparticles, bi-magnetic nanoparticles, ferrites, magnetic properties

1 Introduction

Nanoparticles are defined as particles with at least one of their dimension in the nanometre range (1 – 100 nm). The most important characteristic of nanoparticles is their large surface-to-volume ratio, resulting in a high proportion of the surface atoms [1]. Magnetic nanoparticles have potential in a wide range of technological applications (e.g., in ferrofluids [2], storage and recording media [3], separation, catalysis [4], etc.), in medical diagnostics (in magnetic particle imaging (*MPI*) and magnetic resonance imaging (*MRI*)) and in therapy (drug delivery [5] and cancer treatment with hyperthermia [6]).

Composite nanoparticles are nanomaterials that combine at least two different materials in the one nanoparticle. Compared to single-component nanoparticles, the composite nanoparticles have a large potential to exhibit novel chemical and physical properties that originate from interactions between the different materials [7]. Of particular interest are the composite nanoparticles, where properties of different materials are coupled.

The composite nanoparticles that combine two magnetically different materials are referred to as bi-magnetic nanoparticles. The interaction between the different magnetic phases can result in exchange interactions. The exchange interactions are interactions that occur between electron spins of different magnetic materials at their interfaces. With combination of ferromagnetic and antiferromagnetic phases, the exchange interaction can result as an extra source of anisotropy, which increase the superparamagnetic limit – an important property limiting the miniaturization of recording and storage media [3]. Even more important property of magnetic materials is energy product, $|BH|_{max}$, a figure of merit for the quality of magnets. It depends on the area of the magnetization curve, thus for large $|BH|_{max}$, material with high saturation magnetization (M_S) and high coercivety (H_C) is required. With exchange spring coupling between soft-magnetic and hard-magnetic phases that are combined at nanolevel, $|BH|_{max}$ can be strongly increased [8, 9]. However, for the effective exchange coupling the thickness of the soft phase should not exceed the half of the domain wall width of the hard phase. Such bi-magnetic nanoparticles are ideal building blocks for the preparation of exchange-spring magnets with improved properties. The exchange spring effect can be also applied in engineering of properties of the nanoparticles for desirable applications [9, 10].

Magnetic nanoparticles with efficient conversion of the electromagnetic energy to heat can be potentially used as mediators in magnetic hyperthermia. Magnetic hyperthermia is therapeutic method for cancer treatment that is based on overheating cancer cells by excitation of magnetic nanoparticles internalized in tumour with an AC magnetic field. With a combination of the hard and the soft magnetic phases it is possible to tune the magnetic properties of the nanoparticles to maximize the specific loss power, which defines the conversion of electromagnetic energy into heat. In some cases, the specific loss power values of the composites can be even an order of magnitude larger than in conventional iron-oxide nanoparticles [11, 12].

Since it was found that exchange coupling is stronger in core/shell nanoparticles, than in other composite structures, where contact between different magnetic materials is smaller, majority of bi-magnetic nanoparticles have the core/shell structure [13].

Recently, Primc and Makovec [14] reported the simple method for synthesizing the bi-magnetic composite nanoparticles, composed of hard-magnetic Ba-hexaferrite ($BaFe_{12}O_4$) core nanoplatelet positioned in between two soft magnetic spinel iron-oxide (maghemite, γ-Fe2O_3) layers, forming a sandwich-like structure [14]. The maghemite shell was deposited onto the hexaferrite core nanoplatelets with co-precipitation of the Fe^{3+}/Fe^{2+} ions in an aqueous colloidal suspension of the core nanoparticles. Fe^{3+} precipitates as iron oxide hydroxide (FeOOH) already at pH of 2.8, whereas Fe^{2+} precipitates at pH of 6. If the FeOOH is in its γ-FeOOH structural modification (lepidocrocite) it will react with the precipitated Fe^{2+} ions to form the magnetic spinel. To enable exclusively heterogeneous nucleation, supersaturation of the precipitating species has to be closely controlled. Controlled release was enabled by immobilizing the Fe^{3+} ions in a nitrate complex with urea $[Fe((H_2N)_2C{=}O)_6(NO_3)_3]$ (later Fe-urea complex). The immobilization into the complex postpone the precipitation of Fe^{3+} ions to a higher pH values, thus enabling the simultaneous precipitation of the Fe^{3+}/Fe^{2+} ions. Different hexaferrite nanoplatelets were used as the cores, crucially defining the magnetic properties of the synthesized composite nanoparticles. Ultrafine hexaferrite nanoparticles, approximately 10 nm wide and 3 nm thick, displayed poor magnetic properties and as the result also the properties of the composite nanoparticles were too weak to be applicable. The full advantage of combing the two magnetically-different phases in the composite nanoparticles was only obtained when larger hexaferrite cores were used, over 100 nm wide and approximately 10 nm thick. Here, the magnetic energy product was strongly improved by direct magnetic coupling between the two magnetic materials. However, for some applications such composite nanoparticles were too large. Later, Lisjak et al. [15] showed that the magnetic properties of the small hexaferrite nanoparticles can be strongly improved by applying dopants like In^{3+} or Sc^{3+}. In the present work, the small composite nanoparticles were synthesized by coating In-doped hexaferrite core nanoparticles, approximately 50 nm wide and 5 nm thick, with approximately 2 nm-thick maghemite layers. The nanoparticles showed applicable magnetic properties with saturation magnetization of 23 Am^2/kg.

The bi-magnetic, composite nanoparticles can be potentially used in a magnetic hyperthermia. For their applications, their magnetic properties have to be thoroughly analysed. In the case of plate-like nanoparticles, magnetic properties depend strongly on their orientation. To avoid the problem of unknown orientation, the nanoparticles have to be magnetically oriented prior to magnetic measurements. For the magnetic orientation, the nanoparticles are dispersed in a hot, liquid wax, exposed to a homogeneous magnetic field and cooled to solidify the wax maintaining the orientation provoked by the filed. For this purpose, the stable suspension of the nanoparticles in the liquid wax is required. The main problem during the preparation of stable suspensions of nanoparticles is to overcome the attracting forces between them, thus preventing their agglomeration. All nanoparticles tend to agglomerate due to the short-range van der Waals forces. Magnetic nanoparticles additionally agglomerate by the long-range magnetic dipole-dipole interactions. However, stable suspension of magnetic nanoparticles can be prepared when high enough electrostatic and/or stearic repulsions are provided between the particles by use of appropriate surfactants [16].

In this work, magnetic properties of the composite nanoparticles combining In-doped Ba-hexaferrite platelet core in between of the two maghemite layers were analysed.

2 Experimental

2.1 Materials

Iron (III) nitrate hepta hydrate ($Fe(NO_3)_3$ x $7(H_2O)$, iron (II) chloride ($FeCl_2$), magnesium hydroxide ($Mg(OH)_2$), urea, barium nitrate ($Ba(NO_3)_2$, indium nitrate ($In(NO_3)_3$), sodium hydroxide (NaOH, 98%), nitric acid (HNO_3), ammonia solution (NH_3, 25%), tertt-butanol, dodecylbenzen sulphonic acid (DBSa), tert-butanol and polyvinilpirolidone (PVP) were purchased from Alfa Aesar.

2.2 Synthesis of barium hexaferrite core nanoparticles

Core nanoparticles of In-doped barium hexaferrite (BH) with composition $BaFe_{11.5}In_{0.5}O_{19}$ were synthesized using hydrothermal method [15, 17]. In short, nitrates with the molar ration $n_{Ba} : (n_{Fe}+n_{In}) = 1:5$ were dissolved in water and co-precipitated with NaOH. The slurry was hydrothermally treated at 160 °C at rate of 3 °C/min and naturally cooled to a room temperature. The product was washed with water and nitric acid. For better colloidal stability of the core nanoparticles the PVP was added (C_{PVP} = 2 g/L). According to the ξ-potential measurements, suspension of the core nanoparticles was adjusted to a pH of 4 with ammonia solution.

2.3 Synthesis of the maghemite shell

The spinel iron oxide (maghemite) shell was synthesized using the co-precipitation of Fe^{3+}/Fe^{2+} in aqueous suspension of the core nanoparticles with weak hydroxide according to slightly modified procedure reported in Ref. [14]. Briefly, 80 mL of the stable aqueous suspension containing the core nanoparticles was heated to 60 °C under argon flow and mixed with glass stirrer. The amount of the core nanoparticles was determined according to their overall surface area of 5.45 m^2. The area was calculated in a way, that the determined concentration of Fe precursors would form a 3 nm thick shell. The Fe-urea complex (0.12 mmol) and $FeCl_2$ (0.06 mmol) were admixed in the heated suspension of the core nanoparticles. After the 10 minutes of thermal hydrolysis at 60 °C, the $Mg(OH)_2$ was added (0.024 mmol). After 2 hours on 60 °C and at final pH of 7.6, the reaction mixture was cooled to the room temperature and the product was washed several times with water.

2.4. Adsorption of the didecylbenzene sulphonic acid at the nanoparticles and preparation of the stable suspension

For magnetic orientation, the core and the composite nanoparticles should be magnetically oriented. For that the nanoparticles have to be suspended in hot liquid wax. To be compatible with the hydrophobic wax, the nanoparticles were hydrophobized with DBSa using the same procedure that was previously reported [18]. DBSa was added into a 50 mL aqueous suspension of the core nanoparticles in a mass ratio DBSa : nanoparticles = 2:1. The pH value of the suspension was adjusted to approximately 1.5 with 1 M HNO_3. The reaction mixture was stirred with a glass stirrer at the 100 °C for 2.5 h and cooled to a room temperature. Product was washed with acetone and re-dispersed in tert-butanol with an ultrasonic probe (Sonic Vibrocell 500W) at 300W, using a pulse (1 s on, 1 s off) for 5 minutes. The composite nanoparticles were hydrophobized with the same method, with some exceptions. As the maghemite layer may dissolve at low pH, the pH of the reaction mixture was maintained at pH ≈ 3.5 and the mixture was stirred at the boiling point of water for 30 minutes.

2.4.1. Magnetic orientation of the nanoparticles

After the hydrophobization, the suspension was washed three times with acetone to remove excessive DBSa and mixed with solidified wax. The mixture was heated to 80 °C, where the wax was melted and the tert-butanol evaporated. The suspension of the nanoparticles in the liquid wax was transferred into a small holder and magnetically oriented by exposure to the homogeneous magnetic field of 1T for 30 minutes. The field was produced by coils of a laboratory magnetic separator (Model L-1, Frantz Isodynamic). Finally, the wax was cooled to solidify and preserve the magnetic orientation of the nanoparticles.

2.5. Characterization of the materials

The nanoparticles were characterized using transmission electron microscopy (TEM) in combination with energy dispersive X-ray spectroscopy (EDXS). For the TEM analysis, the nanoparticles were deposited on a copper-grid-supported perforated electron-transparent carbon foil. The hydrodynamic diameter of the composite nanoparticles with adsorbed DBSa was measured with the dynamic light-scattering method (DLS) (Fritshc, ANALYSETTE 12 Dynasizer). The ζ-potential of the nanoparticles in their aqueous suspension was measured using Brookhaven Instrument (Corp. ZetaPALS). Magnetic properties of the nanoparticles were measured at room temperature using a Lake Shore 7312 vibrating-sample magnetometer (VSM). Magnetic properties of the oriented nanoparticles were measured parallel and perpendicular to their preferential magnetic orientation. For comparison the non-oriented powders were also measured.

For comparison with the oriented composite nanoparticles, the non-oriented powders of the hexaferrite core nanoparticles, the maghemite nanoparticles, and their physical mixture were measured. The globular maghemite nanoparticles, approximately 25 nm in size, had a comparable volume to the soft magnetic layer at the hexaferrite core of the composite nanoparticles, and thus presumably comparable magnetic properties. The hydrophobized core nanoparticles and the maghemite nanoparticles were mixed in the weight ration 50 wt.% hexaferrite / 50 wt.% maghemite corresponding to the estimated composite composition. To diminish inter-particle interactions between the nanoparticles, they were homogeneously mixed with a nonmagnetic boron nitride powder in the weight ration 10 wt.% magnetic nanoparticles / 90 wt.% BN.

3. Results and discussion

3.4. Core nanoparticles

Figure 1a represents TEM image of barium hexaferrite core nanoparticles. The TEM image reveals the plate-like nanoparticles, from 20 to 70 nm wide and approximately 5 nm thick. Figure 1b represents a high-resolution TEM (HREM) image of the hexaferrite nanoparticle, oriented edged-on with its basal surfaces parallel to the electron beam. The largest periodicity of 1.15 nm corresponds to the $(0002)_{HF}$ planes of the hexaferrite structure.

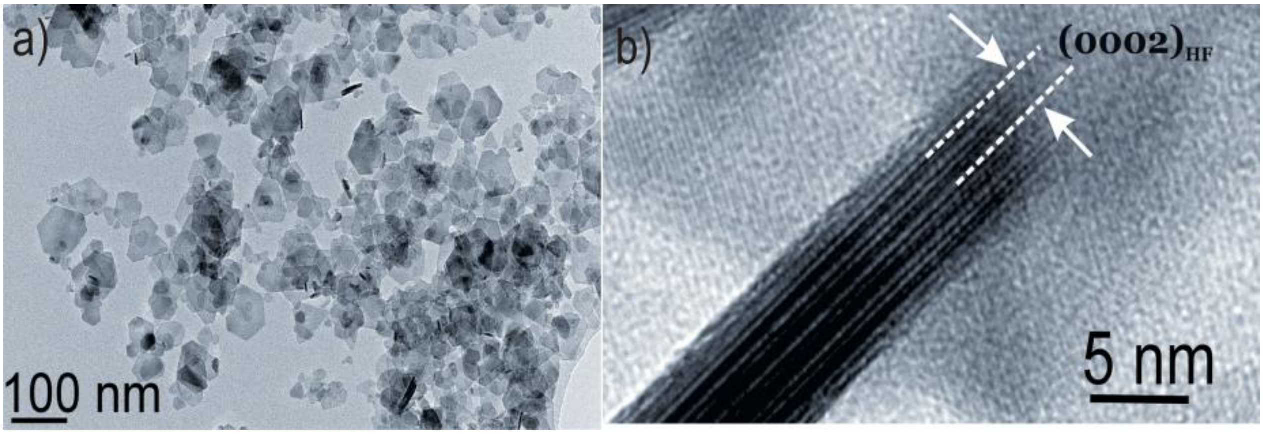

Figure 1: (a) Representative TEM image of the core nanoparticles and (b) the HREM image of the hexaferrite nanoparticle oriented edged-on with its large surface parallel to the electron beam.

3.5. Composite nanoparticles

Figure 2a shows representative TEM image of the composite nanoparticles revealing their platelet morphology. The spinel layer is not easily observed since the vast majority of the platelet nanoparticles lay flat on the specimen support. The structure of the composite nanoparticles can be observed only when they are oriented with its large surfaces parallel to the electron beam (Figure 2b). The 2-nm thick maghemite layer was deposited exclusively on the basal planes of the hexaferrite nanoparticles forming sandwich-like structure. The maghemite grow topotactically on the both basal surfaces of the hexaferrite core nanoparticles with the (111) planes of its cubic spinel structure parallel to the $(0001)_{HF}$ basal planes of the hexaferrite. The separate, homogeneously-nucleated nanoparticles were never observed. Due to the structural similarities, maghemite forms a coherent interface with the hexaferrite core. The maghemite was never observed at the side surfaces of the hexaferrite core nanoparticles, where there is no matching between the two structures [14].

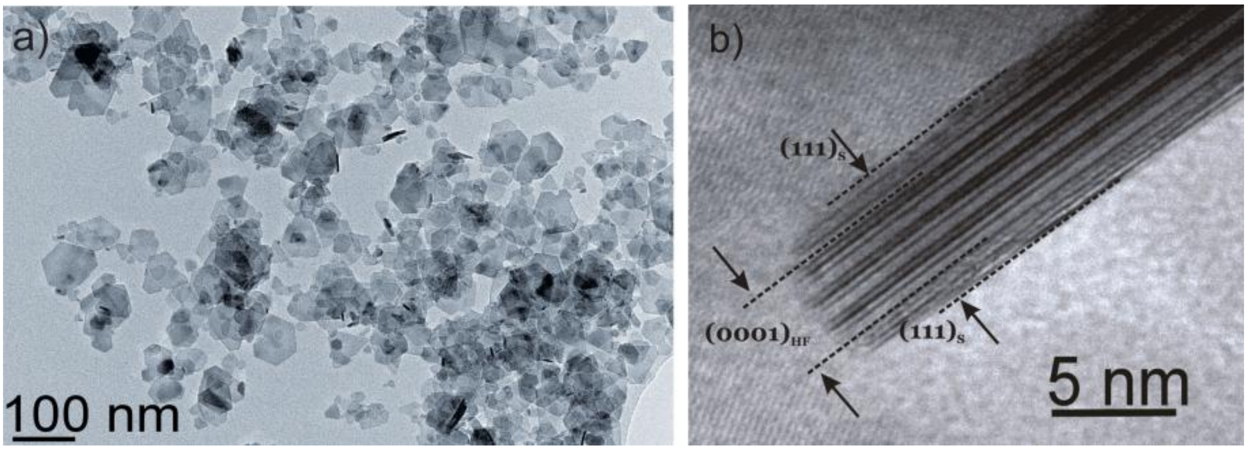

Figure 2: Representative TEM (a) and HREM (b) images of the composite nanoparticles. The nanoparticle in (b) is oriented edged-on with its large surfaces parallel to the electron beam (S ... spinel and HF ... hexaferrite).

3.6. Preparation of stable suspension of the nanoparticles

Stable suspension of the nanoparticles was prepared with adsorption of DBSa onto their surfaces. DBSa, with the chemical formula $HO_3S\text{-}C_6H_6\text{-}C_{12}H_{25}$, has a polar sulphonic group (HO_3S-) and a long, non-polar tail ($-C_{12}H_{25}$) and dissociates via sulphonic groups ($-SO_3^-$) at pH>1. The adsorption of DBSa was performed in an acidic media at the elevated temperature. According to the ξ-potential measurements (Figure3a) the nanoparticles have a large positive surface charge at acidic conditions, which enables the adsorption of the DBSa layer via negatively-charged sulphonic group ($-SO_3^-$) onto the surfaces of the nanoparticle. The DBSa molecules orient with the polar sulphonic group toward the particle's surface, while at the same time the non-polar surfactant tail is oriented into the medium [16]. As the nanoparticles form the stable suspension in water, the adsorbed DBSa obviously forms a bi-layer at their surfaces. If the DBSa would be adsorbed in the monolayer, the nanoparticles should be hydrophobic and would immediately agglomerate. Formation of the bi-layer can also be confirmed with ξ-potential measurements. The composite nanoparticles in the aqueous suspension exhibited large negative ξ-potential over the broad pH region due to the orientation of the ionized ($-SO_3^-$) groups of the second layer toward the aqueous medium (Figure 3a).

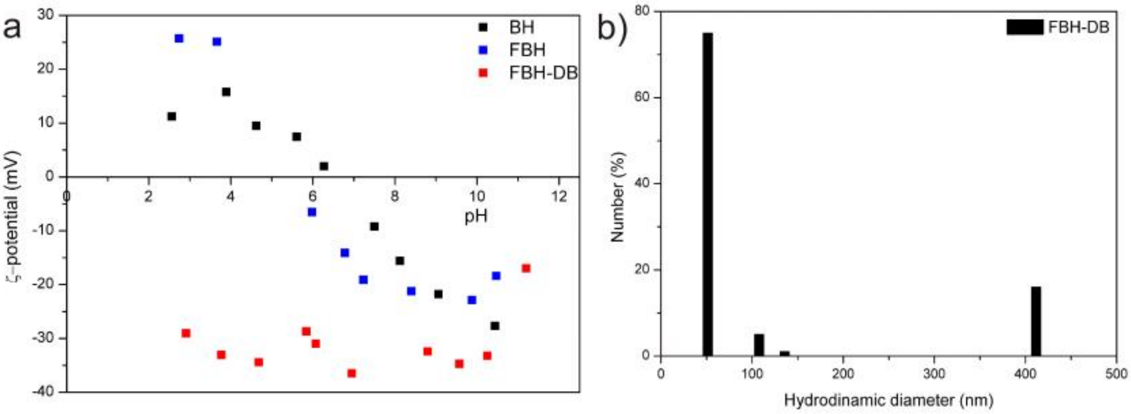

Figure 3: a) ξ-potential measurements of the nanoparticle in aqueous suspension and b) hydrodinamic diameter of the composite nanoparticles in tert-butanol (BH … barium hexaferrite core nanoparticles, FBH … composite nanoparticles, FBH-DB … composite nanoparticles with adsorbed DBSa).

After adsorption in the aqueous suspension, the excess of DBSa in the suspension was washed with acetone. The washed nanoparticles were re-dispersed in tert-butanol where the stable suspension was formed. The hydrodynamic diameter of the composite nanoparticles with the adsorbed DBSa was measured using DLS (Figure 3b). The suspension of the composite nanoparticles displayed bimodal size distribution (Figure 4b). According to the TEM, the composite nanoparticles were between 20 to 70 nm wide. We assume, that the smaller composite nanoparticles (below 40 nm) have hydrodynamic diameter between 50 - 100 nm, while the largest nanoparticles (above 40 nm) form agglomerates with hydrodynamic diameter around 400 nm.

The stable suspension of the nanoparticles was then mixed with wax heated at 80 °C, where tert-butanol was evaporated. The nanoparticles dispersed in a liquid wax were magnetically-oriented by cooling and solidifying the wax in a homogeneous magnetic field preserving the magnetic orientation of the nanoparticles.

3.7. Magnetic properties

First, the dried core and the composite nanoparticles (not oriented) were measured. A comparison between the magnetic hystereses of the core and the composite nanoparticles (Figure 4a and b) showed increased saturation magnetization (M_S) and remanence (M_R), and slightly decreased coercivity (H_C) for the composite nanoparticles, due to the presence of the soft-magnetic maghemite. Although the composite nanoparticle is the combination of the two magnetically-different phases, it displayed a single-phase magnetic hysteresis, suggesting that the two phases are exchanged coupled [10].

To demonstrate the degree of the magnetic coupling between the two magnetic materials, the physical mixture of the core and the maghemite nanoparticles was also measured (Figure 4c and d). The two types of the nanoparticles were mixed in a weight ratio 50 wt.% hexaferrite / 50 wt.% maghemite, corresponding to the estimated composition of the composite. Fig. 4 c and d comperes the hysteresis of the composite nanoparticles with the hystereses of the hexaferrite core nanoparticles, the maghemite nanoparticles, and the physical mixture. To minimize the inter-particle interactions, the nanoparticles were homogeneously mixed with non-magnetic BN prior to the measurement.

The comparison between the hysteresis of the composite nanoparticles and the mixture showed decrease in H_C and M_R for the mixture. However, also the mixture displays a single-phase hysteresis loop, suggesting the interaction between the two magnetic materials. According to a theory, the hysteresis loop has to be constricted if the magnetically-hard and soft phases in the mixture are not magnetically coupled [10]. In the case of non-coupled mixture the hysteresis of the mixture equals the arithmetic sum of the hystereses for the both phases. In Figure 5, the measured hysteresis of the mixture is compared to the corresponding sum of the hystereses for the hexaferrite nanoparticles and the maghemite nanoparticles. The calculated hysteresis is slightly constricted (slightly narrower at $M = 0$), however, the constriction, typical for the hysteresis of the soft-hard mixture, is hardly visible. The measured hysteresis is significantly broader to the calculated, with larger M_R and H_C. The difference most probably arises from magnetic dipole-dipole interactions between the two magnetic materials. Even though the nanoparticles of each type were mixed with nonmagnetic BN and only then to each other, the magnetization of the soft-magnetic maghemite is influenced by the internal field of the hard-magnetic hexaferrite. At the saturated state, the magnetic moments of separated hard and soft magnetic phase in the mixture are pined in the same direction. However, the difference between the measured and the calculated hystereses of the mixture can also partially arise from the different orientation of the platelet nanoparticles in the hexaferrite powder and in the mixture.

Although the measured hysteresis of the mixture is most probably influenced by the magnetic dipole-dipole interactions, it is significantly different to the hysteresis of the composite nanoparticles (Figure 4 c and d). When the magnetic field is reduced, the hysteresis of the mixture starts to drop quicker than a hysteresis of the composite nanoparticles. The magnetic moments of the soft phase in the mixture starts to rotate quicker, since they are not in direct contact with the hard magnetic phase, thus they are not directly pined by the magnetic moments of the hard magnetic phase. This result in a partial relaxation of the magnetic moments of the soft-magnetic phase and decreased M_R compared to the composite nanoparticles.

The difference between the hystereses of the composite and the mixture indicates different magnetic interactions acting between the two magnetically different phases.

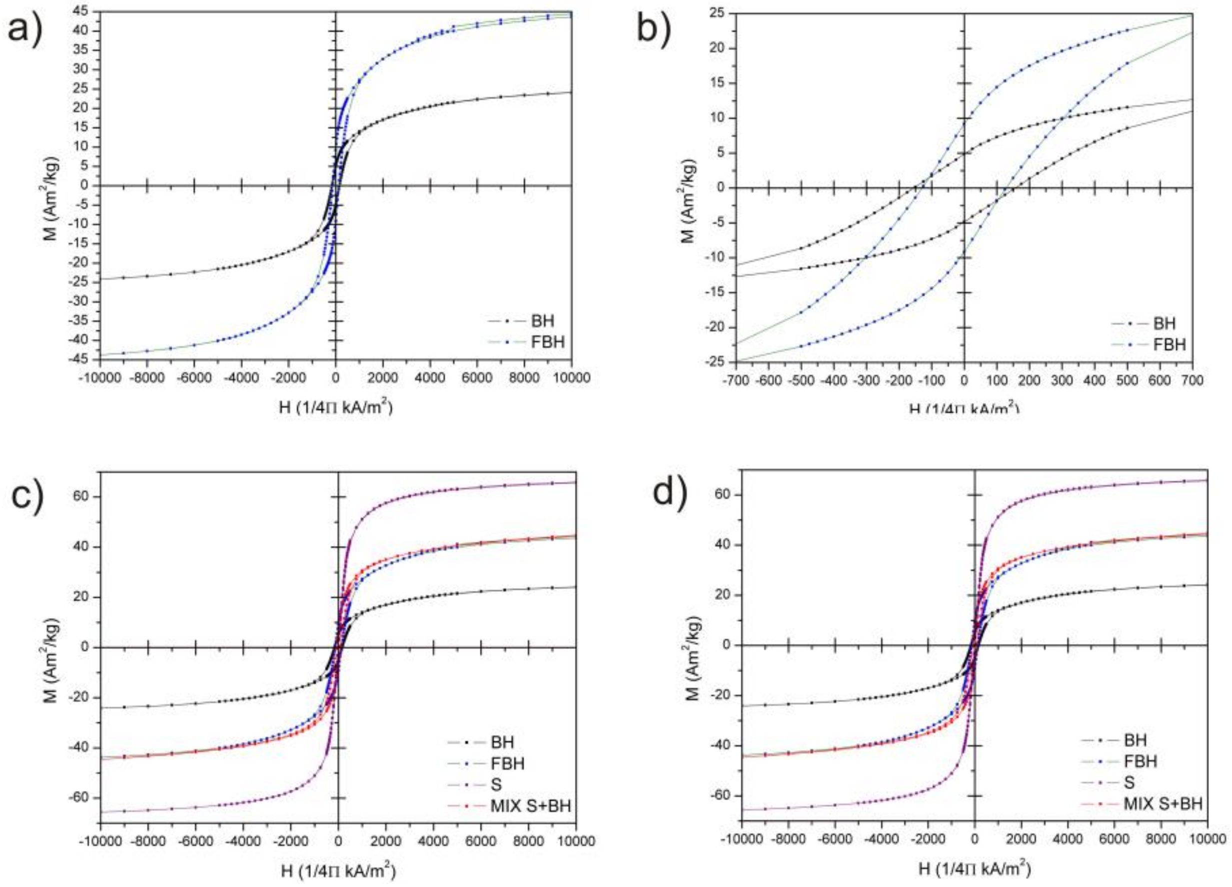

Figure 4: Comparison of the magnetic hysteresis for hexaferrite core nanoparticles (BH) and composite nanoparticles (FBH) ((a) and (b)), and for hexaferrite core nanoparticles (BH), maghemite nanoparticles (S), composite nanoparticles (FBH) and a physical mixture of the two magnetically-different phases (MIX S+HF) (c and d).

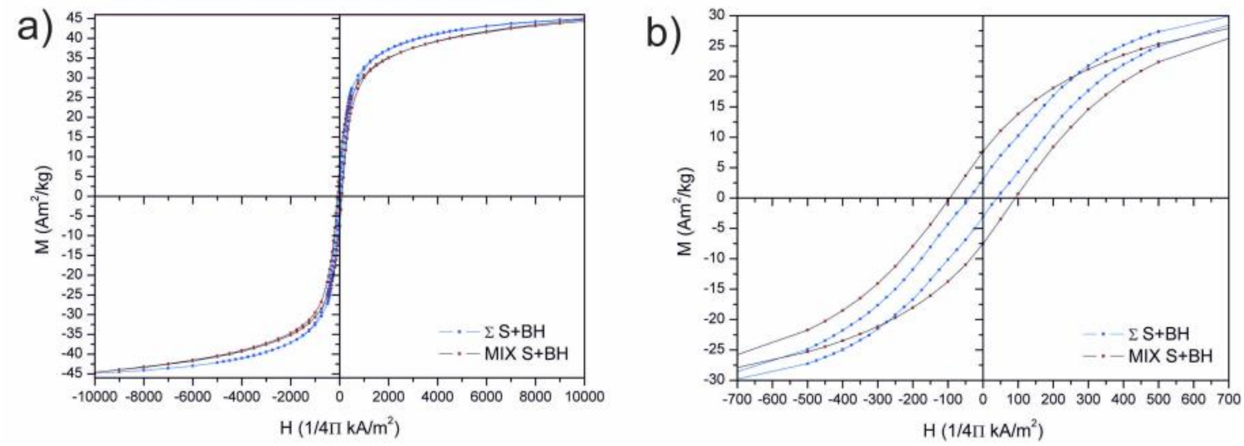

Figure 5: Comparison between the measured and calculated hysteresis of the physical mixture of the BH core and S nanoparticles (Σ S+BH … calculated and MIX S +BH ….. measured hysteresis).

The platelet hexaferrite nanoparticles display easy axes normal to the plate. Their magnetic properties thus strongly depend on their orientation in the powder. Due to their highly anisotropic shape, the nanoparticles tend to spontaneously orient. To avoid the problem of unknown orientation, the platelet nanoparticles should be measured after they ware magnetically orientated. We tried to orient the core and the composite nanoparticles by suspending them in liquid wax and cooling the suspension in a magnetic field. The magnetic measurements were performed perpendicular (in-plane) and parallel (out-of-plane) to their preferential magnetic orientation. Figure 6 represent magnetic hysteresis of the oriented hexaferrite core nanoparticles (Figure 6b and d) and the composite nanoparticles (Figure 6a and b). In both cases, the difference between the in-plane and the out-of the plane hystereses suggested some degree of magnetic orientation, however, the difference seems to be too low for the complete orientation.

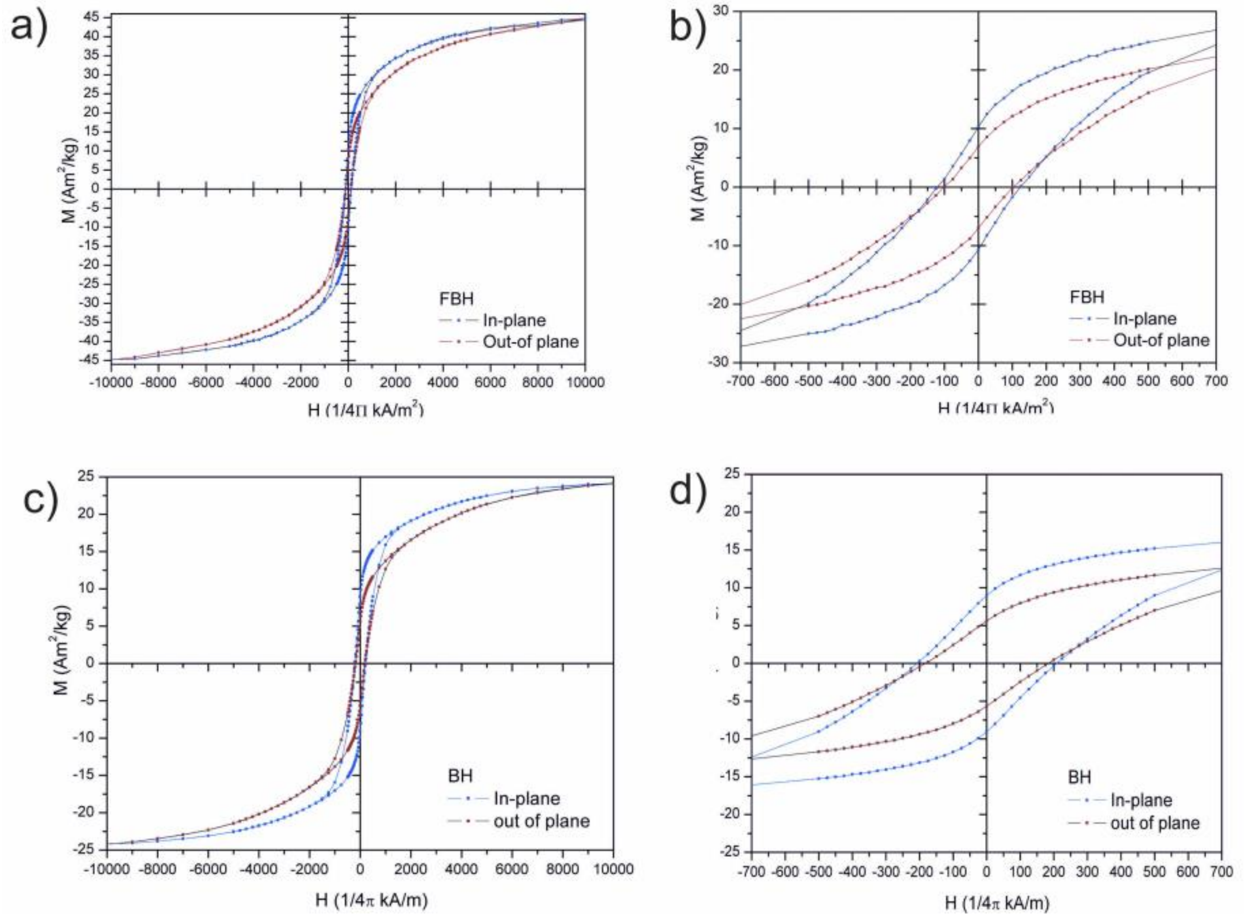

Figure 6: Comparison between the magnetic hysteresis of the in-plane and out-of-plane hysteresis: (c and d) BH core nanoparticles and the ((a) and (b)) FBH composite nanoparticles.

The comparison between the in-plane magnetic hystereses of the core and the composite nanoparticles shows the difference in the shape of the hysteresis (Figure 7a and b) with increased M_S and M_R and slightly decreased H_C for the composite nanoparticle. Although the magnetic orientation seems not to be complete, the measurements additionally support the direct magnetic coupling between the two magnetically-different phases.

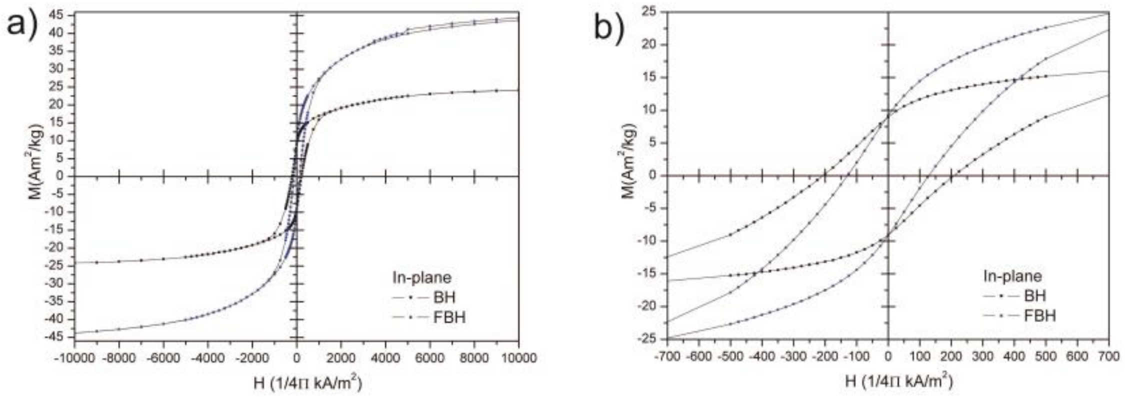

Figure 7: Comparison of the in-plane magnetic hysteresis: ((a) and (b)) BH core nanoparticles and FBH composite nanoparticles.

4. Conclusion

Magnetic properties of bi-magnetic sandwich-like composite nanoparticles composed of a hard-magnetic barium hexaferrite ($BaFe_{12}O_{19}$) core positioned in between two soft-magnetic spinel ferrite iron oxide (γ-Fe_2O_3) layers were presented. The magnetic properties were measured using vibrating sample magnetometer. A comparison between the hystereses of the core and the composite nanoparticles showed increase in saturation magnetization (M_S) and remanence (M_R), and slightly decrease in coercivity (H_C) for the composite, due to the presence of the soft magnetic phase. The composite nanoparticles exhibit single-phase magnetic hysteresis, suggesting that the two magnetically different phases are exchanged coupled. The hysteresis of the composite nanoparticles was compared with the hysteresis of the physical mixture of the hexaferrite core and maghemite nanoparticles. The comparison showed, lower H_C and M_R for the mixture, suggesting direct exchange coupling in the composite nanoparticles. As the magnetic properties of the platelet nanoparticles strongly depend on their orientation we tried to orient them in magnetic field. For this purpose, the nanoparticles were hydrophobised with dodecylbenzen sulphonic acid (DBSa), dispersed in a hot, liquid wax and oriented by cooling and solidification of the wax under homogeneous magnetic field. The difference between in-plane and out-of plane magnetic hysteresis revealed limited magnetic orientation of the samples.

References:

[1] Chaudhuri, R.G. and S. Paria; Core/Shell nanoparticles: Classes, properties, synthesis mechanisms, characterization and applications. *Chem. Rev.* **112**: p. 2373-2433 (2012).

[2] Blums, A., M. Ceberes, and M. Mairov, *Magnetic Fluids* (Walter de Gruyter & Co., Berlin, 1996).

[3] Skumryev, V., et al.; Beating the superparamagnetic limit with exchange bias. *Nature*. **423**: p. 850-853 (2003).

[4] Makovec, D., D. Verhovšek, and M. Sajko, Synthesis of superparamagnetic, photocatalytic nanocomposites for water purification, in *Slovenian Intellectual Property Office*. 2009: Slovenia.

[5] Pankhurst, Q.A., et al.; Applications of magnetic nanoparticles in biomedicine. *J. Phys. D: Appl. Phys.* **36**: p. R167-R181 (2003).

[6] Jordan, A., et al.; Magnetic fluid hyperthermia (MFH): Cancer treatment with AC magnetic field induced excitation of biocompatibile superparamagnetic nanoparticles. *J. Magn. Magn. Mater.* **201**: p. 413-419 (1999).

[7] Camarago, P.H.C., K.G. Satyanarayana, and F. Wypych; Nanocomposites: Synthesis, structure, properties and new application opportunuties *Mater. Res.* **12**: p. 1-39 (2009).

[8] Zeng, H., et al.; Exchange-coupled nanocomposite magnets by nanoparticle self asembly. *Nature*. **420**: p. 395-398 (2002).

[9] Sellmyer, D.J.; Strong magnets by self-assembly. *Nature*. **420**: p. 374-375 (2002).

[10] Kneller, E.F. and R. Hawing; The exchange-spring magnet: A new material principle for permanent magnets. *IEEE Trans. Magn.* **27**: p. 3588-3600 (1991).

[11] Meffre, A., et al.; A simple chemical route toward monodisperse iron carbide nanoparticles displaying tunable magnetic and unprecedented hyperthermia properties. *Nano Lett.* **12**: p. 4722-4728 (2012).

[12] Lee, J.-H., et al.; Exchange-coupled magnetic naoparticles for efficient heat induction. *Nature Nanotech.* **6**: p. 418-422 (2011).

[13] Nandwana, V., et al.; Bimagnetic nanoparticles with enhanced exchange coupling and energy products. *J. Appl. Phys.* **205**: p. 1-5 (2009).

[14] Primc, D. and D. Makovec; Composite nanoplatelets combining soft-magnetic iron oxide with hard-magnetic barium hexaferrite. *Nanoscale*. **7**: p. 2688-2697 (1015).

[15] Lisjak, D. and M. Drofenik; Chemical substitution - an alternative strategy for controlling the particle size of barrium ferrite. *Cryst. Growth Des.* **12**: p. 5174-5179 (2012).

[16] Lisjak, D., S. Ovtar, and M. Drofenik; The stability of BaFe12O19 nanoparticles in polar solvents. *J. Mater. Sci.* **46**: p. 2851-2859 (2011).

[17] Drofenik, M., et al.; The concept of a low-tempearture synthesis for superparamagnetic BaFe12O19 particles. *J. Am. Chem. Soc.* **93**: p. 1602-1607 (2010).

[18] Ovtar, S., D. Lisjak, and M. Drofenik; Barium hexaferrite suspensions for eletrophoretic deposition. *J. Coll. and Interf. Sci.* **337**: p. 456-463 (2009).

For wider interest

Applications of magnetic materials are based on their response to a magnetic field. The response of the magnetic material to the external magnetic field can be described with magnetization curve – hysteresis loop. According to the shape of this loop, the magnetic materials can be classified as magnetically hard or soft materials. The soft magnetic materials are those where relatively low external field is required for their saturation. Typically they exhibit strong saturation magnetization (M_S) and low coercive field (H_C). Contrary, hard magnetic materials exhibit large H_C, however low M_S. Important property of magnetic materials is energy product $|BH|_{max}$. This is a figure of merit for the quality of magnets. It depends on the area of hysteresis loop. Thus for large energy product, material with high M_S and H_C is required. Energy product is difficult to be achieved in a single material. The possibility for improving the M_S and H_C is in the bi-magnetic composite nanoparticles combining hard magnetic and soft magnetic material where phases are direct exchange coupled. Exchange interactions are interactions between spins of the atoms at the interface. The exchange spring interactions between the hard and the soft magnetic materials at the nanometre level could result in strong increase $|BH|_{max}$. When the materials are coupled, the spins of the soft phase is pinned by the spins of the hard phase and during the magnetization process the composite behaves as magnetically single phase.

In our work, we presented the magnetic properties of bi-magnetic composite nanoparticles, which combine hard magnetic barium hexaferrite and soft magnetic maghemite. The composite nanoparticles have “sandwich”-like shape, with a hexaferrite platelet core in between two maghemite layers. Magnetic properties of platelet nanoparticles also depend on their orientation. To avoid the problem of unknown orientation, the nanoparticles have to be magnetically oriented prior to magnetic measurements. For the magnetic orientation, the stable suspension of the nanoparticles in liquid wax was prepared. The nanoparticles were oriented with cooling and solidification of the wax in the homogeneous magnetic field. The problem of suspension preparation is in the magnetic dipole-dipole forces agglomerating the nanoparticles. The stable suspension can be prepared when enough electrostatic or/and steric repulsions are provided between the nanoparticles by applying different surfactants.

IPSSC: Microstructure, mechanical and electrical properties of Glass Fiber Reinforced Composites (GFRC)

Barbara Bertoncelj[1,2], Katarina Vojisavljević[3], Janez Rihtaršič[1], Gregor Jelenc[1], Barbara Malič[3]
[1] Domel, d.o.o., Železniki, Slovenia
[2] Jožef Stefan International Postgraduate School, Ljubljana, Slovenia
[3] Jožef Stefan Institute, Ljubljana, Slovenia
barbara.bertoncelj@domel.com

Abstract. In this study, the influence of E-glass fiber and mineral filler content on the microstructure, physical, mechanical and dielectric properties of Glass Fiber Reinforced Composites (GFRC) was investigated. Five sets of GFRC, based on polymer resin with varying E-grade glass fibers and $CaCO_3$ mineral filler weight fractions (15/64, 20/59, 25/54, 30/49, 35/44), were commercially prepared. Test specimens were prepared by compression molding. Scanning Electron Microscope images revealed that at higher concentrations, the fibers clustered together, resulting in heterogeneous microstructures. Characterization of the composites showed that glass fiber content and distribution significantly affects the mechanical properties. The flexural strength of the composites decreased with increasing glass fiber content. The dielectric constant ε` decreased with increasing fiber content.

Keywords: glass fiber reinforced composites, E-glass fibers, microstructure, flexural strength, electrical properties

1 Introduction

Over the last years, GFRC have gradually replaced traditional structural materials, such as steel and aluminium, especially in applications where strength to weight ratio is important, for example in construction and building industry. Applications of GFRC are also widespread in automotive, electronic and electro industry. Typical products are car panels, internal car parts, switchgears, housings of domestic applications, etc.

Good dimensional stability, chemical and corrosion resistance and good insulating properties are favorable properties of GFRC over steel and Al. Furthermore, manufacturing processes of GFRC products, such as injection molding, is energy less-consuming especially for the reason that molded products are made in one piece and consequently they do not need additional machining. Although, GFRC have been in use for several decades, continuous improvement of properties and competitive price still makes them attractive for an even wider use.

The main components of GFRC are polymer matrix and glass fibers, each of them having its own function. Polymer resin acts like a glue - holding the fibers in a proper spatial orientation, and furthermore helps in stress transfer between the fibers. Since polymers typically have low strength and stiffness, fibers are added to improve the mechanical properties of the composite material. Thus, the final properties of the composite are determined by the type and quantity of the fibers. In combination with the polymer matrix, glass fibers are the most frequently used. Sometimes, inorganic fillers, such as Al_2O_3, mica or $CaCO_3$ are incorporated into the polymer matrix to modify the viscosity of the polymer resin, to lower the overall cost of the material and to achieve some special properties such as improved dimensional stability or self-extinguishing.

Physical and mechanical properties of GFRC are influenced by the phase composition, physical and chemical properties of individual components and fiber distribution and orientation. Therefore, with appropriate selection and ratio of individual constituents, composites with desired properties can be fabricated.

The aim of this work was to study the influence of E-glass fibers on the microstructure, mechanical and electrical properties of GFRC with different weight fractions of glass fibers and mineral filler while keeping the weight fraction of the polymer phase constant.

2 Experimental work

Five sets of GFRC with varying contents of glass fibers and mineral filler were commercially prepared. The compositions of the composites are listed in Table 1. The fibers were 4.5 mm long E-grade glass fibers ("electrical grade" which exhibit low electrical conductivity) [2] with the diameter of 11 μm, as confirmed by scanning electron microscopy (SEM), and the mineral filler was $CaCO_3$ [3]. The polymer phase was kept constant (21 wt%) and was based on thermosetting unsaturated polyester, styrene and additives. Test specimens were prepared by compression molding, according to standard ISO 3167 [4].

Table 1: Composition of GFRC samples.

	Polymer matrix	E-glass fibers	$CaCO_3$
	Content [wt%]		
1	21	15	64
2	21	20	59
3	21	25	54
4	21	30	49
5	21	35	44

The density of the samples was determined by immersion method and calculated using the equation (1),

$$\rho = \frac{m_s}{m_s - m_w} \cdot \rho_w \tag{1}$$

where the m_s is the mass of the sample in the air, m_w is the mass of the sample when immersed in the water and ρ_w is the density of water at room temperature [5].

Test specimens of individual samples were then cut perpendicular to the filling flow direction of the material during compression molding to obtain cross-sectional and plan-view sections for microstructural characterization. Representative scheme of the sample cutting position and the sample dimensions are shown in Figure 1. The cross-sections and plan-view sections of the test specimens were prepared by the standard metallographic technique, i.e. by grinding and polishing, and examined by scanning electron microscope (SEM, JEOL JSM 5800). Prior to the SEM observations the samples were coated with a thin carbon layer. The SEM micrographs were taken at the accelerating voltage of 20 kV.

The flexural strength of the test specimens was measured by three-point bending method (Alpha 50-5), according to standard ISO 178:2003 [6]. The span between the supports was 64 mm and the crosshead speed was 2.0 mm/min. The test was carried out on 15 specimens of each composition and calculated by the equation (2),

$$\sigma_f = \frac{3Pl}{2bh^2} \tag{2}$$

where σ is the flexural strength, P is the maximum fracture load, l is the span between the supports, b is the width of the sample and h is the height of the sample.

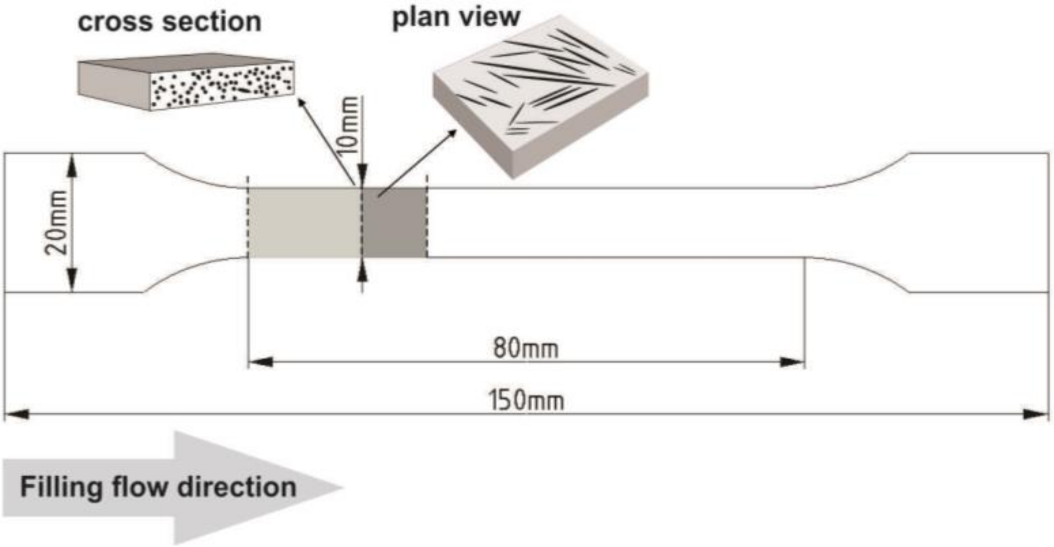

Figure 1: Scheme of the test specimen illustrating the cutting directions for cross-section and plan-view sections for SEM observation. The arrow indicated the flow of the material during molding.

Prior to electrical properties measurement Cr/Au electrodes were applied on the surface of each sample by RF-magnetron sputtering (5 Pascal). The dielectric properties were measured by the Impedance analyzer HP 4284A. The measurements were performed at room temperature over the frequency range from 100 Hz to 1 MHz. The dielectric constant ε' was calculated according to the equation (3),

$$\varepsilon' = \frac{C \cdot d}{\varepsilon_0 \cdot A} \tag{3}$$

where ε' is the dielectric constant, C is the capacitance of the sample, d and A are the thickness of the sample and the area of the electrode, respectively, and ε_0 is the permittivity of free space. The imaginary part of the complex dielectric permittivity ε'' was determined by the equation (4),

$$\varepsilon'' = \varepsilon' \cdot tan\delta \tag{4}$$

where ε'' is the dielectric loss factor, ε' is the dielectric constant and $tan\delta$ is the loss factor.

3 Results and discussion

3.1 Physical properties

The density values are listed in Table 2. The results showed that the samples with different weight fractions of glass fibers have very similar densities, around 2 g/cm^3, which is attributed to the similar densities of EGF (2,54 g/cm^3) and $CaCO_3$ mineral filler (2,65 g/cm^3) [7].

Table 2: Density values of individual GFRC.

Composition (wt% EGF/$CaCO_3$)	Density [g/cm^3]
15/64	2,04
20/59	2,03
25/54	2,02
30/49	2,04
35/44	2,03

3.2 Microstructure

SEM images of plan view and cross-sectional areas are shown in Figure 2. From the micrographs it is evident, that the fibers are mostly oriented perpendicular to the filling direction of the material during molding. At lower EGF content, the distribution of fibers is quite homogeneous (see Figure 2 a), b)). However, at higher fiber contents, above 20 wt%, we observed that fibers are clustered together which is due to the lack of space for fibers to orient in the "proper" direction and consequently the microstructure becomes non-homogeneous with some areas filled only with polymer resin and mineral filler. We observe that a homogeneous distribution of the fibers could not be achieved at higher fiber contents.

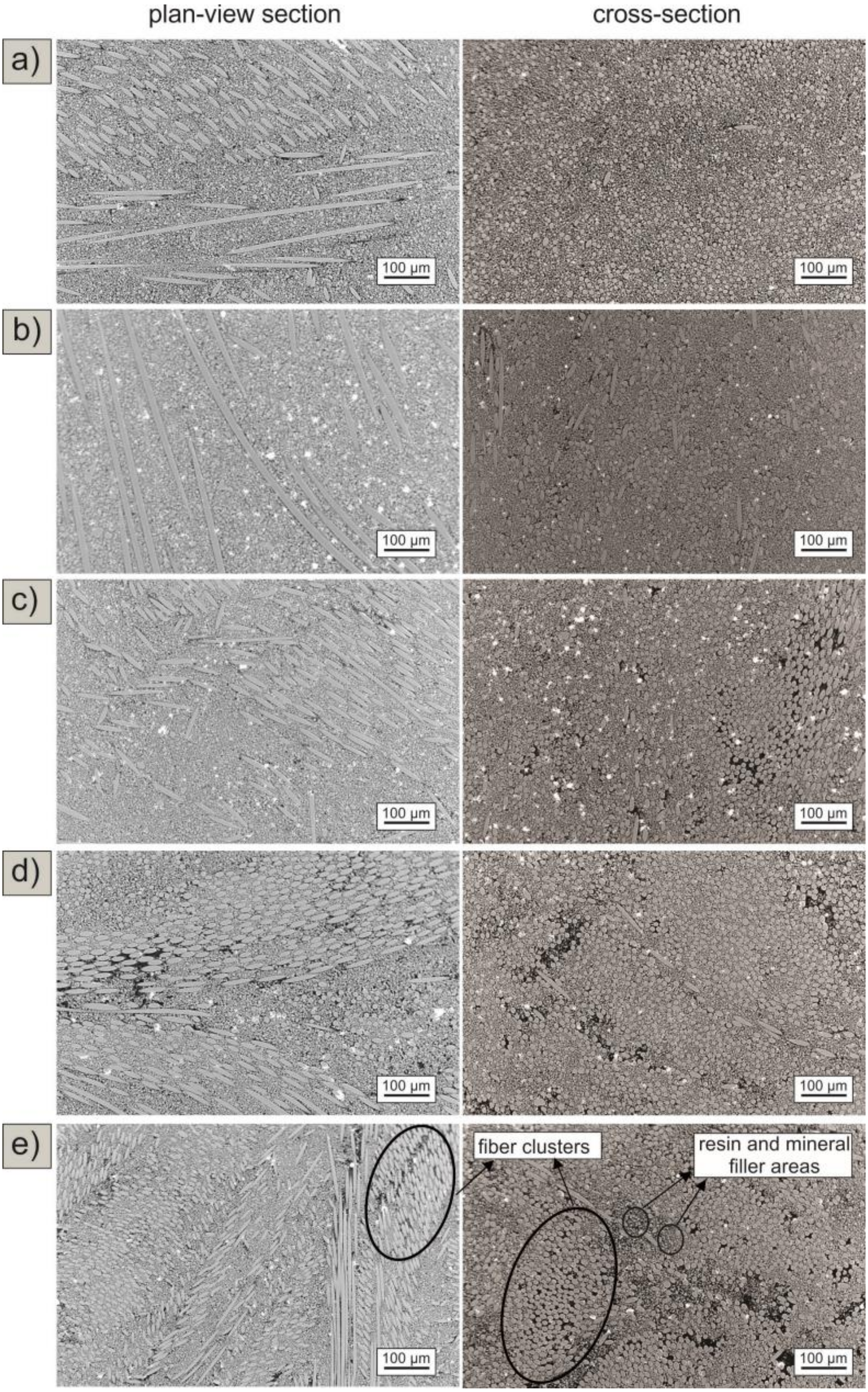

Figure 2: SEM micrographs of plan-view and cross-sectional areas of GFRC: a) 15 wt% of EGF, b) 20 wt% of EGF, c) 25 wt% of EGF, d) 30 wt% of EGF, e) 35 wt% of EGF.

3.3 Mechanical properties

The results of flexural strength measurement of all GFRC are presented in Figure 3. The maximum value of flexural strength was measured with the sample comprising of 15 wt% of EGF, i.e. around 130 MPa. With increasing the EGF content the flexural strength decreased, reaching the final value of 72.3 MPa for the composite with 35 wt% of EGF. The decrease in the flexural strength with increasing EGF content was not expected. However, the deterioration of flexural strength was attributed to the increasingly non-homogeneous fiber distribution in the composites with higher fiber contents. Fiber clustering was observed from the SEM micrographs, which is especially apparent in the composites with fiber contents above 20 wt% (see Figure 2 c),d),e)). Therefore increased fiber-fiber interactions could contribute to the less efficient stress transfer in the material.

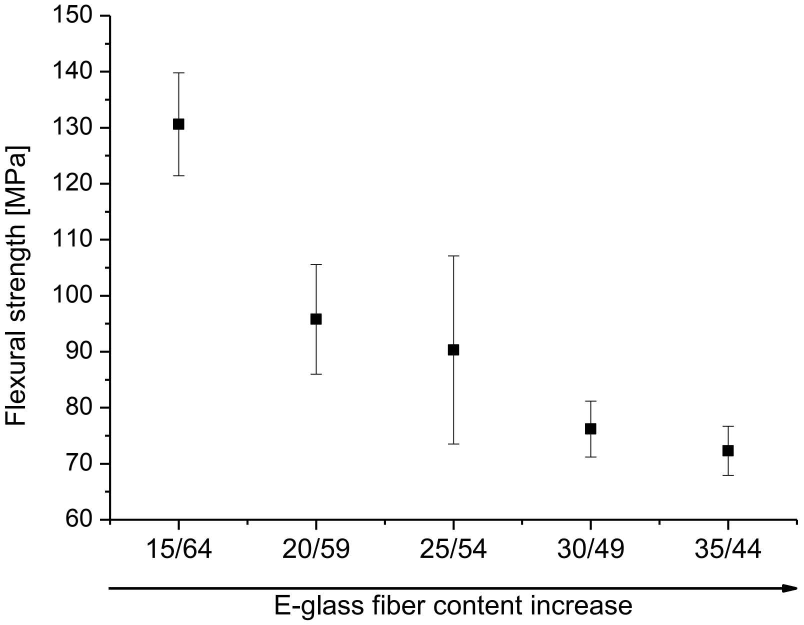

Figure 3: Flexural strength of GFRC samples.

3.4 Dielectric properties

The values of dielectric constant measured at different frequencies are presented in Figure 4. The dielectric constant ε` for the sample with 15 wt% of EGF at 100 Hz was 6.86 and 6.65 at 1MHz. The results show that ε` of all composites decreases with increasing frequency. The result is in agreement with [8]. With increasing the weight fraction of glass fibers the ε` decreases, with the exception of the composition with 35 wt% of EGF. Figure 4 also shows the frequency dependence of dielectric loss factor ε`` for all composites. The value ε`` for the sample with 15 wt% of EGF was 0.14 at 100 Hz and 0.05 at 1MHz. The results also show that ε`` is increasing with increasing glass fiber content.

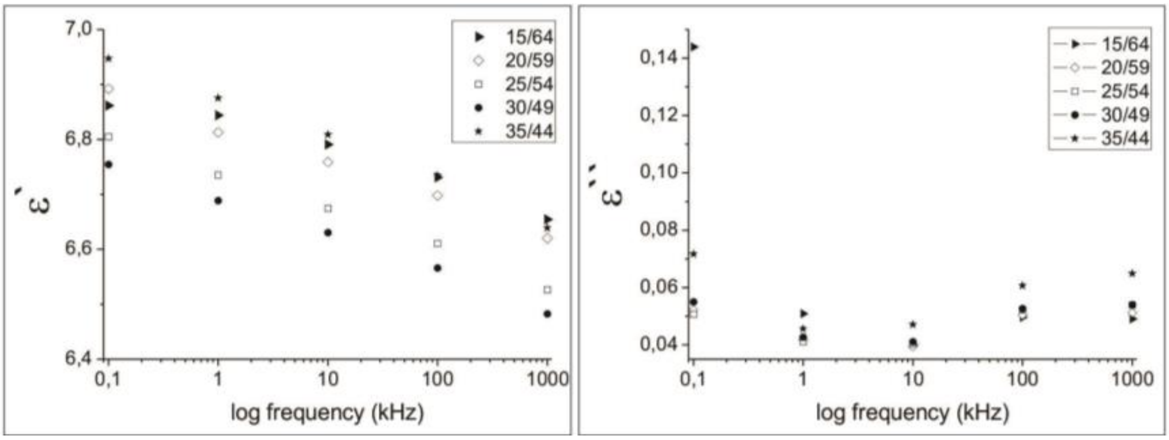

Figure 4: Frequency dependence of dielectric constant ε` and dielectric loss factor ε`` for composites with varying E-glass fiber content.

4 Conclusions

In order to study the effect of EGF content on the microstructure, mechanical and electrical properties 5 sets of GFRC were commercially fabricated with varying fiber and mineral filler contents. The density of GFRC samples did not change with the composition and was around 2 g/cm^3. From the SEM micrographs it was observed that fiber distribution at lower weight fractions of EGF is quite homogeneous. However, microstructures of the samples with higher EGF contents, above 25 wt%, revealed a non-homogeneous distribution of the fibers, i.e. clusters of fibers and areas filled only with the resin and mineral filler. We connect the observed non-homogeneous microstructure at higher fiber contents with the deterioration of flexural strength. The results showed that flexural strength of the composites decreased with increasing EGF content which was in contrast to the expected reinforcing effect of EGF. The room temperature dielectric permittivity in all composites decreased with increasing frequency and with increasing glass fiber content.

5 Acknowledgements

We acknowledge the assistance of colleagues from Electronic Ceramics Department, Jožef Stefan Institute, Silvo Drnovšek and Tanja Pečnik, for their help with measuring dielectric properties. One of the authors (B.B.) gratefully acknowledges the financial support of the Ministry for education, science and sport of Republic of Slovenia and European Commission through the European Social Fund. B.M. and K.V. acknowledge the support of the Slovenian Research Agency (P2-0105).

References:

[1] A. Kelly, C.H. Zweben (eds.). *Comprehensive composite materials*, Elsevier, Amsterdam, 2000.

[2] F.T. Wallenberger, P.A. Bingham (eds.). *Fiberglass and glass technology*. Springer Scince+Business Media, New York, 2010.

[3] B. Bertoncelj, K. Vojisavljević, J. Rihtaršič, G. Jelenc, B. Malič. Characterization of glass fiber reinforced composites for housing of electrical motors. In A. Žemva (Ed.), P. Šorli (Ed.), I. Šorli, (Ed.). *Proceedings of the 49th MIDEM International Conference on Microelectronics, Devices and Material*, Kranjska Gora, Slovenia, 2013.

[4] ISO 3167: Plastics-Multipurpose test specimens. International Organization for Standardization. https://www.iso.org.

[5] Mohamed N. Rahaman. *Ceramics Processing*. CRC Press, Boca Raton, 2007.

[6] ISO 178:2003: Plastics. Determination of flexural properties. International Organization for Standardization. https://www.iso.org.

[7] William D. Callister. *Materials science and engineering*. John Wiley & Sons, New York, 2007.

[8] M. Akram, A. Javed, T. Z. Rizvi. Dielectric properties of industrial polymer composite materials. *Turkish Journal of Physics*, 29(6):355-62, 2005.

For wider interest

Composites consist of two or more distinct materials, whose combination results in improved properties that cannot be achieved only by one of the constituents.

Glass fiber reinforced composites (GFRC) are combination of polymer matrix and glass fibers, each having its own role that contributes to final properties. Polymer matrix surrounds the fibers and holds them in the “proper” spatial arrangement. Since polymers most often have low strength and stiffness, glass fibers are added to reinforce the polymer and improve its mechanical properties.

Final properties of GFRC depend on chemical and physical properties of individual constituents, their relative amounts and spatial orientation and distribution of fibers.

In recent years GFRC have replaced metals and also found new applications in many industry areas, such as in construction, transportation, electro and electronic industry. Main advantages of GFRC over metals are high strength and stiffness in combination with low density. For example, use of GFRC in vehicles results in lower overall weight and consequently increases fuel savings. Such properties make them attractive for an even wider use. Thus, understanding of relationship between *structure-composition-properties* of GFRC can help in developing new composites with improved properties and in optimizing the existing materials.

Photogeneration of Charge Carriers in Few-Layer MoS_2

Tetiana Borzda[1,2], **Christoph Gadermaier**[1,2], **Natasa Vujicic**[1,3], **Peter Topolovsek**[1,2], **Milos Borovsak**[1], **Tomaz Mertelj**[1], **Daniele Viola**[4], **C. Manzoni**[4], **E. A. A. Pogna**[4], **D. Brida**[5], **Maria Rosa Antognazza**[6], **Francesco Scotognella**[6], **Guglielmo Lanzani**[6], **Giulio Cerullo**[4], **and Dragan Mihailovic**[1,2,7]

[1] Department of Complex Matter, Jozef Stefan Institute, Jamova 39, 1000 Ljubljana, Slovenia

[2] Jozef Stefan International Postgraduate School, Jamova 39, 1000 Ljubljana, Slovenia

[3] Institute of Physics, Bijenicka 46, 10000 Zagreb, Croatia

[4] Department of Physics, Politecnico di Milano, P. Leonardo da Vinci 32, 20133 Milan, Italy

[5] Department of Physics, University of Konstanz, PO box M696 78457 Konstanz, Germany

[6] Center for Nano Science and Technology, Italian Institute of Technology, Via Pascoli 70/3, 20133 Milano, Italy

[7] Center of Excellence in Nanoscience and Nanotechnology, Jamova 39, 1000 Ljubljana, Slovenia

tetiana.borzda@ijs.si

Abstract. The two-dimensional semiconductor MoS_2 in its mono- and few-layer form is expected to have a significant exciton binding energy of several 100 meV, leading to the consensus that excitons are the primary photoexcited species. Nevertheless, even single layers show a strong photovoltaic effect and work as the active material in high sensitivity photodetectors, thus indicating efficient charge carrier photogeneration (CPG). Here we use continuous wave photomodulation spectroscopy to identify the optical signature of long-lived charge carriers and femtosecond pump-probe spectroscopy to follow the CPG dynamics. We find that intitial photoexcitation yields a branching between excitons and charge carriers, followed by excitation energy dependent hot exciton dissociation as an additional CPG mechanism. Based on these findings, we make simple suggestions for the design of more efficient MoS_2 photovoltaic and photodetector devices.

Keywords: Two-dimensional crystals, MoS_2, transition metal dichalcogenides, excitons, femtosecond spectroscopy, photomodulation, photophysics, charge generation.

1 Preparation and Characterization of Samples

Recent progress in the exfoliation of layered materials [1], [2] and the nanofabrication of functional structures has revived the interest in two-dimensional materials with properties complementary to graphene, in particular transition metal dichalcogenides [3], [4] (TMDs) such as MoS_2. Depending on the metal atoms' coordination and oxidation state, TMDs can be metallic, semimetallic, or semiconducting. Additionally, some TMDs show superconductivity [5], charge-density waves [6] and hidden electronically ordered phases [7]. Their potential for electronics has become evident by the realization of a field effect transistor [8] (FET) and a logic circuit device [9] based on a single flake of monolayer MoS_2.

The optical absorption of MoS_2 in the visible spectral range shows four excitonic resonances [10], commonly labeled (see Figure 1a) A to D at 1.9, 2.1, 2.7, and 2.9 eV. The spectral positions of these resonances are almost independent of the number of layers, while the indirect band gap is at 1.2 eV in the bulk and grows progressively as the number of layers is reduced, even exceeding the energy of the A exciton resonance for the monolayer. Hence the monolayer, contrary to bi- and multilayers, behaves like a direct gap semiconductor and shows significant fluorescence [11], [12]. The exciton binding energy for bulk MoS_2 has been determined to be 45 meV and 130 meV for the A and B excitons, respectively [13]. Both exciton binding energies increase upon decreasing the sample thickness, with estimates for monolayers [14-16] ranging from 0.4 to 0.9 eV. Despite this high exciton binding energy, monolayer MoS_2 shows a strong photovoltaic effect [17] and potential for high sensitivity photodetectors [18]. Both findings require efficient charge carrier photogeneration (CPG), either via direct excitation of mobile carriers or via exciton dissociation.

The spectral signature of charge carriers has been identified by absorption and fluorescence spectroscopy of MoS_2, where the charge concentration is varied either via the gate voltage in a FET geometry [19] or via adsorption [20] or substrate doping [21]. The absorption peaks of charges are red-shifted by about 40 meV compared to the ground state absorption into the A and B excitons and have been attributed to optical transitions from a charged ground state to a charged exciton (trion). The possibility of alternative interpretations, such as polarons [22], [23] or Stark effect in the local electric field of the charges [24-26] does not compromise the identification of these absorption peaks as belonging to charges.

Here we use continuous wave (cw) photomodulation (PM) and femtosecond pump-probe spectroscopy to identify the spectral features of photogenerated charges and trace their dynamics, starting with their generation either by direct impulsive excitation into the charge continuum or via exciton dissociation. We exfoliated MoS_2 in ethanol, following the protocol in Ref [1]. The dispersion was dried and the obtained few-layer flakes were re-dispersed in a solution of PMMA, a transparent and electronically inert polymer. This dispersion was spin-cast onto a quartz substrate, yielding a macroscopic PMMA film with a homogenous greenish-yellow color characteristic of thin MoS_2 films [27] (see Fig. 1a).

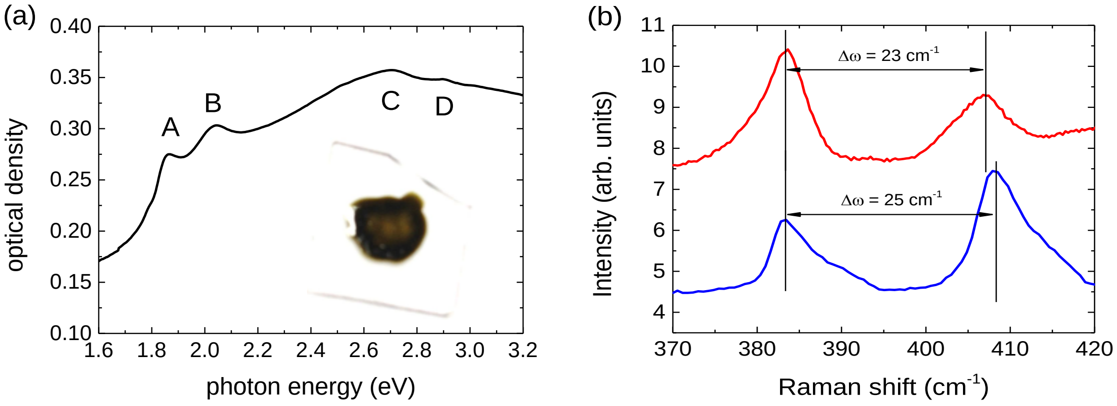

Figure 1: (a) Absorption spectrum of the sample of MoS_2 in PMMA. Inset shows a photograph (the dark area has a diameter of approximately 7-8 mm). (b) Raman spectra for two excitation wavelengths at 633 nm (red line) and 488 nm (blue line).

PMMA in this sample serves as a matrix that holds an ensemble of flakes with lateral size [1] of few-hundred nm. The distance $\Delta\omega$ between the two Raman peaks around 400 cm^{-1} is generally viewed as the most robust measure of the flake thickness [28]. From the Raman spectra in Fig 1b we obtain $\Delta\omega = 23$ cm^{-1} for excitation at 633 nm and $\Delta\omega = 25$ cm^{-1} at 488 nm. Within the distribution, various thicknesses contribute differently at the two excitation wavelengths [29]. Overall, the Raman spectra indicate a flake thickness distribution that is dominated by three- to six-layer flakes.

The advantages of this kind of sample compared to individual flakes are the ease of fabrication and handling and the possibility to use any spectroscopic technique without the need for high-resolution optical microscopy. MoS_2 flakes embedded in PMMA are in a slightly different environment than mono- or few layer flakes on dielectric substrates used in previous femtosecond studies [30], [31]. However, as our results will show, the spectra and the relaxation times of the signal are very similar to those obtained on individual few-layer flakes. Hence the present study directly extends existing knowledge on the femtosecond behavior of few-layer MoS_2.

2 Results and Discussion

The absorption spectrum in Fig. 1a shows the characteristic A and B exciton resonances, which are broader and red-shifted compared to undoped MoS_2, as is typical of commercial MoS_2 of mineral origin [32], which is doped due to dislocations induced by the exfoliation and due to (mostly metallic) impurities. Hence, each of the two absorption peaks is actually an overlap of at least two contributions: neutral ground state to exciton absorption at the higher energy side of each peak and lowest charged state to excited charged state at the lower energy side. For the A peak, an even lower energy contribution has been identified [32], which has alternatively been ascribed to a surface trapped exciton [33], an edge state [34], or a plasmon resonance [35], so that peak A actually arises from the overlap of three peaks. Similar to the notation in Refs 19, 20, and 32, we will use the labels L, A^-, and A^0 for the low energy peak, charge peak and exciton peak of the A resonance, and B^- and B^0 for the charged and neutral contributions to the B resonance. Please note that, contrary to electrical or chemical doping, photoexcitation generates charges in pairs of opposite polarities. However, although we expect the signatures of the corresponding positive charges at the same spectral positions, we know only those of the negative charges, hence our labeling.

To identify long lived photoexcitations we performed cw PM spectroscopy. Here, a cw laser with 3.1 eV photon energy used for exciting the sample is periodically modulated via a mechanical chopper. The relative change $\Delta T/T$ of the transmitted light from a halogen lamp is measured via phase sensitive detection. Those photoexcitations whose population changes significantly over the modulation cycle (i.e. their lifetime is long enough to build up sufficient population while the laser is on and short enough to sufficiently reduce their population while it is off) are identified in the cw PM spectrum via their photoinduced absorption (negative $\Delta T/T$) transitions to higher excited states. Concomitantly with the increase of photoexcited populations, the ground state population and its associated absorption is reduced (photobleaching, positive $\Delta T/T$). The cw PM spectrum at room temperature upon excitation at 3.1 eV, above the C and D exciton resonances, is shown in Fig. 2a. The signal is largely in phase with the modulation of the photoexcitation, with a negligible quadrature contribution. This means that the populations at the origin of the signal can easily follow the modulation at 245 Hz, implying that the lifetimes of the respective photogenerated species are much shorter than the modulation period of ~4 ms.

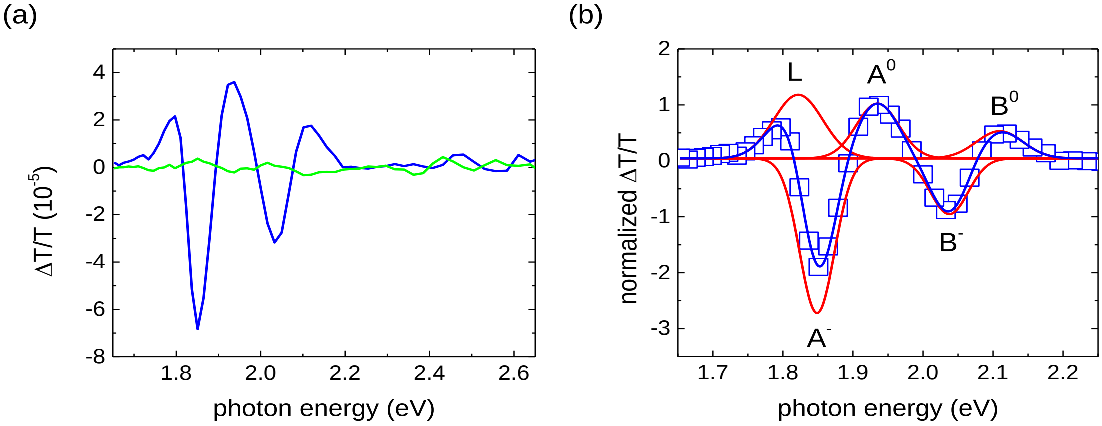

Figure 2: (a) CW photoinduced absorption spectrum of MoS_2 in PMMA at room temperature for excitation at 3.1 eV. In-phase (blue) and quadrature (green) signal components are shown for a modulation frequency of 245 Hz. (b) Five Gaussian fits (red) whose sum (blue) fits the normalized in-phase spectrum (open squares).

The main features of the spectrum are three positive (photobleaching) and two negative (photoinduced absorption) peaks. We fit the spectrum using five overlapping Gaussians (see Fig 2b), which represent the thermal and disorder-induced (in particular by polydispersity of flake thickness) broadening of the electronic resonances. The strong overlap between neighboring peaks makes them appear narrower than their actual lineshape and connected by an almost straight line, masking the inflection points characteristic of isolated Gaussian peaks. The spectral positions of the five peaks correspond very well with the three neutral and two charge peaks discussed in References 19, 20, and 32. Assuming the same origin for the peaks in the PM spectrum, we obtain a straightforward interpretation. Upon photoexcitation, the number of electrons in the neutral ground state is reduced, and the number of charge carriers is increased. Hence the absorption features L, A^0, and B^0 from transitions between neutral states are reduced, resulting in a positive $\Delta T/T$ (photobleaching), while the absorption features A^- and B^- from charges are increased, yielding a negative $\Delta T/T$ (photoinduced absorption).

Alternatively, one could interpret the PM spectrum based on its resemblance of a derivative lineshape. A photoinduced blue shift of the absorption spectrum would result in a ΔT/T contribution that follows the first derivative of the absorption spectrum (or a negative first derivative for a red shift); a photoinduced broadening of the absorption peaks would contribute a negative second derivative. If we interpreted our spectrum in terms of derivative lineshapes, it would be dominated by a positive second derivative, which indicates a photoinduced line narrowing. We are not aware of any such mechanism. However, the A peak is composed of the three overlapping narrower peaks L, A^-, and A^0 (no equivalent to the L peak has yet been identified for the B peak, but we may extrapolate our reasoning also to B). In our proposed scenario photoexcitation generates charges and the middle peak A^- increases at the expense of the other two, which decreases the overall width of the A peak. Hence, CPG leads to an apparent photoinduced line narrowing, which explains the positive second derivative lineshape.

To investigate CPG in real time, we now turn to femtosecond optical pump-probe spectroscopy. Like cw PM, this technique measures the relative change in transmission $\Delta T/T$. However, rather than continuously, the sample is photoexcited at a well-defined point in time by a fs laser pulse (the pump) and the transmission spectrum is measured with a second fs laser pulse (the probe) at a well-defined delay after the pump. Scanning the pump-probe delay allows to follow the evolution of the photoexcitated states' populations. We start by comparing the $\Delta T/T$ signal for excitation at 3.1 eV at long pump-probe delay (300 ps) with the cw PM (see Fig. 3a). The two normalized spectra are very similar, with three important differences: the L peak is absent, there is an additional broad photoinduced absorption feature peaking around 2.45 eV, and the whole spectrum is red shifted. The red shift of the whole spectrum is more pronounced at higher pump intensities (see Fig 3b) and shorter pump-probe delays (see Figs 3c and d).

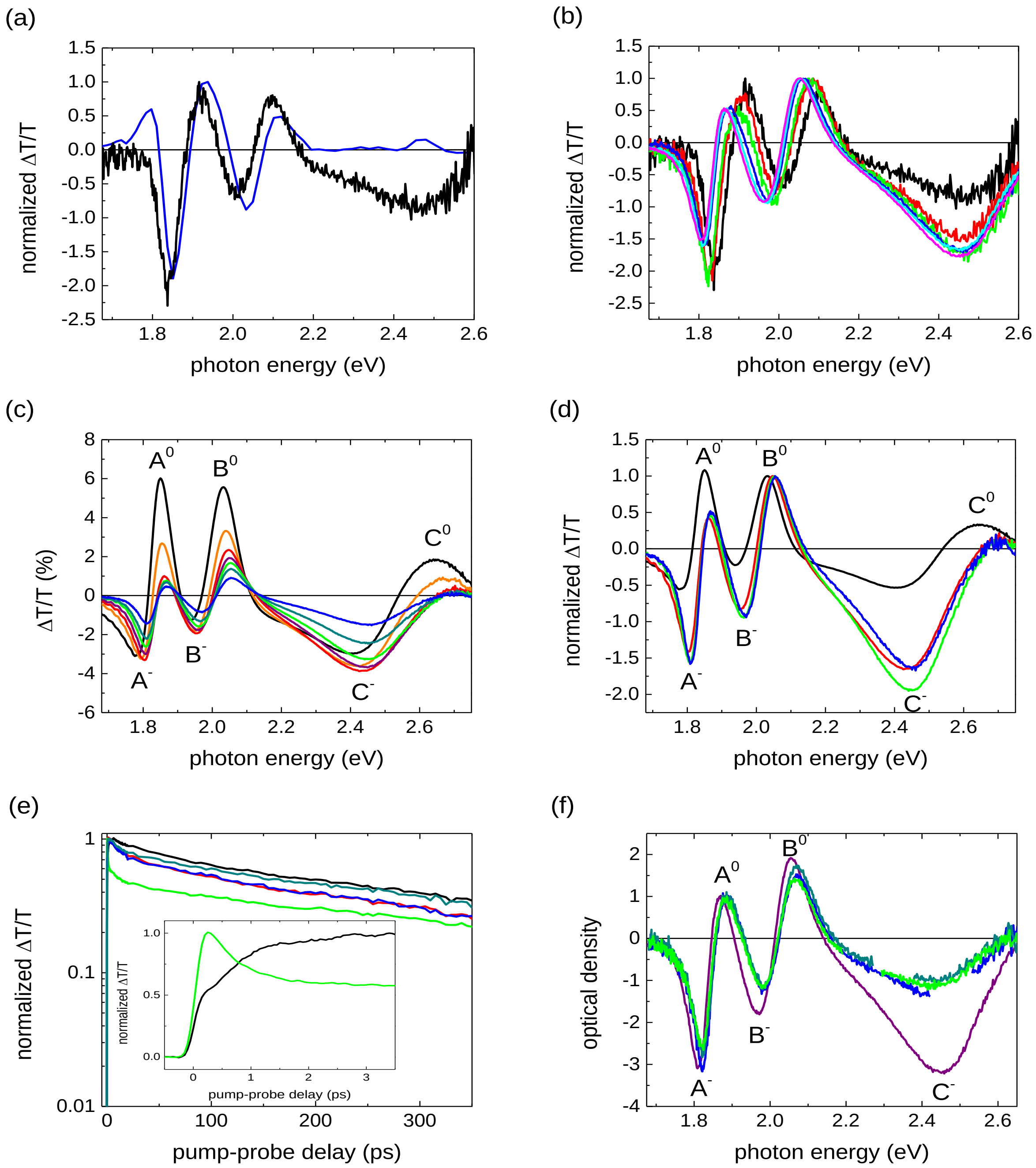

Figure 3: (a) Normalized cw photomodulation spectrum of MoS_2 in PMMA (blue) compared to the fs transient spectrum at 300 ps pump-probe (black) delay for 2 10^{14} cm^{-2} excitation fluence, 3.1 eV pump photon energy (b) pump-probe spectra at 300 ps normalized to the B exciton peak for different pump fluences at 3.1 eV pump photon energy: 2 (black), 3(red), 6 (green), 20 (blue), 40 (cyan) and 80 10^{14} cm^{-2} (c) absolute and (d) normalized (to the B exciton peak) pump-probe spectra for 4 10^{15} cm^{-2} pump fluence at delays 300 fs (black), 1 ps (orange), 3 ps (red), 10 ps (purple), 30 ps (green), 100 ps (dark cyan), and 300 ps (blue) (e) normalized time traces for different probe energies: 2.48 (black), 2.25 (red), 2.07 (green), 1.94 (blue) and 1.80

eV (dark cyan) (f) normalized spectra at 300 ps pump-probe delay for different pump photon energies: 3.10 (purple), 2.48 (blue), 2.34 (dark cyan) and 2.25 eV (green).

Both these correlations suggest that the red shift is stronger for higher concentration of a certain species of excited states. The most intuitive interpretations are Stark effect due to the local field of photogenerated charges, as has been observed in semiconductor nanocrystals [24], organic semiconductors [25], and carbon nanotubes [26], [36] , inter-excitonic interaction [37] or band gap renormalization, as has been found in semiconducting quantum wells upon photoexcitation [38] and inferred in recent works on semiconducting TMDs [39], [40]. This intensity dependent red-shift also explains how the non-linear optical properties of MoS_2 can change from saturable absorption (i.e. photobleaching) to optical limiting (i.e. photoinduced absorption) as a function of pump intensity [41]. After approximately 3 ps, the spectrum decays without any significant shifts or changes of shape, through a dominant process with a time constant of approximately 500 ps (see Fig. 3e), as previously obtained on few-layer MoS_2 supported on a dielectric substrate [30].

In addition to the previously identified A^-, A^0, B^-, and B^0 peaks, we note an additional broad absorption peak and a further positive peak at higher probe energies. Due to its position, we straightforwardly assign the positive peak to bleaching of the C exciton and label it C^0. The absorption peak shows a formation similar to A^- and B^- (see next paragraph), and is similarly long lived, hence it should belong to a charge population. Like the C exciton bleaching, it is absent in cw PM, and strongly reduced for excitation energies below the C exciton resonance, see (Fig 3f), hence we ascribe it to a charge associated with the C exciton, labeled C^-. The C exciton is ascribed either to excitation from a band below the valence band, or between the valence and conduction bands in a region of the bands nesting slightly off the Γ point [42]. In both scenarios it is plausible that the C^0 and C^- feature do not appear in the cw experiment, which probes populations that have relaxed towards the edges of the band gap.

During the first 3 ps the $\Delta T/T$ spectrum undergoes a characteristic change of shape: the positive signal components are formed during the instrumental resolution and decay monotonically, while the main photoinduced absorption features, associated to charges A^-, B^- and C^-, show an initial instrument-limited rise followed by a delayed rise component after the pump pulse and by a slower decay. We can interpret this dynamics by assuming that the pump pulse creates an ensemble of excitons and charges with a combined spectrum $S_1(E)$.

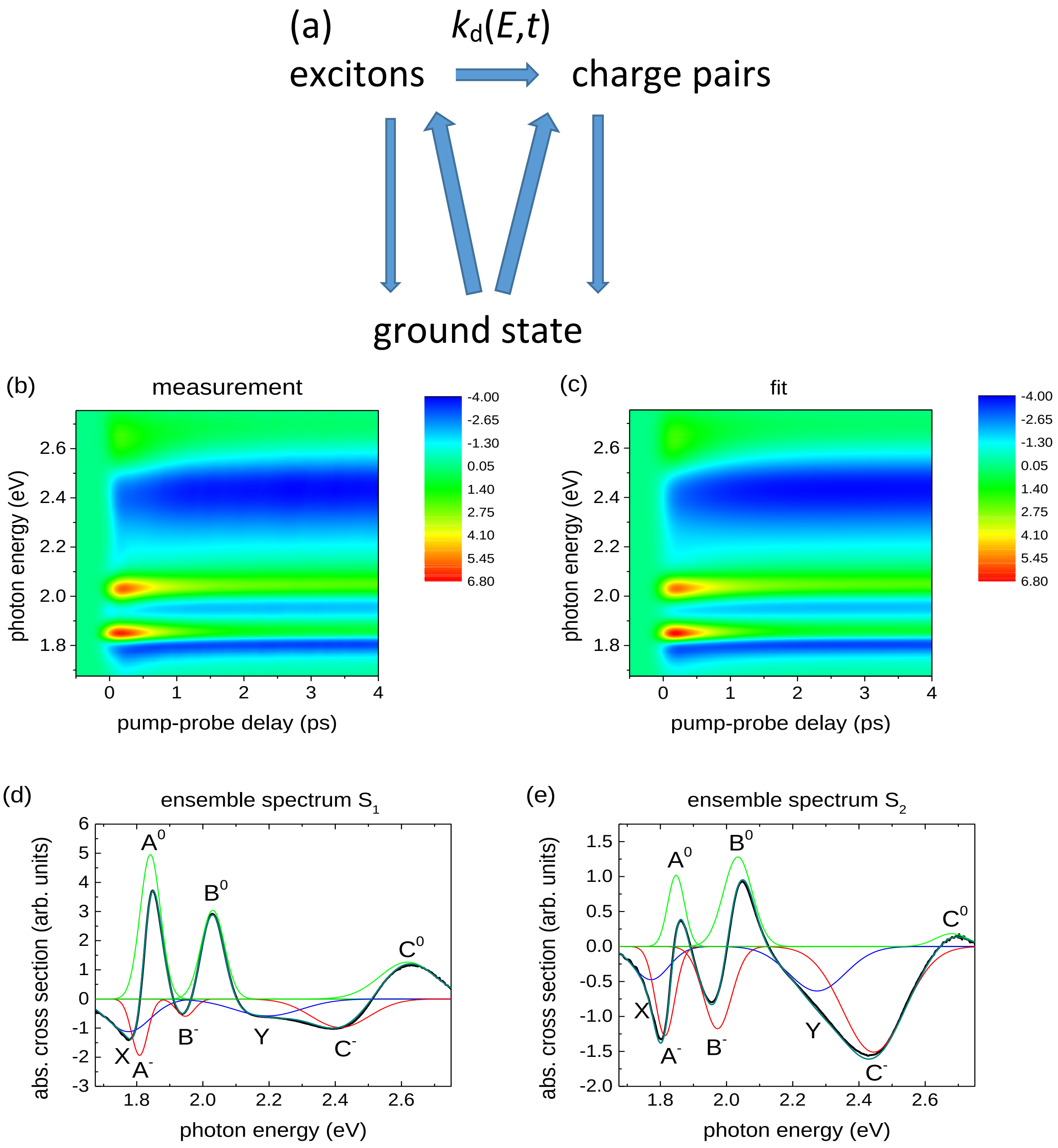

Figure 4: (a) Scheme of the photoexcitation dynamics of excitons and charges. (b) contour plot of the fitted $\Delta T/T$ (in %) (c) contour plot of the measured $\Delta T/T$ (in %) (d) spectrum S_1 described in the text (black) and fit to eight Gaussian peaks (photoinduced absorption from charges: red, photoinduced absorption from

excitons: blue, photobleaching: green) and their sum (dark cyan) (e) spectrum S_2 described in the text with the same color coding as (d).

During the first 3 ps, this ensemble evolves into one with less excitons and more charges, with a combined spectrum $S_2(E)$. Subsequently, the exciton and charge populations decay with very little further change of shape, meaning that either the decay times of excitons and charges are very similar (either by coincidence or due an interdependent relaxation mechanism), or that the population after 3 ps is already dominated by charges. The latter hypothesis is corroborated by the similarity between the fs $\Delta T/T$ spectrum at longer delays and the cw PM spectrum, which should not show any exciton contribution. In the simplest possible case, the ensemble with the spectrum $S_1(E)$ evolves into the one with the spectrum $S_2(E)$ with only one characteristic sub-picosecond relaxation time τ_1. Hence we propose the simple scheme of the underlying photoexcitation dynamics shown in Fig. 4a: The pump pulse generates a mixed population of charge carriers and excitons. Subsequently a certain fraction of the excitons dissociates into charges.

The evolution of the photoexcited states' population according to Fig. 4a is best fitted with a characteristic time $\tau_1 = 680$ fs. The assumption of only one common time constant τ_1 for the dissociation of the A, B, and C excitons may be a gross simplification, but it describes the data remarkably well (Figs 4b+c). The spectra S_1 and S_2 in Figs. 4d and e can be fitted with overlapping Gaussians analogously to the cw PM spectrum. Besides the six already identified charge absorption and exciton bleaching features, there are two additional peaks, which we label X and Y. Since they do not show the delayed formation characteristic of charges, we assign them to photoinduced absorption by one of the exciton populations.

Comparing the relative contributions of the X and Y peaks to the S_1 and S_2 spectra, we can deduce that after 3 ps approximately the exciton population is somewhat decreased (by approximately a factor of 2). On the other hand, if the exciton population followed a curve ~ $exp(-t/\tau_1)$, the remaining exciton population would be only 1%. Hence, τ_1 is not the time constant of the exciton dissociation, but rather the characteristic time with which the dissociation rate diminishes. Besides its time dependent rate, the exciton dissociation yield depends also on the energy of the exciting photons. This is expressed in Fig. 4a as a rate constant $k_d(E, t)$ that depends on the pump energy and on time. Fig 3f shows that the ratio between the absorption peaks due to charges and the respective bleaching peaks is higher for higher photon energy. This is consistent with the lower PL quantum yield for higher excitation energy, which has also been ascribed to charge separation [42].

Detailed studies of the CPG dynamics exist for carbon nanotubes and conjugated polymers, which are materials with exciton binding energies similar to MoS_2. In carbon nanotubes, there is an initial branching between mostly excitons and 1-2% directly excited charges [36], with a higher charge yield for higher excitation energy. In conjugated polymers, there is a similar initial branching, followed by additional CPG via dissociation of “hot” excitons during the first few picoseconds [43]. Elaborate models describe how the surplus energy of hot excitons increases their dissociation probability [44], [45]. The relaxation of the electron and hole to the lowest exciton state are typically faster than our observed 680 fs [46-48], however electron-phonon coupling creates a phonon heat bath that can live on for a few ps [49]. Additionally, exciton migration, which is facilitated by the extra energy and comes to a halt when the exciton reaches a local energy minimum, increases the probability that the exciton reaches a site where its dissociation is facilitated. In MoS_2 flakes, such sites could be surface defects, flake edges, metallic inclusions, crystal faults or small islands of an extra MoS_2 layer. We therefore conclude that the exciton dissociation probability is high while the excitons are hot and mobile and decreases as they reach their energetic minima. CPG in few-layer MoS_2 is a combination of two processes, both which have increased efficiency for higher exciting photon energy: direct excitation of charge pairs (within the 50-100 fs instrument resolution of our experiment) and hot exciton dissociation.

Before we discuss the implications of time- and pump energy dependent hot exciton dissociation, we review how our findings compare to previous femtosecond work on TMDs. Intervalley scattering [50], [51] requires circular polarization and is not probed in our experiment, because all our laser polarizations are linear. On a time scale of 1 ps to 500 ps, Shi et al. obtained results very similar to ours in few layer flakes deposited on a dielectric substrate [30], but they do not discuss the temporal change of shape of the spectrum, which is crucial in understanding exciton dissociation and charge generation. They estimate that for excitation fluences similar to ours, the sample temperature should change by only 0.1 K, thus dismissing sample heating as a possible source of the signal. In our samples, due to the low heat conductivity of PMMA [52], heating could be a bit stronger. However, a signal due to heating would not change its shape with time and, most crucially, its shape would not depend on the excitation photon energy. In Fig 3f, there is a small C^- signal even for excitation below the C exciton resonance. This contribution, which at any delay is 20% or less compared to the spectrum for excitation above the C resonance, may originate from heating or any other mechanism that changes the overall lineshapes and/or peak positions, such as Stark effect or band gap renormalization. Hence, for the combination of all such processes including heating, we estimate an upper boundary of 20% contribution. Any such mechanism is less important in the cw PM experiment, where no appreciable C^- signal is found. Therefore, both the femtosecond and the cw signals are dominated by changes in excited and ground state populations, not pure lineshape/shift mechanisms.

Considering further lineshape/shift mechanisms, inter-exciton interaction is expected to result in a red-shift [37] and line broadening. However, we observe an apparent line narrowing (see discussion of the cw PM spectrum) due to the increase of the central A^- peak at the expense of its neighbors on either side. The Burrstein-Moss effect, which has been observed in substitutionally doped MoS_2 fullerenes [53] should lead to a blue shift with increasing excited state population. Our contrasting observation implies that any Burrstein-Moss contribution is overwhelmed by one or more red-shifting mechanisms.

3 Conclusion and Outlook

We have shown that charge carrier photogeneration in few layer MoS_2 arises from two different processes. First, there is a branching into excitons and charge carriers as the primary photoexcited species. Additionally, there is an increased, excitation energy dependent charge carrier yield from hot exciton dissociation during the first few ps. For monolayer MoS_2, due to the higher exciton binding energy [14], we can expect both CPG processes to have a lower yield. According to our findings, the efficiency of MoS_2 photovoltaic [17] and photodetector [18] devices depends significantly on the excitation wavelength and can be strongly increased, especially in monolayer devices, by facilitating exciton dissociation, e. g. via a strong built-in field using appropriate electrode materials, by engineering a p-n junction [54], [55] , or by combining MoS_2 with a second material [56-58] so one of them acts as electron donor and the other as acceptor in a heterojunction.

References:

[1] Coleman, J. N. *et al.* Two-Dimensional Nanosheets Produced by Liquid Exfoliation of Layered Materials. *Science* 331, 568–571, 2011.

[2] Nicolosi, V.; Chhowalla, M.; Kanatzidis, M. G.; Strano, M. S.;Coleman, J. N. Liquid Exfoliation of Layered Materials. *Science* 340, 1420, 2013.

[3] Wang, Q. H.; Kalantar-Zadeh, K.; Kis, A.; Coleman, J. N.; Strano, M. S. Electronics and optoelectronics of two-dimensional transition metal dichalcogenides. *Nature Nanotech.* 7, 699-712, 2012.

[4] Butler, S. Z. *et al. ACS Nano* 7, 2898-2926, 2013.

[5] Sipos, B.; Kusmartseva, A. F.; Akrap, A.; Berger, H.; Forro, L.; Tutis, E. From Mott state to superconductivity in 1*T*-TaS_2. *Nature Mater.* 7, 960-965, 2008.

[6] Thomson, R.; Burk, B.; Zettl., A.; Clarke, J. Scanning tunneling microscopy of the charge-density-wave structure in 1*T*-TaS_2. *Phys. Rev. B* 49, 16899–16916, 1994.

[7] Stojchevska, L.; Vaskivskyi, I.; Mertelj, T.; Kusar, P.; Svetin, D.; Brazovskii, S.; Mihailovic, D. Ultrafast Switching to a Stable Hidden Quantum State in an Electronic Crystal. *Science* 344, 177-180, 2014.

[8] Radisavljevic, B.; Radenovic, A.; Brivio, J.; Giacometti, V.; Kis, A. Single-layer MoS_2 transistors. *Nature Nanotech.* 6, 147–150, 2011.

[9] Radisavljevic, B.; Whitwick, M. B.; Kis, A. Integrated circuits and logic operations based on single-layer MoS_2. *ACS Nano* 5, 9934–9938, 2011.

[10] Frindt, R. F.; Yoffe A. D. Physical Properties of Layer Structures: Optical Properties and Photoconductivity of Thin Crystals of Molybdenum Disulphide. *Proc. Roy. Soc. A* 273, 69-83, 1962.

[11] Mak, K. F.; Lee, C.; Hone, J.; Shan, J.; Heinz, T. F. Atomically thin MoS_2: a new direct-gap semiconductor. *Phys. Rev. Lett.* 105, 136805, 2010.

[12] Splendiani, A.; Sun, L.; Zhang, Y.; Li, T.; Kim, J.; Chim, C.-Y.; Galli, G.; Wang, F. Emerging photoluminescence in monolayer MoS_2. *Nano Lett.* 10, 1271–1275, 2010.

[13] Evans, B. L.; Young, P. A. Exciton spectra in thin crystals: the diamagnetic effect. *Proc. Phys. Soc.* 91, 475-482, 1967.

[14] Ramasubramaniam, A. Large excitonic effects in monolayers of molybdenum and tungsten dichalcogenides. *Phys. Rev. B* 86, 115409, 2012.

[15] Cheiwchanchamnangij, T.; Lambrecht, W. R. L. Quasiparticle band structure calculation of monolayer, bilayer, and bulk MoS_2. *Phys. Rev. B* 85, 205302-1-4, 2012.

[16] Ye, Z.; Cao, T.; O'Brien, K.; Zhu, H.; Yin, X.; Wang, Y.; Louie, S. G.; Zhang, X. Probing excitonic dark states in single-layer tungsten disulphide. *Nature* 513, 214-218, 2014.

[17] Fontana, M.; Deppe, T.; Boyd, A. K.; Rinzan, M.; Liu, A. Y.; Paranjape, M.; Barbara, P. Electron Hole Transport and Photovoltaic Effect in Gated MoS2 Schottky Junctions. *Sci.Rep.* 3, 1634, 2013.

[18] Lopez-Sanchez, O.; Lembke, D.; Kayci, M.; Radenovic, A.; Kis, A. Ultrasensitive Photodetectors Based on Monolayer MoS_2. *Nat. Nanotechnol.* 8, 497–501, 2013.

[19] Mak, K. F.; He, K.; Lee, C.; Lee, G. H.; Hone, J.; Heinz, T. F.; Shan, J. Tightly Bound Trions in Monolayer MoS2. *Nat. Mater.* 12, 207–211, 2012.

[20] Mouri, S.; Miyauchi, Y.; Matsuda, K. Tunable Photoluminescence of Monolayer MoS2 via Chemical Doping *Nano Lett.* 13, 5944-5948, 2013.

[21] Scheuschner, N.; Ochedowski, O.; Kaulitz, A. M.; Gillen, R.; Schleberger, M., Maultzsch, J. Photoluminescence of freestanding single- and few-layer MoS_2. *Phys. Rev. B* 89, 125406, 2014.

[22] Dean, N.; Petersen, J. C.; Fausti, D.; Tobey, R. I.; Kaiser, S.; Gasparov, L. V.; Berger, H.; Cavalleri, A.; Polaronic Conductivity in the Photoinduced Phase of 1*T*-TaS_2. *Phys. Rev. Lett.* 106, 016401, 2011.

[23] Osterbacka, R.; An, C.; Jiang, X.; Vardeny, Z. Two-Dimensional Electronic Excitations in Self-Assembled Conjugated Polymer Nanocrystals. *Science* 287, 839−842, 2000.

[24] Klimov, V. I.; Ivanov, S. A.; Nanda, J.; Achermann, M.; Bezel, I.; McGuire, J. A.; Piryatinski, A. Single-exciton optical gain in semiconductor nanocrystals *Nature* 447, 441−446, 2007.

[25] Cabanillas-Gonzalez, J.; Virgili, T.; Gambetta, A.; Lanzani, G.; Anthopoulos, T. D.; de Leeuw, D. M. *Phys. Rev. Lett.* 96, 106601, 2006.

[26] Gadermaier, C.; Menna, E.; Meneghetti, M.; Kennedy, W. J.; Vardeny, Z. V.; Lanzani, G. Long-Lived Charged States in Single-Walled Carbon Nanotubes. *Nano Lett.* 6, 301−305, 2006.

[27] Gatensby, R.; McEvoy, N.; Lee, K.; Hallam, T.; Berner, N. C.; Rezvani, E.; Winter, S.; O'Brian, M.; Duesberg, G. S. Controlled synthesis of transition metal dichalcogenide thin films for electronic applications. *Appl. Surf. Sci.* 297, 139-146, 2014.

[28] Lee, C.; Yan, H.; Brus, L. E.; Heinz, T. F.; Hone, J.; Ryu, S.; Anomalous Lattice Vibrations of Single- and Few-layer MoS_2. *ACS Nano* 4, 2695-2700, 2010.

[29] Li, H.; Zhang, Q.; Yap, C. C. R.; Tay, B. K.; Edwin, T. H. T.; Olivier, A.; Baillargeat, D.; From Bulk to Monolayer MoS_2: Evolution of Raman Scattering. *Adv. Funct. Mater.* 22, 1385-1390, 2012.

[30] Shi, H.; Yan, R.; Bertolazzi, S.; Brivio J.; Bao, G.; Kis, A.; Jena, D., Xing, H. G.; Huang, L. Exciton Dynamics in Suspended Monolayer and Few-Layer MoS_2 2D Crystals. *ACS Nano* 7, 1072-1080, 2013.

[31] Mai, C.; Barrette, A.; Yu, Y.; Semenov, Yu. G., Kim, K. W.; Cao, L.; Gundogdu, K. Many-Body Effects in Valleytronics: Direct Measurement of Valley Lifetimes in Single-Layer MoS_2. *Nano Lett.* 14, 202-206, 2014.

[32] Sercombe, D., Schwarz, S., Del Pozo-Zamudio, O.; Liu, F.; Robinson, B. J.; Chekhovich, E. A.; Tartakovskii, I. I.; Kolosov, O.; Tartakovskii, A. I. Optical investigation of the natural electron doping in thin MoS_2 films deposited on dielectric substrates. *Sci. Rep.* 3, 3489, 2013.

[33] Plechinger, G.; Schrettenbrunner, F.-X.; Eroms, J.; Weiss, D.; Schuller, C.; Korn, T. Low-temperature photoluminescence of oxide-covered single-layer MoS_2. *Phys. Stat. Sol. RRL* 6, 126-128, 2012.

[34] Gutierrez, H. R. et al. Extraordinary Room-Temperature Photoluminescence in Triangular WS_2 Monolayers. *Nano Lett.* 13, 3447-3454, 2013.

[35] Yadgarov, L.; Choi, C. L.; Sedova, A.; Cohen, A.; Rosentsveig, R.; Bar-Elli, O.; Oron, D., Dai, H.; Tenne, R. Dependence of the Absorption and Optical Surface Plasmon Scattering of MoS_2 Nanoparticles on Aspect Ratio, Size, and Media. *ACS Nano* 8, 3575-3583, 2014.

[36] Soavi, G.; Scotognella, F.; Brida, D.; Hefner, T.; Späth, F.; Antognazza, M. R.; Hertel, T.; Lanzani, G.; Cerullo, G. Ultrafast Charge Photogeneration in Semiconducting Carbon Nanotubes. *J. Phys. Chem. C* 117, 10849-10855, 2013.

[37] Sim, S.; Park, J.; Song, J.-G.; In, C.; Lee, Y.-S.; Kim, H.; Choi, H. Exciton dynamics in atomically thin MoS_2: Interexcitonic interaction and broadening kinetics. *Phys. Rev. B* 88, 075434-1-5, 2013.

[38] Tränkle, G.; Lach, E.; Forchel, A.; Scholz, F.; Ell, C.; Haug, H.; Weimann, G.; Griffiths, G.; Kroemer, H.; Subbanna, S. General Relation between Band-Gap Renormalization and Carrier Density in Two-Dimensional Electron-Hole Plasmas. *Phys. Rev. B* 36, 6712-6714, 1987.

[39] Wang, Q.; Ge, S.; Li, X.; Qiu, J.; Ji, Y.; Feng, J.; Sun, D. Valley Carrier Dynamics in Monolayer Molybdenum Disulfide from Helicity-Resolved Ultrafast Pump-Probe Spectroscopy. *ACS Nano* 7, 11087-11093, 2013.

[40] Ugeda, M. M. et al. Giant bandgap renormalization and excitonic effects in a monolayer transition metal dichalcogenide semiconductor. *Nature Mater.* advance online publication.

[41] Ouyang, Q. Y.; Yu, H. L.; Zhang, K.; Chen, Y. J. Saturable absorption and the changeover from saturable absorption to reverse saturable absorption of MoS_2 nanoflake array films. *J. Mater Chem C* 2, 6319-25, 2014.

[42] Kozawa, D. et al. Photocarrier relaxation pathway in two-dimensional semiconducting transition metal dichalcogenides. *Nature Commun.* 5, 4543-1-5, 2014.

[43] Gadermaier, C.; Cerullo, G.; Sansone, G.; Leising, G.; Scherf, U.; Lanzani, G. Time-Resolved Charge Carrier Generation from Higher Lying Excited States in Conjugated Polymers. *Phys. Rev. Lett.* 89, 117402, 2002.

[44] Noolandi, J.; Hong, K. M. Theory of photogeneration and fluorescence quenching. *J. Chem. Phys.* 70 3230-3236, 1979.

[45] Arkhipov, V. I., Emilianova, E. V., Bassler, H. Hot exciton dissociation in a conjugated polymer. *Phys. Rev. Lett.* 82, 1321-1324, 1999.

[46] Leitenstorfer, A.; Furst, C.; Laubereau, A.; Kaiser, W.; Trankle, G.; Weimann, G. Femtosecond carrier dynamics in GaAs far from equilibrium. *Phys. Rev. Lett.* 76, 1545-1548, 1996.

[47] Sun, D.; Wu, Z.-K.; Divin, C.; Li, X.; Berger, C.; de Heer, W. A.; First, P. N., Norris, T. B.; Ultrafast Relaxation of Excited Dirac Fermions in Epitaxial Graphene Using Optical Differential Transmission Spectroscopy. *Phys. Rev. Lett.* 101, 157402-1-4, 2008.

[48] Gadermaier, C. *et al.* Strain-Induced Enhancement of the Electron Energy Relaxation in Strongly Correlated Superconductors. *Phys. Rev. X* 4, 011056-1-6, 2014.

[49] Dhar, L.; Roger, J. A.; Nelson, K. A. Time-Resolved Vibrational Spectroscopy in the Impulsive Limit. *Chem. Rev.* 94, 157-193, 1994.

[50] Mai, C.; Barrette, A.; Yu, Y. F.; Semenov, Y. G.; Kim K. W.; Cao, L. Y.; Gudnogdu, K. Many-Body Effects in Valleytronics: Direct Measurement of Valley Lifetimes in Single-Layer MoS_2. *Nano Lett.* 14, 202-206, 2014.

[51] Lagarde, D.; Bouet, L.; Marie, X.; Zhu, C. R.; Liu, B. L.; Amand, T.; Tan, P. H.; Urabaszek, B. Carrier and Polarization Dynamics in Monolayer MoS_2. *Phys. Rev. Lett.* 114, 047401-1-4, 2014.

[52] Assael, M. J.; Botsios, S.; Gialou, J.; Metaxa, I. N. Thermal Conductivity of Polymethyl Methacrylate (PMMA) and Borosilicate Crown Glass BK7. *Int. J. Thermophys.* 26, 1595-1605, 2005.

[53] Sun, Q. C.; Yadgarov, L.; Rosentsveig, R.; Seifert, G.; Tenne, R.; Musfeldt, J. L.; Observation of a Burstein-Moss Shift in Rhenium-Doped MoS_2 Nanoparticles. *ACS Nano* 7, 3506-11, 2013.

[54] Pospischil, A.; Furchi, M. M.; Mueller, T. Solar-energy conversion and light emission in an atomic monolayer p-n diode. *Nature Nanotech* 9, 257-261, 2014.

[55] Bauger, B. W. H.; Churchill, H. O. H.; Yang, Y. F., Jarillo-Herrero, P. Optoelectronic devices based on electrically tunable p-n diodes in a monolayer dichalcogenide. *Nature Nanotech.* 9, 262-267, 2014.

[56] Britnell, L. *et al.* Strong Light-Matter Interactions in Heterostructures of Atomically Thin Films. *Science* 340, 1311-1314, 2013.

[57] Lee, C.-H. et al. Atomically thin p-n junctions with van der Waals heterointerfaces. *Nature Nanotech.* 9, 676-681, 2014.

[58] Hong, X.; Kim, J.; Shi, S.-F.; Zhang, Y.; Jin, C.; Sun, Y.; Tongay, S.; Wu, J.; Zhang, Y.; Wang, F. Ultrafast charge transfer in atomically thin MoS_2/WS_2 heterostructures. *Nature Nanotech.* 9, 682-686, 2014.

For wider interest

MoS_2 – layered semiconducting crystal, which consist of layers with strong in-plane chemical (covalent or ionic) bonds and relatively weak (van der Waals) adhesion between these layers. A single sheet of MoS_2 absorbs more than 5% of the incident light in the visible range. This means that an extremely small amount of material – deposited on a transparent electrode or blended into a transparent polymer – could be efficient for the fabrication of a low-cost, lightweight solar cell that can be applied to many irregular surfaces. Such versatility has so far been the reserve of organic photovoltaics, which is still struggling with photodegradation.

In order to find out how to use semiconducting TMDs for photovoltaics, we need to understand what goes on when they absorb light. Since the expected processes are very fast (occuring in less than a nanosecond or sometimes even less than a picosecond), we use ultrafast lasers to study them. In what we call pump-probe spectroscopy, a first laser pulse of approximately 100 fs duration excites the sample, creating a population of electrons and holes (electron vacancies) at a very well defined point in time, which marks the start for all relaxation processes occurring after excitation. A second, weaker but similarly short laser pulse probes the optical absorption of the sample at a defined point in time after the excitation, which is different for an excited sample compared to a sample in equilibrium. By varying the pump-probe delay we can follow the relaxation processes.

First results on prototype photovoltaic elements of monolayer MoS2 have indicated that their efficiency is limited by the strong interaction between the photoexcited electrons and holes, which hampers their extraction from the device. Here we show that in few-layer MoS2 flakes dispersed in tranparent plastic the separation of electrons and holes is very efficient (close to 100%) and occurs on a time scale of 700 fs. This result suggests that few-layer MoS2, which is even easier to obtain than monolayers, is actually more suitable for photovoltaics.

Non- destructive Analysis of Archaeological Metals

Helena Fajfar[1,2,3], **Zdravko Rupnik**[1], **Žiga Šmit**[1,4]

[1] Department of Low and Medium Energy Physics, Jožef Stefan Institute, Ljubljana, Slovenia

[2] Jožef Stefan International Postgraduate School, Ljubljana, Slovenia

[3] JUVI Domžale d.o.o., Domžale, Slovenia

[4] Faculty of Mathematics and Physics, University of Ljubljana, Ljubljana, Slovenia

helena.fajfar@ijs.si

Abstract. Ion beam analysis is an efficient method for studies of archaeological metals. It is based on excitation of characteristic X-rays and gamma rays. In this paper we present PIXE and PIGE analysis of different metal alloys. Spot analysis was used for analysis of bronzes, which were used for medieval early fiery weapons. In the second part of the paper, the inhomogeneous metal objects are examined. The external beam facility was improved for the mapping measurements, which allow detection of inhomogeneous gilded layers. The new system allows the external beam to be scanned over an area of a few cm^2.

Keywords: PIXE, PIGE, metals, mapping

1 Introduction

Archaeological metals are important testimony of human past. Material identification is basic objective of scientific characterization of ancient objects and provides important clues about fabrication. Elemental analysis of metals provides valuable information about the composition of alloys and may lead to identifying the metal origin. Analytical data on metal composition may also provide interesting insight into past technologies, including mining, melting and metal working [1]. When a unique artefact is found, the analytical methods are required of being non-destructive and able to give the chemical analysis without sampling. PIXE and PIGE methods allow us detection of major, minor and trace elements. An advantage of PIXE compared to other IBA methods is its speed and sensitivity.

Up to now only spot analysis was used in our studies of archaeological metals [2, 3]. In the present paper we report about further development of the method applied on historical metals. The spot analysis was used to measure medieval bronzes of early weapons. Recent development includes application of mapping, using an in-air beam. The new mapping system allows us to provide elemental concentration maps from the PIXE spectra. As an example of metal inhomogeneous composition we studied the structure of a bronze-iron alloy known as aes rude. From the map of a gilded medieval fragment it is possible to identify the metal plating technique.

2 Experimental

The 2 MV particle accelerator at the Microanalytical Center of the Jožef Stefan Institute is equipped with four measuring lines. One line allows measurements with in-air proton beam. The method of Proton Induced X-ray Emission (PIXE) and Particle Induced Gamma-ray Emission (PIGE) were used. PIXE is a non-destructive analytical method. The characteristic X-rays are emitted while filling the inner shell vacancies created by proton bombardment. The respective X-rays intensities are directly related to the concentrations of the corresponding elements. PIXE is used for elements with $Z>12$. For light elements we used gamma rays, because with PIGE we can see deeper below surface. The nominal energy of protons in our measurements was 3 MeV. The beam intensity was a few nA and the counting rate was below 500 cps. The beam was extracted into air through a 2 μm thick tantalum foil. The induced X-ray passed through a 6.0 cm air gap between the target and a Si(Li) detector. The beam profile at the target was Gaussian, with 0.8 mm full width at half maximum. For spot analysis, three spectra were taken in a particular measuring point. The measurement in air provided X-rays of the elements heavier than silicon. For hard X-rays around silver, a 0.3 mm thick aluminum absorber was used. After measuring with the aluminum absorber we repeated the measurement using a selective filter of cobalt, which provided better sensitivity for iron and nickel. The measuring time for one sample was around 7 minutes. The spectra were fitted using the AXIL software package.

The new system for mapping allows the external beam to be scanned over an area of a few cm^2. The sample is fixed on a remote controlled stage driven by high precision stepping motors. After selecting the area of interest of the sample and setting the scanning conditions, the measurement can start. During the scanning process, the measurement process is executed through the following steps: moving the sample to the selected position, acquiring the data, saving the spectra and finally moving the sample to the next position. After measurements the PIXE spectra were processed with the AXIL program and the elemental concentrations were calculated by the program [4]. The elemental maps were performed on the most typical elements for metals and were built up by program ORIGIN 8.0. The images were composed of 10 x 7 points and 10 x 20 points, so the scanned area measured 10 mm x 7 mm and 1 cm x 2 cm. The accuracy of the procedure was within 5% for major elements, about 10% for the elements with concentrations below 1%, and about 15% for trace elements.

3 Results

3.1 Medieval bronzes for weapons

Medieval weaponry spanned a range from simple tools and farm implements to sophisticated siege engines. Europeans certainly had firearms by the first half of the 1300s. In army different kind of weapons were used. One of them was called handgonne or hand cannon. The hand cannon was a simple weapon, effectively consisting of a barrel with some sort of handle, and it came in different shapes and sizes. It was constructed of metal and attached to some kind of stock, usually wooden. Due to the poor quality of powder that was often used in these weapons and their crude construction, they were not effective missile weapons, as early examples often lacked sufficient power to punch through light armor [5, 6].

Three different fragments of handgonnes were measured (Table 1). They were all found in south Slovenia in the vicinity of castle ruins [7]. The tin concentration in all samples was lower than 5%. With such a low concentration of tin the alloys remains tough, i.e. not too hard and not too fragile. Samples also contained antimony (0.87% - 2.66%) and arsenic (0.61% - 2.20%), so we can conclude that the copper was extracted from polymetallic ores tennantite and tetrahedrite ($(\mathrm{(Cu,Fe)_{12}Sb_4S_{13}})$). The sample no. 1 (Fig. 1) contained 9.46% Pb. Lead has the effect of making the alloys of copper easier to cast. Such a high concentration (sample no.1) improved the fluidity of the alloy in the melt, but reduced the mechanical strength of the metal. In sample no. 2 we detected 1.71% Pb. It is generally accepted that such a small concentration is impurity in the raw materials and has not been added intentionally. The highest concentration of zinc was in the sample no. 3 (4.63%) and the lowest in sample no. 1 (0.71%). We believe that there were different reasons for the explosion of handgonnes. For sample no. 1 and 2 it was certainly the quality of material. No. 1 contains only about 4% Sn, which in a pure Cu-Sn alloy would make the metal ductile, however, the presence of 2.66% antimony and 9.46% lead would render material with worse material properties, especially as such an amount of lead cannot dissolve in copper but forms distinct globules. According to their composition, bronzes no. 1 and 2 are quite similar to the alloys used in Late Bronze Age, so it is not impossible the material was collected from a prehistoric hoard. It is only no. 3 that contains about 4-5% tin and zinc that qualify it as gunmetal. It was the use of improved gunpowder in granular form that turned out fatal for many early fiery weapons [5]. The bore in no. 3 is not cylindrical, but slightly spherical as an indication of being blown up. In this case the reason for explosion might not be material, but imprecise, non-centred boring.

Table 1: Analysis of three pieces of handgonnes (in mass %)

No./Location	Caliber [mm]	Fe	Ni	Cu	Zn	As	Ag	Sn	Sb	Pb
1. Čretež	25	0.15	0.37	82.0	0.71	0.61	0.14	3.95	2.66	9.46
2. Kostel	13	1.61	2.53	85.6	0.80	2.20	0.29	3.93	1.37	1.71
3. Šumberk	16	0.67	0.48	85.2	4.63	0.68	0.20	3.61	0.87	3.68

Figure 1: Fragments of three different handgonnes from south Slovenia.

3.2 Aes rude

The AES RUDE (raw bronze) indicates cast bronze used in Italy between the 8th and 4th centuries BC. In that time a pre-monetary system was valid in Italy, which featured bronze or copper ingots cast in a rough shape, which the Romans called aes. Different forms of these metals were found. The oldest specimens were just worked lumps of copper or bronze. Rome obtained inspiration from the ingot shape to establish its own currency system. It was called aes signatum [8, 9]. It was based on ingots made of cast copper or bronze and stamped on each side.

A sample of aes rude from Košana, Slovenia was measured and traces amounts of As, Zn, Mo and Pb were detected. Zinc and arsenic impurities are correlated with copper. We also found out that the molybdenum is correlated with iron. Aes rude is technologically useless, so the metal ingots that circulated among prehistoric settlements were either intended for further processing or they were just used for commercial exchange. The scanning area of the sample was 7 x 10 mm.

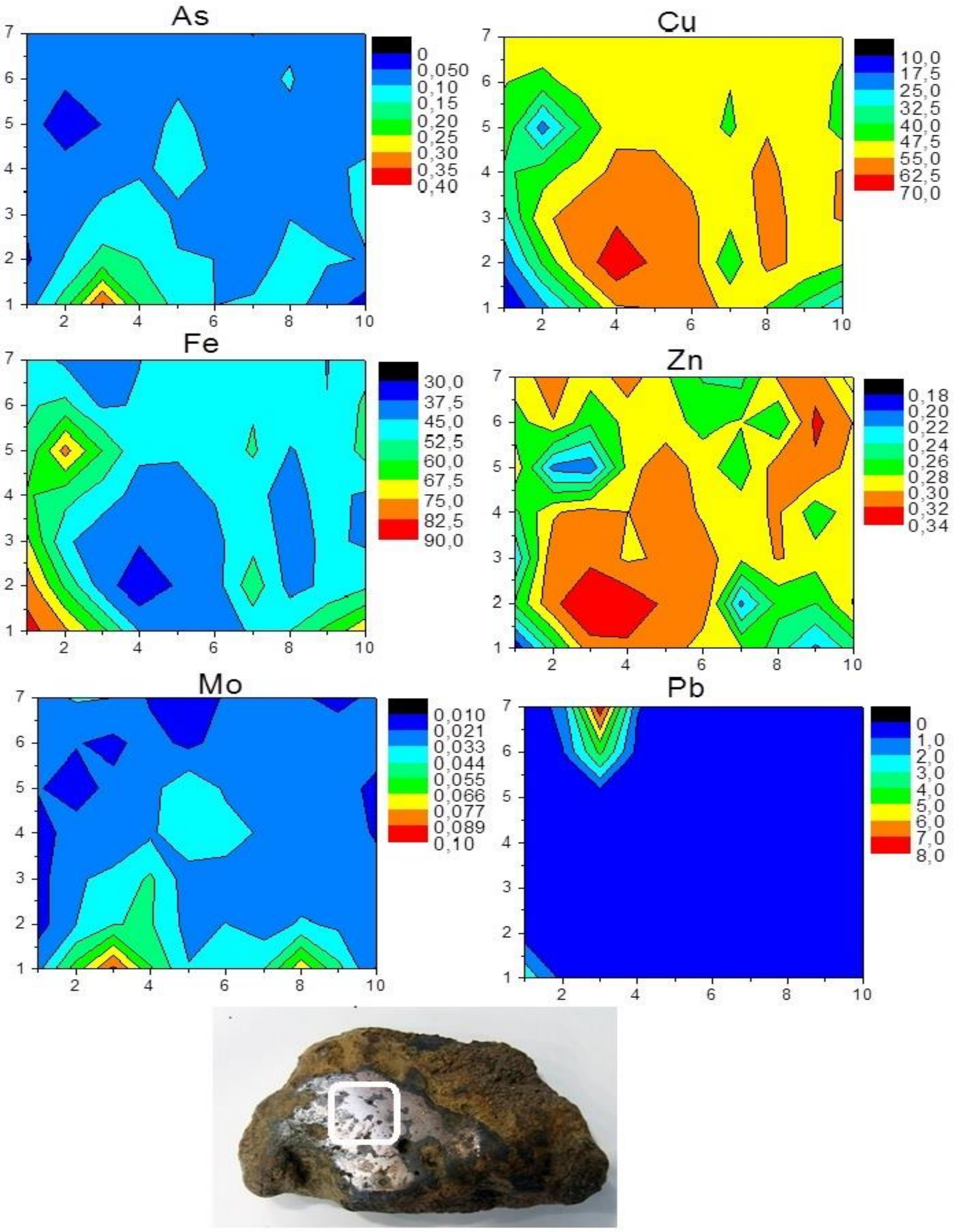

Figure 2: Elemental maps on the sample of aes rude. The scanning area was 10 mm x 7 mm. The color scale reflects weight %.

3.3 Gilded fragments

Gilding is application of gold to the surface of some other material. In Roman and medieval period the gilding techniques included the process of fire gilding, depletion gilding, application of golden leaves and dipping into molten gold [10, 11]. Fire gilding is also known as amalgamation gilding or mercury gilding [11-14]. This type of gilding was often used to gild small areas of the object, yet the gilding spread over the edge of the intended area. For this process small gold fragments were first dissolved in liquid mercury at a moderate temperature to obtain an amalgam, and that amalgam was applied onto the metal object which was then heated to a temperature higher than the mercury boiling point (356.5°C) in order to evaporate it. In practice, the objects to be gilded generally made of copper, bronze or brass were first coated and then heated with the amalgam decomposed. Amalgamation gilding was used extensively in the Roman and medieval period. The depletion gilding is a method for producing a layer of nearly pure gold on an object made of low-grade gold alloy by removing less noble metals from its surface. The surface was etched with acids, resulting in a surface of porous gold. The porous surface is then remelted, resulting in a shiny gold surface.

In Fig. 3, analysis of a medieval fragment from Kolovec, Slovenia (probably part of a cross, dating to 14th - 15th century and showing the scene of annunciation) is presented. High concentration of mercury in the range up to 11% indicates that the technique used was fire gilding. The object was made of copper (the lowest concentration was 30%). The correlated maps of gold and mercury confirm that the method of amalgamation was applied. The concentration of gold reached up to 55% at the surface. The silver content in this sample was low (< 1%). The silver is correlated with gold, which shows it was an admixture to gold before an amalgam was made.

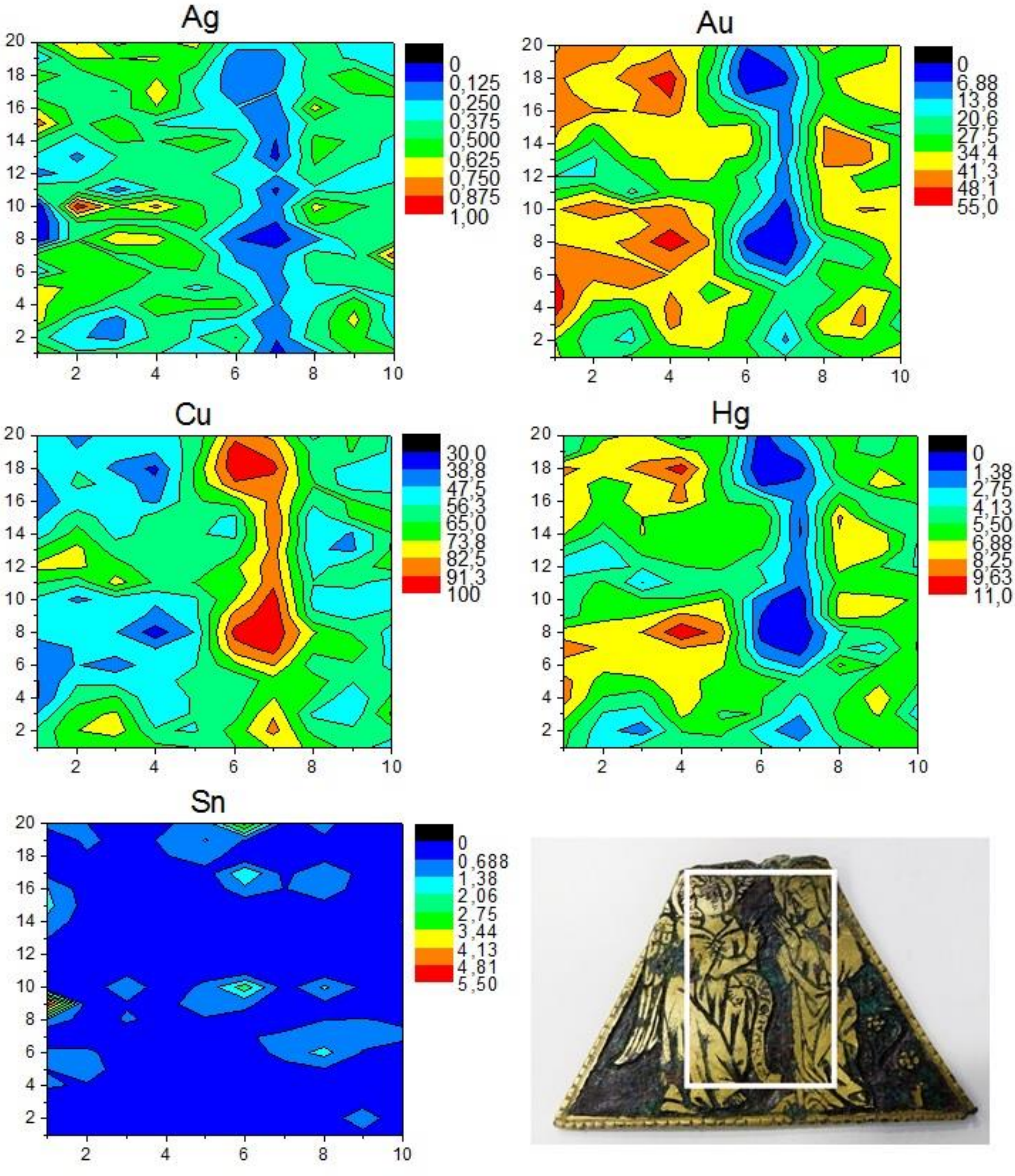

Figure 3: Elemental maps of the fragment of a cross showing the scene of Annunciation. The color scale is in weight %. The scanning area was 10 x 20 mm.

4 Conclusion

Ion beam analysis techniques were used to characterize metals of cultural heritage objects. With spot analysis three bronzes of medieval weapons were measured. They are of low quality, with large amounts of added impurities. More information about the sample composition can be obtained with mapping. Elemental mappings provide more information, because we investigate a large area of the sample. The correlated maps of gold and mercury on the fragment of medieval cross indicated that the method of amalgamation was applied.

References:

[1] M. F. Guerra, I. Tissot, The role of nuclear microprobes in the study of technology, provenance and corrosion of cultural heritage: The case of gold and silver items, *Nucl. Instr. Meth.* B 306: 227-251, 2013.

[2] Ž. Šmit, J. Istenič, V. Gerdun, Z. Milić and A. Mladenović, Archaeometric analysis of Alesia group brooches from sites in Slovenia, *Arheološki vestnik* 56: 213-233, 2005.

[3] Ž. Šmit, J. Istenič and S. Perovšek, PIXE analysis of Late La Tėne scabbards with non-ferrous openwork plates (and associated swords) from Slovenia, *Arheološki vestnik,* 61: 165-173, 2010.

[4] Ž. Šmit, P. Pelicon, J. Simčič, J. Istenič, Metal analysis with PIXE: The case of Roman military equipment, *Nucl. Instr. Meth. B* 239: 94-99, 2005.

[5] I. V. Hogg, The story of the gun, New York, 1996.

[6] *http://www.handgonne.com*, [access, December 2014].

[7] Ž. Šmit, Strelna cev, *Vojnozgodovinski zbornik* 28, 2007.

[8] E. A. Sydenham, Aes Grave, a Study of the Cast Coinages of Rome and Central Italy, London, 1926.

[9] *http://www.nbbmuseum.be,* [access, December 2014].

[10] Ž. Šmit, J. Istenič, T. Knific, Plating of archaeological metallic objects – studies by differential PIXE, *Nucl. Instr. Meth.* B 266: 2329-2333, 2008.

[11] S. L. Niece, in Metal Plating and Patination, Butterworth-Heinemann, 1993.

[12] K.N. Lechtman, Ancient methods of gilding silver: examples from the old and new worlds, In *Science and Archaeology, Cambridge,* 1971.

[13] T. Trojek, M. Hložek, X-ray fluorescence analysis of archaeological finds and art objects: Recognizing gold and gilding, *Applied Radiation and Isotopes,* Vol. 70: 1420-1423, 2012.

[14] V. Corregidor, L.C. Alves, N.P. Barradas, M.A. Reis, M.T. Marques, J.A. Ribeiro, Characterization of mercury gilding art objects by external proton beam, *Nucl. Instr. Meth.* B 269: 3049-3053, 2011.

For wider interest

Material identification is basic objective of scientific characterization of ancient objects and provides important clues about fabrication. The chemical composition of ancient objects is important for their authentication. The nature as well as the relative amounts of major, minor, and trace elements in any object are useful for determining the authenticity and production details of ceramics, glass, or metal alloys. We can use different analytical methods for the determination of cultural heritage objects and objects of art. In our measurements we used only non-destructive techniques.

The measurements are executed at the Tandetron accelerator, using proton beam in-air, so the analysis is generally done without sampling. Our methods are X-ray and gamma ray spectroscopy. Particle-induced X-ray emission (PIXE) and Particle-induced gamma-ray emission (PIGE) are non-destructive spectroscopic methods for analyzing different materials, especially useful for archaeological objects. This is a good choice if the chemical composition of an unknown substance is to be determined quickly. Liquid, solid and powdered samples can be analyzed. Soft X rays are absorbed in the air gap between target and detector. For this reason, PIXE is useless for soft element analysis. For light elements we measure gamma yields rather than X- rays. With PIGE we can analyze deeper below surface. The elements emit gamma photons after the collisions with protons. Photon energies vary between 100 keV and 2 MeV. Measuring the gamma spectra with PIGE, we obtain relative photon yields of light elements with respect to the standard. The X-ray and gamma ray data are then recalculated into concentrations simultaneously, estimating the matrix effects by an iterative procedure.

Up to now only spot analysis was used in our studies of archaeological metals. The new system for mapping allows the external beam to be scanned over an area of a few cm^2. The sample is fixed on a remote controlled stage driven by high precision stepping motors. The measurement starts with the selection of an area of interest and setting the initial conditions. The scanning process is based on the following cycles: moving the sample, data acquisition, saving the spectra, and moving to the next measuring point. Elemental mappings provide more information, because we investigate a large area of the sample.

Solution-derived Ta_2O_5 high-*K* thin films for gate dielectric applications

Raluca C. Frunză[1,2], Pedro Barquinha[3], Hermine Stroescu[4], Măriuca Gartner[4], Barbara Malič[1]

[1] Jožef Stefan Institute, Ljubljana, Slovenia
[2] Jožef Stefan International Postgraduate School, Ljubljana, Slovenia
[3] CENIMAT-I3N, Departament of Material Science and CEMOP/UNINOVA, Faculty of Science and Technology, Caparica, Portugal
[4] Ilie Murgulescu Institute of Physical Chemistry of the Romanian Academy, Bucharest, Romania

raluca.frunza@ijs.si

Abstract. Ta_2O_5 is a promising high-*K* dielectric, due to its high refractive index, high dielectric permittivity (in the range 22-28 for the amorphous state) and good thermal and chemical stability. The present study reports the preparation of solution-derived Ta_2O_5 thin films processed at low temperatures suitable for applications in transparent electronics. The investigated thin films exhibited promising properties for capacitors and thin-film transistors.

Keywords: Ta_2O_5, amorphous high-*K* dielectrics, sol-gel chemistry

1 Introduction

Transparent electronics emerges as a promising technology distinct from the conventional silicon one, and its viability depends on the performance, reliability and cost of both passive and active electronic applications. A lot of effort has been put in the research and development of transparent thin-film transistors (TFTs), which are mainly used as on-off switches in active matrix backplanes of flat panel displays. Their main components are a semiconductor layer, three electrodes, *i.e.*, gate, source and drain, and a dielectric layer between the gate and the semiconductor, also referred to as the gate dielectric. All of them are deposited in the form of thin films onto an insulator substrate. A TFT is a special type of field-effect transistor and its

working principle relies on the modulation of the current flowing in the semiconductor.
The development of transparent TFTs requires among other also high-quality amorphous high-*K* dielectrics processed at low temperatures, and tantalum-pentoxide thin films are of great interest.

The Ta_2O_5-based thin films presented herein were deposited from solution on selected substrates and were processed at temperatures not exceeding 400 °C. The influence of the processing temperature upon the structural and electrical properties of films was investigated. Their functionality was tested in passive and active electronic devices, namely thin film capacitors and TFTs.

2 Experimental details

The precursor was prepared by alkoxide-based sol gel synthesis. Further details on solution preparation and processing can be found elsewhere [1]. Thin films were deposited on platinized silicon ($Pt/TiO_2/SiO_2/Si$ or shortly Pt/Si) substrates by spin coating. After each deposition, the films were heated in air on the hot plates at 150 °C for 2 minutes and at 250, 300, 350 or 400 °C for additional 2 minutes. Note that as a typical high-*K* material, tantalum pentoxide begins to crystallize at 600 °C and it is crystalline above 700 °C [2]. In this study, the samples were processed at low temperatures, in order to ensure their amorphous structure, which is generally preferred in TFTs [3].

For all samples, the spinning–heating procedure was repeated ten times. The sample thickness values (estimated from the FE-SEM analysis of the fracture surfaces) decreased considerably with the processing temperature, from about 190 nm to about 115 nm for the samples heated at 250 °C and 400 °C, respectively. This was related to the process of densification [4].

The Fourier-transform infrared (FT-IR) analyses were performed using a Perkin Elmer Spectrum 100 FT-IR spectrometer. The transmittance data were collected in the range 4000-380 cm^{-1}, in the Attenuated Total Reflectance (ATR) mode. The spectrum of a bare Pt/Si substrate was measured as the background. All spectra were baseline corrected.

The samples were investigated by spectroscopic ellipsometry using a UV-Vis Variable Angle Spectroscopic Ellipsometer (VASE) with rotating analyzer from J.A. WOOLLAM. The experimental spectra were modelled as multi-layer structures given on the used substrate, rendering good agreement with the experimental data.

The surface morphology of the samples was analysed by an Asylum Research Molecular Force Probe 3D (MFP-3D-S™) atomic force microscope.

Au electrodes of 0.4 mm diameter were sputtered on top of the Pt/Si samples. Capacitance and loss factor, tan δ, were measured at room temperature with a driving signal of 50 mV, using a HP 4284A impedance analyzer. The relative permittivity values, ε, were calculated at the frequency of 100 kHz. The current–voltage characteristics were measured using a Keithley 2602A system sourcemeter and a HP 16058A test fixture combined setup. More details and comprehensive results are given in previous reports [1, 5].

Solution derived Ta_2O_5 dielectric thin films processed at 300 and 350 °C, of ≥ 250 nm, were used to fabricate TFTs with sputtered gallium indium zinc oxide (GIZO) channel layer [6]. The TFTs on Corning Eagle glass substrates had a width-to-length ratio (W/L) of 45 μm / 90 μm.

3 Results and discussion

To investigate the effect of the processing temperature on the chemical composition of the films deposited on Pt/Si, a FT-IR analysis was employed. The broad bands located below 1000 cm^{-1} are assigned to vibrations of Ta–O bonds [7, 8]. As expected, the bands that could be ascribed to residual functional groups became less distinct when increasing the heating temperature from 250 °C to 400 °C (see Fig. 1(a)). The band at 1100 cm^{-1}, which is presumably due to an overlapping of several vibrations belonging to residual organics, *i.e.*, to the C–C and C–O bending modes [7], was eliminated as some organics were decomposed upon heating at temperatures above 300 °C. Also, the signal of the modes due to the deformation of C–H (*i.e.*, at 1450 cm^{-1} and 1380 cm^{-1} in the case of the film processed at 250 °C) decreased with the processing temperature. The 350 °C sample showed an overlapped broader peak with a minimum at 1420 cm^{-1}, which was no longer visible in the spectrum of the sample heated at 400 °C. Even though the band at about 1600 cm^{-1}, presumably corresponding to the modes of adsorbed water and amino groups, was present in the spectra recorded for all the samples, its intensity decreased with the processing temperature. In addition, a shift towards lower wavenumbers from 1645 cm^{-1} to 1620 cm^{-1} for the samples heated at 250 °C and 400 °C, respectively, was observed. The broad band ranging up to 3600 cm^{-1}, with the minimum around 3200 cm^{-1}, corresponding to the stretching vibrations of water and hydroxyl groups (O−H) [7], could be assigned to residual H_2O.

Thereby, in the case of the samples processed at 400 °C, the presence of residual organic groups could not be excluded, however they could be detected in a much smaller amount as compared to the samples processed at lower temperatures.

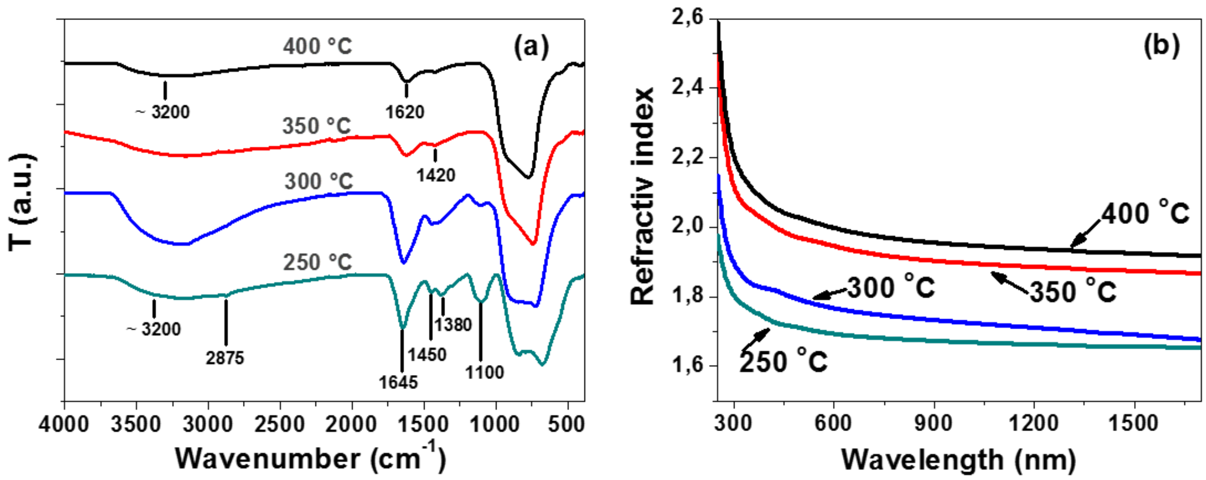

Figure 1: (a) FT-IR spectra of the Ta_2O_5 thin films prepared on Pt/Si and processed at the selected temperatures. (b) Refractive index dispersion of the thin films.

Spectroscopic ellipsometry measurements were also employed to determine the optical constants of the Ta_2O_5-based thin films. The determined refractive indices as a function of wavelength are given in Fig. 1(b). The refractive index increased with the processing temperature, in agreement with the consequent densification taking place at higher heating temperatures. The refractive index (at 600 nm) ranged from 1.7 to 1.99 for the samples processed at 250 °C and 400 °C, respectively. The Cauchy dispersion of the refractive index and its processing temperature dependence are in agreement with reports in the literature about solution-derived Ta_2O_5 thin films [3, 7, 9-11].

The surface morphology of the samples was characterized in terms of the root-mean-square (RMS) vertical roughness by AFM. The investigated thin films had uniform surface morphologies without any evident microstructural details, in agreement with their amorphous structure. The average vertical RMS surface roughness values were up to 0.3 nm. For a conclusive representation, the surface profiles were obtained from the topography images using an AFM software (*i.e.*, Igor Pro 6.34A). Typical AFM surface profiles are depicted in Fig. 2.

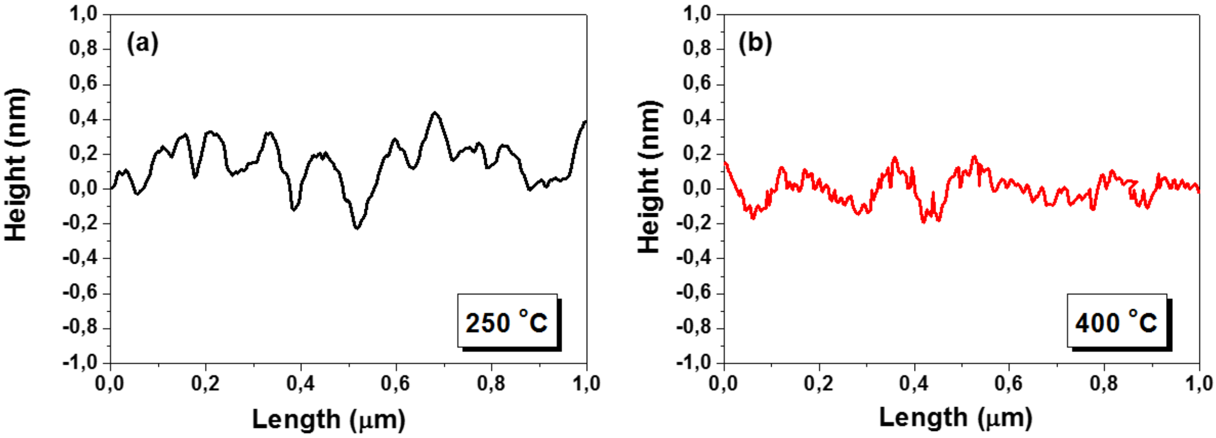

Figure 2: AFM surface profiles of the (a) 250 °C and (b) 400 °C samples.

These results are in agreement with other reports on chemical solution deposited thin films. In their study on Ta_2O_5 thin films prepared by metal-organic solution deposition technique, Joshi *et al.* [11] reported a smooth surface morphology of the films deposited on Pt/Si and no appreciable effect of the annealing temperature on their microstructure up to 600 °C.

The electrical properties of the metal-insulator-metal capacitors are given in Fig. 3. Amorphous Ta_2O_5 thin films have been reported to exhibit a relative dielectric permittivity in the range of 20 – 28 [2, 12]. In the current study, the highest permittivity value of 27 ± 2 was obtained for the film heated at 400 °C. However, a lower processing temperature led to an important and continuous decrease in the permittivity of the samples (see Fig. 3(a)). All samples exhibited dielectric losses up to about 5% at 100 kHz (Fig. 3(b)). The leakage currents of the investigated thin films increased with the processing temperature. The current density values measured at 160 kV/cm for all samples are given in Fig. 3(c).

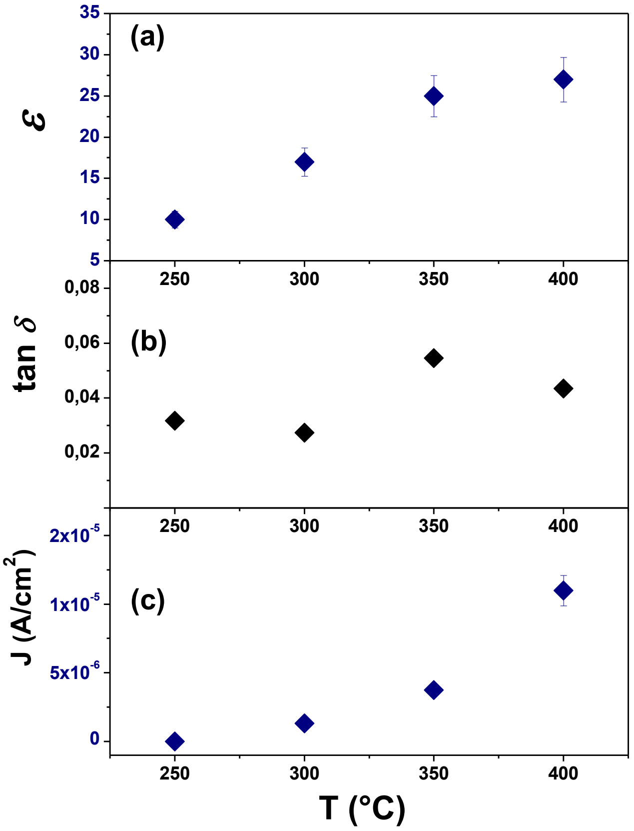

Figure 3: Electrical properties of the Ta_2O_5 thin films as a function of the processing temperature: (a) dielectric permittivity and (b) loss factor at 100 kHz, and (c) leakage current density at the applied field of 160 kV/cm.

Altogether, the electrical properties of the investigated samples depended on the thermal budget of the dielectric, and as previously shown, the optimal processing temperature should be at least 300 °C in order to ensure a good material yield. Therefore thin films processed at 300 and 350 °C were further employed in TFTs.

To evaluate the performance of the devices, the transfer characteristics (*i.e.*, the plots of the drain current (I_D) versus the gate voltage (V_G) at a constant drain voltage (V_D)) were recorded. Fig. 4 depicts the obtained plots together with two of the parameters that can be extracted from such curves. The *on/off* ratio is defined as the ratio of the maximum to the minimum drain current, and it evaluates the quality of the device from the point of view of an electronic switch application. It should be as large as possible, and values above 10^6 are typically reported [12]. The *subthreshold swing* (*S*) is the parameter that reflects the *gate voltage* required to increase *the drain current* by one decade, *i.e.*, it is the inverse of the maximum slope of the transfer characteristics. Small values of *S* ensure low power consumption of the device, and values of about 0.1-0.5 V/dec are generally required [13]. Compared to reports in the literature [14-16], the gate dielectrics from solution rendered high *on/off* values and low *subthreshold swing* values. The processing temperature of 350 °C rendered a slight improvement in terms of *field-effect mobility, i.e.,* 21 cm^2/V compared to the value of about 16 cm^2/V obtained for the TFT with the 300 °C dielectric.

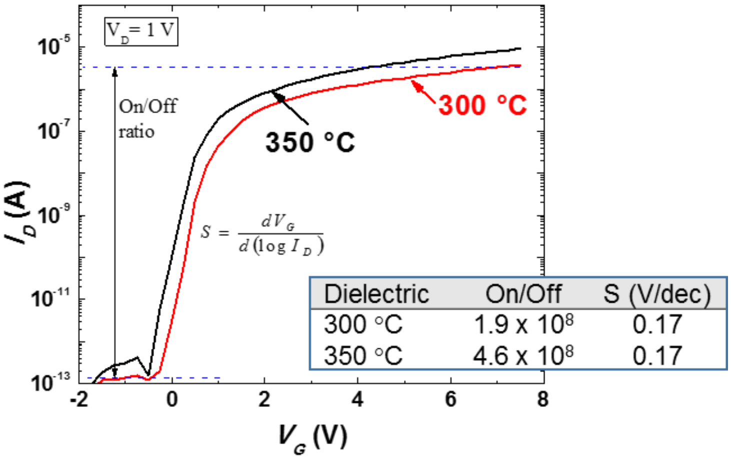

Dielectric	On/Off	S (V/dec)
300 °C	1.9×10^8	0.17
350 °C	4.6×10^8	0.17

Figure 4: Transfer characteristics of GIZO TFTs (W/L = 45/90) with the solution-processed Ta_2O_5 dielectrics, which were obtained at $V_D = 1V$. Some electrical properties extracted for these devices are given in the inset table.

4 Conclusions

Solution-derived Ta_2O_5 thin films were processed at temperatures not exceeding 400 °C. The amorphous thin films exhibited smooth and flat surfaces with low average roughness values. Residues of functional groups remained in the films upon heating at 250 °C, and they could be detected in a much lower amount upon heating at 400 °C, as evidenced by the FT-IR. In accordance with the densification taking place at higher heating temperatures, the refractive index ranged from 1.7 to 1.99 for the processing temperatures in the range 250–400 °C. Moreover, the samples processed at higher temperatures exhibited higher permittivity values. The film processed at 400 °C exhibited the permittivity value of 27± 2. Yet, the leakage currents increased with the heating temperature.

Spin-coated Ta_2O_5 thin films processed at 300 and 350 °C were studied aiming to give a proof of concept for their integration as components in active electronic devices. The TFTs rendered good operating properties, such as *on/off* ratios of the order of 10^8 and a field-effect mobility larger than 10 cm^2/Vs, with slight improvements obtained in the case of the processing temperature of 350 °C. Therefore, the investigated Ta_2O_5 thin films from solution exhibited promising properties for both passive and active electronic devices.

Acknowledgements:

The authors would like to thank the groups of Prof. Dr. Elvira Fortunato and Prof. Dr. Rodrigo Martins from CENIMAT-I3N and CEMOP/UNINOVA, Portugal for fabricating the TFT structures. We would like to thank to the Centre of Excellence NAMASTE, for the use of AFM.

We acknowledge the financial support of the Slovenian Research Agency (Young researcher programme, contract number: 1000-10-310134; projects: J2-4173, P2-0105, and bilateral project PR-04253, contract number: BI-RO/12-13-001), and of the EU7FP Project "ORAMA", Grant Agreement NMP3-LA-2010-246334.

References:

[1] R. C. Frunză, B. Kmet, M. Jankovec, M. Topič, B. Malič. Ta_2O_5-based high-K dielectric thin films from solution processed at low temperatures. *Materials Research Bulletin*, 50:323-328, 2014.

[2] C. Chaneliere, J. L. Autran, R. A. B. Devine, B. Balland. Tantalum pentoxide (Ta_2O_5) thin films for advanced dielectric applications. *Materials Science and Engineering: Reports*, R22(6):269-322, 1998.

[3] P. G. Clem, N.-L. Jeon, R. G. Nuzzo, D. A. Payne. Monolayer-Mediated Deposition of Tantalum(V) Oxide Thin Film Structures from Solution Precursors. *Journal of the American Ceramic Society*, 80(11):2821-2827, 1997.

[4] G. Scherer. Sintering of sol-gel films. *Journal of Sol-Gel Science and Technology*, 8(1-3):353-363, 1997.

[5] R. C. Frunză, M. Jankovec, B. Kmet, M. Topič, B. Malič. Current transients in dielectric Ta_2O_5-based thin films from solution. *Informacije MIDEM*, 44(1):21-26, 2014.

[6] P. Barquinha, L. Pereira, G. Gonçalves, R. Martins, D. Kuščer, M. Kosec, E. Fortunato. Performance and Stability of Low Temperature Transparent

Thin-Film Transistors Using Amorphous Multicomponent Dielectrics. *Journal of The Electrochemical Society*, 156(11):H824-H831, 2009.

[7] D. Saygin-Hinczewski, K. Koc, I. Sorar, M. Hinczewski, F. Z. Tepehan, G. G. Tepehan. Optical and structural properties of – thin films. *Solar Energy Materials and Solar Cells*, 91(18):1726-1732, 2007.

[8] J.-Y. Zhang, B. Lim, I. W. Boyd. Thin tantalum pentoxide films deposited by photo-induced CVD. *Thin Solid Films*, 336(1–2):340-343, 1998.

[9] F. Z. Tepehan, F. E. Ghodsi, N. Ozer, G. G. Tepehan. Optical properties of sol–gel dip-coated Ta_2O_5 films for electrochromic applications. *Solar Energy Materials and Solar Cells*, 59(3):265-275, 1999.

[10] J.-Y. Zhang, L.-J. Bie, V. Dusastre, I. W. Boyd. Thin tantalum oxide films prepared by 172 nm Excimer lamp irradiation using sol–gel method. *Thin Solid Films*, 318(1–2):252-256, 1998.

[11] P. C. Joshi, M. W. Cole. Influence of postdeposition annealing on the enhanced structural and electrical properties of amorphous and crystalline Ta_2O_5 thin films for dynamic random access memory applications. *Journal of Applied Physics*, 86(2):871-880, 1999.

[12] P. Barquinha, L. Pereira, R. Martins, E. Fortunato. *Transparent Oxide Electronics: From Materials to Devices*. Chichester, UK: John Wiley & Sons, Ltd, 2012.

[13] J.-S. Park, H. Kim, I.-D. Kim. Overview of electroceramic materials for oxide semiconductor thin film transistors. *Journal of Electroceramics*, 32(2-3):117-140, 2014.

[14] L. Zhang, J. Li, X. W. Zhang, X. Y. Jiang, Z. L. Zhang. High performance ZnO-thin-film transistor with Ta_2O_5 dielectrics fabricated at room temperature. *Applied Physics Letters*, 95(7 - 072112):1-3, 2009.

[15] P. Barquinha, L. Pereira, G. Gonçalves, R. Martins, E. Fortunato, D. Kuscer, M. Kosec, A. Vilà, A. Olziersky, J. R. Morante. Low-temperature sputtered mixtures of high-κ and high bandgap dielectrics for GIZO TFTs. *Journal of the Society for Information Display*, 18(10):762-772, 2010.

[16] C. J. Chiu, W. Y. Weng, S. J. Chang, S.-P. Chang, T. H. Chang. A Deep UV Sensitive Ta_2O_5/a - IGZO TFT. *IEEE Sensors Journal*, 11(11):2902-2905, 2011.

For wider interest

In the past years, transparent electronics emerged as a promising technology considered to have the potential to be the next generation of optoelectronics. Thin film transistors (TFTs) are the key components in most modern circuits used to amplify or switch electronic signals. A TFT is a special type of field-effect transistor formed by placing a thin dielectric layer (also referred to as the *gate dielectric*) as well as an active semiconductor layer and metallic contacts (*i.e.*, source, drain, gate) onto a supporting substrate. Furthermore, the fabrication of transparent TFTs requires low cost deposition of thin films with suitable properties onto substrates needing low temperature processing, as glass or even plastic.

Several different high-*K* (*K*= permittivity, dielectric constant) metal oxides have been researched for gate dielectric applications. Ta_2O_5 thin films were found to be suitable for metal–oxide–semiconductor field-effect transistors and high density memory cells due to their high dielectric permittivity, in the range from 20 to 28 for the amorphous state, high refractive index and chemical and thermal stability. In the past years, the use of Ta_2O_5 as a gate dielectric in transparent TFTs has also been proposed.

For microelectronic and optoelectronic applications, high quality thin films (both from the structural and electrical point of view) are required, and various deposition techniques may be employed for their fabrication. As regarding Ta_2O_5 gate dielectrics, it was found that the properties and performance of the thin films depend strongly on the fabrication process. Ta_2O_5 thin films fabricated by physical deposition methods and processed at low temperatures were employed in transparent TFTs. However, little work has been done on the sol-gel preparation of such materials.

The current work reports the preparation and characterization of solution-derived Ta_2O_5 thin films and provides a proof of concept for their use in transparent TFTs.

Matrix degradation as a mechanism for nanoparticles release from food contact materials

Viviana Golja[1,2], Goran Dražić[2,3,4], Martina Lorenzetti[4], Maša Zalaznik[5], Mitjan Kalin[5], Saša Novak[2,4]

[1] National Institute of Public Health, Ljubljana, Slovenia

[2] Jožef Stefan International Postgraduate School, Ljubljana, Slovenia

[3] Laboratory for Materials Chemistry, National Institute of Chemistry, Ljubljana, Slovenia

[4] Department of Nanostructured Materials, Jožef Stefan Institute, Ljubljana, Slovenia

[5] Laboratory for Tribology and Interface Nanotechnology, Faculty of Mechanical Engineering, University of Ljubljana, Slovenia

Viviana.Golja@nijz.si

Abstract.

Materials in contact with foodstuffs may contain nanoparticles which improve their properties. However, transfer of nanoparticles from the material into foodstuffs is not desirable. When nanoparticles are embedded in the matrix, probability of transfer is small, but release can be promoted by matrix degradation. Matrix degradation of quasi-ceramic coating on commercially available pans was studied. The most probable mechanisms of degradation were identified as mechanical, thermal and chemical. Our results show that matrix degradation during the worst case conditions of use may cause particles release into foodstuffs.

Keywords: food contact, nanoparticles, matrix degradation, release

1 Introduction

During the preparation, food comes into contact with different materials. Recently, new food contact materials are developed containing nanoparticles (Chaudhry et al., 2008). Possibility of nanoparticles release from materials into the food cause safety concerns as materials in nano size have different biological properties in comparison with bulk materials (Nel et al., 2006, EFSA, 2009).

It is not much known about nanoparticles release into the food. One possible mechanism identified to describe the release of nanoparticles from food contact materials into food is matrix degradation. The aim of our study was to investigate such process for so called quasi-ceramic non-stick pan coating containing micro and nano particles of TiO_2 and SiO_2 embedded in silicone matrix.

2 Materials and methods

Pan with quasi-ceramic non-stick coating was purchased from the Slovenian market. Microstructure of the coating surface was observed by field emission scanning electron microscopy (FE SEM, JEOL JSM 7600F, Japan), cross section of the coating was observed by focused ion beam scanning electron microscopy (FIB SEM, FEI Nanolab Helios 650 dual beam, OR, USA).

The thermal degradation of the coating was examined by differential scanning calorimetry/thermogravimetric analysis (DSC/TG, NETZSCH STA 449 C/6/G Jupiter – QMS 403) during heating up to 700 °C, with a rate of 10 ^{o}C /min.

Mechanical resistance of the coating toward scratching with metallic objects (e.g. cutlery) was studied by linear progressive scratch test on the sample P2 using a diamond indenter (Revetest Scratch tester CSM Instruments RST S/N 01-04283, Switzerland). The load was progressively increased from 1 N to 30 N, with a rate of 93,10 ± 0,01 mm/min and scratch length of 3 mm. The appearance of the wear debris was observed by stereo microscope (Zeiss Discovery V8, Germany), field emission scanning electron microscopy (FE SEM, JEOL JSM 7600F, Japan) and focused ion beam scanning electron microscopy (FIB SEM, FEI Nanolab Helios 650 dual beam, OR, USA).

The long-term wear behaviour of the coating P2 was tested on dedicated tribological tester (UMT-2, CETR, CA, USA) in a form of a pin-on-disk reciprocal sliding configuration to mimic the worst case conditions. The tribological tests were conducted for one hour at normal load of 3 N, with a stroke of 5 mm and sliding velocity of 0.03 m/s (3 Hz). Polymeric (PA6) and ceramic (Al_2O_3) pins were used against the pan sample, with contact pressures ranging from 1 MPa to 300 MPa, in order to simulate various scenarios of severity during cutlery contact with the pan surface. It is estimated that a normal use of wooden or polymer cutlery would result in pressures well below 100 MPa; however, metal contacts with forks or even knifes in a pan will easily exceed 300 MPa. After the tests, the appearance of the wear scar and the presence of the debris were observed by stereo microscope.

3 Results and discussion

Matrix degradation is one among possible mechanisms of nanoparticles release from nanoparticles containing food contact materials (Newsome, 2014, Noonan et al., 2014) besides desorption, diffusion and dissolution. In the case of quasi-ceramic coatings, which contain TiO_2 and SiO_2 nanoparticles embedded in polymer matrix (microstructure of the coating surface and cross section is shown in Figure 1), desorption of the TiO_2 and SiO_2 nanoparticles is not expected.

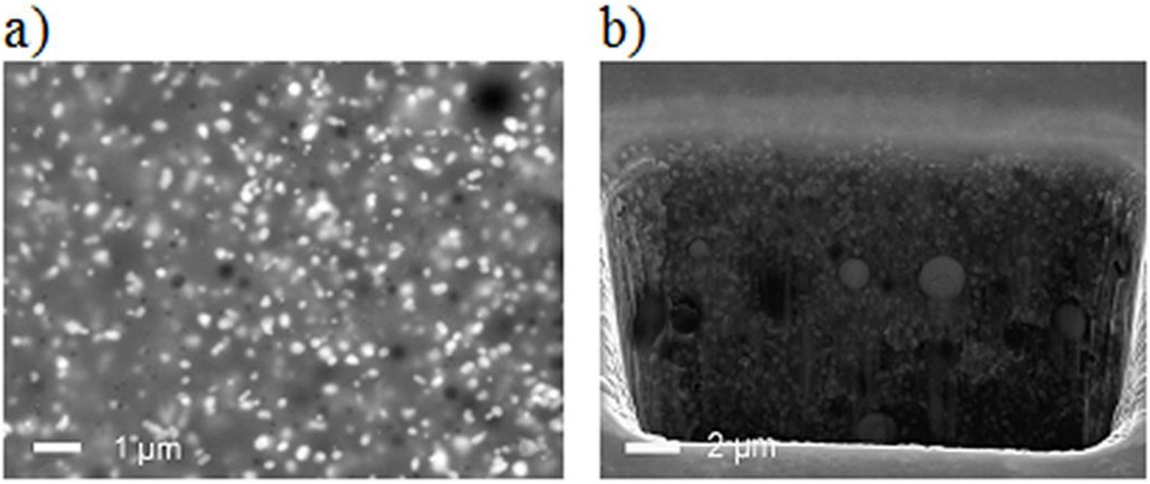

Figure 1: (a) Microstructure of the coating surface observed by FE SEM and (b) cross-section of the coating observed by FIB SEM

For the same reason, diffusion is not an important mechanism. Due to the very limited solubility of TiO_2 within the whole pH region, the mechanism of dissolution and migration of Ti-ions into food can also be considered as negligible. On the other hand, the solubility of SiO_2 is much larger and is relevant in particular in alkaline solutions such as, for example, in dishwashing machines. The dissolution of silica from the matrix and dissolution of the matrix (silicone) will highly likely result in the release of small fragments of SiO_2 and much less soluble TiO_2 nanoparticles. Thus, it might be presumed that the matrix degradation, including chemical degradation, is the most probable mechanism of the particle release from the examined quasi-ceramic pan coatings.

Other than chemical degradation, possible mechanisms of the matrix degradation are also thermal and mechanical ones.

The thermal stability of the pan coating was examined by DSC/TG analysis up to 700 °C (data not shown). Within the temperature range of cooking stove, the weight loss is minor, and the total weight loss up to 700 °C was ~7 % . The peak at 600 °C is accompanied by the formation of CO and CO_2. Furthermore, the first exothermic change, indicating decomposition of the material, appears only over 500 °C, which is above the temperature of exposure during the use.

The appearance of the sample after the DSC/TG analysis is presented in (Figure 2a). After heating at 700 °C, the white TiO_2 particles are not firmly incorporated into the matrix anymore and fine, nano-sized particles became visible (Figure 2b, 2c, 2d).

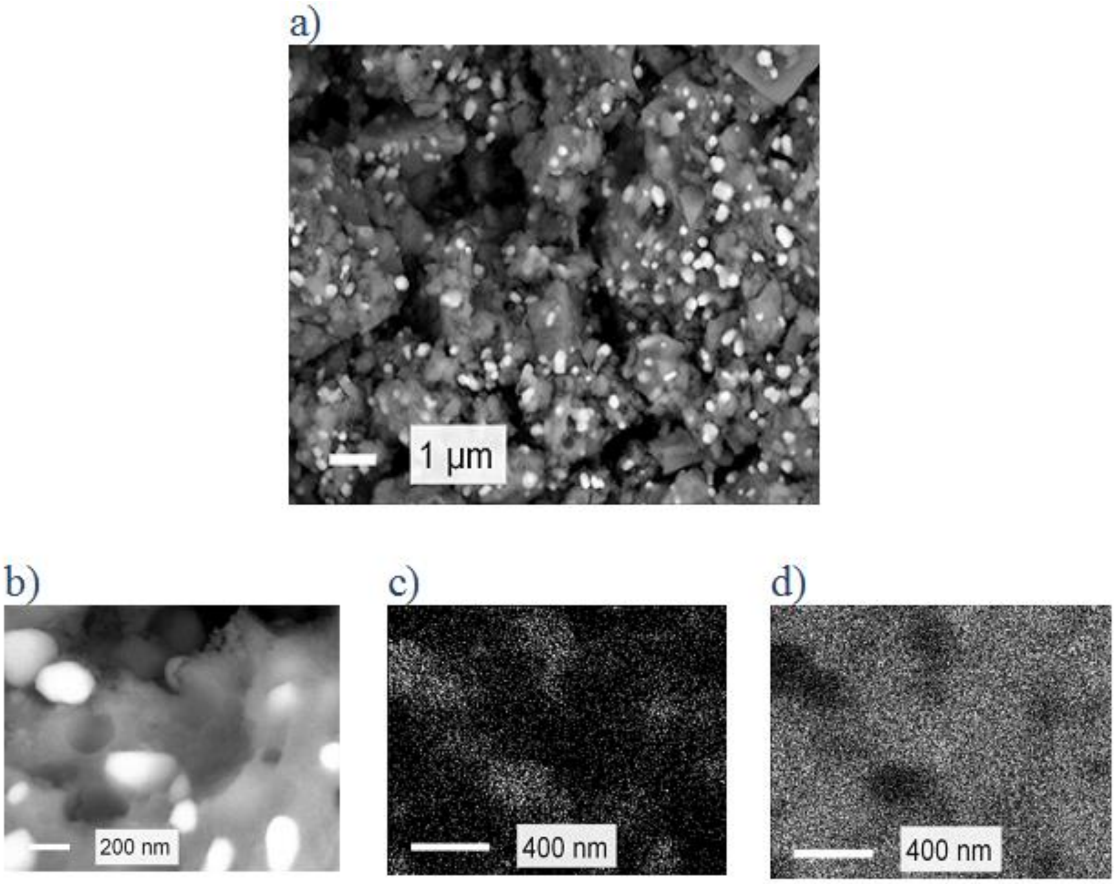

Figure 2: (a) Scanning electron micrograph of the sample after heating at 700 °C (DSC analysis), (b), (c) and (d) mapping of titanium and silicon distribution

The mapping of the area by EDX analysis (Figure 3a, 3b and 3c) confirmed white particles as being Ti-rich (TiO_2) and the surrounding material as Si-rich (SiO_2). It has to be pointed out that the temperature at which the SiO_2 nanoparticles appeared well visible exceeded the temperature at kitchen stoves; however, these results indicate that, under certain conditions, silica and, consequently, TiO_2 particles can be possibly released from the matrix.

The results of the analysis suggest that under the foreseeable conditions of use the examined coating is relatively stable and the TiO_2 and SiO_2 nanoparticles are not expected to be released by thermal decomposition of the silicon-based matrix, at least in a short term use. However, it is supposed that they can be released into food under more severe conditions, i.e. by (overheating).

Mechanical degradation of the coating was tested by scratch and wear tests. A scratch test was performed under increased load (simulating the worst case of use by e.g. knives, forks), while the wear resistance at constant load for a long time was used to simulate a long term use.

Scratch test was performed, with the load of the pin increased up to 30 N. Visible deformations appeared only at loads above 4 N, where scratches followed by chipping of the material at high loads were observed (Figure 3a). The particles created by chipping of the coating material were small, some were below 1 µm, and had irregular shapes (Figure 3b).

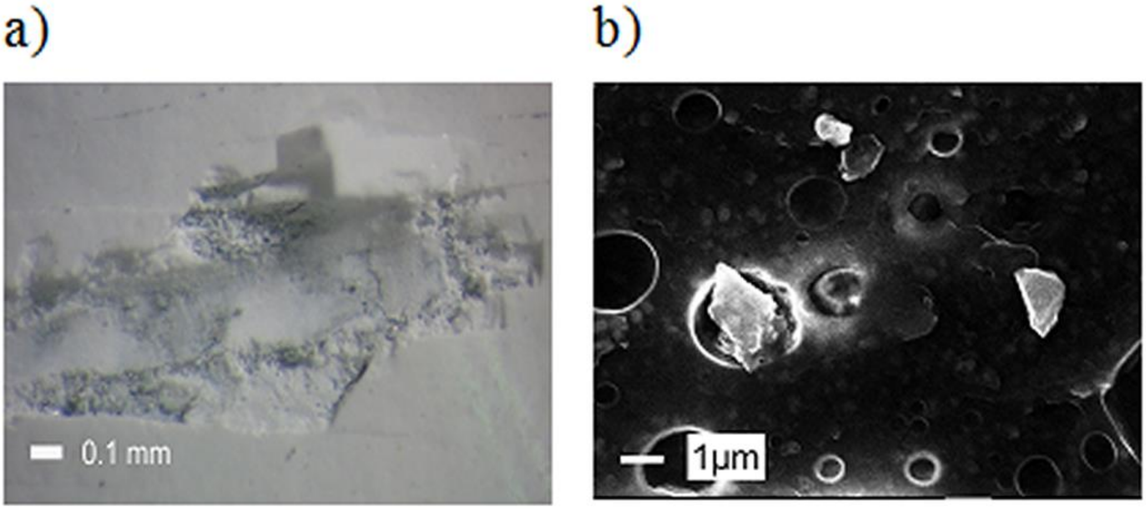

Figure 3: (a) Low magnification image of the scratch and (b) SEM image of the formed particles

This reveals a change from a predominantly elastic deformation at low loads to a brittle fracture under increased load. The appearance of the cracks after scratching the silicon-based coating with high crosslink density was reported to happen even under less severe conditions (Tiwari and Hihara, 2012), where the load was only 0.5 N.

The use of tableware was simulated under mild and more severe tribological conditions for a long time (1 h). Mild conditions simulated recommended use, more severe conditions simulated inappropriate contacts of the pan with any hard and sharp object, such as a fork or a knife.

Under mild conditions (polymer loaded at pressures less than 50 MPa), no visible wear appeared. In contrast, when higher contact pressures were applied by using steel or ceramic counterparts, i.e. above 200 MPa, the brittle nature of the coating became evident, especially above 300 MPa (Figure 4a). Some of produced wear debris was nanosized and had equiaxial shape (Figure 4b). As expected, the debris composition was in agreement with that one of the coating determined by the EDX analysis before the wear test, i.e. predominantly SiO_2 with some TiO_2.

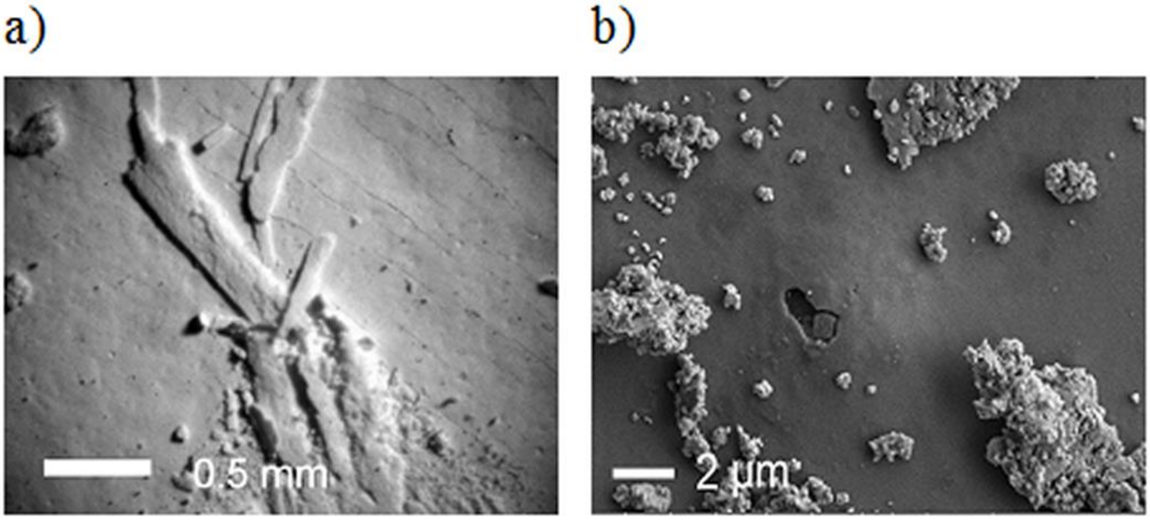

Figure 4: (a) Debris after wear test: stereomicroscope image and (b) SEM micrograph

Finally, photocatalytic degradation after exposure to UV light may also take place to some extent (because TiO_2 particles are present), as described by Wang (Wang et al., 2011). However, it is known that anatase is a much stronger photocatalyst than rutile (van Dyk and Heyns, 1998); regardless of that, indoor exposure of food contact materials to UV light is not particulary relevant.

4 Conclusions

Nanoparticles firmly bonded within the organic phase can be released by degradation of the silicone matrix. Three possible mechanisms of matrix degradation and consecutive particles release were identified: (i) thermal decomposition (overheating or possible long-term heating), (ii) mechanical wear (cutting, scratching) and (iii) chemical (dissolution in alkaline media).

During the worst case conditions of use matrix degradation may cause nanoparticles release into foodstuffs.

Acknowledgments

The authors would like to thank Dr. N. Drnovšek for SEM imaging, Dr. M. Maček for DSC/TG analysis and Dr. S. Paskvale for scratch testing

References:

[1] Q. Chaudhry, M. Scotter, J. Blackburn, B. Ross, A. Boxall, L. Castle, R. Aitken, R. Watkins. Applications and implications of nanotechnologies for the food sector. *Food Addit Contam Part A Chem Anal Control Expo Risk Assess,* 25, 241-58, 2008

[2] EFSA The Potential Risks Arising from Nanoscience and Nanotechnologies on Food and Feed Safety. *The EFSA Journal*, 1-39, 2009

[3] A. Nel, T. Xia, L. Madler, N. Li. Toxic potential of materials at the nanolevel. *Science,* 311, 622-627, 2006

[4] R. Newsome. 2013 IFT International Food Nanoscience Conference: Proceedings. *Comprehensive Reviews in Food Science and Food Safety,* 13, 190-228, 2014

[5] G.O. Noonan, A.J. Whelton, D. Carlander, T.V. Duncan. Measurement Methods to Evaluate Engineered Nanomaterial Release from Food Contact Materials. *Comprehensive Reviews in Food Science and Food Safety,* 13, 679-692, 2014

[6] A.Tiwari, L.H. Hihara. Effect of inorganic constituent on nanomechanical and tribological properties of polymer, quasi-ceramic and hybrid coatings. *Surface & Coatings Technology,* 206, 4606-4618, 2012

[7] A.C. Van Dyk, A.M. Heyns. Dispersion stability and photo-activity of rutile (TiO2) powders. *Journal of Colloid and Interface Science,* 206, 381-391, 1998

[8] D.L. Wang, S.S. Watson, L.P. Sung, I.H. Tseng, C.J. Bouis, R. Fernando. Effect of TiO2 pigment type on the UV degradation of filled coatings. *Journal of Coatings Technology and Research,* 8, 19-33, 2011

For wider interest

New food contact materials may contain nanoparticles which can be released into foods. Nanoparticle release is not desirable. We examined such material (commercially available pan coatings) and find out that coating, in which nanoparticles were firmly bonded before use, decompose if used without care - after scratching with sharp utensils (knives, forks), after overheating during cooking or by dissolution in alkalis (washing in dishwasher machines). Because of coating degradation, nanoparticles may be released into foods.

Controlling the composition of electrodeposited Fe-Pd nanowires and thin films via determination of the diffusion and electrode kinetic parameters

Nina Kostevšek[1,2], Darja Pečko[1], Boris Pihlar[3], Spomenka Kobe[1], Kristina Žužek Rožman[1]

[1] Department for nanostructured materials, Jožef Stefan Institute, Ljubljana, Slovenia

[2] Jožef Stefan International Postgraduate School, Ljubljana, Slovenia

[3] Faculty of Chemistry and Chemical Technology, University of Ljubljana, Ljubljana, Slovenia

nina.kostevsek@ijs.si

Abstract. Fe-Pd alloys have many potential applications because of their unique chemical and magnetic properties, which can be tailored by changing their composition. We have investigated the kinetic parameters for depositing Fe and Pd and their influence on the Fe-Pd alloy's composition, while performing the deposition on a flat Au electrode and into an Au-sputtered porous alumina template. The electrodeposition of Fe and Pd was found to be irreversible and diffusion-controlled. The diffusion coefficient was found to be lower for both metallic ions, by 2-3 times, when the template was used as a working electrode. However, the exchange current densities are comparable for Fe^{2+} and Pd^{2+} on both working electrodes. This indicates that the kinetics of the electrodeposition process is not influenced by the electrode geometry. Because of similar diffusion-coefficient ratios and similar kinetics on both the investigated working electrodes, using the same deposition conditions results in Fe-Pd-based thin films and nanowires having similar compositions.

Keywords: Fe-Pd alloy, electrodeposition, kinetics, flat electrode, alumina template

1 Introduction

Fe-Pd alloys have recently attracted a lot of attention because of their many potential applications that arise from the alloys' specific chemical compositions. In alloys with a Pd content of 28-31 at.% a magnetic shape-memory effect can be observed [1-5]. Alloys containing about 50 at.% of Pd represent promising candidates for micro-electro-mechanical systems (MEMS) due to their high magnetocrystalline anisotropy [6-7]. Pd-rich alloys exhibit catalytic properties, which can result in a high hydrogen-adsorption capacity [8]. In a variety of experiments Fe-Pd thin films [3,7,9], nanowires [6,10] and nanotubes [11,12] with different compositions were fabricated. Electrochemical synthesis represents a cost-effective and efficient method for preparing metals and alloys. The shape of the deposited alloy can be easily modified using the appropriate geometry of the working electrode (WE). If a flat electrode is used as the WE, thin films can be deposited. Furthermore, arrays of nanowires/nanotubes can be obtained if a porous template with a large number of straight cylindrical pores and a narrow size distribution is used. Many studies were dedicated to investigating the physical properties of Fe-Pd alloys [1-4], whereas less attention has been given to the electrochemical aspects.

Rezaei et al. [13] investigated the electrodeposition process for Fe-Pd thin films on a Cu wire electrode. However, the complexity of the deposition process increases when the aim is to deposit an alloy into a porous template. Slow diffusion into long, nonconductive, template channels represents the main barrier for the deposition and the experimental challenge. The mass transport can be additionally hindered due to poorer wetting of the alumina template with an aqueous solution [14]. Therefore, in order to control the deposition and composition of Fe-Pd alloys into porous templates an understanding of the mass transfer and kinetics is of vital importance. The aim of this study was to compare the diffusion and the kinetic parameters of the same electrode process for Fe and Pd deposition by varying the electrode geometry, i.e., a flat electrode and a porous alumina template. A similar kinetic investigation of the deposition parameters was made for gold nanowires into a track-etched polycarbonate template [15]; however, no comparison with the process on a non-porous working electrode was made.

In this work a direct comparison of the mass transport and kinetic parameters of the Fe and Pd deposition on a flat electrode and into a porous alumina template was performed. Cyclic voltammetry (CV) and Butler-Volmer analyses at low over-potentials were used to provide a better understanding of the deposition processes and to calculate the kinetic and diffusion parameters.

2 Experimental

The electrolyte contained 200-mM $FeCl_3$ (Sigma Aldrich, >99.9%) and 30-mM $PdCl_2$ (Sigma Aldrich, 99%). Diammonium hydrogen citrate $(NH_4)_2C_6H_6O_7$ (Fluka, 99%) and ammonia (Merck, 25% aqueous solution) were used as complexing agents for the iron and palladium ions, respectively. In the Butler-Volmer analysis $(NH_4)_2Fe(SO_4)_2x6H_2O$ (Sigma Aldrich, 99%) was used as the source of Fe^{2+} ions. The pH of the prepared solution was adjusted to 9.0 by adding ammonia. All the experiments were performed in a three-electrode cell at room temperature without agitation. Before the measurements were performed the solutions were de-aerated with N_2 gas for 15 min. The reference electrode was an SSCE electrode (Ag/AgCl/3.5-M KCl, HANA Instruments GmbH – type HI5311). A circular platinum mesh was used as the counter electrode (Fig. 1). Two different working electrodes were used, i.e., a commercially available anodized alumina (AAO) template (Whatman Anopore, pore diameter 200 nm) as the porous electrode and glass sputtered with a conductive layer of Au served as the flat electrode. The AAO template and the flat electrode were sputtered with Au in the same batch (20-nm-thick layer of Cr for adhesion and a 600-nm-thick Au conductive layer). A 600-nm-thick layer of Au was sufficient to completely cover the pores of the template. The experiments were conducted in a Teflon cell with the template (Fig. 1a) and the flat electrode (Fig. 1b) facing upwards.

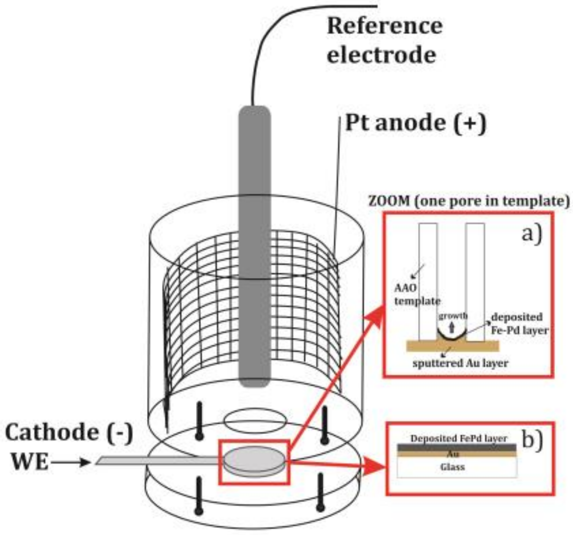

Figure 1: Scheme of the three-electrode cell where a) the WE is an AAO template attached to a holder (the deposition process during the initial stage in the bottom of one pore is schematically shown in the red square) and b) the WE is glass sputtered with Au (the initial stage of the thin film deposition is shown in the red square). The counter electrode is a circular Pt mesh.

For the cyclic voltammetry measurements a potentiostat/galvanostat Gamry Reference 600 equipped with PHE 200 software was used. The scan rate was varied in the range 5-150 mV/s. Thin films and nanowires were deposited potentiostatically at different cathodic potentials from -0.8 V to -1.3 V for 200 s and 900 s, respectively. Scanning electron microscopy (JEOL JSM 7600F) combined with energy-dispersive X-ray spectroscopy (EDXS) was used to determine the chemical composition of the deposited alloy. An accelerating voltage of 7 kV was used for the EDXS analysis. Under such analytical conditions the depth of the x-ray generation for the Fe-L_{α} and Pd-L_{α} spectral lines was about 120 nm, which is suitable for examining deposited nanowires with a diameter of 200 nm as well as thin films.

3 Results and discussion

1.1 Cyclic voltammetry of Fe and Pd complexes

The standard reduction potential of iron Fe^{2+}/Fe is -0.44 V vs. the standard hydrogen electrode (SHE), and for palladium Pd^{2+}/Pd the value is +0.95 V (vs. SHE). In order to bring the potentials of both metals closer together and enable their co-deposition, ammonia and diammonium hydrogen citrate (abbrev. Cit) were used as the complex-forming ligands [13]. In Fig. 2 the cathodic part of the cyclic voltammograms for the ammonium citrate, the Fe electrolyte, the Pd electrolyte and the Fe-Pd electrolyte recorded at the flat electrode and in the AAO template are shown. Since we are interested in the deposition of an Fe-Pd alloy, differences in the cyclic voltammograms of a common electrolyte compared to a single-ion electrolyte are important. The black curve in Fig. 2 represents the background electrolyte (only ammonium citrate) where no metal ions are present. The significant increase in the current density at -1.0 V corresponds to the reduction of H_2O, according to the reaction $2H_2O + 2e^- \rightarrow H_2 + 2OH^-$. Similar behaviour can also be observed for the citrate solution in the template (black curve in Fig. 2b). It can be seen that the reduction peaks of the Fe-Pd electrolyte are not in the same positions as in the case of the single-ion electrolyte for both investigated WEs. The reduction peak C_{1Pd} shifts towards more positive values when the Fe-Pd electrolyte was used, as was observed by Rezaei [13]. If the concentration of the Pd complex was reduced, the height of the first peak C_{1Pd} was decreased (not shown), which confirms that the first peak in the Fe-Pd electrolyte corresponds to the Pd reduction process and the second peak C_{1Fe} corresponds to the Fe^{3+}-Cit → Fe^{2+}-Cit reduction. The peak for the second reduction step (Fe^{2+}-Cit → Fe^0) was hidden in the hydrogen evolution region at more cathodic potentials. It is clear that the reduction peaks C_{1Fe} and C_{1Pd} in the Fe-Pd electrolyte appeared at very similar potentials at both WEs.

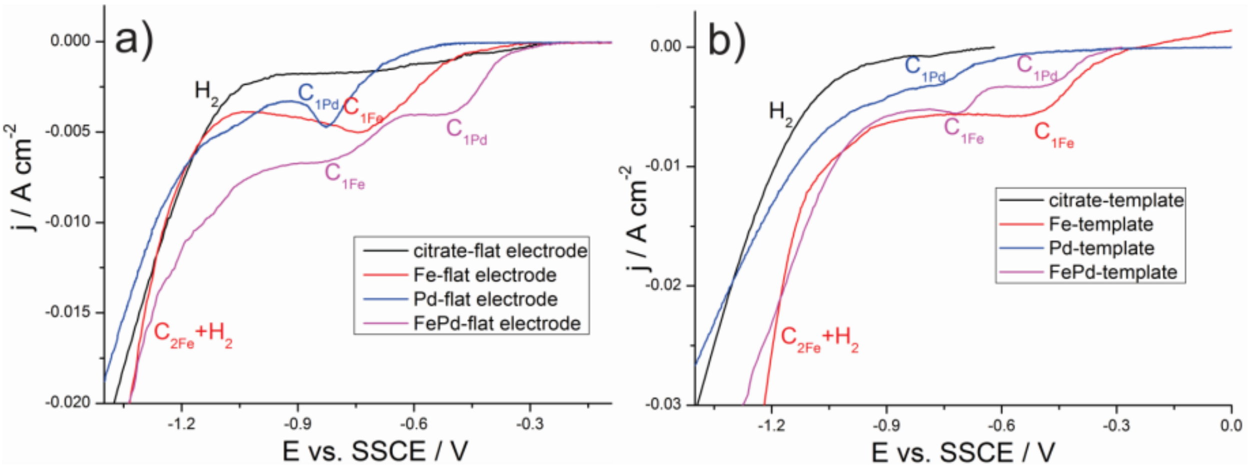

Figure 2: Linear sweep voltammograms of citrate, Fe, Pd and Fe-Pd electrolytes a) at the flat electrode and b) in the template. Scan rate was 20 mV/s.

1.2 Determination of the diffusion and the kinetic parameters using cyclic voltammetry analysis

Fe electrolyte and Pd electrolyte were used to determine diffusion coefficients and kinetic constants for both metallic ions on the flat electrode and in the template at different scan rates (5-150 mV/s).

Reduction peak for the first reduction step for Fe (reaction Fe^{3+}-Cit → Fe^{2+}-Cit) and the reduction peak for the reaction $[Pd(NH_3)_4]^{2+}$→ Pd^0 were used in the calculations. Because of the Fe^{3+} ion being transported from the bulk to the electrode surface, and not Fe^{2+}, which is produced at the electrode surface, we used the peak for the first reduction step ($Fe^{3+} \rightarrow Fe^{2+}$) to determine the diffusion coefficient. From the obtained cyclic voltammograms, therefore, we can evaluate only the charge-transfer rate for the first Fe-reduction step, which should be a simple one-electron transfer reaction, while the second reduction step is much more complex [33]. Peak potentials E_p and the peak heights i_p depend on the scan rate on both electrodes for both metallic ions, thus indicating that the reduction is irreversible for the observed time scale. The dependence of the peak current on the square root of the scan rate was found to be linear, which is characteristic for electrodeposition reactions where the rate is determined by diffusion. Therefore, the diffusion coefficient for the irreversible diffusion-controlled process of Fe and Pd deposition was calculated using the Randles-Sevcik equation [16]:

$$i_p = 0{,}496nF^{3/2} \cdot AC_0^* D_0^{1/2} \nu^{1/2} \left(\frac{n\alpha}{RT}\right)^{1/2} \qquad (1)$$

where F, α, n, A, D_0, C_0^*, R, T are the Faraday constant, the charge-transfer coefficient, the number of exchanged electrons involved in the electrode process, the active surface area (cm^2), the diffusion coefficient (cm^2/s), the solution bulk concentration (mol/cm^3), the scan rate (V/s), the gas constant and the temperature (K), respectively. In Table 1 the diffusion coefficients for the Fe and Pd electrodeposition process obtained from the voltammetric analyses are listed.

The charge-transfer coefficient α was determined using the Delahay equation [16]:

$$\left|E_p - E_{p/2}\right| = \frac{1{,}857RT}{\alpha n_\alpha F} \qquad (2)$$

where E_p, $E_{p/2}$ and n_α are the peak potential (V), the potential where $j = j_{p/2}$ and the number of electrons in the rate-determining step, respectively.

Dependence of $E_{p-Ep/2}$ vs. (scan rate)$^{1/2}$ is linear, which is characteristic for the irreversible reaction. Charge-transfer coefficients are listed in Table 1.

The diffusion coefficient for Fe^{3+} on the flat electrode is found to be higher (2.1×10^{-5} cm^2/s) than in the AAO template (0.7×10^{-5} cm^2/s). The same trend can be observed in the case of Pd, where the diffusion coefficient for Pd^{2+} on the flat electrode is higher (5.1×10^{-5} cm^2/s) than in the AAO template (2.7×10^{-5} cm^2/s).

From the obtained values it can be seen that the diffusion coefficient in the template is reduced by 2-3 times. Napolskii et al. [17] reported that the diffusion of Ni^{2+} is much slower in the AAO template compared to bulk diffusion, which was attributed to the suppression of diffusion by the electric double layer in the nanochannel. The diffusion coefficient calculated for the $[Pd(NH_3)4]_{2+}$ complex on the flat electrode ($5.1x10^{-5}$ cm^2/s) is slightly higher than in the reports by other authors ($2.2x10^{-5}$ cm^2/s [13] and $1.02x10^{-5}$ cm^2/s [18]). This could be attributed to the different experimental conditions (pH and concentration of the solution). However, in the work of Liang [19] the value for the diffusion coefficient for an Fe(III)-Cit complex of $1\text{-}4x10^{-5}$ cm^2/s is in good agreement with our value ($2.1x10^{-5}$ cm^2/s) for the flat electrode.

From the collected data it can be seen that the obtained charge-transfer coefficient for the Fe^{3+} complex is close to 0.5 at both WEs, which indicates a symmetric process; however, for the Pd^{2+} complex at the flat electrode and in the template the charge-transfer coefficient α is lower than 0.5, which means that the transition state between the oxidation and the reduction form is more asymmetric.

From the analysis of the cyclic voltammograms the kinetic constant k_0 for the rate-determining step in the Fe reduction process ($Fe^{2+} \rightarrow Fe^0$) could not be calculated, because the peaks for this reduction step in the cyclic voltammograms are hidden in the HER region. Therefore, in order to study the kinetics of the Pd^{2+} and Fe^{2+} reduction process a Butler-Volmer analysis at low overpotentials was performed, where the Butler-Volmer equation can be expressed in the form:

$$j = j_0 \frac{F}{RT} \eta, \tag{3}$$

which shows that the net current is linearly related to the overpotential in a narrow potential region near the equilibrium potential E_{eq} [20]. To determine the exchange current density j_0 for this reduction process, the current was measured with a scan rate of 0.2 mV/s at E_{eq} ±20 mV. For these measurements $(NH_4)_2Fe(SO_4)2x6H_2O$ salt was used as a source of Fe^{2+} ions. The exchange current was normalized to the unit area and the calculated exchange-current densities j_0 are shown in Table 1.

Table 1: Charge transfer coefficients α, diffusion coefficients D and exchange current densities j_0 for Fe and Pd electrodeposition on the flat electrode and in the template (T=25°C)

Ion	Electrode	α	D (cm^2/s)	j_o (A cm^{-2})
Fe^{3+}	Flat electrode	0.46 ± 0.05	$(2.1 \pm 0.1)x10^{-5}$	$(1.1 \pm 0.1)x10^{-4}$ ($Fe^{2+} \rightarrow Fe^0$)
Fe^{3+}	Template	0.63 ± 0.05	$(0.7 \pm 0.1)x10^{-5}$	$(1.5 \pm 0.1)x10^{-4}$ ($Fe^{2+} \rightarrow Fe^0$)
Pd^{2+}	Flat electrode	0.42 ± 0.05	$(5.1 \pm 0.1)x10^{-5}$	$(1.2 \pm 0.1)x10^{-4}$ ($Pd^{2+} \rightarrow Pd^0$)
Pd^{2+}	Template	0.35 ± 0.05	$(2.7 \pm 0.1)x10^{-5}$	$(1.4 \pm 0.1)x10^{-4}$ ($Pd^{2+} \rightarrow Pd^0$)

1.3 Electrodeposition of the Fe-Pd thin films and nanowires

In order to investigate the influence of the kinetic parameters (i.e. the applied voltage) on the final composition, the electrodeposited Fe-Pd nanowires and thin films, deposited into the Au-sputtered AAO templates and on the flat Au electrode, respectively, were investigated. SEM images of Fe-Pd nanowires and thin films deposited at -1.2 V are shown in Figure 3b and 3c, respectively.

The Fe-Pd thin-film depositions were performed potentiostatically using different applied potentials from -0.8 V to -1.3 V vs. SSCE. The Fe content of the thin-film deposits increased from 27 to 75 at. % when the deposition potential changes from -0.8 V to -1.3 V vs. SSCE (Fig. 3a). In the case of the deposition in porous templates, the same potential range was used to deposit Fe-Pd nanowires. When the cathodic potential was changed from -0.8 V to -1.3 V vs. SSCE the Fe content in the nanowires increased from 31 to 76 at. % (Fig. 3a). At more cathodic potentials (more negative than -1.3 V), hydrogen evolution prevailed and disturbed the metal deposition and non-homogenous deposits were obtained (not shown). It can be seen from Fig. 3a that the WE geometry does not influence the alloy composition since the same composition of thin films and nanowires was obtained at the same applied potential. This is consistent with the observation in cyclic voltammograms of the Fe-Pd electrolyte (Fig. 2) where reduction peaks can be found at similar potentials for both WEs. Although the bulk deposition of Fe starts at approx. -1.1 V, a significant amount of Fe in the alloy can be detected at much more positive potentials, which can be related to the Fe underpotential co-deposition [13], like it was observed in the Fe-Pt co-deposition [19,21].

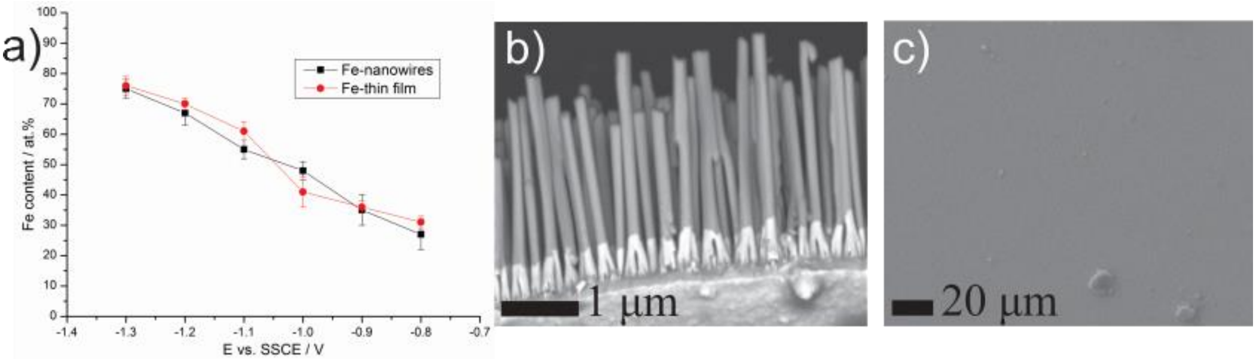

Figure 3: Graph indicating the influence of the cathodic potential on the Fe content in the Fe-Pd alloy in nanowires (template, black squares) and in thin films (flat electrode, red circle), SEM images of b) Fe-Pd nanowires after AAO template removal and c) Fe-Pd thin films at -1.2 V.

The conditions for the Fe-Pd alloy deposition differ from those for single-element Fe and Pd depositions; therefore, the diffusion and kinetic parameters obtained for a single ion are difficult to directly correlate with an alloy formation [22]. However, some conclusions can be made. It can be seen from Fig. 3a that the same composition of thin films and nanowires was obtained if the same deposition conditions were used (i.e., solution and applied potential). From this observation it can be concluded that the deposition process does not differ significantly for the flat electrode and the template. It was calculated that the exchange current densities for Fe^{2+} and Pd^{2+} are similar on both WEs, and because the same composition of the alloy on both WEs was achieved, this could indicate that the kinetics of the alloy deposition is not affected by the WE geometry. Besides the kinetics, also the diffusion should be taken into account when discussing the alloy deposition. A lower diffusion coefficient for both metallic ions in the template is observed not to have a significant influence on the alloy composition. The diffusion coefficients for Fe and Pd ions are reduced in the template by a similar amount (2-3x) in comparison to the diffusion coefficients calculated on the flat electrode. Due to the similar ratio of diffusion coefficient $D_{\mathrm{Fe}}/D_{\mathrm{Pd}}$ the thin-film or nanowire-alloy compositions are practically the same. The diffusion coefficient is reduced in the template in a similar proportion for both the Fe and the Pd ions and, consequently, the same alloy composition can be achieved on both WEs.

4 Conclusions

The kinetics and the diffusion of the electrodeposition process for Fe and Pd were evaluated on a flat Au electrode and in an Au-sputtered porous AAO template. The complexation of both ions, i.e., Fe with citrate and Pd with ammonia, is necessary to make the bath stable and to enable the ion co-deposition. The electrodeposition of Fe and Pd is a irreversible and diffusion-controlled process, both on the flat Au electrode and in the Au-sputtered porous AAO templates. The diffusion coefficient is found to be higher on the flat electrode for both investigated ions, due to the hindered mass transport in long non-conductive AAO pores; furthermore, the Pd diffusion coefficient is found to be larger than that of the Fe for both electrodes. The kinetics of the Fe-reduction process could not be evaluated via a cyclic volammogram analysis, because the peak for the second and rate-determining step of the Fe reduction ($Fe^{2+} \rightarrow Fe^{0}$) overlaps with the HER; however, the kinetics can be investigated by using the Butler-Volmer model at low overpotentials. From the Butler-Volmer calculations it is clear that the obtained exchange current densities j_0 for Fe^{2+} and Pd^{2+} are very similar for the flat electrode and in the template. This was expected, because the rate of the charge transfer across the same metal surface is equal, hence it follows that the geometry of the electrode has no significant influence on the rate of the deposition reaction. An almost equal alloy composition of thin films and nanowires was obtained when the same deposition conditions were used due to the comparable kinetics for both ions and the similar diffusion coefficients ratios $D_{\mathrm{Fe}}/D_{\mathrm{Pd}}$ for both WEs.

Acknowledgment

This work was supported by Slovenian Research Agency (ARRS) via project J2-4316.

References:

[1] J. Buschbeck, S. Hamann, A. Ludwig, B. Holzapfel, L. Schultz, S. Fähler. Correlation of phase transformations and magnetic properties in annealed epitaxial Fe–Pd magnetic shape memory alloy films, *Journal of Applied Physics*, 107: 113919, 2010

[2] T. Cohen-Karni, J. J. Vlassak, Y. Sugimura. Fe-Pd alloy ferromagnetic shape memory thin films, *Journal of Materials Research*, 20: 2279-2287, 2004.

[3] F. Wang, S. Doi, K.I. Hosoiri, H. Yoshida. Nanostructured Fe–Pd thin films for thermoelastic shape memory alloys—electrochemical preparation and characterization, *Electrochimica Acta*, 51: 4250-4254, 2006

[4] M. Sugiyama, R. Oshima, F. E. Fujita. Martensitic transformation in the Fe-Pd alloy system, *Transactions of the Japan Institute of Metals*, 25: 585-592, 1984

[5] I. Kock, T. Edler, S. G. Mayr. Growth behavior and intrinsic properties of vapor-deposited iron palladium thin films, *Journal of Applied Physics,* 103: 46108, 2008

[6] X. L. Fei, S. L. Tang, R. L. Wang, H. L. Su, Y. W. Du. Fabrication and magnetic properties of Fe–Pd nanowire arrays, *Solid State Communications*, 141: 25-27, 2007

[7] S. C. Hernandez, B. Y. Yoo, E. Stefanescu, S. Khizroev, N. V. Myung. Electrodeposition of iron–palladium thin films, *Electrochimica Acta*, 53: 5621–5627, 2008

[8] P. V. Jasen, E. A. Gonzalez, N. J. Castellani, A. Juan. Theoretical study of hydrogen adsorption on FePd face-centered cubic alloy surfaces, *Physical Rewievs*, 71: 235422, 2005

[9] X. N. Sun, X. Y. Xu, Z. B. Tang, G. S. Dong, X. F. Jin. Structure and magnetic properties of Fe_xPd_{1-x} thin films, *Physical Letters A*, 372: 1687–1690, 2008

[10] B. Jeon, S. Yoon, B. Yoo, Electrochemical synthesis of compositionally modulated Fe_xPd_{1-x} nanowires, *Electrochimica Acta*, 56: 401-405, 2010

[11] K. Žužek Rožman, D. Pečko, S. Šturm, U. Maver, P. Nadrah, M. Bele, S. Kobe. Electrochemical synthesis and characterization of Fe70Pd30 nanotubes for drug-delivery applications, *Materials Chemistry and Physics*, 113: 218-224, 2012

[12] H. Liu, F. Wang, Y. Zhao, J. Liu, K. Chul Park, M. Endo. Synthesis of iron–palladium binary alloy nanotubes by template-assisted electrodeposition from metal-complex solution, *Journal of Electroanalytical Chemistry*, 633: 15-18, 2009

[13] M. Rezaei, M. Ghorbani, A. Dolati. Electrochemical investigation of electrodeposited Fe–Pd alloy thin films, *Electrochimica Acta*, 56: 483-493, 2010.

[14] R. Redón, A. Vázquez-Olmos, M. E. Mata-Zamora, A. Ordóñez-Medrano, F. Rivera-Torres, J. M. Saniger. Contact angle studies on anodic porous alumina, *Journal of Colloid and Interface Science*, 287: 664-670, 2005.

[15] L. Soleimany, A. Dolati, M. Ghorbani. A study on the kinetics of gold nanowire electrodeposition in polycarbonate templates, *Journal of Electroanalytical Chemistry*, 645: 28-34, 2010.

[16] R. S. Nicholson, I. Shain. Theory of stationary electrode polarography. Single scan and cyclic methods applied to reversible, irreversible, and kinetic systems, *Analytical Chemistry*, 36: 706-723, 1964

[17] K. S. Napolskii, I. V. Roslyakov, A. A. Eliseev, D. I. Petukhov, A. V. Lukashin, S.-F. Chen, C.-P. Liu, G. A. Tsirlina. Tuning the microstructure and functional properties of metal nanowire arrays via deposition potential, *Electrochimica Acta*, 56: 2378-2384, 2011.

[18] R. Le Penven, W. Levason, D. Pletcher. Studies of the electrodeposition of palladium from baths based on $[Pd(NH_3)_2X_2]$ salts. I. $[Pd(NH_3)_2Cl_2]$ baths, *Journal of Applied Electrochemistry*, 20: 399-404, 1990

[19] D. Liang, J. J. Mallett, G. Zangari. Underpotential codeposition of Fe–Pt alloys from an alkaline complexing electrolyte: Electrochemical studies, *Journal of Electrochemical Society*, 158: D149-D157, 2011.

[20] A. J. Bard, L. R. Faulkner, *Electrochemical methods, Fundamentals and applications*, New York, John Wiley and Sons, 2001.

[21] K. Leistner, S. Oswald, J. Thomas, S. Fähler, H. Schlörb, L. Schultz. Potential dependence of composition and structure of electrodeposited Fe–Pt films, *Electrochimica Acta*, 52: 194-199, 2006

[22] J. J. Mallett, E. B. Svedberg, S. Sayan, A. J. Shapiro, L. Wielunski, T. E. Madey, W. F. Egelhoff, T. P. Moffat. Compositional control in electrodeposition of FePt films, *Electrochemical and Solid State Letters*, 7: C121-C124, 2004

For wider interest

Fe-Pd alloys have many potential applications because of their unique chemical and magnetic properties, which can be tailored by changing their composition. In alloys with a Pd content of 28-31 at.% a magnetic shape-memory effect can be observed, alloys containing about 50 at.% of Pd represent promising candidates for micro-electro-mechanical systems (MEMS) due to their high magnetocrystalline anisotropy and Pd-rich alloys exhibit catalytic properties, which can result in a high hydrogen-adsorption capacity. Electrochemical synthesis represents a cost-effective and efficient method for preparing metals and alloys. The shape of the deposited alloy can be easily modified using the appropriate geometry of the working electrode. Fe-Pd alloy in form of thin films, nanowires and nanotubes with different compositions can be fabricated.

In this study we have investigated the kinetic parameters for depositing Fe and Pd and their influence on the Fe-Pd alloy's composition, while performing the deposition on a flat Au electrode to get Fe-Pd thin films and into an Au-sputtered porous alumina template to get Fe-Pd nanowires. The electrodeposition of Fe and Pd was found to be irreversible and diffusion-controlled. Diffusion coefficients and charge-transfer coefficients were determined by cyclic voltammetry and the exchange current densities for both metallic ions in the porous alumina template and on the flat electrode were determined via a Butler-Volmer analysis. From the obtained results we can conclude that the kinetics of the electrodeposition process is not influenced by the electrode geometry. Moreover, similar diffusion-coefficient ratios $D_{\mathrm{Fe}}/D_{\mathrm{Pd}}$ and similar kinetics on the both investigated working electrodes under the same deposition conditions (i.e., solution and applied potential) results in Fe-Pd-based thin films and nanowires having similar compositions.

In summary, understanding diffusion and kinetic parameters of the electrochemical deposition process allow us to fabricate Fe-Pd alloy with different shapes (thin films, nanowires) and, at the same time, precisely control the composition.

Inkjet printing of alkoxide-based precursor solution for use in transparent electronics

Aleksander Matavž[1,2], Raluca C. Frunză[1], and Barbara Malič[1]

[1] Jožef Stefan Institute, Electronic Ceramics Department, Ljubljana, Slovenia

[2] Jožef Stefan International Postgraduate School, Ljubljana, Slovenia

matawzh@gmail.com

Abstract. We have studied the fabrication of inkjet-printed, a few 10 nm thick 2D-structures of a Ta_2O_5-based dielectric for possible use in transparent electronics. The precursor solution, consisting of Ta-, Al-, and Si-alkoxides dissolved in 2-methoxyethanol and ethanol, was modified in terms of viscosity and surface tension to be suitable for piezoelectric inkjet printing. The viscosity of the solution was increased by admixing a more viscous solvent, i.e. glycerol. The as-prepared ink was stable and jetting even after long periods of time. We adjusted the printing parameters to achieve the best patterning quality on indium tin oxide (ITO) covered glass substrates. The functional properties of the inkjet-printed layers were compared to the state-of-the-art spin-coated films.

Keywords: transparent electronics, inkjet printing, thin films, nanotechnology, sol-gel, metal oxides.

1 Introduction

Transparent electronics has received a lot of attention during the past decade, as a range of new applications and devices can be produced with this technology. It aims towards low manufacturing costs, low temperature processing of materials, and employment of large area deposition techniques that are scalable for industrial production. [1] Nowadays, photolithography is the most widely used patterning technique and it is renowned as a high-resolution technique, yet time consuming and expensive. The deposition technique that meets the requirements of transparent electronics is inkjet printing. It is fast, cost-effective and produces no waste.

The specific fluid requirements represent a large restriction for inkjet printing as the fluids should have the viscosity below 40 mPa·s and the surface tension larger than 20 mN/m. The optimization of the printing procedure with the aim to obtain structures with well-defined geometry and good functional properties is still an ongoing process. A lot of work has been done to determine the printing range of fluids in terms of fluid's physical properties [2-4], and to avoid the so-called "coffee stain" drying phenomena. [5-7] However, there are only handful reports on inkjet printing of metal oxide precursor solutions.

In our study we have chosen to print and investigate dielectric structures based on tantalum(V) oxide, suitable for applications in transparent electronics. Ta_2O_5 has a high dielectric constant of ~25 in the amorphous phase, high refractive index, and high chemical stability. [8, 9] A rather small band gap of tantalum(V) oxide results in relatively large leakage currents. The leakage characteristics can be improved by incorporating materials with a larger band gap, e.g., Al_2O_3 or SiO_2, as previously proposed. [10, 11] The high chemical stability of Ta_2O_5 makes respective thin films difficult to etch, and patterning by inkjet printing arises as a potential solution.

On one hand, chemical solution deposition (CSD) of thin films is a well-established research field, and the physical and chemical properties of the precursor solutions or sols have been established, i.e. viscosity, wetting behavior, chemical reactivity/stability and so on. [12] On the contrary, the deposition of functional materials by inkjet printing is still facing problems.

Following the approach of Tellier et al. [13], we modified the 2-methoxyethanol-based CSD-precursor solution in terms of viscosity and surface tension. We optimized the printing process and prepared structures with well-defined geometry. We investigated the quality of printed layers in terms of profilometry, atomic force microscopy, dielectric and electrical characterization.

2 Experimental

Preparation of the solution and the ink. Alkoxide-based precursor solutions (0.1 M) were prepared at room temperature in an inert nitrogen atmosphere as described in [10]. The ternary composition Ta_2O_5-Al_2O_3-SiO_2 with Ta:Al:Si = 8:1:1, further denoted as TAS solution, was prepared by mixing the precursor solutions in 8:1:1 volume ratio. The ink was prepared by admixing 30 vol. % of glycerol to the TAS solution. The final concentration of the ink was set to 0.05 M.

Characterization of liquids. Viscosity and surface tension were measured at 25 °C using a Physica MCR 301 rheometer and a KRÜSS EasyDrop DSA20E tensiometer, respectively.

Chemical solution deposition. Thin-films were prepared by spin-coating the TAS solution for 30 sec at 3000 rpm on ITO-covered glass. The films were heated in air on a hot plate at 150 °C for 10 min and at 350 °C for 10 min after the deposition of each layer. The process was repeated 5 or 10 times to increase the thickness of film to ~25 or ~55 nm, respectively.

Inkjet printing. Inkjet printing was performed using a Dimatix DMP 2831 piezoelectric printer equipped with a 10 pL cartridge (DMC-11610). The optimal printing parameters were: drop spacing of 20 µm, jetting frequency of 20 kHz, driving voltage of 21 V, height between the cartridge and the substrate of 0.7 mm. The temperature of the cartridge and the substrate was set to ambient. The as-printed structures were heated in air on a hot plate at 150 °C for 10 min and at 350 °C for 10 min after each layer deposition.

Characterization of layers. The surface morphology and cross-sections were investigated by Asylum Research MFP-3D-STM atomic force microscope and JEOL Ltd. JSM-7600F field-emission SEM, respectively. For the dielectric and electrical measurements, we sputtered top contacts through a shadow mask to fabricate the metal-insulator-metal (MIM) capacitors. The capacitance and dielectric losses were measured at room temperature with a driving signal of 50 mV at 100 kHz using a HP 4284A impedance analyzer. The leakage currents were measured using the Aixacct TF 2000E system with the voltage step of 0.1 V and the measurement time of 2 seconds.

3 Results

For a proper drop formation, the Z number (eq. 1) of a fluid should be between 1 and 10. [4] The TAS solution designed for CSD had a relatively high surface tension and low viscosity. The calculated Z number of the solution was 17, which is too high for a stable drop formation. We increased the viscosity of the TAS solution by admixing more viscous glycerol. The density, viscosity, surface tension, and calculated Z number of the solution and the ink are presented in Table 1.

$$Z = \frac{\mathrm{Re}}{\sqrt{\mathrm{We}}} = \frac{\sqrt{a\,\rho\,\gamma}}{\eta} \quad , \qquad (1)$$

where Re is the Reynolds number, We is the Weber number, a is the nozzle diameter, ρ is the density, γ is the surface tension, and η is the viscosity.

Table 1: Physical properties of the CSD solution and the ink.

	Density g cm^{-3}	**Viscosity mPa s**	**Surface tension mN m^{-1}**	**Z**
TAS solution	0.971	1.6	29.6	17
TAS solution + 30% glycerol	1.062	10.1	32.9	3

The solution and the ink were transparent, without agglomerates, and stable for more than 1 month. Both exhibited a constant viscosity at the shear rate ranging from 10 to 500 s^{-1}, suggesting Newtonian behavior. The ink could be jetted from a 10 pL nozzle with a stable drop formation and without occurrence of satellites as shown in Figure 1. The drop volume evaluated by the graphical analysis of the in-flight image was 12 pL.

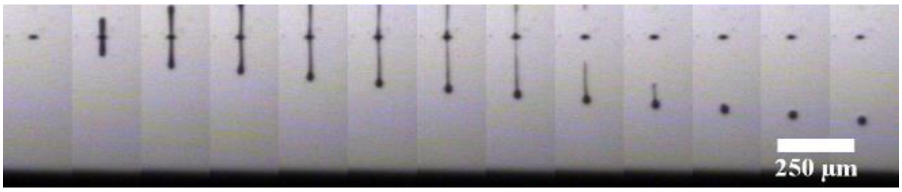

Figure 1: Image sequence of the drop formation upon jetting the ink. The image sequence of the drop formation is separated by 5 µs increments.

During the printing trials we noticed that the contact angle between the ink and the ITO-covered glass decreased when the substrate was annealed prior printing on it. The decrease was induced at temperatures higher than 300 °C and it was time dependent. The contact angle in inkjet printing has to be precisely adjusted. A high contact angle may result in the dewetting process or shape distortion, and low contact angle decreases the resolution of printing. By adjusting the annealing time we were able to control the contact angle and obtain the best printing results.

We printed an array of squares with the lateral dimensions of the squares of 500 x 500 μm^2 and the separation distance between two nearest squares of 250 μm. The drop spacing of 20 μm was selected for printing. The sections of the as-printed, dried and pyrolyzed patterns are shown in Figure 2.

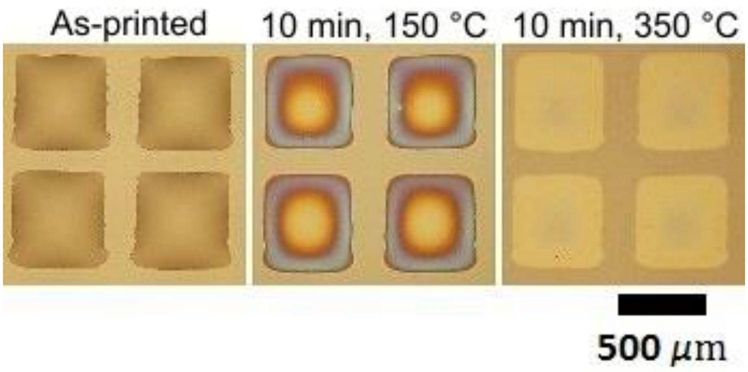

Figure 2: Optical micrographs of the middle part of the inkjet-printed array of squares.

The squares heated at 150 °C [Figure 2 and Figure 3(a)] had a color gradient from the edge toward the center, which corresponded to the thickness variation. The optical observations were confirmed by profilometry measurements shown in Figure 3(b). The measurements of the structures heated at 350 °C revealed higher deposits at the edge of squares. This so-called "coffee stain effect" was more pronounced for the structures consisting of 2 and 3 printed layers.

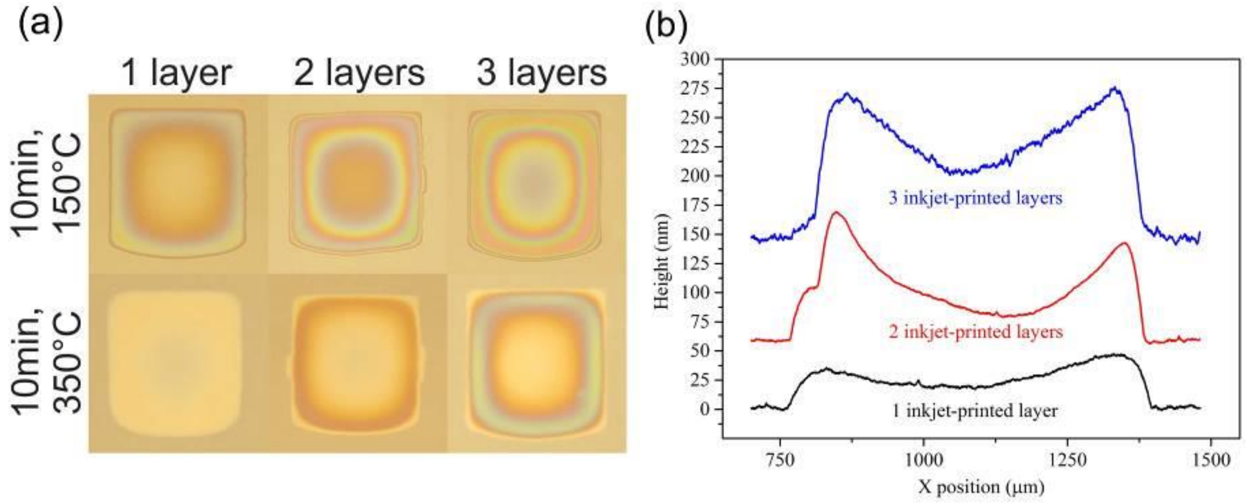

Figure 3: (a) Structures consisting of 1, 2 or 3 inkjet-printed layers. (b) Profilometry measurements of the structures consisting of 1, 2 or 3 inkjet-printed layers, heated at 350 °C.

The surface morphology was investigated by AFM measurements. The printed 2D structures and spin-coated films had uniform surfaces without any evident microstructural details. The Root Mean Square (RMS) surface roughness was found to be in all cases below 0.5 nm for the scan area of 5 x 5 μm^2, confirming that the films were smooth, which agrees with their amorphous nature. [10]

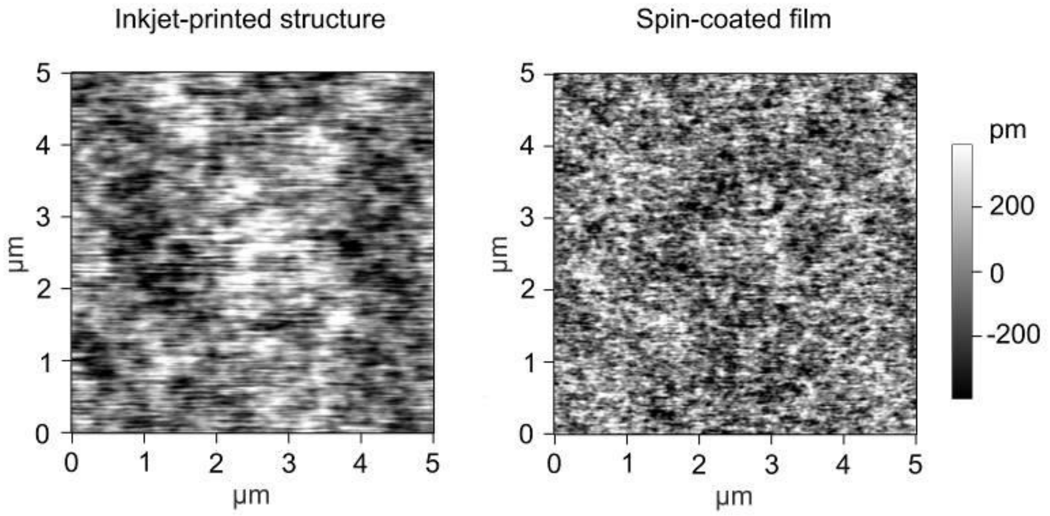

Figure 7: AFM topography image of the structure consisting of 1 layer inkjet-printed and the structure consisting of 10 spin-coated layers on ITO covered glass substrate, heated at 350 °C. The RMS roughness was under 0.5 nm for both samples.

Finally, we investigated the dielectric and electrical performance MIM capacitors. The results are presented in Table 2. The dielectric constant of inkjet-printed structures and spin-coated samples was comparable (~16 at 100 kHz). Regardless of the deposition technique, the dielectric losses decreased with increasing number of layers.

Table 2: The dielectric and electrical performance of thin-film capacitors. The dielectric properties were measured at 100 kHz.

	Dielectric constant	**Dielectric losses**	**J at 200 kV/cm μA/cm²**
1 inkjet-printed layer	**15** ± 2	**0.18** ± 0.06	**8.2** ± 3
2 inkjet-printed layers	**16** ± 2	**0.16** ± 0.06	**1.3** ± 0.1
3 inkjet-printed layers	**15** ± 2	**0.05** ± 0.01	**0.7** ± 0.15
5 spin-coated layers	**17** ± 2	**0.14** ± 0.03	**0.3** ± 0.05
10 spin-coated layers	**16** ± 2	**0.04** ± 0.01	**0.25** ± 0.05

The leakage current measurements revealed a distinct difference between inkjet-printed and spin-coated films (Figure 4). The structures consisting of 1 inkjet-printed layer exhibited the highest leakage currents, about 30 times higher than that of the spin-coated samples. The latter exhibited the lowest leakage currents, with the value below 0.3 μA/cm² at the applied electric field of 200 kV/cm. The leakage current of the inkjet-printed structures decreased in with the increasing number of printed layers. The improved performance of multi-layer structures suggests that for a stable operation the printed structure should consist of at least 2 inkjet-printed layers.

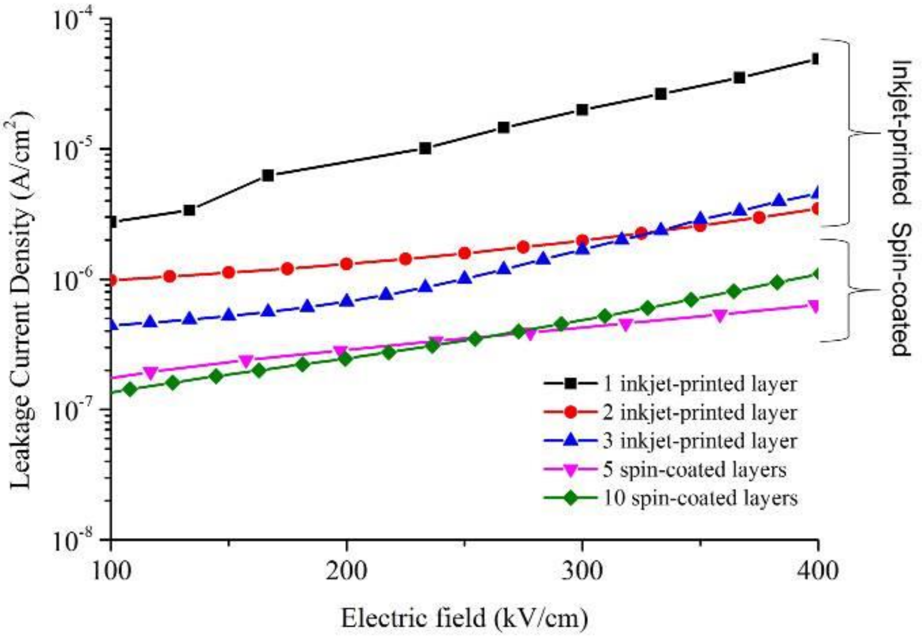

Figure 4: Leakage current measurements of the structures consisting of 1, 2 or 3 inkjet-printed layers and spin-coated films.

4 Conclusions

We successfully modified the alkoxide-based precursor solution originally designed for spin coating to be suitable for inkjet printing. With the addition of a more viscous glycerol we adjusted the physical properties of the TAS spin-coating solution. The jetting of the ink resulted in a stable drop formation, without satellites. The ink could be jetted even after long periods of time, proving good chemical stability of the inks.

We optimized the parameters involved in inkjet printing and fabricated the structures, consisting of 1, 2 or 3 inkjet-printed layers of TAS.

The fabricated features had smooth surfaces, without evident surface details. We compared the dielectric and electrical properties of the inkjet-printed and state-of-the-art spin-coated thin-film capacitors. Both deposition techniques rendered the capacitors with comparable dielectric properties. The spin-coated samples exhibited lower leakage currents, presumably due to the improved film quality with increasing the number of deposited layers.

Acknowledgments

We would like to thank the Centre of Excellence NAMASTE and Nanocenter for providing their equipment. Special thanks go to Aljaž Drnovšek for all profilometry measurements.

We acknowledge the financial support of the Slovenian Research Agency (projects: J2-4173, P2-0105).

References:

1. J.F. Wager, R.E. Presley, and D.A. Keszler. *Transparent electronics*. New York: Springer, 2008.
2. J.E. Fromm. *Numerical calculation of the fluid dynamics of drop-on-demand jets* in IBM Journal of Research an Development, **28**(3): 322-333, 1984.
3. D. Jang, D. Kim, and J. Moon. *Influence of fluid physical properties on ink-jet printability* in Langmuir: the ACS journal of surfaces and colloids, **25**(5): 2629-2635, 2009.
4. N. Reis and B. Derby. *Ink Jet Deposition of Ceramic Suspensions: Modeling and Experiments of Droplet Formation* in MRS Online Proceedings Library, **625**, 2000.
5. E. Tekin, P.J. Smith, and U.S. Schubert. *Inkjet printing as a deposition and patterning tool for polymers and inorganic particles* in Soft Matter, **4**(4): 703-713, 2008.
6. R.D. Deegan, O. Bakajin, and T.F. Dupont. *Capillary flow as the cause of ring stains from dried liquid drops* in Nature, 389: 827-829, 1997.
7. H. Hu and R.G. Larson. *Marangoni effect reverses coffee-ring depositions* in The journal of physical chemistry B, **110**(14): 7090-7094, 2006.
8. P. Barquinha, R. Martins, L. Pereira, E. Fortunato. *Transparent Oxide Electronics*. United Kingdom: John Wiley & Sons, 2012.
9. C. Chaneliere, J.L. Autran, R.A.B Devine, B. Balland. *Tantalum pentoxide (Ta_2O_5) thin films for advanced dielectric applications* in Materials Science & Engineering R-reports, **22**(6): 269-322, 1998.
10. R.C. Frunză, B. Kmet, M. Jankovec, M. Topič, B. Malič. *Ta_2O_5-based high-K dielectric thin films from solution processed at low temperatures* in Materials Research Bulletin, **50**: 323-328, 2014.
11. P. Barquinha, L. Pereira, G. Gonçalves et al. *Low-temperature sputtered mixtures of high-κ and high bandgap dielectrics for GIZO TFTs* in Journal of the Society for Information Display, **18**(10): 762-772, 2010.
12. T. Schneller, R. Waser, M. Kosec, D. Payne, eds. *Chemical Solution Deposition of Functional Oxide Materials*. Wien: Springer, 2013.
13. J. Tellier, B. Malič, D. Kuščer, G. Trefalt, M. Kosec, *Ink-Jet Printing of In_2O_3/ZnO Two-Dimensional Structures from Solution* in Journal of the American Ceramic Society, **94**(9): 2834-2840, 2011.

For wider interest

Inkjet printing is a fairly old deposition technique with the beginnings in 1950s. Since then, it has been extensively used in home and small office applications with a simple task of depositing colored inks on paper. Recently, the technique has caught the interest of scientists as it could be used for micromanufacturing and rapid prototyping.

Inkjet technology has a large potential in transparent electronics as it is economical, produces almost no waste, and is scalable for large-area deposition. In this contribution, we report the fabrication of inkjet-printed capacitors based on tantalum(V) oxide. Dielectrics with high dielectric permittivity, such as tantalum oxide, are essential components of the next generation electronic devices, e.g. field-effect transistors and capacitors.

The physics of drop formation sets restrictions on the viscosity and surface tension of the ink. The precursor solution had a too low viscosity for stable drop formation, thus we admixed 30 vol. % of the highly viscous glycerol. We printed the as-prepared ink onto glass substrates with an ITO conductive coating and fabricated thin-film capacitors with the thickness of the dielectric layer in the nanometer range. The poor electrical performance observed for capacitors consisting of 1 inkjet-printed layer was improved for capacitors consisting of 2 or 3 inkjet-printed layers. The electrical performance of those multi-layer structures was comparable to spin-coated films.

Because of the complexity of inkjet printing, there are only handful reports on printing of metal oxide solutions. We believe our work presents an important contribution to the improvement and the realization of inkjet technology.

Amino-acid-iron-oxide-nanoparticles: adsorption studies and colloidal properties

Klementina Pušnik[1,2], Gregor Marolt[3], Sašo Gyergyek[1], Darko Makovec[1,2,]
[1] Department for Materials Synthesis, Jožef Stefan Institute, Ljubljana, Slovenia
[2] Jožef Stefan International Postgraduate School, Ljubljana, Slovenia
[3]Faculty of Chemistry and Chemical Technology, Ljubljana, Slovenia
klementina.pusnik@ijs.si

Abstract.
For majority of different applications of superparamagnetic iron-oxide nanoparticles in medicine and technology, stable aqueous suspensions are required. One possible type of nontoxic and biocompatible molecules used in the stabilization of aqueous nanoparticles suspensions are amino acids. In this work the adsorption of aspartic amino acid (ASP) onto the iron-oxide nanoparticles and the colloidal properties of their aqueous suspensions were studied. Even the ASP-adsorbed nanoparticles display moderate zeta potential; they form the colloidally-stable aqueous suspensions. Direct analysis of ASP in the supernatant of the ultracentrifuged suspensions using an ion chromatography with pulsed amperometric detection suggested adsorption of the ASP in the form of large molecular associates, sterically stabilizing the suspensions.

Keywords: colloidal stability, adsorption, iron-oxide nanoparticles, amino acids, aspartic acid.

1 Introduction

Superparamagnetic iron-oxide nanoparticles are used in a broad range of technological and biomedical applications. In technology they are mainly used in ferrofluids and in relation to magnetic separation [1]. In medicine they can be used in numerous applications in vitro (e.g., the detection, separation, or sorting of specific cells, magnetofection, etc.) and in vivo for diagnostics (e.g., for contrast enhancement in magnetic resonance imaging (MRI) and in magnetic particle imaging (MPI) and in therapy (e.g., for targeted drug delivery and for cancer treatment using magnetically mediated hyperthermia [2-13]. The iron-oxide nanoparticles are considered safe and have been approved by the US Food and Drug Administration (FDA) for in-vivo applications [2].

Generally, the surface properties of the nanoparticles have to be adapted to meet requirements of different applications. Usually, organic molecules are covalently bonded or adsorbed onto the nanoparticles' surfaces to engineer their surface properties, e.g., surface charge, hydrophilicity/hydrophobicity, or availability of specific functional groups. As the nanoparticles are usually applied in a form of stable suspensions, the surface modification has to provide compatibility with the liquid medium and repulsive forces between the nanoparticles preventing the agglomeration. For in vivo applications, the organic shell of the molecules should be nontoxic and biocompatible. The surface shell at the nanoparticles also significantly determines the interactions of the nanoparticles with living systems, for example, their interaction with the blood. It influences adsorption of plasma proteins onto the nanoparticles, interactions with cells, e.g., the amount of nanoparticles internalized in the cells, a blood-circulation time, and fate of the nanoparticles after intravenous administration. Additionally, it is usually necessary that the surface shell of organic molecules provides specific functional groups (functionalization) for further bonding / (bio)conjugation of different molecules that are needed in a specific application, e.g., targeting ligands, therapy agents, fluorophores, etc.

One possible type of nontoxic and biocompatible molecules that can be used for engineering of the nanoparticles' surface properties and for stabilization of their aqueous suspensions is amino acids. The large number of different amino acids gives opportunity to change the properties, e.g., surface charge and availability of different surface functional groups, in a broad range. Different amino acids have been applied to prepare stable suspensions of iron-oxide nanoparticles [14-20]. It was also proposed, that the adsorbed amino acids can be used for functionalization of the nanoparticles providing specific functional groups at the nanoparticles' surfaces for further bonding of different molecules [14, 15, 18]. As the amino acids play a very important role in the body, their adsorption onto the magnetic nanoparticles was proposed for their targeted delivery [20]. For all mentioned applications the molecules should be bonded to the nanoparticles' surfaces through a strong and stable bond, which will prevent the molecules to be detached from the surface or exchanged with other ligands present in the liquid medium.

Adsorption of the amino acids onto the surfaces of different minerals, including iron oxide, has been intensively studied. Apart from the possible preparation of the nanoparticles suspensions, the adsorption of the amino acids is also important for prebiotic chemistry, in the general frame of evaluating Bernal's hypothesis of prebiotic polymerization in the adsorbed state as a step in organization of molecules in the sequence of organizational events leading to the emergence of life [21]. The interactions between the amino acids and nanoparticles are also very important for understanding the interactions of the nanoparticle with polypeptides and proteins.

It is widely accepted that the amino acids adsorb onto the iron-oxide surface in the form of their respective salts [14-16, 18]. However, the mechanisms of the amino acids adsorption onto the nanoparticles' surfaces are not clear yet and the literature results are frequently inconsistent.

In this work the adsorption of aspartic acid (ASP) onto the iron-oxide maghemite nanoparticles and the preparation of the stable aqueous suspensions have been systematically studied. ASP is an α- amino acid with one amino group and two carboxyl groups ($HOOC-CH_2-CH-(NH_2)COOH$). Sousa et al. [14] showed using FTIR and Raman spectroscopy that the ASP adsorb on the oxide surface by forming a chemical bond of chelate type involving Fe(III) surface species and a carboxylate group. The ASP-modified nanoparticles formed a stable colloidal solution at a pH of 5-8. Mikhaylova et al. [15] reported that an isoelectric point of the suspension of iron-oxide nanoparticles is shifted from neutral pH to alkaline (pH ~ 8.5) suggesting adsorption of ASP with both carboxyl groups onto the surface, leaving the amino group oriented outward the aqueous medium (Scheme 1a). The conductometric measurements have shown that the maximum adsorption of ASP onto the surfaces of iron oxide occurs when the solution pH is near 3. For increasing pH values the uptake of the ASP decreases systematically. The surface saturation at pH ~3 was achieved at approximately 15×10^{-19} mol of the ASP/cm^2 of the oxide surface, corresponding to approximately 90 molecules of ASP/nm^2 [14]. This value is very high and does not support the simple adsorption model based on the adsorption of amino-acid monolayer.

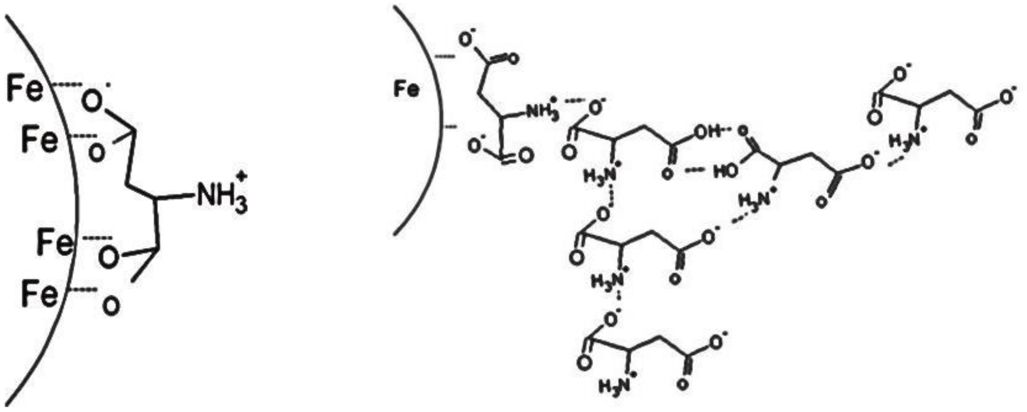

a) b)

Sheme 1: Schematic presentation of aspartic acid adsorption onto iron-oxide nanoparticles as single molecular layer (a) and in the form of molecular associates (b).

2 Experimental Section

The iron-oxide nanoparticles were synthesized using coprecipitation of Fe^{3+} and Fe^{2+} ions from the aqueous solution with aqueous ammonia [22]. Transmission electron microscopy (TEM) revealed that the nanoparticles exhibited a globular shape (Figure 1a). The size distribution (Figure 1a) obtained by measuring at least 150 nanoparticles and fitted by a log-normal distribution showed the equivalent diameter of 10 ± 2 nm. The specific surface area of the nanoparticles was estimated from the TEM average size to be approximately $100 m^2/g$. X-ray diffractometry XRD showed only broad peaks corresponding to a spinel structure. As the nanoparticles were synthesized in an ambient air, it is reasonably to conclude that the Fe^{2+} was completely oxidized and the nanoparticles can be specified as maghemite (γ-Fe_2O_3). The chemical analysis of the nanoparticles synthesized using the same procedure supports this conclusion [22].

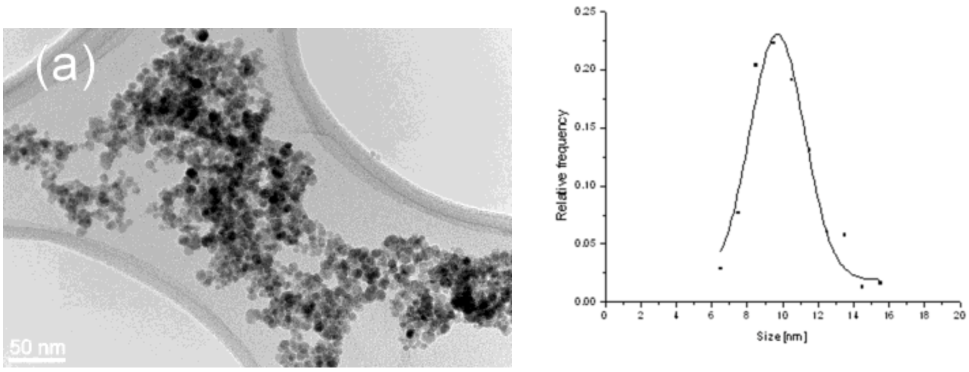

Figure 1. TEM image and the corresponding size distribution of iron-oxide nanoparticles.

Adsorption of ASP onto the iron-oxide nanoparticles was studied indirectly, by observing colloidal properties of the final aqueous suspension of the ASP-adsorbed nanoparticles, and directly, by measuring quantity of the adsorbed ASP in the supernatant of the suspensions.

For the preparation of the stable suspension 2,89 g of ASP was mixed with 450 mL of aqueous suspension containing 1 g of the iron-oxide nanoparticles. The pH of the suspension was set to 4.0 using ammonia and the suspension was mixed for 5 hours. Then, the pH was increased to 11.0 using ammonia. The excess, non-adsorbed ASP was washed from the suspension using ultrafitration (100 mL of the suspension was washed with 300 mL of water). The colloidal properties of the suspensions were investigated by measuring the zeta-potential (Brookhaven, Instruments Corporation, Zeta PALS) and the hydrodynamic-size distribution using the dynamic light-scattering method (DLS) (Fritsch, ANALYSETTE 12 Dynasizer).

The adsorption of the ASP by the nanoparticles was evaluated by measuring of the ASP concentrations in the supernatants of the suspensions after ultracentrifugation of the nanoparticles. First, mother suspension was prepared by mixing 1 g of the iron-oxide nanoparticles in 450 mL of water and setting pH to 4.0 with diluted HCl. The mother suspension was separated in vials containing 45 mL of the suspension with 0.1 g of the nanoparticles. Then, in the vials different amounts of ASP were dissolved, while the pH was maintained at 4.0 with ammonia. After mixing the suspensions for long time (1 week) allowed to reach equilibrium, the nanoparticles were sedimented using ultacentrifugation. The ASP concentrations in the supernatants were measured using ion chromatography (IEC) with pulsed amperometric detection.

3 Results and Discussion

Stable aqueous suspensions of iron-oxide nanoparticles were prepared using aspartic acid (ASP) as the surfactant. First, the ASP was absorbed onto the nanoparticles in aqueous medium at pH = 4. The ASP (HOOC-CH_2-CH-(NH_2)COOH) has two carboxyl groups and one amino group, with pK_1= 2,09, pK_2= 3,86, pK_3= 9,82. We assumed that the ASP at pH = 4 will be attracted to the positively charged surface of nanoparticles with the negatively charged, dissociated carboxyl groups. Figure 2 shows calculated curves showing relative fraction of individual ASP species as a function of pH. At pH = 4 mixture is present, which contains molecules with protonated amino group, and the one or the both carboxyl groups dissociated.

It was directly shown with FTIR and Raman spectroscopy that the aspartic acid forms a chemical bond of chelate type with Fe ions at the iron-oxide surfaces [14-15]. According to a simple model usually described in the literature the amino acid adsorbs onto iron-oxide nanoparticles in a single layer with carboxyl groups attached to the surfaces and amino group oriented toward the medium (see scheme 1a). That should result in a positive surface charge at neutral pH and the shift of the isoelectric point of the aqueous suspension from neutral pH toward an alkaline region [15]. However, zeta-potential measurement (Figure 3) showed no significant differences between the suspensions of the as-synthesized iron-oxide nanoparticles and the ASP-adsorbed-nanoparticles. The as-synthesized nanoparticles exhibited an isoelectric point (IEP) around pH 6. The adsorption of the ASP onto the nanoparticles caused no significant change in the IEP. Also the absolute values of the zeta potential above and below the IEP remained relatively low. The absolute value of zeta potential is related to electrostatic repulsive forces preventing agglomeration of the nanoparticles in the aqueous suspension. Usually, it is assumed that the stable suspension can be formed if the zeta potential exceeds 30 mV [23]. However, when the ASP-absorbed nanoparticles were dispersed at high pH (~ 11) the aqueous suspension seemed colloidally stable, even the zeta potential at that pH was below 30 mV.

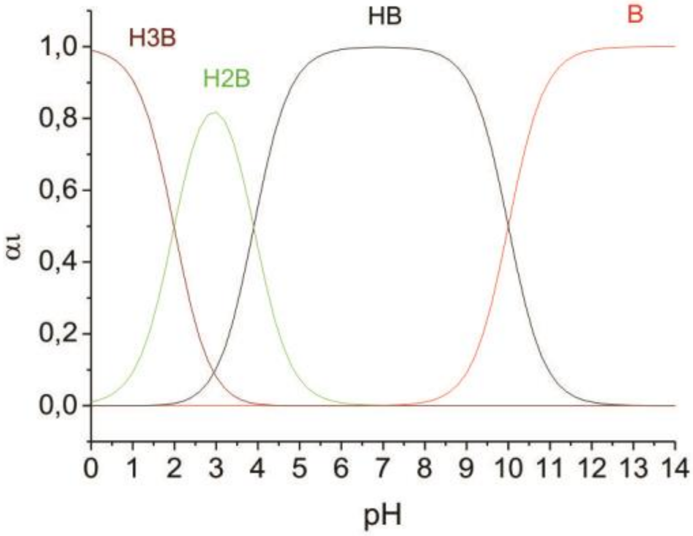

Figure 2. Calculated curves showing relative fraction of individual ASP species as a function of pH (marked in the graph with H3B, H2B, HB, B for undissociated, one carboxyl group dissociated, two carboxyl groups dissociated, amino group deprotonated, respectively).

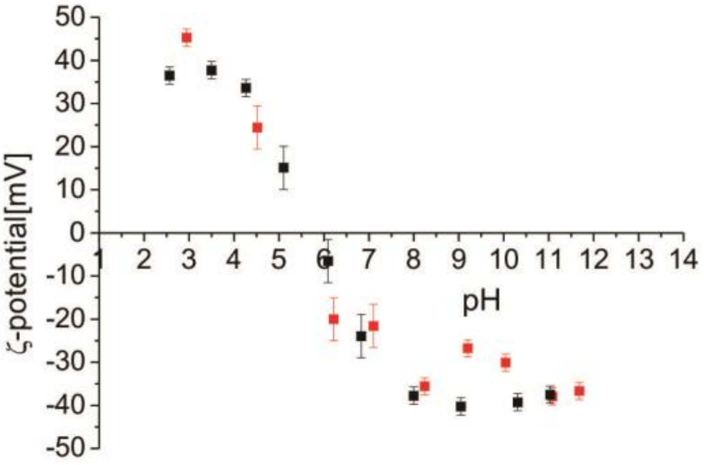

Figure 3. ζ-potential of iron-oxide nanoparticles (black dots) and aspartic-acid-adsorbed iron-oxide nanoparticles (red dots).

The stability of the aqueous suspensions of the aspartic-acid-adsorbed iron-oxide nanoparticles was followed with the DLS measurements. The number-weighted size distribution in Fig. 4 shows that the vast majority of the nanoparticles in the suspension (at concentration of 5 mg of nanoparticles per mL) has hydrodynamic size of approximately 40 nm, however, some larger particles with sizes between approximately 70 nm and 130 nm, were also present. The size did not change significantly with the time. However, after very long time of approximately one month some degree of flocculation was observed in the suspension. The results of DLS measurements also did not change significantly, if the suspension was diluted to 0.1 mg/mL, however, at dilution to 0.05 mg/mL the slow flocculation was visible. The suspension of the as-synthesized nanoparticles was unstable, independently on the pH.

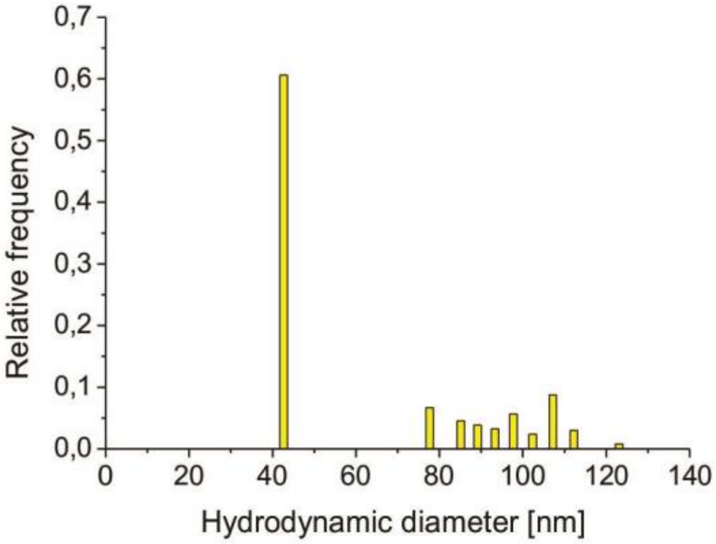

Figure 4. Number-weighted particles size distribution of aspartic-acid-adsorbed iron-oxide nanoparticles in aqueous suspension (5 mg/mL, pH = 11).

The presented zeta potential and DLS measurements are not consistent with adsorption of the ASP onto the iron oxide surfaces in a single molecular layer. Also the good colloidal stability of the ASP-absorbed nanoparticles' suspension is unusual, because the relatively weak electrostatic repulsive forces are expected due to low zeta potential. The hydrodynamic size of the nanoparticles in the suspension measured with DLS (~ 40 nm) is significantly larger the size measured from TEM images (10 nm), suggesting a thicker layer of the molecules at the nanoparticles.

To solve this puzzle, the adsorption of the ASP onto the nanoparticles was systematically studied. The nanoparticles in the aqueous medium were equilibrated with different amounts of the ASP and two different pH values of the suspension. Then, the suspension was ultra-centrifuged to sediment the nanoparticles and the supernatant was analysed using ion chromatography. As the stable colloidal suspension was prepared by adsorption of the ASP onto the nanoparticles at pH=4.0 and their dispersion in water at pH=11, the adsorption of ASP at those two values of pH was measured.

Figure 5 (a) shows the concentration of the ASP in the supernatant of the suspension of the iron-oxide nanoparticles equilibrated with the ASP with different concentrations of the ASP at pH = 4 and pH = 11. The concentrations of the ASP added in the suspensions are expressed in mmol of ASP/g of the nanoparticles. At pH = 4 only very low concentration of the non-adsorbed ASP was present in the supernatant even for the largest addition of the ASP of 21.7 mmol/g of nanoparticles. Thus, the surface concentration of the ASP adsorbed onto the nanoparticles increases almost linearly with the concentration of the added nanoparticles. In the graph of Figure 5b the concentrations of the added ASP and the absorbed ASP are expressed in mmol/cm^2 of the nanoparticles. If the entire added ASP would adsorb at the nanoparticles, the adsorption curve would follow the dashed line in the graph of Figure 5b.

Usually, the adsorption curves show saturation of the surface with the adsorbed ligand. Our results of direct measurements of the ASP in the supernatant of the suspension at pH = 4 did not reach the saturation, even the highest concentration of the ASP added to the suspension of the nanoparticles was close to the solubility limit of the ASP in water. Contrary to our results, Sousa et al. [14] showed by conductometric measurements that the aspartic acids adsorb onto the maghemite surface following an adsorption isotherm. They added the aspartic acid to nanoparticles in the solution of HNO_3 at pH =3. The differences in observed adsorption curves can be related to different procedures.

In the graph of Figure 5a the concentrations of the absorbed ASP are also expressed in number of molecules / nm^2 (right axis). At the highest concentration of the added ASP, more than 120 molecules attach per nm^2 of the nanoparticles' surface. This value is very large and suggests that the ASP is adsorbed in the form of large molecular associates. Most probably, the molecules of ASP in the associates are bonded with hydrogen bonds and also with electrostatic interactions, as schematically presented in Scheme 1b.

The adsorption of the ASP, as well as the formation of the associates depend on the degree of dissociation of the molecules and therefore are a function of the pH. At pH = 11 significantly larger concentration of the ASP remained in the supernatant (Figure 5a). However, the surface concentration of the adsorbed ASP on the nanoparticles is still large, almost 50 molecules of ASP / nm^2 for the highest concentration of the added ASP of 2.17x10^{-5} mmol/cm^2.

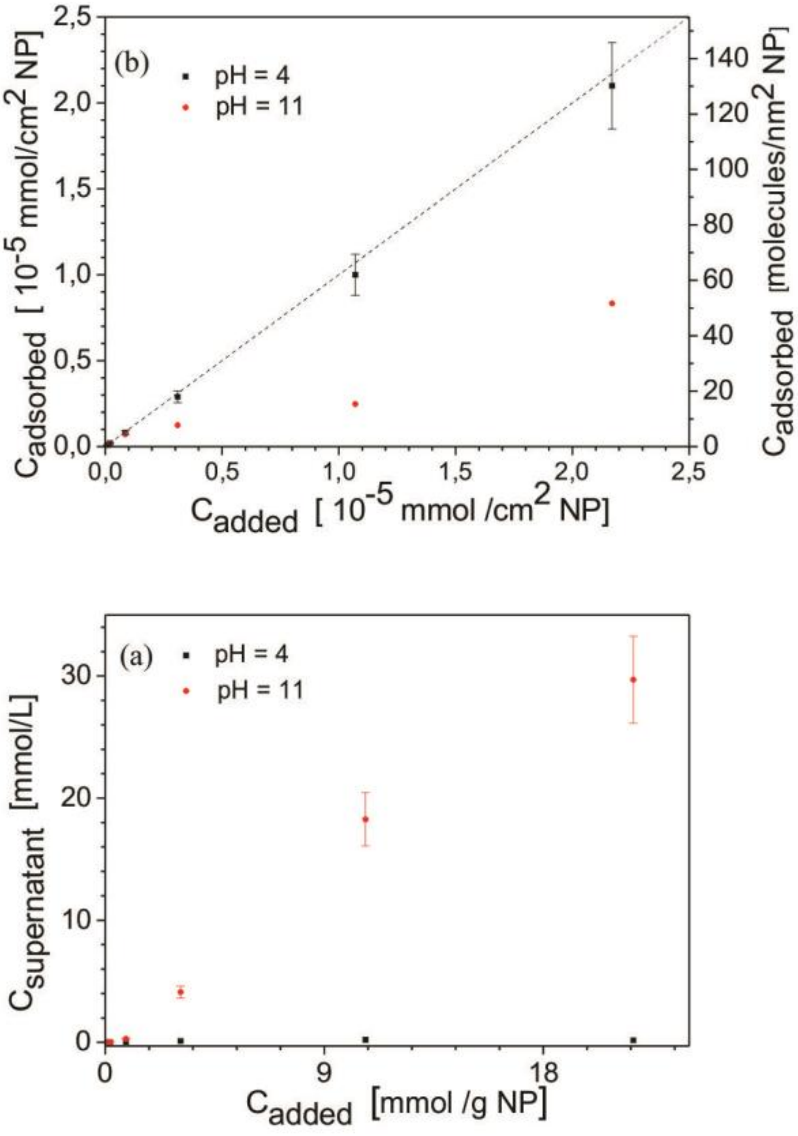

Figure 5: Adsorption isotherm of ASP at pH=4 and pH=11.

The adsorption curves strongly suggest that the ASP is adsorbed onto the nanoparticles' surfaces in the form of the large molecular associates. This is also in accordance with the zeta potential measurements, showing no change in IEP of the suspension with adsorption of the ASP and relatively good colloidal stability of the suspension at relatively low absolute values of the zeta potential. It seems that the suspensions are additionally sterically stabilized by the molecular associates. The presence of the ASP on the nanoparticles' surfaces in the form of the associates also explains the large hydrodynamic size of the nanoparticles in the suspensions measured with DLS, compared to their TEM size.

4 Conclusions

The adsorption of aspartic acid (ASP) on the iron-oxide (maghemite) nanoparticles in aqueous suspension does not change their zeta potential significantly. There is no change in isoelectric point and the absolute values of the zeta potential remained relatively low. However, even the absolute values of zeta potential were low; the suspension of the ASP-adsorbed nanoparticles at basic pH was relatively stable. The adsorption curves measured by direct analysis of ASP in the supernatant of the ultracentrifuged suspensions using an ion chromatography with pulsed amperometric detection suggested that the adsorption of the ASP does not follow an adsorption isotherm. Very high concentrations of the ASP attached onto the nanoparticles suggest that the ASP is adsorbed in the form of large molecular associates, which sterically contribute to stabilization of the suspension.

References:

[1] Primc, D.; Makovec, D. Composite Nanoplatelets Combining Soft-Magnetic Iron Oxide with Hard-Magnetic Barium Hexaferrite. *Nanoscale*, **00**:1-3 (2014).

[2] Magnetic Nanoparticles: From Fabrication to Clinical Applications, T. K. N. Thanh, , Ed.; CRC Press: Boca Raton, USA, 2012.

[3] Safarik I. and Safarikova M. In Magnetic Nanoparticles: From Fabrication to Clinical Applications; N. T. K. Thanh, Ed.; CRC Press: Boca Raton, USA, 2012, pp. 215-241.

[4] Weissleder, R.; Nahrendorf M. and M. J. Pittet, *Nature Mater.*, **13:**125−138 (2014).

[5] Gleich B. and. Weizenecker, J. *Nature*, **435**: 1214−1217 (2005).

[6] Timko, B. P.; Whitehead, K.; Gao, W.; Kohane, D. S.; Farokhzad, O.; Anderson D. and Langer Ann R. *Rev. Mater. Res.*, **41**: 3.1–3.20 (2011).

[7] Yu, M. K.; Jeong, Y. Y.; Park, J.; Park, S.; Kim, J. W.; Min, J. J.; Kim K. and Jon, S. *Angew. Chem. Int. Ed.*, **47**: 5362−5365 (2008).

[8] Lee, J.-H.; Jang, J.-T.;. Choi, J.-S; Moon, S.-H.;. Noh, S.-H; Kim, J.-W. ; Kim, J.-G.; Kim I.-S., Park K.-I. and Cheon J., *Nature Nanotechnol.* **6**: 418−422 (2011).

[9] Meffre, A.; Mehdaoui, B.; Kelsen, V.; Fazzini P. F. and Carrey, J. *Nano Lett.* **12**: 4722−4728 (2012).

[10]Thiesen B. and Jordan, A. *Int. J. Hyperthermia* 24: 467–474 (2008).

[11]Pollert E. and Závêta K. In Magnetic Nanoparticles: From Fabrication to Clinical Applications; N. T. K. Thanh, Ed.; CRC Press: Boca Raton, USA, 2012, pp. 449−478.

[12]Cherukuri, P.; Glazer E. S. and Curley, S. A. *Adv. Drug. Deliv. Rev.*, **62**: (339–345) 2010.

[13]Veverka, P.; Pollert, E.; Závêta, K.; Vasseur S. and Duguet, E. *Nanotehnology* **19**:(215705-1−215705-7)2008.

[14] Sousa, M.H.; Rubim, J.C.; Sobrinho, P.G.; Tourinho,F.A; Biocompaible magnetic fluid precursors based on aspartic and glutamic acid modified maghemite nanostructures. *Journal of Magnetism and Magnetic Materials,* **225**: 67-72 (2001).

[15] Mikhaylova, M.; Kim, D.K.; Berry, C.C.; Zagorodni, A.; Toprak, M.; Curtis. A.S.G.; Muhammed, M. BSA Immobilization on Amine-Functionanalized Superparamagnetic Iron Oxide Nanoparticles. *Chemistry of Materials*, **16**: 2344-2354 (2004).

[16] Durmus, Z.; Kavas, H.; Toprak, M.S.; Bayakal, A.; Altinçekiç T.G.; Aslan.A.; Bozkurt, A.; Coçgun,S. L-lysine coated iron oxide nanoparticles: Synthesis, structural and conductivity characterization. *Journal of Alloys and Coumpounds*, **484**: 371-376 (2009).

[17]Marinescu, G.; Patron, L.; Culita, D. C.; Neagoe, C.; Lepadatu, C. I.; Balint, I.; Bessais, L.; Cizmas, C. B. Synthesis of magnetite nanoparticles in the presence of aminoacids. *Journal of Nanoparticle Research*, **8:** 1045–1051 (2006).

[18]Qu, H.; Ma, H.; Zhou, W.; O'Connor, C. J. In situ surface functionalization of magnetic nanoparticles with hydrophilic natural amino acids. *Inorganica Chemica Acta,* **389**: 60-65 (2012).

[19]Park., Y.J.; Choi, E.S.; Baek, M.J.; Lee, G.H.; Colloidal stability of amino acid coated magnetite nanoparticles in physiological fluid. Materials Letters, 63: 379-381 (2009).

[20]Patel, D.; Chang, Y.; Lee, G.H.; Amino acid functionalized magnetite nanoparticles in saline solution. *Curr. Appl. Phys.* **9** S32–S34 (2009).

[21]Lambert, J.L. Adsorption and Polymerization of Amino Acids on Mineral Surfaces: A Review. *Orig Life Evol Biosph* **38**:211–242 (2008).

[22] Kralj, S.; Drofenik, M.; Makovec, D. Controlled surface functionalization of silica-coated magnetic nanoparticles with terminal amino and carboxyl groups. *J Nanopart Res,* **13**: 2829-2841 (2010).

[23]Tadros, Th. F., 1987. Solid/Liquid Dispersions. Academic Press Inc., London.

[24]Theerdhala, S.; Bahadur, D.; Vitta, S.; Perkas, N.; Zhong, Z.; Gedanken, A. Sonochemical stabilization of ultrafine colloidal biocompatible magnetite nanoparticles using amino acid, L-arginine, for possible bio applications. *Ultrasonics Sonochemistry*, **17**: 730-737(2010).

[25]Viota, J.L.; Arroyo, F.J.; Delgado, A.V.; Horno, J. Electrocinetic characterization of magnetite nanoparticles functionlized with amino acids. *Journal of Colloid and Interface Science*, **344**: 144-149 (2010).

For wider interest

Nano-sized materials such as magnetic nanoparticles, which are a major class of nanoscale materials (ferro/ferrimagnetic materials, such as iron, nickel, cobalt, and magnetic oxides like iron oxides, including magnetite and maghemite), have fascinating physical-chemical properties that if tuned properly, can design new bio-diagnostics and therapeutic strategies, as well as, innovative biotechnology methodologies. The most common synthesis methods of iron-oxides nanoparticles are: co-precipitation, thermal decomposition, hydrothermal synthesis, microemulsion, sonochemical synthesis. Generally, the nanoparticles are used in the form of stable aqueous suspensions.

For biological applications, the magnetic nanoparticles are adsorbed with biocompatible organic molecules, which prevent agglomeration of the iron-oxide nanoparticles in the aqueous suspensions and enables bonding of different molecules needed in application to their surfaces. For in vivo applications, the organic molecules should be nontoxic and biocompatible. One possible type of molecules used in the stabilization of aqueous nanoparticles suspensions is amino acids. The amino acids also play an important role in the body.

In our study, aspartic acid was used for preparation of the stable aqueous suspensions of magnetic iron-oxide nanoparticles. The adsorption of the aspartic acid onto the nanoparticles and the colloidal properties of the suspensions were studied.

Selectivity in the Synthesis of Unsymmetrical Tetraoxanes

Katarina Starkl[1,2], **Jernej Iskra**[1]
[1] Department of Physical and Organic Chemistry (K-3), Jožef Stefan Institute,
Ljubljana, Slovenia
[2] Jožef Stefan International Postgraduate School, Ljubljana, Slovenia
katarina.starkl@ijs.si

Abstract. Unsymmetrical tetraoxanes are representatives of synthetic cyclic peroxides which evolved from artemisinin, a natural product used in the first-line treatment for malaria and a promising antitumor, antiparasitic and antiviral agent. Tetraoxanes might exhibit enhanced antimalarial activity due to two peroxide groups in the molecule that are essential for bioactivity of cyclic peroxides. Chemical synthesis of unsymmetrical 1,2,4,5-tetraoxanes could be straightforward with acid-catalysed cyclization of *gem*-dihydroperoxide and ketone, however problems with formation of various side-products hampers their development. We have studied the cyclization of cyclic *gem*-dihydroperoxides and various ketones in order to develop a general method for synthesis of unsymmetrical tetraoxanes was developed with an emphasis on selectivity of tetraoxanes. The method was adopted for the synthesis of various 1,2,4,5-tetraoxanes which will be evaluated for in-vitro antibacterial and antitumor activity.

Keywords: tetraoxanes, peroxides, artemisinin, antimalarial activity.

1 Introduction

Natural products containing peroxide groups exhibit broad spectrum of bioactivity but they have not been fully exploited as therapeutic agents due to their low availability [1]. Artemisinins and its semi-synthetic derivatives are one of the most important representatives and are recommended as the first-line treatment for malaria for more than a decade (Figure 1). Beside antiparasitic activity, artemisinins exhibit also antitumor, antiviral, antibacterial and anti-inflammatory activity, for which an endoperoxidic group is essential [2].

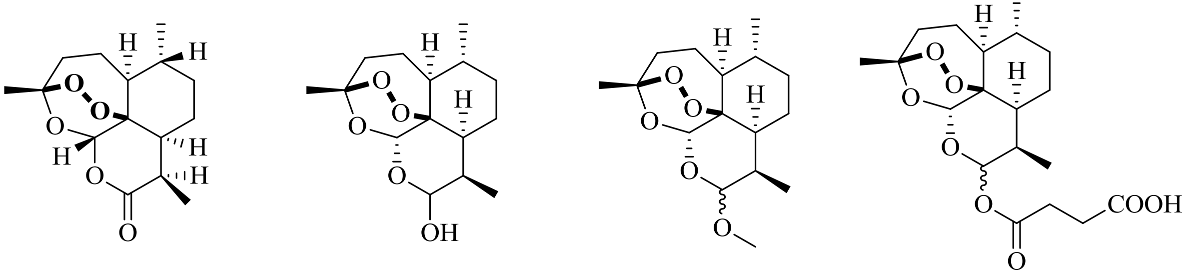

artemisinin dihydroartemisinin artemeter artesunate

Figure 1: Artemisinin and its semi-synthetic derivatives

Simplification of artemisinin structure, needed to facilitate the production and to improve pharmacokinetic properties, resulted in development of synthetic cyclic peroxides as peroxide bond is essential for their activity (Figure 2).

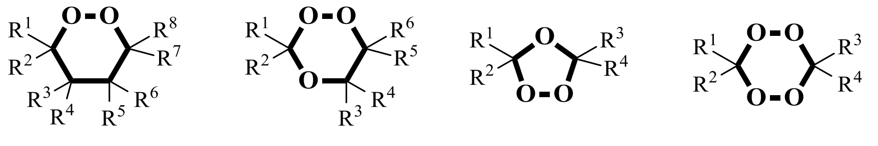

1,2-dioxane 1,2,4-trioxane 1,2,4-trioxolane 1,2,4,5-tetraoxane

Figure 2: Structural scaffolds of synthetic peroxides

An importance of synthetic peroxides for antimalarial therapy was confirmed in 2011 when the combination of synthetic peroxide arterolane (Figure 3) and quinoline-based drug piperaquine was approved for treatment of uncomplicated malaria [3]. Amongst synthetic peroxides, 1,2,4,5-tetraoxanes may exhibit an enhanced pharmacological activity due to two peroxide groups in the molecule [4]. RKA182 (Figure 3) was identified as the most potent antimalarial candidate with tetraoxane scaffold [5] and, recently, it is undergoing preclinical trials [6].

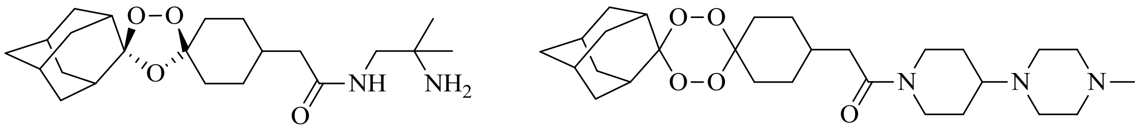

arterolane RKA182

Figure 3: Structure of the most promising synthetic peroxides

In accordance with an increasing role of artemisinins and synthetic peroxides in therapy accompanied by indications of potent bioactivity of tetraoxanes, an interest for development of new synthetic approaches for producing tetraoxanes is augmenting. Symmetrical tetraoxanes could be synthesized directly from carbonyl compounds, while unsymmetrical ones, that hold better potential due to wider structural scope, could only be prepared in two-step procedure with *gem*-dihydroperoxides as intermediate products (Scheme 1) [7].

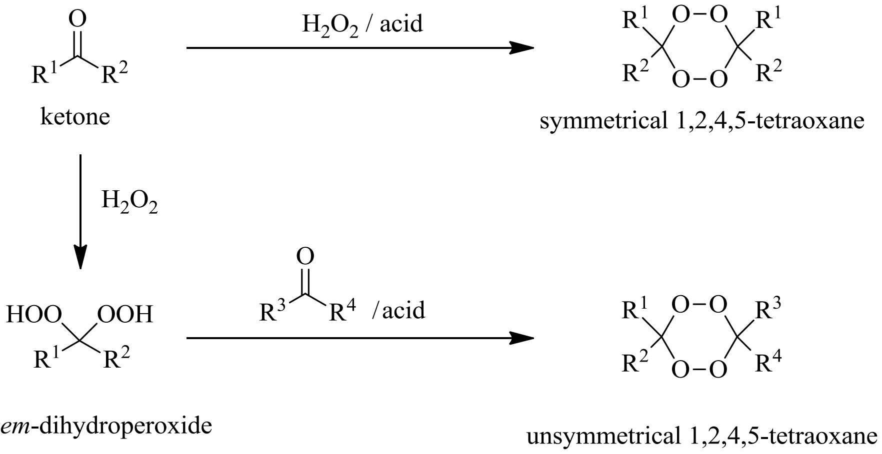

Scheme 1: Synthesis of symmetrical tetraoxanes and two-step procedure for synthesis of unsymmetrical tetraoxanes via *gem*-dihydroperoxides.

The main obstacle of acid catalysed peroxidations of ketones is selectivity due to formation of Baeyer-Villiger products and/or other cyclic products (Figure 4) [8]. Most of all, it is of great importance to avoid formation of 1,2,4,5,7,8-hexaoxonanes which have negligible bioactivity [9] and cannot be separated from desired product due to similar polarity.

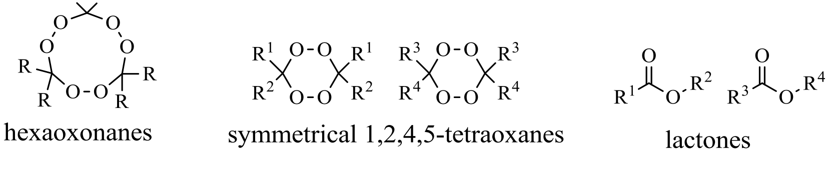

Figure 4: By-products in the acid catalysed peroxidation of ketones

2 Results and discussion

Our research focuses on synthesis of structurally diverse tetraoxanes under simple reaction conditions with emphasis on using hydrogen peroxide as a source of peroxide bond. Unsymmetrical 1,2,4,5-tetraoxanes can be synthesized by cyclization of *gem*-dihydroperoxide and ketone under acidic conditions but the reaction faces problems with formation of various side-products. Absence of formation of 1,2,4,5,7,8-hexaoxonanes and symmetrical tetraoxanes is of crutial importance as they are very difficult to separate from the desired product.

When searching for the best reaction conditions, we oriented our research towards finding of good combination of solvent, temperature and time in order to optimally activate cyclization to avoid formation of hexaoxonanes, while on the other hand, too activating conditions lead to decomposition of tetraoxanes into Beayer-Villiger products.

Optimization of reaction conditions were performed in reaction of cyclization of 4-phenylcylohexyl-1,1-diyl dihydroperoxide and 4-methylcyclohexanone as model substrates in the presence of one equivalent of HBF_4 (Scheme 2). Reaction of cyclization was studied in two solvents (1,1,1-trifluoroethanol - TFE, acetonitrile - MeCN) at different temperatures (0 °C, room temperature) and the outcome of the reaction was analysed after 5 minutes or 1 hour (Table 1). Performing reaction at room temperature for 1 hour resulted mainly in the formation of Baeyer-Villiger products in both solvents. Stopping reaction after 5 minutes at the same temperature in TFE still leads to lactones as major products. On the other hand, using less activating solvent MeCN results in good and selective formation of unsymmetrical tetraoxanes (52% yield). By lowering temperature to 0 °C, reaction system is deactivated and hexaoxonanes start to appear in the mixture of products especially when reaction is stopped after 5 minutes.

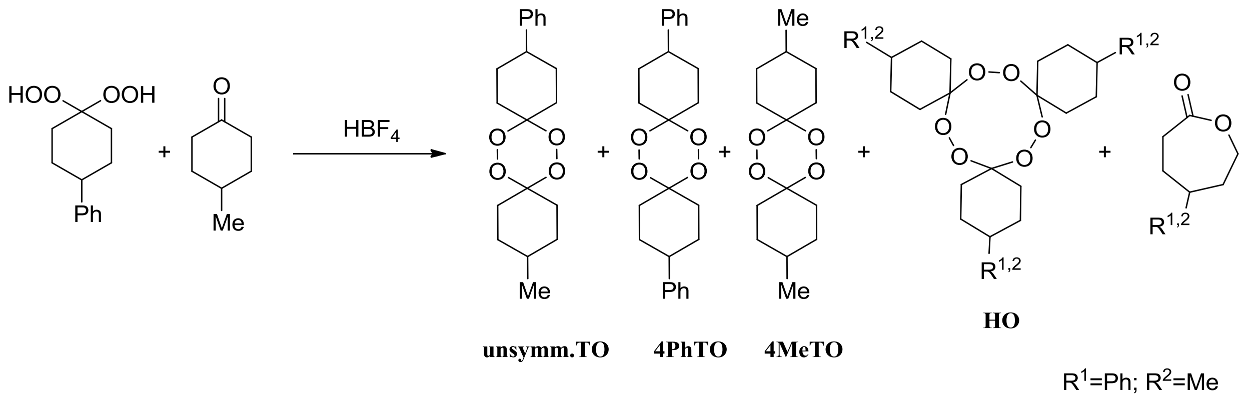

Scheme 2: Products that can be formed in the acid-catalysed cyclization of 4-phenylcylohexyl-1,1-diyl dihydroperoxide with 4-methylcyclohexanone.

Table 1: Distribution of products after the cyclization of 4-phenylcylohexyl-1,1-diyl dihydroperoxide with 4-methylcyclohexanone in different reaction conditions.

				Distribution of cyclic peroxides		
solvent	**t (min)**	**T (°C)**	**cyclic peroxides (%)[d]**	**unsymm.TO[a] (%)[e]**	**4PhTO[b] (%)[e]**	**HO[c] (%)[e]**
TFE	60	22	25	16	84	/
MeCN	60	22	19	53	47	/
TFE	5	22	28	29	71	/
MeCN	**5**	**22**	**52**	**100**	**/**	**/**
TFE	60	0	37	89	11	/
MeCN	**60**	**0**	**82**	**100**	**/**	**traces**
TFE	5	0	78	79	/	21
MeCN	5	0	71	56	/	44

[a] Unsymmetrical tetraoxane (3-methyl-12-phenyl-7,8,15.16-tetraoxadispiro[5.2.5.2]-hexadecane).

[b] Symmetrical tetraoxane (3,12-diphenyl-7,8,15.16-tetraoxadispiro[5.2.5.2]-hexadecane).

[c] Hexaoxonane.

[d] Isolated yield of the mixture of cyclic peroxides or pure compound after column chromatography.

[e] Distribution of cyclic peroxides was determined by NMR spectra of the mixture of cyclic peroxides after column chromatography.

Furthermore, we were interested in the effect of acid on the selectivity of formation of unsymmetrical tetraoxanes and experiments with different amount of acid (0,1 to 2 equivalents of HBF_4) were performed (

Table 2). As expected, less acidic conditions in MeCN promote formation of hexaoxonane. On the other hand, smaller amount of acid in reaction in TFE increases the yield of unsymmetrical tetraoxane and, interestingly, retains the selectivity. By increasing the quantity of acid in this reaction, formation of hexaoxonane is discouraged and the yield of unsymmetrical tetraoxane is reduced, while reaction had to be stopped after 5 min as longer reaction time would lead to preferential formation of lactones.

Table 2: The effect of acid on the cyclization of 4-phenylcylohexyl-1,1-diyl dihydroperoxide with 4-methylcyclohexanone.

					Distribution of cyclic peroxides		
equiv. HBF_4	**solvent**	**T (min)**	**T (°C)**	**cyclic peroxides (%)[a]**	**unsymm.TO (%)[b]**	**4PhTO (%)[b]**	**HO (%)[b]**
1	MeCN	5	RT	52	100	/	/
0,1	MeCN	5	RT	95	36	/	64
1	TFE	60	0	37	89	11	/
0,1	TFE	60	0	54	100	/	traces
1	TFE	5	0	78	79	/	21
2	TFE	5	0	41	100	/	traces

[a] Isolated yield of the mixture of cyclic peroxides or pure compound after column chromatography.

[b] Distribution of cyclic peroxides was determined by NMR spectra of the mixture of cyclic peroxides after column chromatography.

Results showed that TFE might be more appropriate solvent for general method of cyclization keeping in mind that no formation of hexaoxonane is preferential to a slightly higher yield of unsymmetrical tetraoxanes. Also less reactive starting materials would demand more activation so performing reaction in TFE at room temperature would increase yield of formation of unsymmetrical tetraoxanes. Taking all that into account, various unsymmetrical tetraoxanes were synthesized (Scheme 3). From the results we can summarize that we cannot use one set of reaction conditions for all substrates and instead for the selective conversion of substrates into unsymmetrical tetraoxanes reaction conditions should be modified based on reactivity of substrates.

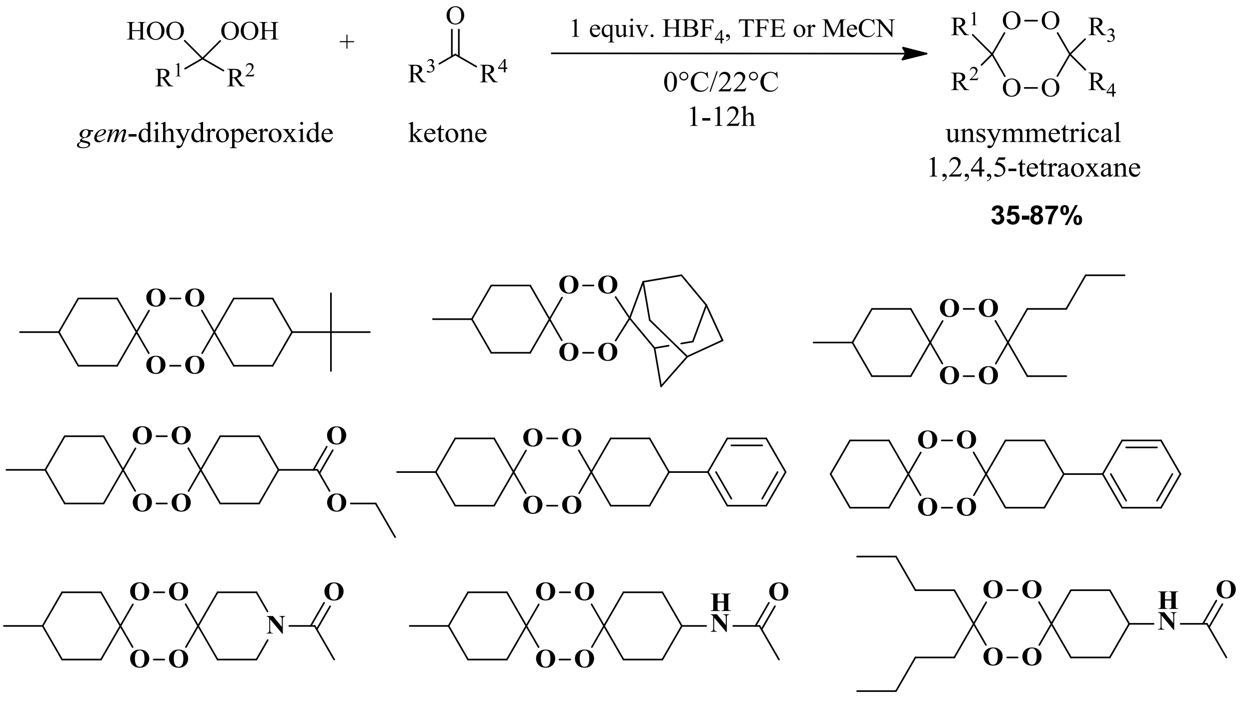

Scheme 3: Conversion of several *gem*-dihydroperoxides and ketones into unsymmetrical tetraoxanes (isolated yields are reported).

3 Conclusions

We have studied cyclization of *gem*-dihydroperoxides with carbonyl compound to deliver simple and selective method for synthesis of unsymmetrical 1,2,4,5-tetraoxanes. The effect of reaction conditions on the selectivity of reaction was studied and various unsymmetrical tetraoxanes were isolated. Due to different reactivity of *gem*-dihydroperoxides and ketones it is not possible to develop a general method for synthesis of unsymmetrical tetraoxanes, however, our study gives guidelines for predicting the optimal reaction conditions based on reactivity of substrates.

4 Acknowledgements

The authors are grateful to Slovenian Research Agency (Programme P1-0134 and Young Researcher Fellowship) for the financial support.

5 References

[1] Jung M, Kim H, Lee K, Park M. Naturally Occurring Peroxides with Biological Activities. Mini Reviews in Medicinal Chemistry 2003;3:159-65.

[2] Krishna S, Bustamante L, Haynes RK, Staines HM. Artemisinins: their growing importance in medicine. Trends in Pharmacological Sciences 2008;29:520-7.

[3] Anthony M, Burrows J, Duparc S, JMoehrle J, Wells T. The global pipeline of new medicines for the control and elimination of malaria. Malaria Journal 2012;11:316.

[4] Kumar N, Singh R, Rawat DS. Tetraoxanes: Synthetic and Medicinal Chemistry Perspective. Medicinal Research Reviews 2012;32:581-610.

[5] O'Neill PM, Amewu RK, Nixon GL, Bousejra ElGarah F, Mungthin M, Chadwick J, et al. Identification of a 1,2,4,5-Tetraoxane Antimalarial Drug-Development Candidate (RKA 182) with Superior Properties to the Semisynthetic Artemisinins. Angewandte Chemie International Edition 2010;49:5693-7.

[6] Flannery EL, Chatterjee AK, Winzeler EA. Antimalarial Drug Discovery: Approaches and Progress towards New Medicines. Nature reviews Microbiology 2013;11:849-62.

[7] Zmitek K, Zupan M, Iskra J. alpha-Substituted organic peroxides: synthetic strategies for a biologically important class of gem-dihydroperoxide and perketal derivatives. Organic & Biomolecular Chemistry 2007;5:3895-908.

[8] Zmitek K, Stavber S, Zupan M, Bonnet-Delpon D, Iskra J. Fluorinated alcohol directed formation of dispiro-1,2,4,5-tetraoxanes by hydrogen peroxide under acid conditions. Tetrahedron 2006;62:1479-84.

[9] Dong Y, Creek D, Chollet J, Matile H, Charman SA, Wittlin S, et al. Comparative Antimalarial Activities of Six Pairs of 1,2,4,5-Tetraoxanes (Peroxide Dimers) and 1,2,4,5,7,8-Hexaoxonanes (Peroxide Trimers). Antimicrobial Agents and Chemotherapy 2007;51:3033-5.

Selectivity in the Synthesis of Unsymmetrical tetraoxanes

Katarina Starkl[1,2], **Jernej Iskra**[1]
[1] Department of Physical and Organic Chemistry (K-3), Jožef Stefan Institute, Ljubljana, Slovenia
[2] Jožef Stefan International Postgraduate School, Ljubljana, Slovenia
katarina.starkl@ijs.si

Natural products containing peroxide groups exhibit broad spectrum of bioactivity. Unsymmetrical tetraoxanes are representatives of synthetic cyclic peroxides which were developed based on the structure of artemisinin, a natural cyclic peroxide used in first-line treatment for malaria and a promising antitumor, antiparasitic and antiviral agent. Tetraoxanes might exhibit enhanced antimalarial activity due to two peroxide groups in the molecule that are essential for bioactivity of cyclic peroxides. Chemical synthesis of unsymmetrical 1,2,4,5-tetraoxanes could be straightforward with acid-catalysed cyclization of *gem*-dihydroperoxide and ketone, however problems with formation of various side-products hampers their development. We have studied the reaction conditions in the cyclization of model substrates in order to develop a general method for synthesis of unsymmetrical tetraoxanes with an emphasis on selectivity. The method was adopted for the synthesis of various 1,2,4,5-tetraoxanes which will be evaluated for in-vitro antibacterial and antitumor activity.

IPSSC: Oligomerization properties of G-quadruplex structures with GC end groups

Blaž Tašič[a,b], Irena Drevenšek Olenik[b,c], Katarína Tlučková[d], Viktor Víglaský[d], Lea Spindler[e,b]

a Study programme Nanosciences and Nanotechnologies, Jozef Stefan International Postgraduate School, Jamova 39, 1000 Ljubljana, Slovenia

b Department of Complex Matter, Jozef Stefan Institute, Jamova 39, 1000 Ljubljana, Slovenia

c Faculty of Mathematics and Physics, University of Ljubljana, Jadranska 19, 1000 Ljubljana, Slovenia

d Department of Biochemistry, Institute of Chemistry, Faculty of Sciences, P. J. Safarik University, Moyzesova 11, Kosice, Slovakia

e Faculty of Mechanical Engineering, University of Maribor, Smetanova 17, 2000 Maribor, Slovenia

blaz.tasic@gmail.com

Abstract. Guanine-rich DNA sequences have the ability to grow into long nanowires made up of guanine (G:G:G:G) tetrads. These so called G-wires can be deposited on solid substrates and are due to their mechanical and thermal stability interesting candidates for molecular electronic devices. Our recent investigation showed that the sequence 5'-GCGGTG$_4$TGGCG-3' forms G-wires via formation of (G:C:G:C) tetrads [1]. To obtain more insight into the related self-assembly mechanism, we performed a comparative study of assembly properties of four analogous oligonucleotides: the above denoted one and the three similar ones with either 5', 3' or both GC-ends missing. Circular dichroism (CD) and polyacrylamide gel electrophoresis (PAGE) were used to investigate the structure, thermal stability, ageing, and the effect of adding different cations to the formation of G-quadruplex structures and to their oligomerization properties.

Keywords: G-quadruplex, Circular Dichroism, Polyacrylamide Gel Electrophoresis, Nanowire, G-wires

1 Introduction

When deposited on solid substrates, guanosine monophospate and guanine-rich DNA sequences have the ability to grow into long nanowires made up of guanine (G:G:G:G) tetrads [2-4]. These so called G-wires are due to their mechanical and thermal stability very suitable candidates for applications in optoelectronic, electronic, electromechanical and electrochemical devices.

To avoid discontinuities in the G-wire formation, it is essential that the DNA quadruplex stem remains uninterrupted. One possibility to achieve this aim is to use G-rich DNA sequences with CG "sticky-end" overhangs. Previous studies [5,6] showed that sequences with the structure d(GCGGXGGAT) (where X was either T, TT, A, or TC) first assembled into a dimer by two sequences forming a bimolecular quadruplex linked by the (G:G:G:G) tetrads. In the next step, two such dimers growed into a multimer by their CG overhangs arranging into the (G:C:G:C) tetrads, which established a link in the middle of the two dimers.

For our study we selected the sequence **GC**G$_2$TG$_4$TG$_2$**CG** with CG overhangs at both ends. This sequence forms long nanowires when deposited onto a mica substrate [7]. The growth of these G-wires is expected to be stimulated by the formation of (G:C:G:C) linking tetrads at both, 5' and 3', ends. The proposed basic structure for the selected sequence is a bimolecular quadruplex as depicted in Scheme I. To more clearly elucidate the role of CG ends, three control sequences were selected: 5'-GCG$_2$TG$_4$TG$_2$ (Scheme II), G$_2$TG$_4$TG$_2$CG-3' and G$_2$TG$_4$TG$_2$.

Preliminary measurements by UV-Vis absorption spectrometry confirmed the formation of G-quadruplexes from all four sequences in 100 mM NaCl and 10 mM NaPi solutions. Dynamic light scattering (DLS) further revealed that G-wires are indeed formed at suitable conditions [1].

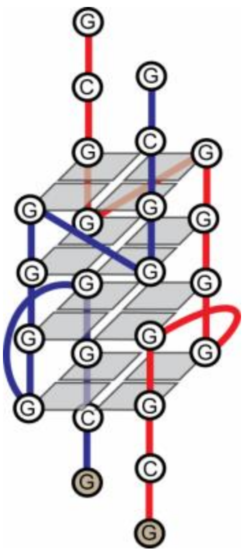

I GCG$_2$TG$_4$TG$_2$CG

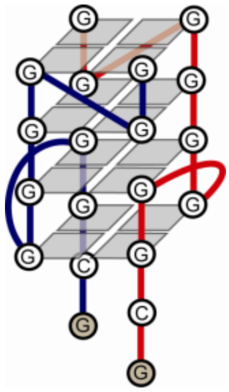

II 5'-GCG$_2$TG$_4$TG$_2$

To resolve additional details of the above described oligomerization process, we used polyacrylamide gel electrophoresis to investigate G-wire growth under various solution conditions (different oligonucleotide concentration, added salt, etc.). Besides this, we used circular dichroism to determine thermal stability of the investigated structures.

2 Methods and Materials

The oligonucleotides used in our experiments were: d(**GC**GGTG$_4$TGG**CG**), d(**GC**GGTG$_4$TGG), d(GGTG$_4$TGG**CG**) and d(GGTG$_4$TGG). All oligonucleotides were purchased from Eurogentec, Belgium, as 4 mM water solutions. They were at first purified on a Sephadex-15 coloumn and were subsequently diluted in 100 mM NaCl solution buffered with 10 mM sodium phosphate buffer (pH = 6.8).

Native polyacrylamide gel electrophoresis (PAGE) was run in a temperature-controlled vertical electrophoretic apparatus (Z375039-1EA; Sigma–Aldrich, San Francisco, CA) at 10 °C with 16 % of acrylamid in gel. Electrophoreses were run at 80 V for 3 - 5 hours. For staining Stains-All dye (Sigma-Aldrich) was used.

Circular dichroism melting curves were obtaind with spectrometer Jasco J-810. The heating rate was 1 °C per minute. Melting curves were recorded at 263 nm.

3 Results and Discussion

As can be resolved in *Figure 1*, all sequences except **GC**GGTG$_4$TGG folded differently before and after they were purified on a Sephadex 15 coloumn. From purified samples the sequence **GC**G$_2$TG$_4$TG$_2$**CG** (lane 1) forms two structures, which can be most probably attributed to a single quadruplex and to two quadruplexes linked by the (G:C:G:C) tetrads. The sequence **GC**G$_2$TG$_4$TG$_2$ (lane 3) is characterised by a large smeared band that could result from two different structures in rapid exchange and one hardly seen band higher above that represents 4 stacked quadruplexes. We observed only one strong band for G$_2$TG$_4$TG$_2$**CG** (lane 5), which we attribute to two stacked quadruplexes. The sequence G$_2$TG$_4$TG$_2$ (lane 7) shows a ladder effect which is typical for a long structure. We therefore conclude that this sequence definitely forms long G-wires.

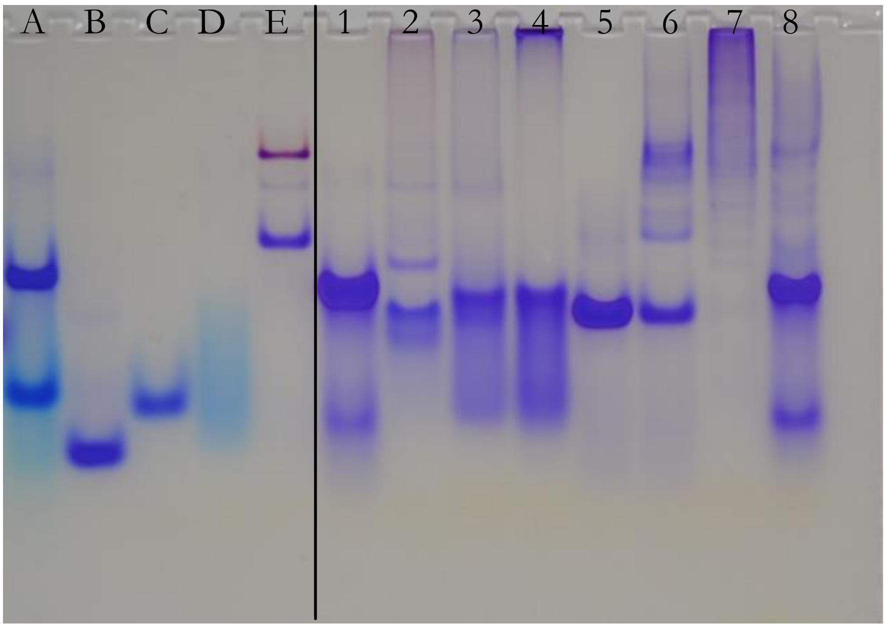

Figure 1: References *A) AC18 + AC36, B) [$G_3T_2A]_3G_3$, C)TBA, D) [$G_3T_2]_3G_3$, E) HIV*

***GC**$G_2TG_4TG_2$**CG**:* *1) purified, 2) not purified*

***GC**$G_2TG_4TG_2$:* *3) purified, 4) not purified*

*$G_2TG_4TG_2$**CG**:* *5) purified, 6) not purified*

$G_2TG_4TG_2$: *7) purified, 8) not purified*

3.1 Melting temperatures

With circular dichroism we obtained melting temperatures of different structures. In accordance with the PAGE results (*Figure 1*), which show that the sequences **GC**$G_2TG_4TG_2$**CG** and $G_2TG_4TG_2$**CG** form only a single structure, the associated CD spectra exhibit only one melting temperature (*Figure 2, Figure 4*).

In contrast, the sequence **GC**$G_2TG_4TG_2$ (*Figure 3*) exhibits two melting temperatures during heating and only one melting temperature during cooling (performed immediately after heating). This is because larger aggregates cannot form in such a short time.

The sequence $G_2TG_4TG_2$ (*Figure 5*) shows two melting processes at relatively high temperatures (T_{m1} = 66°C, T_{m2} = 82°C). This sequence is the longest and it most probably forms G-wires. When T_m is measured at cooling, only one melting temperature (T_m = 34°C) is obtained also in this case. This is the T_m of single quadruplexes. If we wait for a longer time (3 days), we observe a mixture of less and more stable structures (three melting temperatures).

The thermal stability of basic quadruplex structures (T_{m1}) decreases in the order **GC**GGTG$_4$TGG**CG** > **GC**GGTG$_4$TGG > GGTG$_4$TGG**CG** > G$_2$TG$_4$TG$_2$. These results indicate that GC-ends significantly stabilise the basic quadruplex stem.

Figure 2: GCGGTG$_4$TGG**CG**

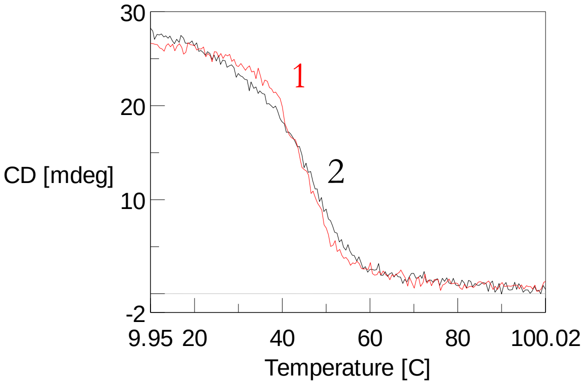

Figure 3: GCGGTG$_4$TGG

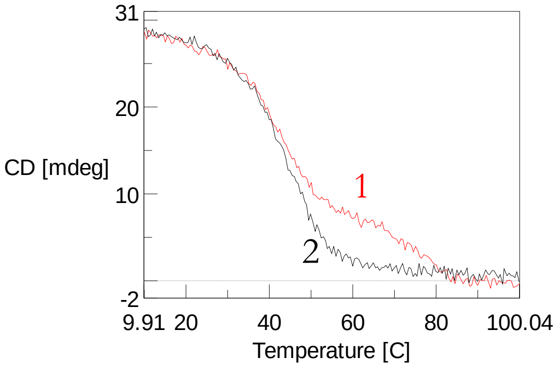

Figure 4: GGTG$_4$TGG**CG**

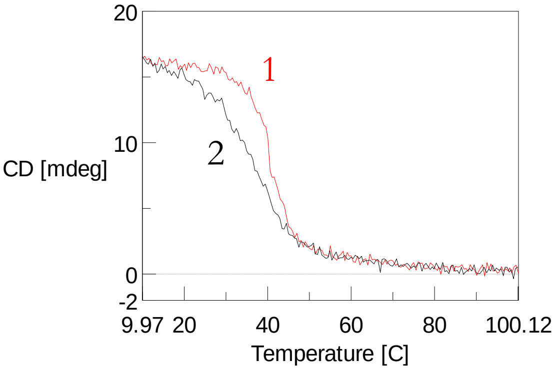

Figure 5: G$_2$TG$_4$TG$_2$

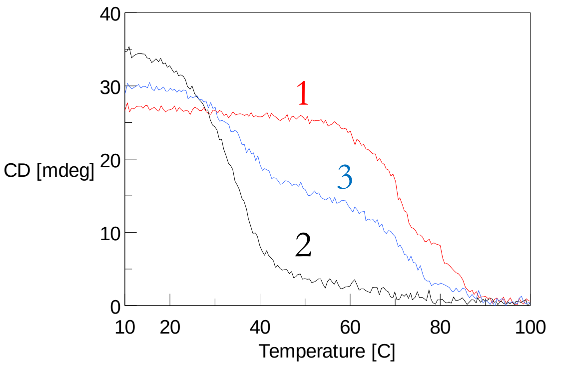

*1: Heating (**red**), 2: Cooling (**black**), 3: Second heating after 3 days (**blue**)*

3.2 Ageing

In *Figure 6* the growth of sequence G$_2$TG$_4$TG$_2$ by the sample aging is presented. The sample was heated at high concentration (c = 1 mM) and the buffer was added just before the measurement. When analogous measurement was repeated at a lower concentration of the oligonucleotide (c = 0.06 mM), different results were obtained (*Figure 7*), i.e. the growth of G-wires was much slower.

The sequence GGTG$_4$TGG**CG** forms long structures only at high concentration, but these structures are not stable for a long time.

The other two sequences (**GC**GGTG$_4$TGG**CG** and **GC**GGTG$_4$TGG) after three days formed the same structures regardless of their concentration.

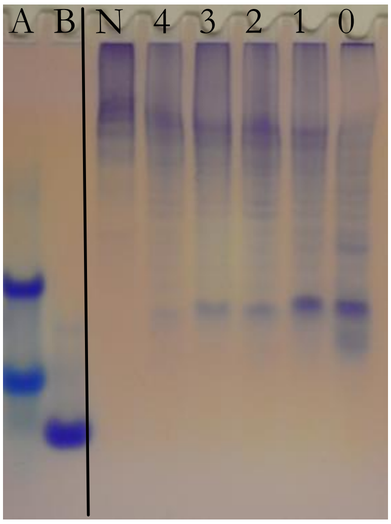

Figure 6: Ageing of $G_2TG_4TG_2$.

A) AC18+AC36, B) $[G_3T_2A]_3G_3$, *N) Not heated, 4) 4 days old sample, 3) 3 days old sample, 2) 2 days old sample, 1) 1 day old sample, 0) 0 days old sample.*

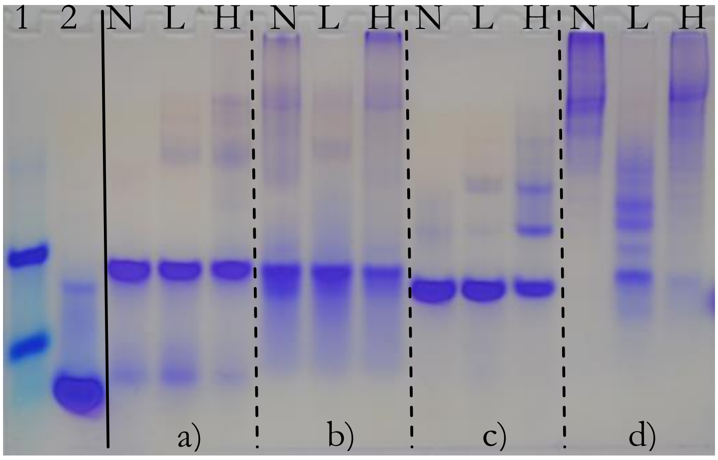

Figure 7: Ageing in High/Low concentration of oligonucleotides.

1) AC18+AC36, 2) $[G_3T_2A]_3G_3$, *a)* **GC**$G_2TG_4TG_2$**CG**, b) **GC**$G_2TG_4TG_2$, c) $G_2TG_4TG_2$**CG**, d) $G_2TG_4TG_2$; *N – not heated, L – heated at low concentration, H – heated at high concentration.*
All samples are 3 days old.

3.3 Effect of adding cations

We added different cations at high concentration (*c* = 1 M) to our samples (Fig. 8, 9, 10, 11). For a specific sequence, all CD curves had the same shape regardless of the added ion species. From this it can be concluded that the same quadruplex structure forms independent of the type of cations. The cations thermally stabilized the investigated G-quadruplexes in the following order **K^+ > Na^+ > Li^+**, which agrees with the well-established quadruplex-stabilising cation series.

Figure 8: GCG$_2$TG$_4$TG$_2$**CG**

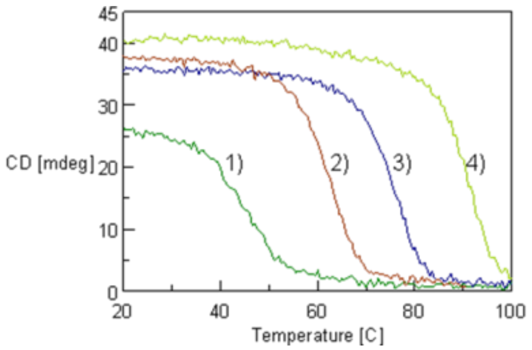

Figure 9: GCG$_2$TG$_4$TG$_2$

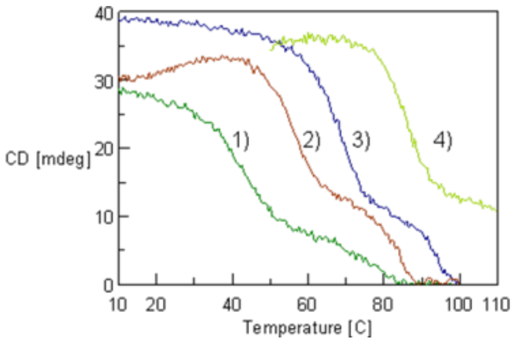

Figure 10: G$_2$TG$_4$TG$_2$**CG**

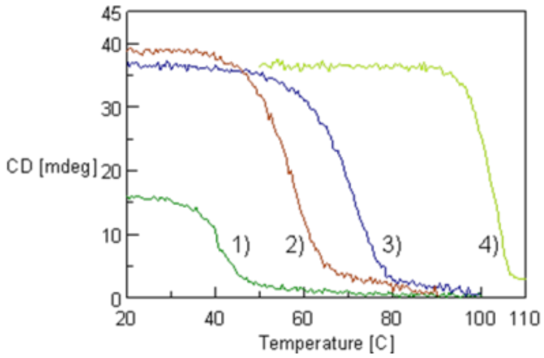

Figure 11: G$_2$TG$_4$TG$_2$

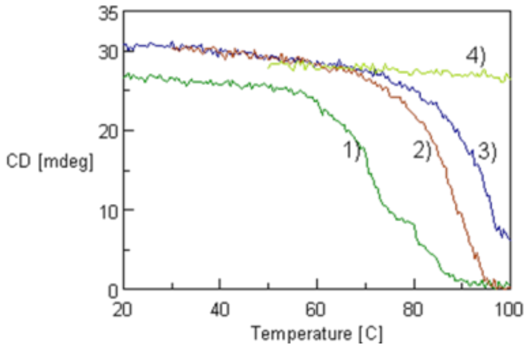

1) 100 mM NaCl, 2) 1 M LiCl + 100 mM NaCl, 3) 1 M NaCl, 4) 1 M KCl + 100 mM NaCl

4 Conclusion

The results of our CD measurements show that the oligonucleotides with GC-ends are more thermally stable than those without GC-ends. They also reveal that adding monovalent cations notably increases the thermal stability of the quadruplex structures. Both, the CD melting curves and the PAGE analysis, confirmed formation of multimer structures for the sequences GCG$_2$TG$_4$TG$_2$ and G$_2$TG$_4$TG$_2$. Surprisingly, no G-wires in solution were observed for the sequence GCG$_2$TG$_4$TG$_2$CG, although this sequence forms extended G-wire networks on mica substrates. This finding indicates that in addition to the quadruplex stacking and GC linking processes that are present already in the solution, G-wire formation may be facilitated also by the surface interactions taking place during solution deposition.

References:

[1] T. Ilc, P. Šket, J. Plavec, M. Webba da Silva, I. Drevenšek-Olenik, L. Spindler, J. Phys. Chem. C **117**, 23208–23215 (2013).

[2] K. Kunstelj, F. Federiconi, L. Spindler, I. Drevensek-Olenik, Colloids and Surfaces B: Biointerfaces **59**, 120-127 (2007).

[3] J. Vesenka, D. Bagg, A. Wolff, A. Reichert, R. Moeller, W. Fritzsche, Colloids And Surfaces B-Biointerfaces **58**, 256-263 (2007).

[4] N. Borovok, N. Iram, D. Zikich, J. Ghabboun, GI Livshits, D. Porath, A. Kotlyar, Nucleic Acids Research **36**, 5050-5060 (2008).

[5] M. Webba da Silva, Biochemistry **42**, 14356-14365 (2003).

[6] J-L. Mergny, A. De Cian, S. Amrane, M. Webba da Silva, Nucleic Acids Res. **34**, 2386-2397 (2006).

[7] T. Troha, "Površinsko urejanje z gvaninom bogatih sekvenc DNK", diploma work, 2013.

For wider interest

DNA sequences that contain a lot of guanosine (G) have the ability to form special four-stranded macromolecular structures known as G-quadruplexes. When deposited on solid substrates and also in aqueous solutions, G-quadruplexes can associate into long G-wires, which have promising properties for applications in molecular electronics devices. Consequently there exists a broad interest to obtain understanding and control of the G-wire formation process. We performed a systematic investigation of the G-wire formation in solutions of four very similar G-rich DNA oligonucleotides and discovered that a presence/absence of the GC end groups strongly affects the wire growth. We also investigated the effect of various cations on the stability of the formed assemblies and found that potassium acts as the most efficient stabilization agent.

The optimization of cleaning pre-treatment of aluminium alloy AA 7075

Urša Tiringer[1,2]

[1] Department of Physical and Organic Chemistry, Jožef Stefan Institute, Ljubljana, Slovenia [2] Jožef Stefan International Postgraduate School, Ljubljana, Slovenia

ursa.tiringer@ijs.si

Ingrid Milošev[1]

[1] Department of Physical and Organic Chemistry, Jožef Stefan Institute, Ljubljana, Slovenia ingrid.milosev@ijs.si

Abstract. Aluminum and its alloys belong to light metals and are most commonly used in transportation industry. Present work aims to study the effect of cleaning of aluminium alloy of series AA 7075 with two different alkaline cleaners, first based on 0.01 M NaOH and exposed to 50% HNO_3 and second supplied by SurTec which is based on phosphates. According to the results obtained by electrochemical method, the cleaner based on NaOH and HNO_3 causes the passivation of AA 7075, while the potentiodynamic curve of surface cleaned with SurTec is similar to pure aluminium. XPS results show that both discussed cleaners remove contamination quite effectively. High resolution spectrum of Al 2p shows that in all samples aluminium is mostly present in its oxide state. Moreover, after both cleaning, with NaOH/HNO_3 and SurTec, the surface of AA 7075 becames almost superhydrophilic, while the untreated sample is hydrophilic.

Keywords: aluminium, aluminium alloy, surface cleaning, alkaline cleaners

1 Introduction

Reduction of CO2 emission is an important goal set by the directives of the European Union. One of the possible ways to achieve this goal is to use light alloys in transportation industry. Aluminum and its alloys belong to the group of light metals and are most commonly used in transport industry such are aircraft industry, automotive industry, train industry and marine industry.

Despite the fact that aluminum resists corrosion well, its alloys may not be corrosion resistant in various environments. Chromate conversion coatings have been effective as aluminium protection against corrosion for many years. Nowadays their use is becaming increasingly limited because of their toxicity. Many studies have been focused on the development of technologies alternative to chromates. Before any kind of surface treatment, it is necessary to perform a proper cleaning of the surface which will be treated. Cleaning of aluminum is necessary for hygiene (in food industry), for maintenance (for buildings and transport equipment) and for quality control. The goal of cleaning is to remove inorganic and organic residues that are present on the surface of aluminum and its alloys. There are three issues that should be controlled during cleaning and are labeled and described below:

- The chemical issue; cleaning agent should not attack the substrate
- The physical issue; dirt is removed from the surface by modifying its surface tension
- The mechanical issue; dirt which is insoluble in cleaning agent can be removed from the surface by brushing or by high-pressure water jets.

Most cleaning agents consist of acidic or alkaline media which have different functions. They can have a role of pickling agents, detergents, degreasing agents or of corrosion inhibitors. Suitable cleaning agent has to be compatible with aluminum or its alloys, nontoxic for human health and nonpolluting for environment. As aluminum and its alloys are amphoteric, they can be attacked by acids and by bases. In highly alkaline medium the oxide film is formed which is difficult to modify, but, on the other hand, use of alkaline cleaner increases the corrosion resistance of these materials. Products based on acids form stable and insoluble salt with aluminum and alloys, but do not increase their corrosion resistance.

Our goal is to optimize the cleaning process of aluminum alloy AA 7075 by finding a proper cleaning agent. The original composition (in atomic percent) of aluminum alloy AA 7075 is the following: Zn (5.6-6.1), Mg (2.1-2.5), Cu (1.2-1.6) and less than half percent of Si, Fe, Mn, Ti, Cr and other metals. In our research we compared two different alkaline cleaners, the first was based on 0.01 M NaOH including desmutting process and the second was manufactured by SurTec and based on phosphates.

2 Material and methods

2.1 Preparation of the samples

Samples of aluminium alloy AA 7075 were ground using 2400 and 4000-grid SiC emery papers, ultrasonically cleaned in ethanol for 5 minutes, rinsed with deionized water and dried with a stream of N_2. Samples of AA 7075 were divided into three groups:

- Followed by the first was immersed in the 0.01 M NaOH for 3 minutes and than in 50% HNO_3 for 30 seconds.
- The second was cleaned using SurTec product, which was formed by combination of 3% SurTec132 liquid recyclable builder and of 0.5% SurTec089 recyclable detergent component. The sample was immersed in the mixture for three minutes at 40°C.
- The third was untreated sample.

The comparison of cleaners was carried out by electrochemical polarization method, X-ray photoelectron spectroscopy, profilometer, tenziometer and scanning electron microscopy.

2.2 Electrochemical measurements

Electrochemical measurement were performed in 0.1 M NaCl at room temperature. An Autolab corrosion cell with a volume 0.350 L was used. The working electrode was embedded in a Teflon holder with exposed area 0.87 cm^2. Graphite electrode served as a counter electrode and saturated calomel electrode (SCE) was a reference electrode (E = 0.214 V vs. standard hydrogen electrode, SHE). After 1 h stabilization at open circuit potential (OCP) measurements were performed in the following order: linear polarization, ±10 mV versus OCP, using a scan rate of 0.1 mV/s and potentiodynamic measurements starting from -250 mV vs. OCP up to -0.5 V using a scan rate of 1 mV/s. Experiments were repeated in triplicate and representative measurement is presented in graphical form.

2.3 X ray photoelectron spectroscopy (XPS)

The X-ray photoelectron spectroscopy analysis was carried out on the PHI-TFA XPS spectrometer (Physical Electronics Inc.). The vacuum during the XPS analyses was in the range of 10^{-9} mbar. The analyzed area was 0.4 mm in diameter and the analyzed depth was about 3 - 5 nm. Sample surfaces were excited by X-ray radiation from monochromatic Al source at photon energy of 1486.6 eV. Spectra were analyzed by a Multipak software, version 8.0 (Physical Electronics Inc company).

Prior and after the immersion test the morphology, topography and contact angle of the surface were examined.

2.4 Measurement of surface morphology, topography and contact angle

Scanning electron microscopy (SEM) images were taken with JEOL JSM-7600F microscope equipped with chemical analysis (EDXS).

A profilometer, model Bruker DektakXT, was employed for analysis of surface topography. The instrument has a lateral resolution of 1 μm and vertical resolution 5 nm. It measures the surface profile in one direction. Measurements were performed at 1 mm^2 spot size on the sample. The data were processed with TalyMap Gold 6.2 software. 3-D surface topography and calculation of the mean surface roughness (S_a) were obtained.

The contact angles (Θ) were measured using the tensiometer Krüss DSA 20 (Krüss GmbH, Hamburg, Germany). A Drop-shape-analysis software enables the fitting of the image of the deionized water drop on the sample surface and allows a precise determination of the contact angle value. Each contact angle value is the mean of at least three measurements made on different positions of the same sample.

3 Results and discussion

Potentiodynamic curves for untreated and samples cleaned with NaOH/HNO3 and with Surtec phosphate cleaner are presented in Figure 1.

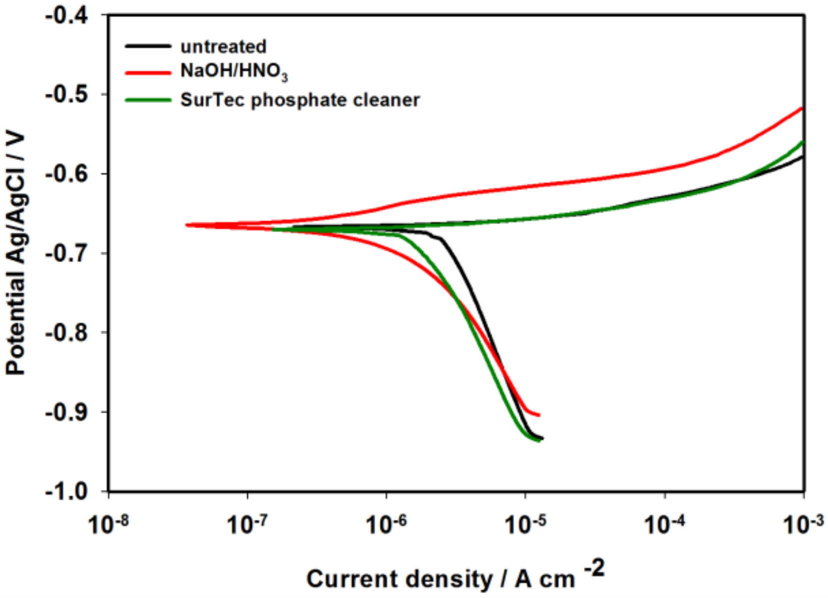

Figure 1: Polarization curves of AA 7075 samples cleaned with $NaOH/HNO_3$, SurTec phosphate cleaner and of untreated AA 7075 sample. Curves were recorded in 0.1 M NaCl.

According to the results obtained by electrochemical method, the cleaner based on NaOH and HNO_3 causes the passivation of AA 7075, while the potentiodynamic curve of surface cleaned with SurTec is similar to the curve of pure aluminium.

The concentration of elements obtained by X-ray photoelectron spectroscopy after various surface treatments are presented in Figure 2.

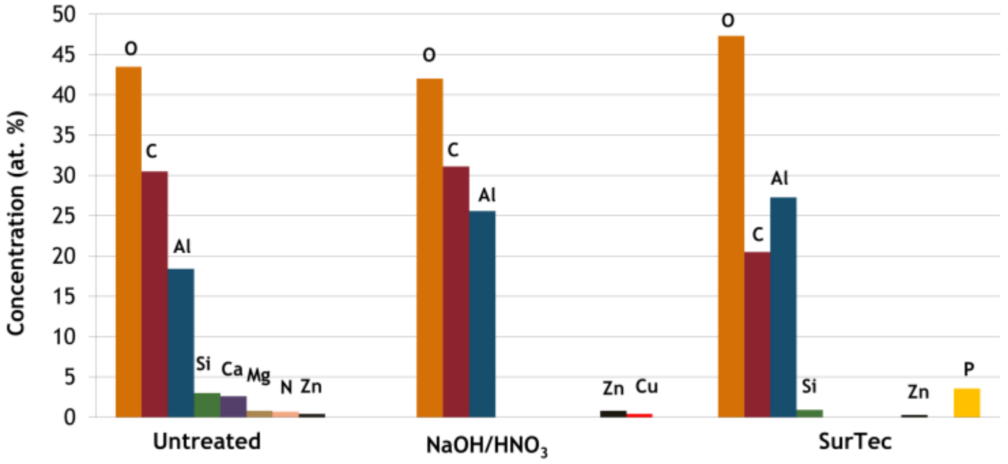

Figure 2: The concentration of elements obtained by XPS after various surface treatments: untreated, exposed to 0.01 M NaOH and HNO_3 and exposed to SurTec cleaner.

Results obtained by XPS technique show that carbon and nitrogen contaminations are reduced by cleaning. At the same time oxygen and aluminium content increased and alloying elements Mg and Si are removed. After using NaOH and HNO_3 the content of copper increased while after using SurTec cleaner the content of phosphorus increased.

Aluminium, which is the major element in alloy AA 7075, was interpreted in details, with high resolution spectra-qualitative analysis and fitting-quantitative analysis. Figure 3 presents XPS high resolution spectra of Al 2p.

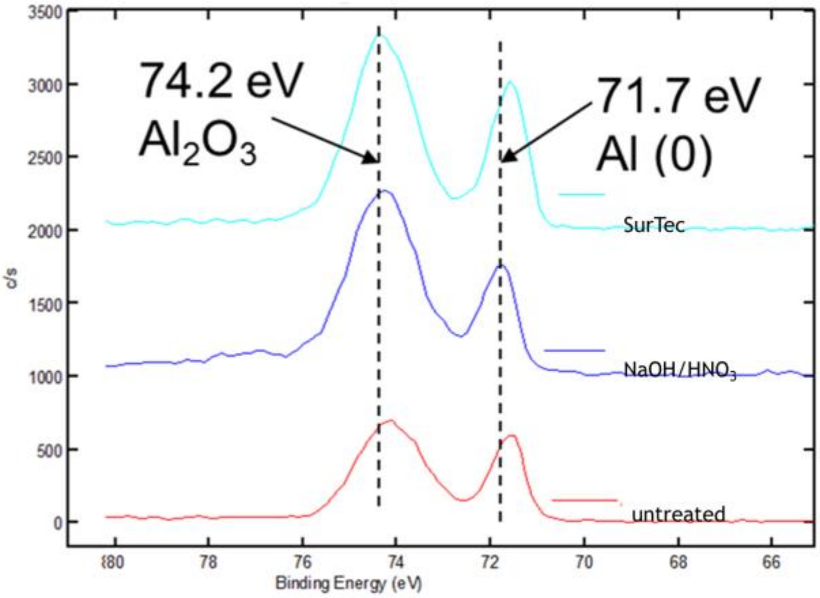

Figure 3: High resolution spectra of Al 2p obtained by XPS technique show the formation of aluminium oxide on differently cleaned samples.

As it is seen from Figure 3, two peaks of aluminum were detected on all three samples. One of them corresponds to energy of 74.2 eV, which belongs to oxide state of aluminum, and other of energy 71.7 eV, which belongs to elemental (metallic) state of aluminum.

Top view of profiles obtained by profilometer and values of surface roughness (S_a) of untreated sample, sample cleaned with NaOH and HNO_3 and with SurTec cleaner are presented in Figure 4. The colouring is according to the scale on the right which spans in the +- 1.5 μm. Image spot size is 1 mm x 1mm range.

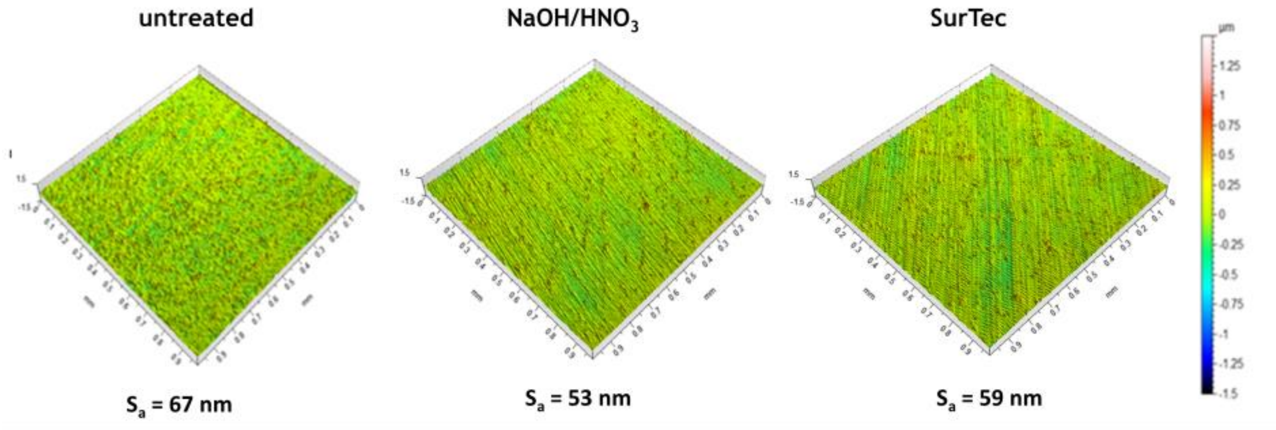

Figure 4: Top view of profiles obtained by profilometer and values of surface roughness (S_a) of untreated sample, sample cleaned with NaOH and HNO_3 and with SurTec cleaner.

As it is seen from Figure 4 images and surface rougness obtained by profilometer do not indicate the difference in surface topography of of untreated sample, sample cleaned with NaOH and HNO_3 and with SurTec cleaner.

SEM images of the surface cleaned with SurTec cleaner is presented in Figure 5.

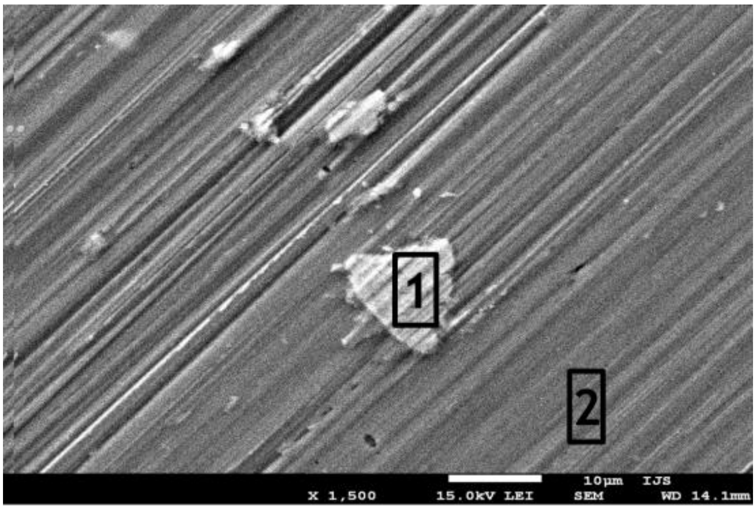

Figure 5: SEM analysis of sample AA 7075 cleaned with SurTec.

EDX analysis which is carried out at different locations at the treated sample AA 7075 as denoted in Figure 5 are presented in Table 1.

Table 1: EDX analysis carried out at different locations at the treated sample as denoted in Fig. 5.

[at.%]	**Al**	**Zn**	**Mg**	**O**	**Fe**	**Cu**
Spectrum						
1	82.4	3.3	2.3	5.3	1.9	4.8
2	94.6	2.5	8.9	/	/	/
δ	8.6	0.57	4.67	/	/	/

Images of water drops on the surface and values of contact angles (CA) of untreated sample, cleaned with NaOH and HNO_3 and with SurTec cleaner, are presented in Figure 6.

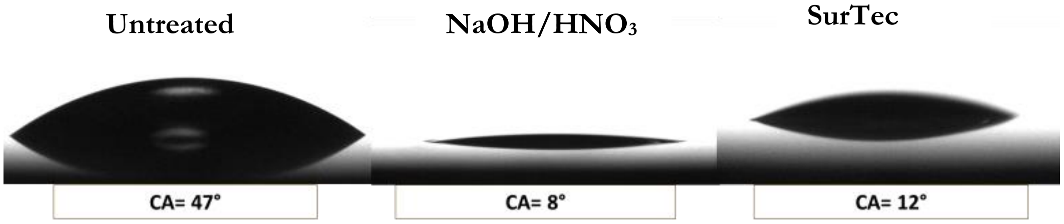

Figure 6: Images of water drops on the surface after different treatment and the values of contact angles.

After cleaning with NaOH/HNO_3 and with SurTec cleaner, the surface of aluminum alloy AA 7075 becomes almost superhydrophilic because the contact angle in this case is less than 10°. The surface of untreated sample is hydrophilic. The contact angle in this case is 47°.

4 Conclusions

According to the results obtained by electrochemical method the cleaner based on NaOH and HNO_3 causes the passivation of AA 7075, while the potentiodynamic curve of surface cleaned with SurTec is similar to the curve of pure aluminum.

Results obtained by XPS technique show that carbon contamination is reduced by cleaning. At the same time oxygen and aluminum content increased and alloying elements Mg and Si are removed. After using NaOH and HNO_3 the content of copper increased. After using SurTec cleaner the content of phosphorus increased. High resolution spectrum of Al 2p shows that in all samples aluminum is mostly present in its oxide state. Energy of 74.2 eV denotes to the oxide state of aluminum and of energy 71.7 eV, elemental aluminum.

Images and surface roughness obtained by profilometer do not indicate the difference in surfaces topography of differently treated samples.

SEM image shows that the surface of AA 7075 cleaned with SurTec in addition to aluminum consists of alloying elements zinc, magnesium, iron and copper, while inclusion (1) is probably zinc oxide.

After cleaning with NaOH/HNO_3 and with SurTec cleaner the surface of aluminum alloy AA 7075 becomes almost superhydrophilic ($CA \leq 10°$), while the untreated is hydrophilic (CA = 47 °).References:

References:

[1]

[2] I. H. Witten and E. Frank. *Data Mining: Practical machine learning tools and techniques, 2nd Edition*. Morgan Kaufmann, 2005.

[3] D. Petelin, J. Kocijan. Evolving Gaussian process models. In *Proceedings of the IEEE Symposium Series on Computational Intelligence 2011*, Paris, France, 2011.

[4] IPSSC submission form. 5th Jožef Stefan International Postgraduate School Student's Conference. http:// ipssc.mps.si/submission.asp, 2013

[5] J. R. Quinlan. Improved use of continuous attributes in C4.5. *Journal of Artificial Intelligence Research*, 4(1):77-90, 1996

[6] I. H. Witten and E. Frank. *Data Mining: Practical machine learning tools and techniques, 2nd Edition*. Morgan Kaufmann, 2005.

[7] D. Petelin, J. Kocijan. Evolving Gaussian process models. In *Proceedings of the IEEE Symposium Series on Computational Intelligence 2011*, Paris, France, 2011.

[8] IPSSC submission form. 5th Jožef Stefan International Postgraduate School Student's Conference. http:// ipssc.mps.si/submission.asp, 2013

Cobalt-Platinum alloy nanostructures as potential candidates for Racetrack Magnetic Data Storage Devices

Muhammad Shahid Arshad[1,2], **Darja Pecko**[1,2], **Janez Zavasnik**[3], **Saso Sturm**[1], **Spomenka Kobe**[1,4], **Kristina Žužek Rožman**[1]

1 Department for Nanostructured materials K7, Jozef Stefan Institute, Ljubljana, Slovenia

2 Jožef Stefan International Postgraduate School, Ljubljana, Slovenia

3 Centre for Electron Microscopy and Microanalysis (CEMM), Ljubljana, Slovenia

4 Center of Excellence on Nanoscience and Nanotechnology (CENN Nanocenter), Ljubljana, Slovenia

shahid.arshad@ijs.si

Abstract. Magnetic hard disk drives have been the prime repository of digital data for more than half a century. Over this period of time, the area of one magnetic bit, use to store information has decreased in size by about around nine order to magnitudes; it is now so tiny that it is reaching fundamental limit that are difficult or too expensive to overcome. A number of alternatives to the magnetic disk drive have been suggested. Among them racetrack memory devices seems to be potential candidates and close to the realization. Such devices are based on magnetic nanowires with magnetic domains which can be move with electrical current. In this article we will present the possibilities to produce nanowires which can be use in racetrack memory devices and we will also present the methods to manipulate magnetic domains in nanowires.

Keywords: Magnetic nanowires, Racetrack memory devices, Magnetic Domains

1 Introduction

Co-based alloys are integral part of modern magnetic recording media such as hard disk drive (HDD) due to their excellent magnetic properties. Alloying Co with metals like Pt enhances its intrinsic magnetic properties such as magnetocrystalline anisotropy. In addition it shows excellent chemical stability, higher coercivity and resistance against corrosion which makes such alloys suitable candidates for magnetic data storage devices. Due to size-confinement-trend in magnetic storage devices, it is reasonable to expect that Co-Pt alloy nanostructures such as nanowires (NWs) and nanotubes (NTs) would replace their counterparts in future. One of such ideas are racetrack memory devices, where information is stored in the form of magnetic domains with opposite magnetization along the length of the nanowires. One of the fascinating point of such devices is domains in nanowires can move forward or backward direction depending on current direction. Many researcher believes that such devices have potential to keep the Moore's law going and big IT companies like IBM are funding for research on racetrack memory devices. [1] Main features of such devices are enlisted below

1. Non-volatile (information remains stored even if there is no power, such as HDD and flash)
2. Higher Density (upto 10x information in comparison to HDD can be stored)
3. Super Speed (reading and writing of information would be equivalent or higher than SRAM)
4. Universal Memory devices (such devices can replace all type of memory devices such as SRAM, DRAM and flash memory)

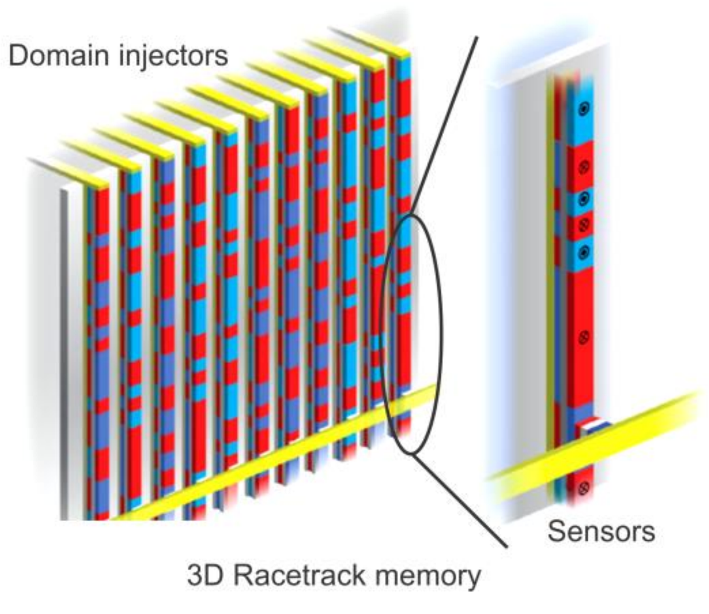

Figure 1: Schematic of Racetrack memory devices showing working principle of device. After [2]

For such devices to function properly it is necessary to have 1) magnetic domains with opposite magnetization as shown by red and blue boxes in Fig.1 and 2) it is also important to have pinning sites for the domains to manipulate them efficiently. In the present work, the Co-Pt nanostructures have been synthesized into polycarbonate (PC) as well as anodic alumina oxide (AAO) membranes with diameter range from 200-50 nm. We have studied the magnetic domains in such Co-Pt nanowires and investigated the manipulation of domains. We have utilized micromagnetic simulations (NMAG) to understand magnetization reversal in such nanowires. Due to the page limitation and to make the text more fluent we will focus on results which are mainly concerned here. For further details we suggest readers to read our published articles.

2 Results and Discussions

We will present three main concepts to produce and manipulate magnetic domains in Co-Pt nanowires in the following

I. Periodic Magnetic Domains in Co-Pt Nanowires

As-deposited Co-Pt alloys can exhibit either a disordered phase (fcc-based L11-CoPt) and/or a hcp-based D019-Co3Pt crystal structure depending on the composition between Co and Pt. X-ray diffraction (XRD) and transmission electron microscope (TEM) was employed to study the microstructure and crystal structure of Co-Pt nanowires (NWs) with 200 nm diameter. Results are given elsewhere. [3] Detailed analysis on NWs have shown the presence of a textured fcc and hcp phases with the [111] of fcc and [001] of hcp crystal planes almost perpendicular to NWs long axis. Such analysis have explained periodic domains structure observed with magnetic force microscope (MFM) along the length of the NWs as shown in Fig.2. Such domain structure is ideal for racetrack memory devices. In future we are planning to perform current induced domain wall motion experiments to move these domain along the length of NWs.

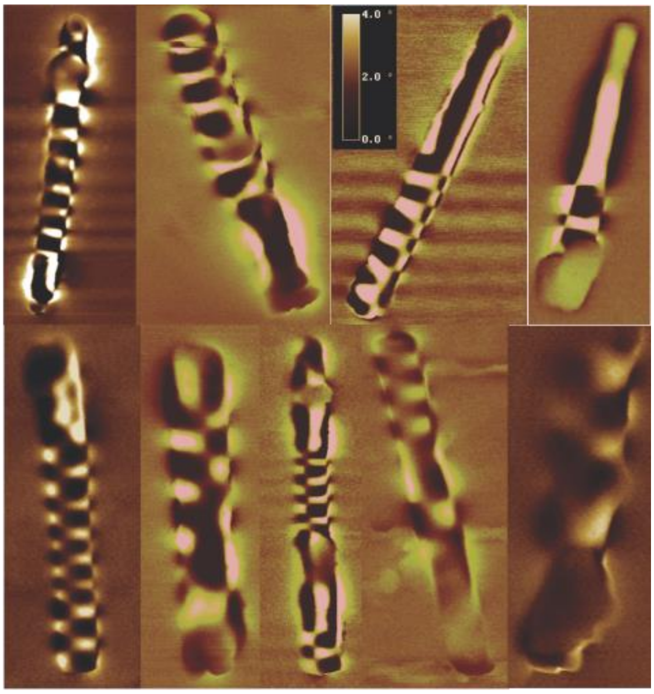

Figure 2: Periodic domain structure along the length of the Co-Pt nanowires with diameter around 200 nm.

II. Nanostructures with tube-wire morphology

We have successfully fabricated Co-Pt nanostructures with 200 nm diameter with tube-wire morphology as shown in Fig.3. We have studied their magnetization reversal and it turns out that transverse as well as vortex domain wall nucleation contribute to the magnetization reversal depending on the geometrical parameters. A plateau (kink) in the hysteresis curve (Fig. 4a) was observed which may be attributed to the partial pinning of the domain walls at the tube-wire interfaces.

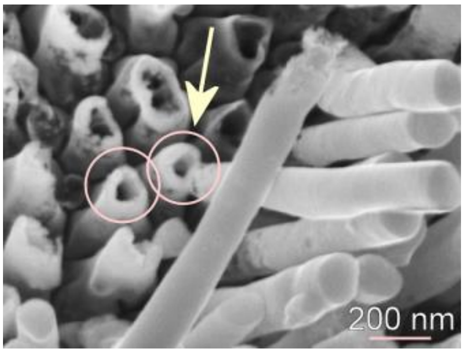

Figure 3: SEM image of nanostructure with tube-wire morphology.

We have performed micromagnetic simulation using a micromagnetic simulator [4] based on Landau-Lifshitz-Gilbert equations. Co-Pt nanostructures with tube-wire morphology were invested and we found out that this kink is present in the hysteresis loop as shown in Fig. 4b. This kink is representing a partial domain pinning during the magnetization reversal at the interface between tube and wire. [5]

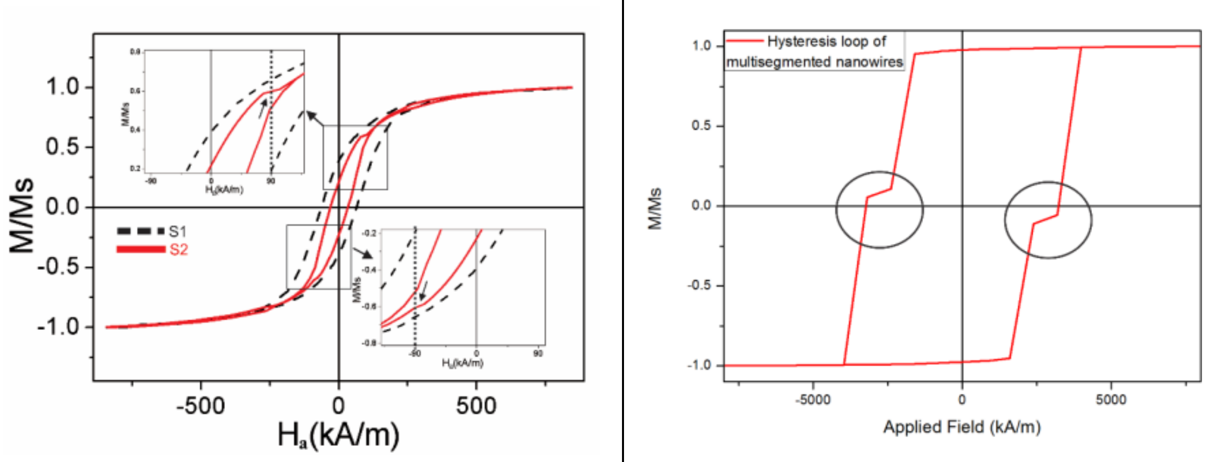

Figure 4a: Hysteresis loop of nanostructure with tube-wire morphology. **b:** Simulation hysteresis of nanostructure with tube-wire morphology

Pinning of the domains at the interface is represented in simulation as shown in Fig. 5.

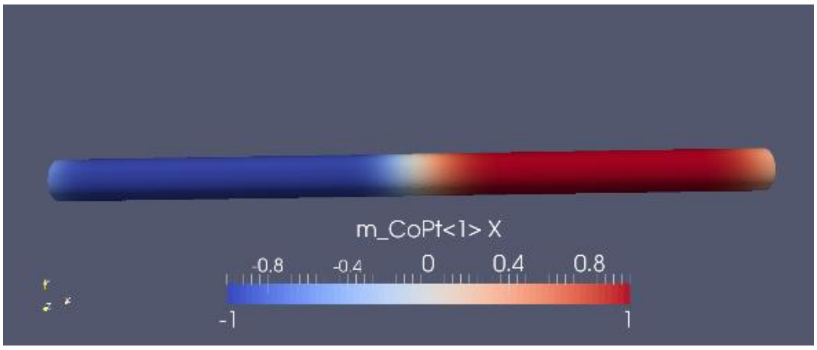

Figure 5: Micromagnetic simulation results of nanostructure with tube-wire morphology showing domain pinning at the interface between tube and wire.

III. Pinning of domain wall with physical notches on Nanowires

Recently a focused ion beam (FIB) was utilized to produce notches with different sizes and shapes along the length of the Co-Pt NWs with 50 nm diameters. MFM imaging was applied to observe magnetic domain patterns in NWs lying horizontally on substrates. In order to inject the domain walls into the wire a magnetic field (~500 Oe) was applied perpendicular to NW axis. We were successful to trap the domain walls in the Co-Pt NWs at the induced notches with the depth ~50% of the NWs diameters as shown in Fig. 6. However, further optimization of notches in the Co-Pt NWs is necessary in order to utilize them for racetrack memory devices. Moreover, micromagnetic simulations of notched NWs are in progress which will be followed by spin-induced domain wall motion experiments in the future.

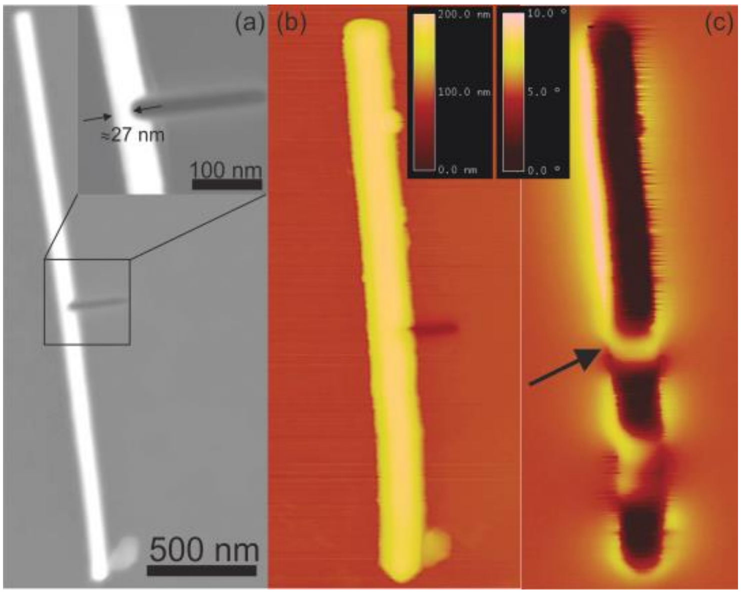

Figure 6: (a) SEM image of the Co-Pt nanowire with a notch in the middle, (inset) closeup image of the notch area. (b) AFM image (c) MFM image

References:

[1] http://researcher.watson.ibm.com/researcher/view_group_subpage.php?id=3811, 04-04-2015.

[2] S. S. P. Parkin, M. Hayashi and L. Thomas, "Magnetic Domain-Wall Racetrack Memory," *Science* vol. 320, pp. 190-194, 2008.

[3] M. S. Arshad, S. Šturm, J. Zavašnik, A. Espejo, J. Escrig, M. Komelj, P. McGuiness, S. Kobe and K. Rožman, "Effect of magnetocrystalline anisotropy on the magnetic properties of electrodeposited Co–Pt nanowires," *Journal of Nanoparticle Research* vol. 16, pp. 1-16, 2014.

[4] Nmag — a micromagnetic simulation environment, http://www.soton.ac.uk/~fangohr/nsim/nmag, 2012.

[5] M. S. Arshad, D. Pecko, S. Sturm, J. Escrig, M. Komelj, P. J. McGuiness, S. Kobe and K. Z. Rozman, "Angular Dependence of the Coercivity in Electrodeposited Co-Pt Nanostructures With a Tube-Wire Morphology," *IEEE Trans. Magn.* vol. 50, pp. 1-4, 2014.

For wider interest

Magnetic hard disk drives have been the prime repository of digital data for more than half a century. Over this period of time, the area of one magnetic bit, use to store information has decreased in size by about around nine order to magnitudes; it is now so tiny that it is reaching fundamental limit that are difficult or too expensive to overcome. A number of alternatives to the magnetic disk drive have been suggested. Among them racetrack memory devices seems to be potential candidates and close to the realization. Such devices are based on magnetic nanowires with magnetic domains which can be move with electrical current. In this article we have presented the possibilities to produce such nanowires which can be utilized in racetrack memory devices and we have also presented the methods to manipulate magnetic domains in nanowires.

Kazalo Avtorjev (List of Authors)

Sodelujoča podjetja in organizacije:

Institut
”Jožef Stefan”
Ljubljana, Slovenija

ISO Fd Food ERA Chair
Safety
Quality
Traceability

greener

ADORA

IZVOR
by OriginTrail

SPIRIT SLOVENIJA
JAVNA AGENCIJA
I FEEL SLOVENIA

REPUBLIKA SLOVENIJA
MINISTRSTVO ZA GOSPODARSKI
RAZVOJ IN TEHNOLOGIJO

LJUBLJANSKI UNIVERZITETNI
INKUBATOR


ECO
samples
compounds
tea
bread
mercury
high
products
temperature
activity
separation
release
environment
provide
care
milk
gas
MoS2
PPCPs
organic
applied
chromatographic
fractionation
materials
fate
results
different
work
confirm
spite
run
exist
human
data
information
stable
enables
Monolithic
experiments
presence


IPS
materials
magnetic
nanoparticles
new
applications
properties
high
methods
network
sensor
sensors
coding
compounds
activity
model
drug
data
using
process
system
based
samples
learning
wireless
machine
information
node
mercury
organic
physical
human

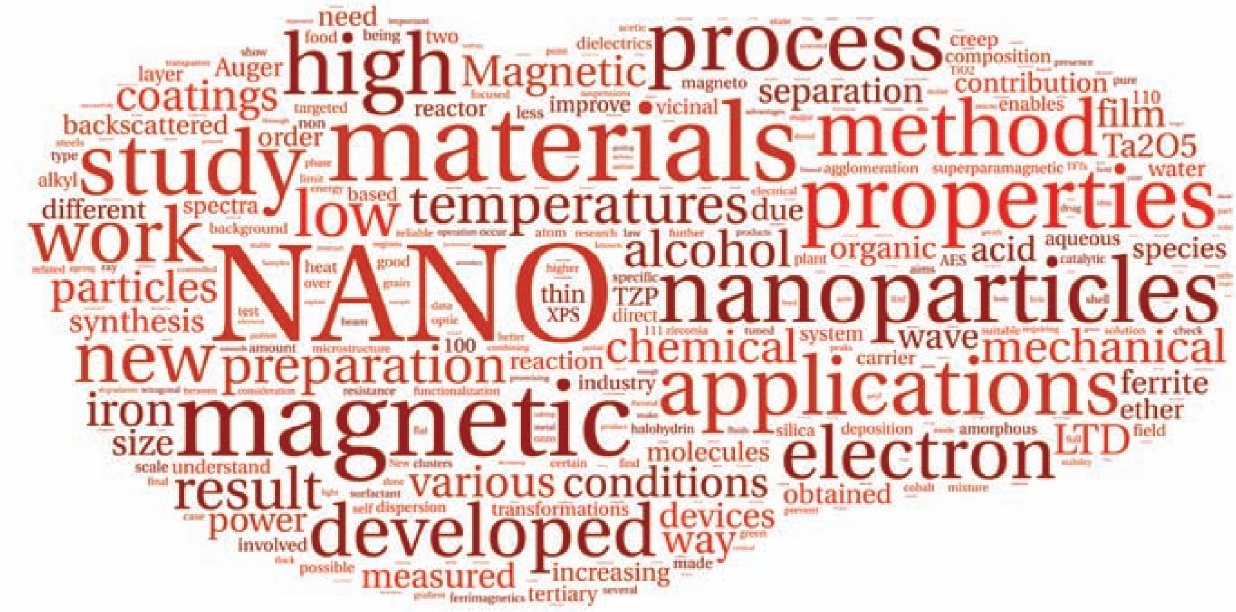
NANO
materials
magnetic
nanoparticles
properties
process
high
study
method
applications
temperatures
electron
developed
new
work
low
preparation
particles
synthesis
alcohol
chemical
mechanical
Magnetic
coatings
separation
result
various
conditions
iron
size
power
measured
devices
way
film
Ta2O5
LTD
ferrite
reaction
organic
acid
species
wave
film

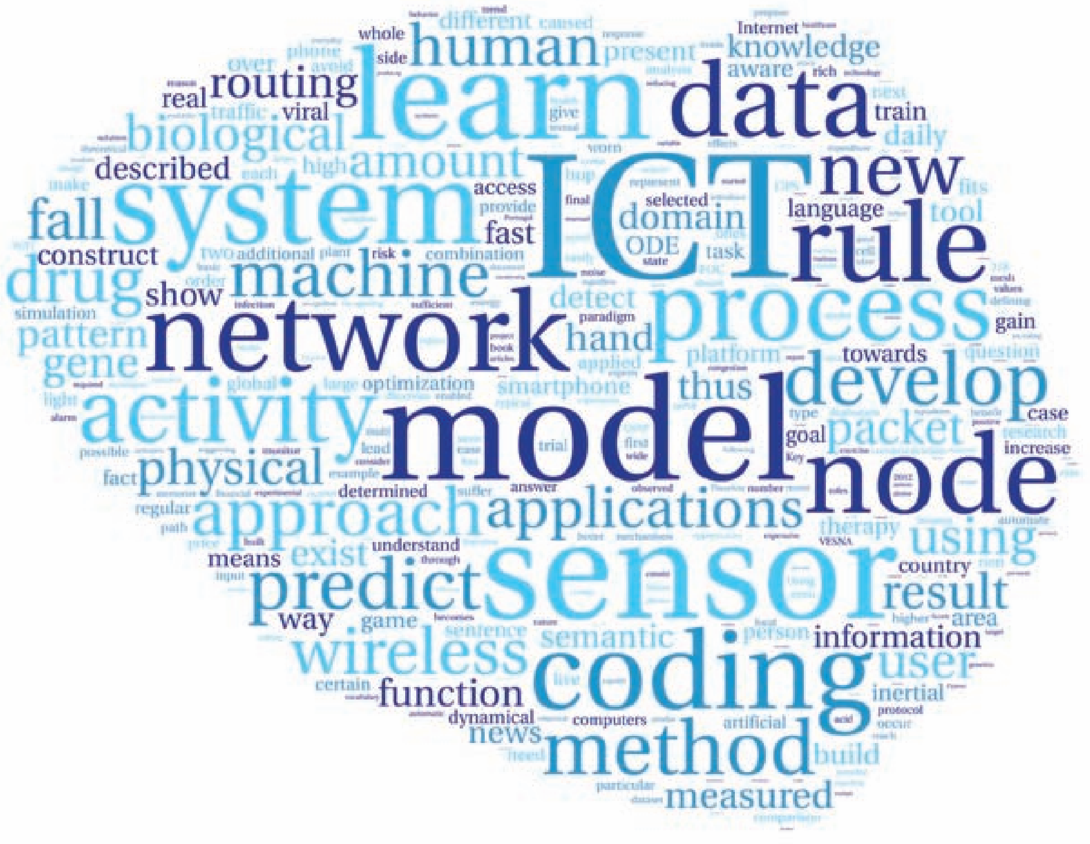
ICT
model
network
learn
data
system
rule
process
sensor
coding
node
activity
approach
develop
method
applications
new
human
machine
predict
wireless
physical
drug
biological
routing
amount
domain
fall
packet
using
result
user
information
semantic
function
measured
build
knowledge
pattern
gene
hand
thus
tool
language

MEDNARODNA
PODIPLOMSKA ŠOLA
JOŽEFA STEFANA

JOŽEF STEFAN
INTERNATIONAL POSTGRADUATE SCHOOL

Jamova 39, SI-1000 Ljubljana

T +386 (0)1 477 31 00
F +386 (0)1 477 31 10

E info@mps.si
www.mps.si

ISBN 9789619287194

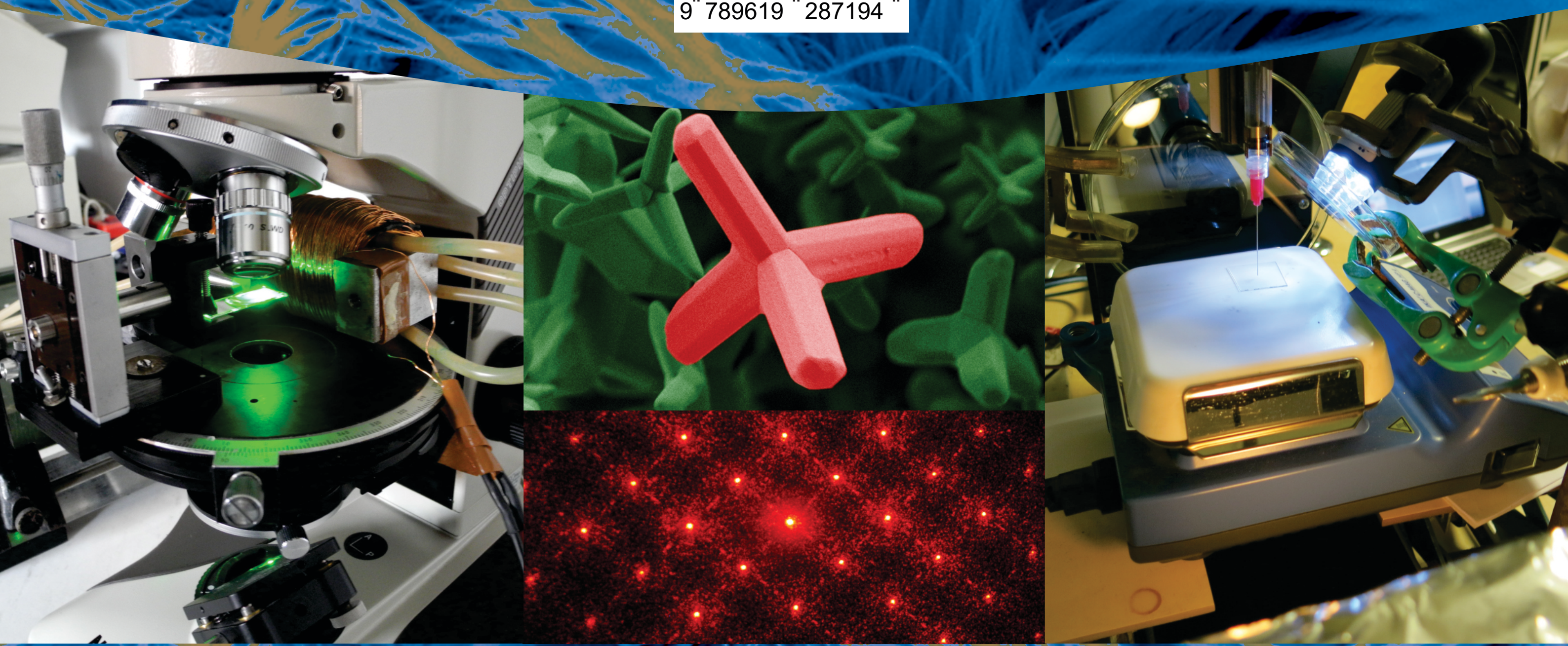

20. - 21. 05. 2015, Ljubljana